NASA CR-143745

OPTO-MECHANICAL SUBSYSTEM OF A 10 MICROMETER WAVELENGTH RECEIVER TERMINAL

•

WAVEGUIDE LASER LOCAL OSCILLATOR

•

SERVO SYSTEM

FINAL REPORT

MARCH 1975

•

NASA Contract No. NAS 5-21859

Prepared By

HUGHES AIRCRAFT COMPANY

Prepared For

NATIONAL AERONAUTICS AND SPACE ADMINISTRATION

GODDARD SPACE FLIGHT CENTER

GREENBELT, MARYLAND

SCG 50096R

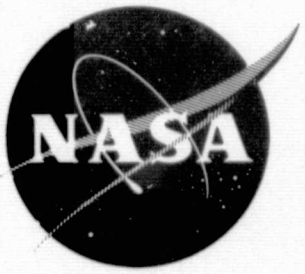

OPTO-MECHANICAL SUBSYSTEM OF A 10 MICROMETER WAVELENGTH RECEIVER TERMINAL

•

WAVEGUIDE LASER LOCAL OSCILLATOR

•

SERVO SYSTEM

FINAL REPORT

MARCH 1975

•

NASA Contract No. NAS 5-21859

Prepared By

HUGHES AIRCRAFT COMPANY

Prepared For

NATIONAL AERONAUTICS AND SPACE ADMINISTRATION

GODDARD SPACE FLIGHT CENTER

GREENBELT, MARYLAND

SCG 50096R

CONTENTS

1. INTRODUCTION AND SUMMARY

The objective of this program is to develop an engineering model opto-mechanical subsystem for a 10.6 μm laser heterodyne receiver, and to provide the CO_2 waveguide local oscillator and servo electronics for the receiver. This final report, Contract NAS 5-21859, combines the previously published interim test report on the opto-mechanical subsystem with the final reports on the waveguide local oscillator (Section 9) and the servo control subsystem (Section 10).

The complete 10.6 μm receiver requires the receiver front end, consisting of the detector and wideband preamplifier; the receiver back end, consisting of the IF, doppler tracking, and data demodulation electronics; and the radiation cooler for detector cooling. The back and front ends were built by Airborne Instruments Laboratory; the cooler is being developed by A. D. Little Company. These components are currently being integrated into a complete receiver package by Hughes under a separate contract.

1.1 OPTO-MECHANICAL SUBSYSTEM

1.1.1 Design Goals

An important characteristic of the 10.6 μm laser heterodyne system concept is that, unlike optical systems using direct detection, solar background has very little effect on the heterodyne system. Advantage can be taken of this feature in space only if satisfactory solutions can be found to the thermal problems encountered with the sun's energy entering the aperture of the optical system. The primary goal of the design phase, therefore, has been to achieve a design of good thermal/mechanical as well as optical characteristics.

A direct way to keep solar energy out of the aperture of the system is through the use of a germanium window appropriately coated to reflect most of the sun's energy. The germanium window is, however, heavy and expensive, and limits the wavelength of operation (such as for a beacon) to wavelengths longer than about 2 μm. The secondary goal, therefore, has been to achieve a design having direct exposure to the sun without the use of a germanium window.

The technical approach to the OM design was to achieve the above general goals within the more specific program schedule and equipment specifications.

1.1.2 Assumptions and Guidelines

The following assumptions and general guidelines were used in the design approach of the receiver opto-mechanical subsystem:

- The receiver subsystem will operate on a synchronous satellite capable of receiving signals from a low altitude or earth-based transmitter station.
- The receiver subsystem assumes a thermal/mechanical spacecraft interface similar to that for ATS-G.
- The optical heterodyne receiver will use a tunable CO_2 waveguide laser as a local oscillator and as developed as a separate task under this contract.
- The optical aperture of the receiver subsystem will be exposed to direct solar radiation.
- The detector will be cooled with the A. D. Little passive radiation cooler as described by Gabron at the 20th IRIS Symposium, May 1972, design details provided through NASA/GSFC, Sk-11972-1, Rev. B.
- Piezoelectric beam steerers, GTE Model PBM-8G, will be used as beam steering elements in the receiver subsystem (Appendix A).
- The beacon to be used for acquisition and tracking modes will be the Sperry Rand 250 watt gallium aresenide laser illuminator (Appendix B), although the detailed optical design of this beacon is not required in this program and is not included in the report.
- Critical optical elements, including the pointing mirror, primary mirror, secondary mirror, and diagonal folding mirror are made of beryllium.
- The OM structure is made of beryllium.
- Optical coatings will be of high solar reflectivity such as OCLI No. 6065001 (see Appendix C) having a total integrated solar absorptivity of 3.6 percent.

1.1.3 Achievements

The theoretical performance of the receiver optical system is essentially ideal. The confocal arrangement of the folded Gregorian system leads to zero spherical aberration on-axis, and negligible coma and astigmatism off-axis. What is more important is that the configuration can withstand relatively large misalignments without noticeable deterioration in the signal and is therefore particularly suitable for space applications.

An opto-mechanical design has been achieved that can operate with negligible distortion while directly exposed to the sun. The optical performance evaluation during the worst case conditions shows a signal loss of only 1.5 percent, a value considered negligible from a system point of view. The design assumed the use of beryllium optics isothermally mounted with the best solar rejection coatings. It is clear that considerable relaxation of specifications of components could be tolerated without seriously affecting the optical performance.

The optical system selected is an all reflective system that permits the use of any wavelength from the visible through the far infrared. The 0.9 μm gallium aresenide laser beacon can therefore be diplexed through the same optical system as described in this report.

The OM package design is intended for laboratory test purposes only, but can be upgraded to a flight prototype configuration without basic design changes. The guidelines used in the design of the structure are based on proven flight optics hardware and proven laser heterodyne techniques. The package size is approximately 10 x 10 x 22 inches, weighs 25 pounds, and has a maximum diagonal dimension of 23.5 inches.

The gimbal design has the capability of operating closed loop with the GT&E beam steering elements while acquiring and tracking a 10.6 μm signal. The stepper motor design is somewhat different than that originally proposed in order to provide a basis for a workable closed loop configuration. The servo system design is reported in Section 9 of this report.

Table 1-1 lists the important design specifications for the OM receiver subsystem as compared with the values achieved in the Hughes design. The Hughes design meets or exceeds all of the design specifications, and easily meets the test specifications. (Section 7 of this document reports the testing of the subsystem against Specification GSFC 524-P-1.)

TABLE 1-1. COMPARISON OF DESIGN SPECIFICATIONS AND PROGRAM DESIGN RESULTS

Parameter	Design Specification	Hughes Design
Weight	25 lb maximum	24.78 lb
Volume of structural frame	2500 in^3 maximum	2349 in^3
Diagonal	27 in. maximum	24 in.
Antenna gain over 0.26° field of view	93 dB minimum	93.7 dB
Gimbal coarse pointing range	±10°	±10°
Pointing accuracy	0.02°	0.02°
Step size	0.06° maximum	0.002°
IMC pointing accuracy (reset)	0.0083°	0.0083°
Beam tilt at mixer	2.5×10^{-3} rad maximum	1.76×10^{-3} rad
Parameter	**Test Specifications**	**Hughes Design**
System loss	3.0 dB maximum	2.18 dB
Loss at 0.13° off-axis	1.0 dB maximum	0.01 dB
Loss in 1 g environment (any orientation)	1.0 dB maximum	0.0 dB

1.2 WAVEGUIDE LASER LOCAL OSCILLATOR

1.2.1 Design Goals

The purpose of the waveguide laser local oscillator task was to increase the tuning range of the local oscillator in the receiver. A minimum tunability of ±200 MHz from line center was specified to accommodate the AIL tracking receiver electronics. A design goal of ±800 MHz was included in an attempt to completely accommodate the doppler shift encountered in low-altitude-to-synchronous links.

1.2.2 Achievements

Using a circular bore waveguide laser, a 3 dB tuning range of ±300 MHz was achieved. Power output at line center is 600 mW with less than 20 watts of power dissipation in the tube. The development of this unit has led to more advanced metal-ceramic fabrication techniques; later models with square bores and greater tuning range are now under development under Contract NAS 5-20623.

1.3 OPTO-MECHANICAL SERVO SYSTEM

1.3.1 Requirements and Constraints

The basic requirement of the servo system is that it acquire and track a signal anywhere within the 20° by 20° field of view of the gimbals. Further, the peak tracking error must be such that the communication signal-to-noise

ratio is not significantly degraded. The 3 dB beamwidth of the system is 80 μ rad. The maximum target rate assumed during acquisition is 0.03 deg/sec.

The general requirement for the servo system is that it be space qualifiable, have the basic capability for long life, and operate on low electrical power. All three of these requirements tend to favor the use of stepper motors and dry lubrication gears to achieve the gimbal motion. Thus the stepper motor-gear configuration was used.

1.3.2 Design Goals and Achieved Performance

A static tracking error of 7 μrad was achieved against a goal of 5 μrad. A peak tracking error of 70 μrad with stepper disturbance was achieved as compared with a 50 μrad goal. The large peak error during a step is caused by the 45 Hz mechanical resonance of the mirror in the tilt axis. Although good tracking stability is maintained, the S/N dip of about 7 dB in the communication channel is too large for space flight equipment. Reduction of the step size to one-half its present value, lighting the pointing mirror, and stiffening the gimbal are recommended for any flight program.

This effort has demonstrated that conical scan-track techniques are sufficiently precise and reliable to be useful for space-laser applications. This permits dual use of the single-point detector, i.e., for communications as well as acquisition and tracking.

2. OPTICAL DESIGN

2.1 OPTICAL TRADEOFFS

The optical tradeoff study reviewed a number of possible optical designs with respect to their applicability to the receiver subsystem. Computer design analysis of each of the trial configurations was conducted in order to evaluate its respective optical performance. Each of the configurations was optimized in order to take advantage of its strong points and work around its weak points. As a result, four configurations were considered. These are described in the same order in which they were reviewed along with the pros and cons of each design.

2.1.1 Newtonian

This configuration features the use of refractive elements in a configuration in which the focus is relayed back to provide accessibility for field stop and image motion compensators (IMCs), and to avoid space interference with the pointing mirror gimbal system. It also employs the use of a hyperboloidal primary mirror as a means of reducing the spherical aberration of the system. The layout of this configuration is shown in Figure 2-1.

Advantages

- Essentially perfect performance on- and off-axis.
- Accessibility of relayed focus.
- Full use is made of the primary mirror (16 cm diameter) since there is no central obscuration and no vignetting.
- Excellent rejection of solar radiation.

Disadvantages

- Refractive elements introduce loss and are temperature sensitive.

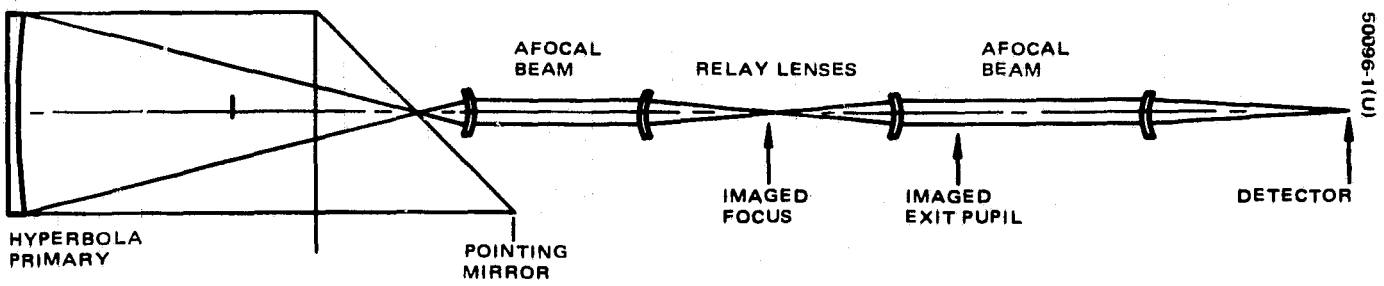

FIGURE 2-1. NEWTONIAN I SYSTEM: HYPERBOLOIDAL PRIMARY – FOUR SPHERICAL GERMANIUM LENSES

- The four refractive optical elements, in addition to the two reflective elements and detector element, complicate the optical alignment and stability problem.
- Hyperbolic primary makes checking of primary element difficult.

The results are that of excellent optical performance.

2.1.2 Gregorian

The Gregorian offers exceptionally fine optical performance because of the nearly confocal arrangement of the primary and secondary elements. The confocal nature of the mirrors provides elimination of spherical aberration and coma over a substantial field of view.

The configuration was not strongly considered at first because it lacks the excellent solar rejection capability of the Newtonian arrangements. During the study, it was realized that the central obscuration can be made very small and that the solar rejection can be improved by optimization of the elements' positions. The layout of this configuration is shown in Figure 2-2.

Advantages

- Perfect optical performance on- and off-axis.
- Paraboloidal primary permits easy testing of that element.
- All reflective system permits convenient system test with visible light or use of two wavelengths.
- Moderately good rejection of solar radiation.

Disadvantages

- IMC must be located extremely close to secondary optical elements.

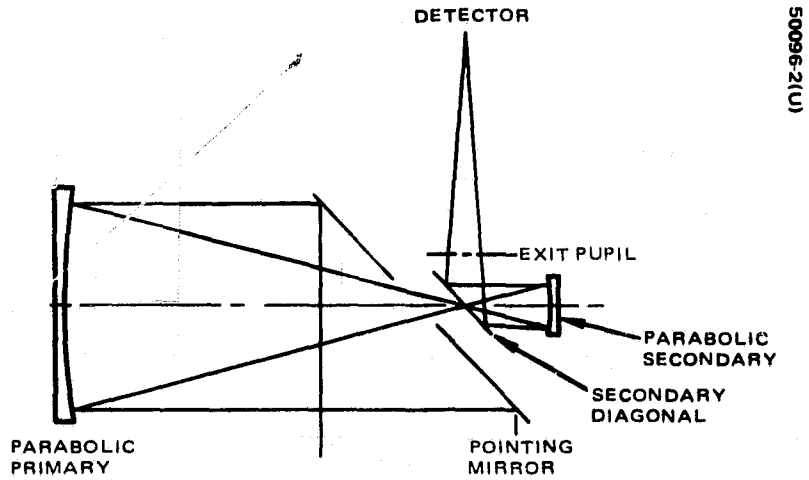

FIGURE 2-2. GREGORIAN SYSTEM: PARABOLOIDAL PRIMARY – NEAR CONFOCAL ELLIPSOIDAL SECONDARY EXCELLENT OPTICAL PERFORMANCE

- Vignetting and central obscuration require the use of a 18.2 cm diameter primary and 18.2 x 25.7 cm pointing mirror, 30 percent more mass than used for Newtonian systems.

The results are that of excellent optical performance.

2.1.3 Newtonian II

Because of the excellent solar rejection capability of the Newtonian concept and the efficient use of the telescope aperture, a second Newtonian configuration was considered. This configuration was aimed at eliminating the use of the relay lenses that required changing the gimbal design to allow the IMC elements to be located close to the secondary. Further, using a parabolic primary mirror rather than a hyperbola to permit easy checking of the figure of the primary was desirable. The results of this design approach are disappointing for several reasons as can be seen in the list of disadvantages. The layout of this configuration is shown in Figure 2-3.

Advantages

- Good performance on-axis.
- Excellent solar rejection.
- Full use is made of primary mirror (16 cm).

Disadvantages

- Secondary lens requires four elements introducing loss and these are temperature sensitive.

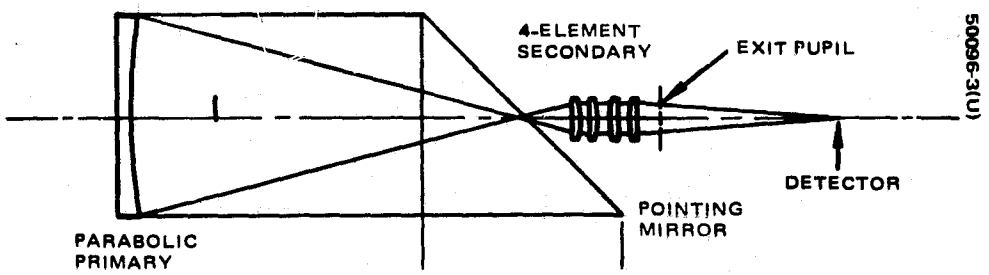

FIGURE 2-3. NEWTONIAN II SYSTEM: PARABOLIC PRIMARY – FOUR ELEMENT SECONDARY INCLUDING ASPHERIC ELEMENT

- Off-axis performance of telescope is not acceptable; >20 percent loss is realized at 0.13° off-axis.
- The beam is 1 1/4 inches in diameter at the exit pupil and requires a larger IMC.

The results show that off-axis performance is unacceptable.

2.1.4 Cassegrain

During the proposal effort, the cassegrain configuration was believed to have had something to offer in compactness and in being an all-reflective system. The particularly difficult problem of phase matching the signal and local oscillator (LO) beams was solved by introducing the LO beam at the position of the image of the exit pupil. During this study, however, it was learned that with the requirements for an f/8 signal beam, IMCs are incompatible with the cassegrain system. These findings are evident from the sketch in Figure 2-4. Thus, if an f/2 primary were employed, the cassegrain focus would be located at the primary mirror position. If an f/1.5 primary is employed, the cassegrain focus is only 6 cm behind the primary mirror. The cassegrain can be used to advantage only in cases where the IMCs are not required and where the detector may be located at the primary mirror.

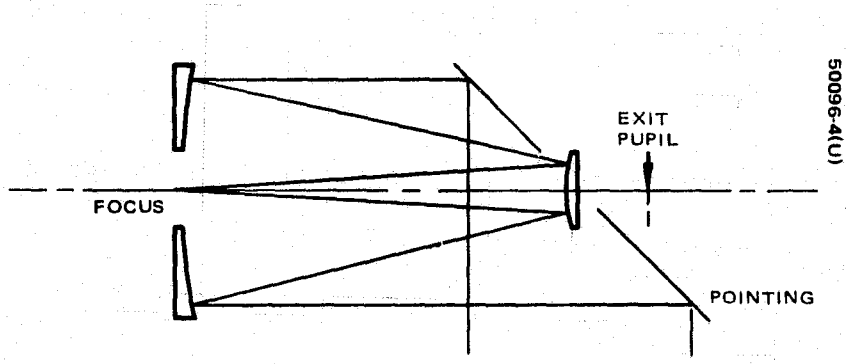

FIGURE 2-4. CASSEGRAINIAN SYSTEM: CONSTRAINTS OF f/2 PRIMARY AND f/8 CASSEGRAIN PLACE PRIMARY FOCUS AT PRIMARY MIRROR

Advantages

- None

Based upon the results of optical performance analysis and the consideration of thermal and mechanical factors, it was concluded that the Gregorian configuration prepresented the best compromised design solution for the heterodyne receiver.

In this report, the finalized Gregorian system is presented in paragraph 2.2, where an optical schematic layout of the design is also shown. A discussion of the misalignment tolerances in terms of the degradation in the relative peak intensities is given in 2.3. In connection with the thermal analysis of the pointing mirror, the out-of-focus patterns of the image of the sun at six different positions across the mirror surface have been examined, and graphical results are described in 2.4. Finally, a scheme of incorporating a beacon in the receiver system is briefly discussed in 2.5.

2.2 GREGORIAN HETERODYNE RECEIVER SYSTEM

A schematic optical layout and the optical characteristics of the Gregorian receiver system are presented in Figure 2-5 and Table 2-1, respectively. The ellipsoidal secondary mirror is located so that its first focus coincides with the focus of the paraboloidal primary, and the final image is located at the second focus of the secondary. The f number of the system is f/8.0. The input acquisition field is 20° x 20°, and this is achieved with the pointing mirror covering a range of scan of ±5°, about the nominal 45° tilt relative to the optical axis, and a range of roll of ±10°. The pointing accuracy of this gimbal-mounted mirror is ±0.13°, and this defines the field coverage of the receiver system.

The axial input signal beam, after reflecting off the pointing and primary mirrors, is brought to a focus at the center of the folding mirror (see Figure 2-5). The signal beam is then reflected off the secondary, and directed toward the image motion compensators via the folding mirror. In the nominal setup, the pair of IMCs are tilted at 45° relative to the optical axis; and the axial input beam, after reflecting off the IMCs, is focused onto the on-axis detector.* For off-axis inputs, the IMCs are suitably tilted so that the signal beam is once again focused on the same on-axis detector.

2.2.1 Location of Image Motion Compensators

The most favorable location of the IMCs would be at the exit pupil of the receiver system; this location makes possible the IMCs perfectly

*The detector is located on the nominal optical axis of the system with a diameter of 0.207 mm. The size of detector is matched to the Airy disk diameter of the f/8 system.

SURF	ELEM	DWG	RAD	MATERIAL	THK	OUTER LIMIT RAY	INNER LIMIT RAY
1	GUARD SHIELD		∞	AIR	10.478	11.086	1.218
2	I		∞	AIR	36.873		
3	II		-82.265 BASE R.D. 14.150 BASE R.D.	AIR	-50.292	8.388	1.245
4	III		∞	AIR	9.291	2.144	.186
5	IV		∞	AIR	4.053		
6	V		∞	AIR	1.270		
7	STOP		∞	AIR	1.270	.957	.144
8	VI		∞	AIR	3.175		
9	VII		∞	AIR	5.398		
10	VIII		∞	G_a	.200		
11			∞	AIR	5.478		
12			∞			.300	

OPTICAL CHARACTERISTICS	
EQUIVALENT FOCAL LENGTH	132.080 CM
F-NUMBER OF SYSTEM	8.0
F-NUMBER OF PRIMARY	2.22
F-NUMBER OF SECONDARY	1.94
FIELD OF VIEW	±0.13°
INPUT ACQUISITION FIELD	20° X 20°
ACTUAL DETECTOR SIZE	.207 MM

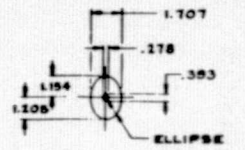

COMBINING MIRROR BEAM PATTERN

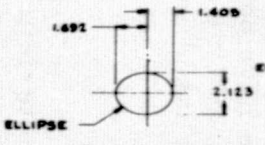

1ST IMC MIRROR BEAM PATTERN

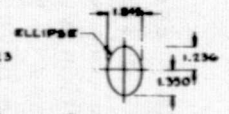

2ND IMC MIRROR BEAM PATTERN

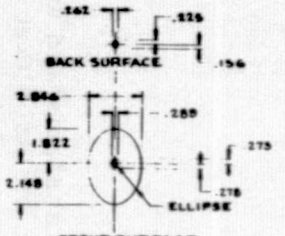

FOLDING MIRROR BEAM PATTERN

9 PARABOLOIDAL, C.C. = -1.0

99 ELLIPSOIDAL, C.C. = -.28264

ALL DIMENSIONS ARE IN CENTIMETERS

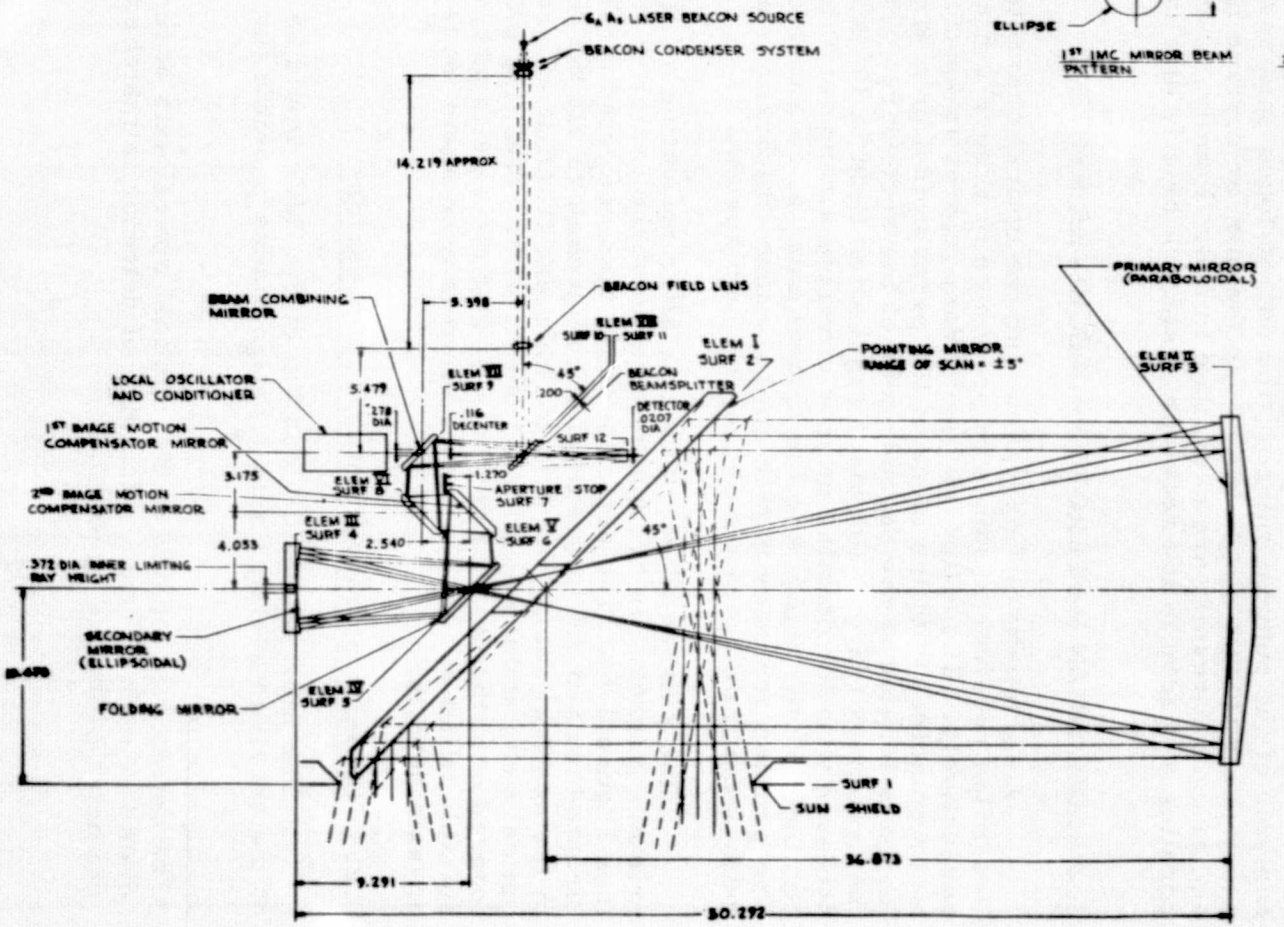

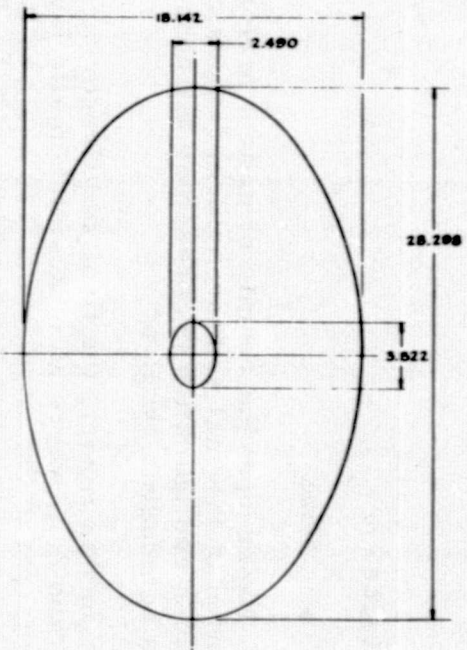

FIGURE 2-5. 10.6 MICROMETER LASER HETERODYNE RECEIVER OPTICAL LAYOUT

TABLE 2-1. OPTICAL CHARACTERISTICS OF GREGORIAN HETERODYNE RECEIVER

Parameter	Value
Design configuration	Gregorian system with paraboloidal primary and ellipsoidal secondary
Diameter of primary	18.50 cm
Diameter of secondary	4.80 cm
Diameter of input beam	16.50 cm
Diameter of exit pupil	1.92 cm
f number of system	8.00
f number of primary	2.22
f number of secondary	1.94
Focal length of primary	41.00 cm
Focal distances of secondary	9.291 cm
	30.135 cm
Magnification	4.41
Separation: primary/secondary	50.292 cm
Spectral region	10.60 μm
Field coverage	$\pm 0.13^{o}$
Input acquisition field	$\pm 10^{o}$
Image diameter	0.60 cm
Distance from center of exit	
Pupil to: a) First IMC	-1.27 cm
b) Second IMC	1.27 cm

realigning the off-axis pupil ray with the nominal optical axis of the system. The advantage of this is that an auxiliary, axial, laser beam of the local oscillator may be conveniently injected into the signal beam path, in between the IMCs and the detector; and if this LO beam is also coaxial with the nominal optical axis, then it would combine coaxially with the signal beams associated with both the on- and off-axis inputs, thereby maximizing the detecting efficiency.

In practice, it is not possible to locate the pair of IMCs precisely at the exit pupil, and the best compromised design solution is that shown in the optical layout (Figure 2-5). Referring to this figure, the aperture stop and the exit pupil of the system are combined, and the first and second IMC are located before and after the stop, respectively. The position of the aperture stop is chosen to provide just sufficient mechanical and optical clearances for accommodating the first IMC above the main optics. Note that, since the IMCs are not precisely located at the exit pupil, it would not be possible for the IMCs to perfectly realign the off-axis pupil ray with the LO beam axis; however, since the IMCs are located very close to the exit pupil, the resulting beam misalignment* associated with the off-axis input is slight and the corresponding loss in efficiency in the signal detection is small.

*The maximum value of the beam misalignment is of the order of 1.76 mr.

When the off-axis signal beam is corrected by the IMCs, the optical deflection produced by the latter will result in the image being slightly defocused at the detector. This effect can be minimized by placing the exit pupil and the IMCs as far back from the detector as possible. The optimum location of the exit pupil is given in the optical layout (Figure 2-5).

2.2.2 Local Oscillator Beam Injection

Referring to Figure 2-5, the LO beam is injected into the signal beam path through the central aperture cutout in the beam combining mirror, and the beam is coaxial with the nominal optical axis of the receiver system. The LO beam is focused at the detector and has an effective f number of f/40. The focusing of the beam is controlled by the LO conditioner unit.

2.2.3 Energy Loss Due to Obscurations

In a lossless optical system with no obscuration, only 84 percent of the energy entering the aperture falls within the Airy disk. For an optical system such as this, with its diameter centrally obscured by 0.2 times the overall diameter, there is 76.5 percent of the energy in the Airy disk. The additional loss caused by the central obscuration is thus 7.5 percent.

In the heterodyne receiver with the detector size precisely matched to the Airy disk of an f/8 signal beam and a coaxial f/40 local oscillator, the heterodyne mixing efficiency is 50 percent of that which could be achieved if all the energy entering the aperture were phase matched with the local oscillator. This complex problem has been analyzed thoroughly and is reported in Section 6. It has been learned, for example, that if the detector diameter is slightly smaller than the Airy disk (72 percent), the mixing efficiency improves to 72 percent of ideal.

2.2.4 Beamsplitter Plate for Laser Beacon

The heterodyne receiver has been so designed that a beacon device may be conveniently incorporated into the system. One approach is as shown in Figure 2-5, in which a 0.9 μm wavelength laser beacon is injected into the receiver optics via a germanium beamsplitter. The beacon beam, after reflecting off the beamsplitter, traverses through the receiver optical train toward the primary and pointing mirrors. If the source was a GaAs laser of 0.042 cm square beam cross section with an output angular coverage of ±20°, then it could be considered as an extended source, and consequently, the beacon beam emerging from the receiver system would be relatively unimpaired by the central obscuration of the receiver optics. Further details related to the beacon device are discussed in Appendix B.

Referring to the beacon beamsplitter in Figure 2-5, its location between the beam combining mirror and the detector was dictated by mechanical packaging requirements. Based on optical coating considerations, it would be advantageous for the beamsplitter to transmit the signal and LO beams (both of 10.6 μm wavelength) and to reflect the 0.9 μm beacon beam.

The performance of the receiver system has been optimized with the beamsplitter in place; because of the f/8 aperture of the receiver and the small thickness (0.2 cm) of the beamsplitter; the final performance of the system is essentially perfect (see following subsection).

2.2.5 Performance Evaluation of Gregorian System

The optical performance was evaluated in terms of the relative peak intensity* (RPI) of the system. The definition of RPI is given by the ratio

$$RPI = \frac{I}{I_o}$$

where I is the peak intensity of the diffraction image in presence of geometrical aberrations, and I_o is the value of I in the absence of aberration. One basic assumption made in the computation of RPI was that the input signal beam arriving at the receiver had a uniform amplitude distribution; this, in practice, is substantially correct, in view of the fact that the receiver is effectively sampling a very small portion of the gaussian amplitude wavefront originated from the distant transmitter. The advantage of considering a uniform amplitude input beam is that, for a highly corrected system, the RPI may be computed directly from Marechal's formula without first having to evaluate the Fraunhofer diffraction integral. Marechal's formula is given by the expression

$$RPI = \left[1 - \frac{2\pi^2}{\lambda^2} E\right]^2$$

for RPI ≥ 0.8, where λ is the wavelength and E is the variance of the wave aberration. For the purpose of performance and tolerance analyses, the range of validity of Marechal's formula is adequate, and the approach of computing RPI based on Equation 1 provides an efficient and direct method for the performance evaluation.

The performance data of the Gregorian heterodyne receiver are presented in Table 2-2, with RPI values computed for different input field angles and for various IMC tilts. The data clearly indicate that the theoretical performance of the receiver is essentially perfect for the 10.6 μm wavelength considered. It is well known that the confocal configuration of the Gregorian system leads to zero spherical aberration on-axis, and negligible coma and astigmatism off-axis when the field coverage is small; what is even more important is that the configuration also can withstand relatively large misalignments without noticeable deterioration in the RPI, and is therefore particularly suitable for space applications. Details concerning the misalignment tolerances are presented in 2.3.1.

*Also known as the Strehl ratio.

TABLE 2-2. PERFORMANCE OF GREGORIAN HETERODYNE RECEIVER

Input Field Angle, deg	Image Height, cm	IMC Tilt (relative to vertical axis)		Relative Peak Intensity
		First IMC, deg	Second IMC, deg	
0	0.0	45	45	0.997
0.13	-0.3	45	45	0.998
	0.0	45.5171	45	0.998
		45	44.3891	0.998
-0.13	0.3	45	45	0.998
	0.0	44.4825	45	0.998
		45	45.6111	0.998

2.3 OPTICAL TOLERANCES

2.3.1 Misalignment and Defocusing Tolerances

For the tolerance study, degraded performances were studied corresponding to the following misalignment and defocusing parameters:

1) Primary mirror tilt

2) Secondary mirror tilt

3) Primary/secondary decentration

4) Primary/secondary separation error

5) Image plane defocusing

The degraded performance of the perturbed system was evaluated in terms of the on-axis RPI at appropriate diffraction focus. The results of the RPI evaluation, corresponding to different amounts of primary and secondary mirror tilts, are presented in Figure 2-6. Referring to this figure, the upper (broken line) curve corresponds to the secondary tilts only: assuming that no vignetting occurs in the optical train (see Figure 2-5), a 0.2° tilt by the secondary mirror results in almost negligible performance degradation. This is not a surprising result since, for a small tilt by the secondary mirror, the on-axis performance should follow closely to the equivalent off-axis performance of the nominal system, and this result serves to confirm the excellent off-axis performance of the nominal system (see Table 2-2). The lower curve (solid line) in Figure 2-6 corresponds to the plot of RPI versus primary mirror tilts, and it can be seen from the graph that the system performance is considerably more sensitive to tilts of the primary than that of the secondary. It should be pointed out here that each of the transverse focal shifts, ΔY, given in Figure 2-6, represents the distance measured from the axial image focus to the corresponding diffraction focus, the latter being the location at which RPI was evaluated.

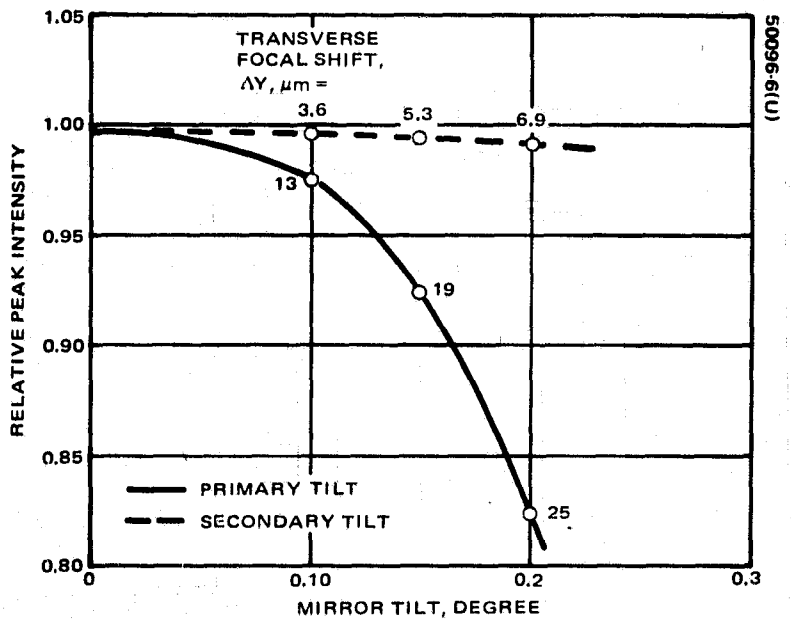

FIGURE 2-6. RELATIVE PEAK INTENSITY VERSUS PRIMARY/SECONDARY MIRROR TILTS

The graph in Figure 2-7 shows RPI versus primary/secondary mirror decentrations; the values of ΔY associated with curve have the same meaning as that just explained. Figure 2-8 presents the plot of RPI versus primary/secondary mirror separation error for a fixed, nominal image plane location. Figure 2-9 shows the effects of image plane defocusing upon RPI; the relatively slow degradation of performance with respect to longitudinal focal shift is a consequence of the large f-number of the system (f/8). The values of RPI are independent of the algebraic signs of the image plane defocus, and consequently, only the positive defocusing is considered in Figure 2-9.

2.3.2 Mirror Surface Tolerances

For diffraction limited optical systems, the RPI value should not fall below the limit of 80 percent. In order to maintain this level of performance, the total misalignment errors, together with the sum of mirror surface errors, should not introduce a resultant wavefront deformation of greater than $\lambda/4$ at the wavelength $\lambda = 10.6$ μm, an amount equal to 8 fringes of 6328 Å light. Based on the analyses of misalignment sensitivity of the receiver system (see 2.3.1), a set of mirror surface tolerance specifications has been established (see Table 2-3). The specifications presented are compatible with standard optical fabrication techniques, and, although the surface tolerances are quite stringent, the specifications are still at the tolerance level where there would be no significant fabrication cost savings even if the tolerances were relaxed by a factor of two. Only if many systems were to be fabricated would there be some advantages in relaxing the specifications to reduce cost and delivery time.

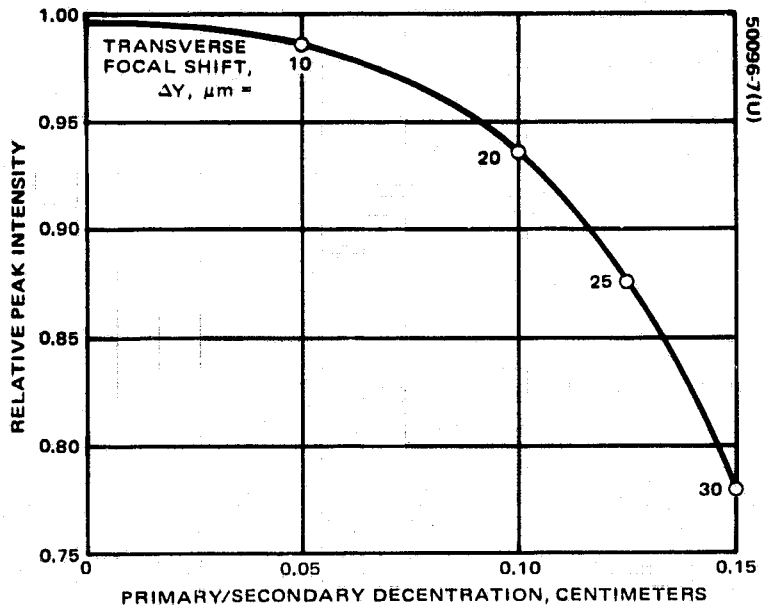

FIGURE 2-7. RELATIVE PEAK INTENSITY VERSUS PRIMARY/SECONDARY MIRROR DECENTRATION

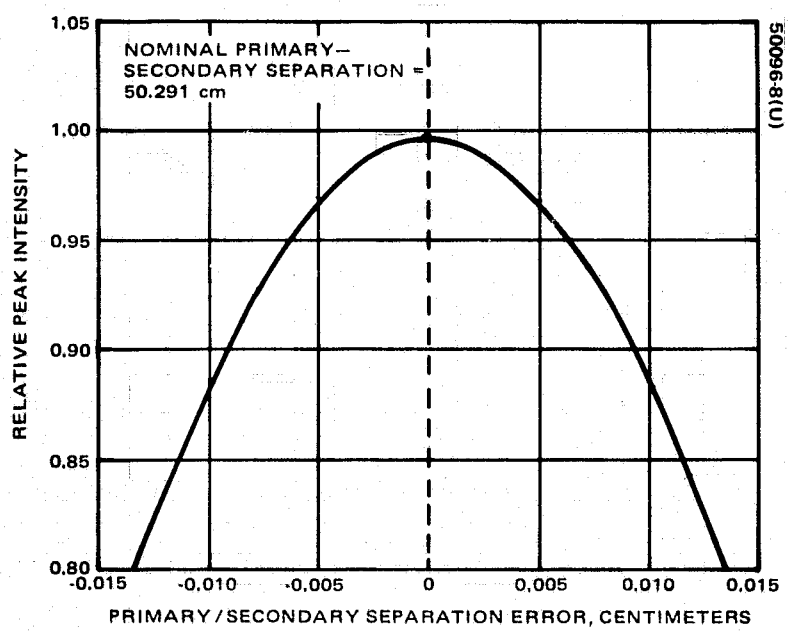

FIGURE 2-8. RELATIVE PEAK INTENSITY VERSUS PRIMARY/SECONDARY MIRROR SEPARATION ERROR

TABLE 2-3. OPTICAL ELEMENTS SURFACE SPECIFICATIONS

Optical Element*	Surface Finish	Surface Figure**
Pointing mirror (I)***	60-40	3 fringes, flat
Primary mirror (II)***	60-40	1 fringe, paraboloid
Secondary mirror (III)***	60-40	1 to 2 fringes, ellipsoid
Folding mirror (IV)*	60-40	1 fringe, flat

Note: For actual test data, see Section 6.

*All elements are beryllium.
**Testing wavelength at 6328Å (HeNe laser).
***Element number (see optical layout, Figure 2-5).

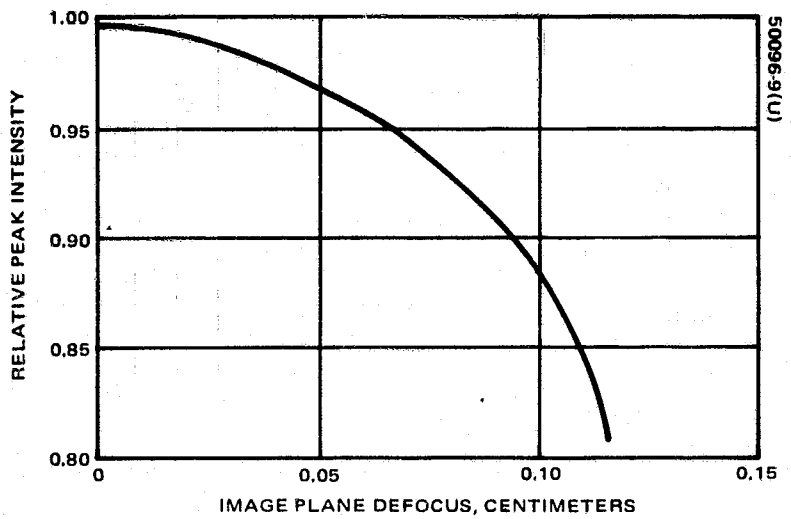

FIGURE 2-9. RELATIVE PEAK INTENSITY VERSUS IMAGE PLANE DEFOCUS

2.4 ANALYSIS OF SOLAR IMAGE BLUR PATTERN ON POINTING MIRROR

Figure 2-5 shows the nominal configuration of the receiver with limiting rays traced corresponding to the field of view of ±0.13°. As the sun traverses across the field of view of the receiver, solar radiation enters the receiver through the sun shield. After reflecting off the pointing and primary mirrors, only input beams that are within the ±0.13° field of view pass through the hole in the pointing mirror; those failing to pass are intercepted by the pointing mirror, thereby giving rise to out of focus patterns of the image of the sun. Over the period of time in which the pointing mirror is directly exposed to sunlight, the solar image blur traced out on the mirror can lead to localized thermal distortion of the mirror surface. Since the

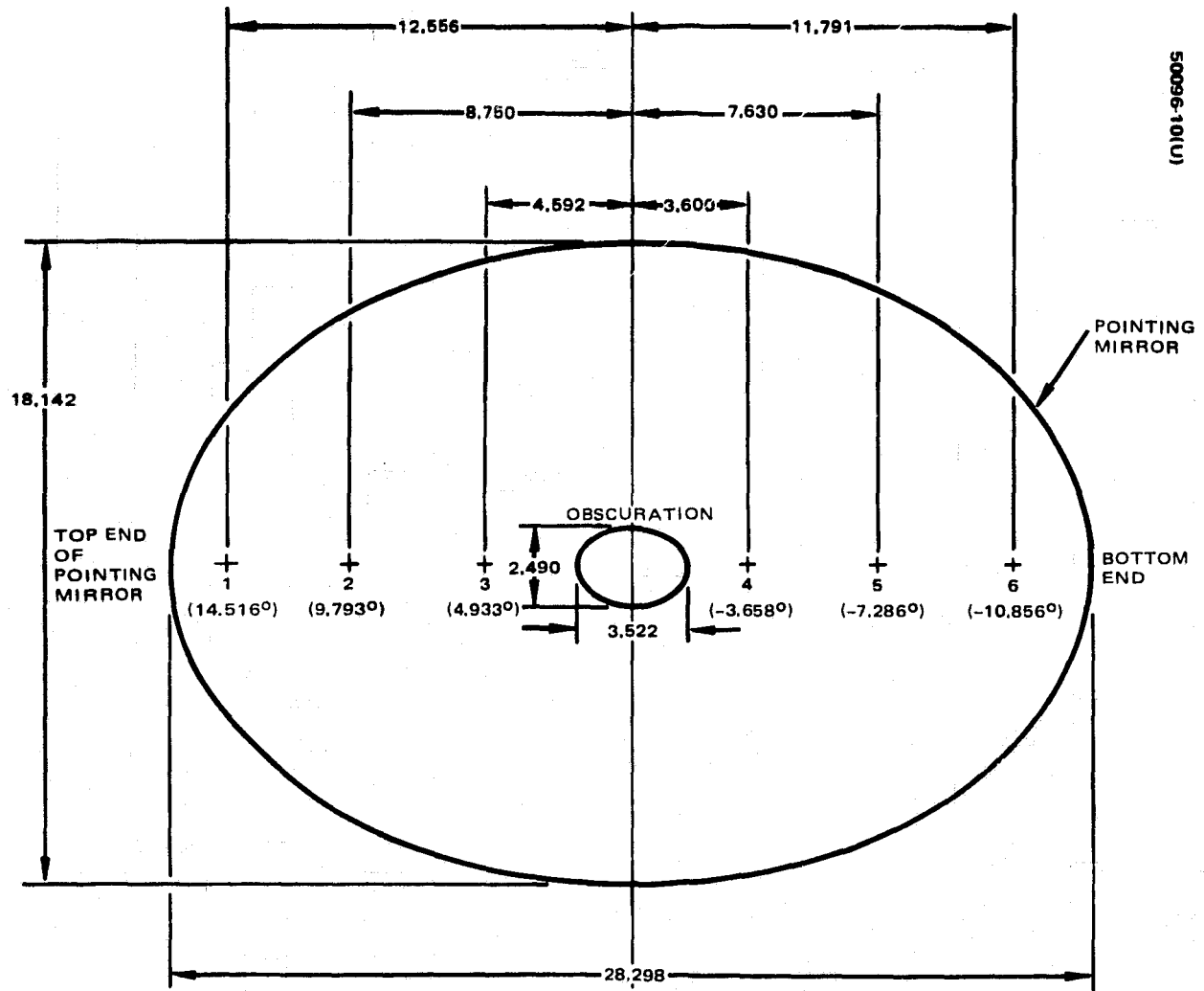

FIGURE 2-10. LOCATIONS OF IMAGE-BLUR CENTROIDS OF SUN ON POINTING MIRROR

heterodyne receiver is designed to operate even during the passage of sun across its field of view, thermal distortion of the pointing mirror surface can lead to phase distortion of the input signal beam. The aim of present study is to evaluate the energy distribution of these solar image blur patterns on the pointing mirror. The results serve as part of the input data for thermal analysis of the pointing mirror.

As shown in 2.1, the pointing mirror has a range of scan of ±5° about its nominal position of 45° relative to the optical axis; however, for the present purpose, only the nominal position of pointing mirror need be considered. It is evident from Figure 2-5 that, as the sun traverses across the field of view, the resulting solar image blur pattern on pointing mirror varies in size.

In the present analysis, a total of six field positions of the sun were considered (the limiting fields of 14.516° and -10.856° were defined by the limiting rays which, after reflecting off the primary mirror, would fall on the upper and lower edges of the pointing mirror): 14.516°, 9.793°, 4.933°, -3.658°, -7286°, and -10.856°. For each field position, 1200 rays were aimed at the pointing mirror*, with the rays distributed uniformly over the mirror surface. The solar image blur pattern on the pointing mirror** was determined by spot diagram and knife-edge analyses, and the energy contained within the image-blur was expressed as a percentage of the on-axis energy transmission.

Figure 2-10 shows the location on the pointing mirror surface, the centroid of energy distribution corresponding to each of the six image blurs. The six solar image blur patterns in question are presented graphically in Figures 2-10 and 2-11; each blur pattern has its centroid position clearly marked and the relative energy content indicated. Thus, referring to Figure 2-11a, field position 1 shows the blur pattern corresponding to the sun at 14.516° off-axis, and the energy contained within the blur pattern is 39.3 percent of the on-axis transmitted energy. Note that, in computing the relative energy values, the input energy at the field angle θ has been corrected by the obliquity factor $\cos\theta$, and that the energy contained within the image blur represents the nonvignetted portion of input energy.

---

*For the present purpose, the pointing mirror may be regarded as the entrance pupil.

**Here the rays were impinging on the pointing mirror for the second time, after reflecting off the primary mirror. In this particular situation, the pointing mirror surface may be considered to be a tilted image surface.

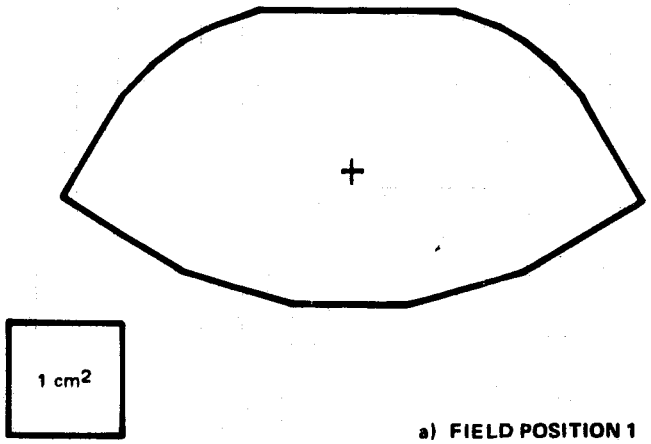

+ CENTROID OF IMAGE-BLUR

50096-11(U)

SUN AT 14.516° OFF-AXIS WITH
IMAGE-BLUR CONTAINING
39.3% OF ON-AXIS ENERGY

a) FIELD POSITION 1

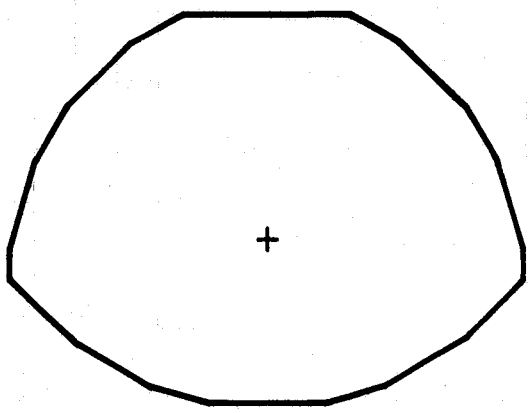

50096-12(U)

SUN AT 9.793° OFF-AXIS WITH
IMAGE-BLUR CONTAINING
64.0% OF ON-AXIS ENERGY

b) FIELD POSITION 2

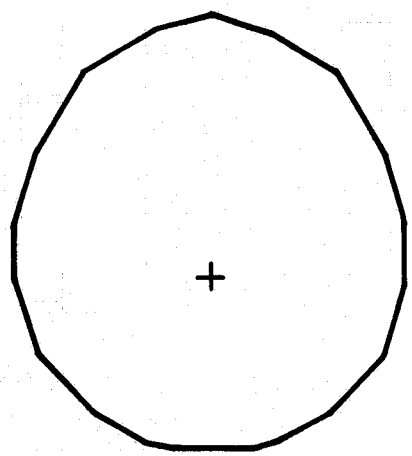

50096-13(U)

SUN AT 4.933° OFF-AXIS WITH
IMAGE-BLUR CONTAINING
87.3% OF ON-AXIS ENERGY

c) FIELD POSITION 3

FIGURE 2-11. EXTENT OF SUN'S IMAGE-BLUR ON POINTING MIRROR

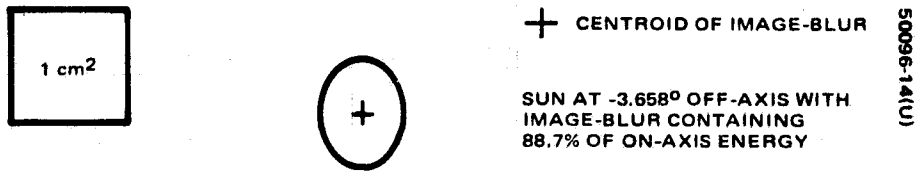

d) FIELD POSITION 4

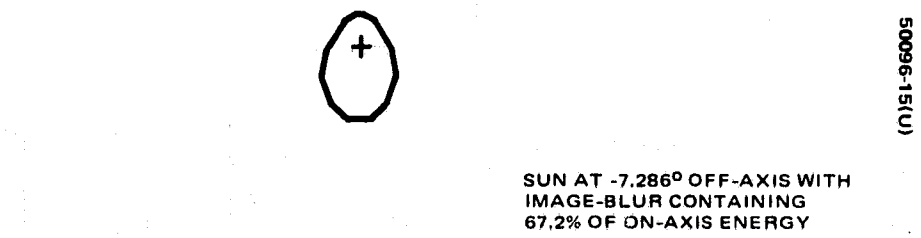

e) FIELD POSITION 5

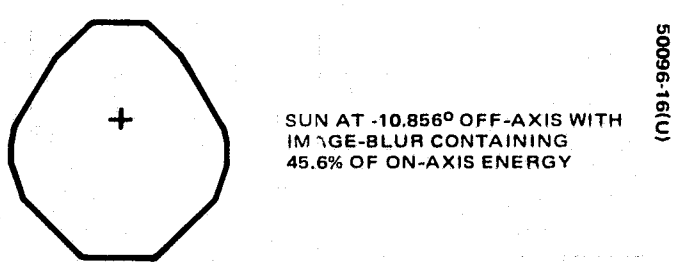

f) FIELD POSITION 6

FIGURE 2-11 (CONTINUED). EXTENT OF SUN'S IMAGE-BLUR ON POINTING MIRROR

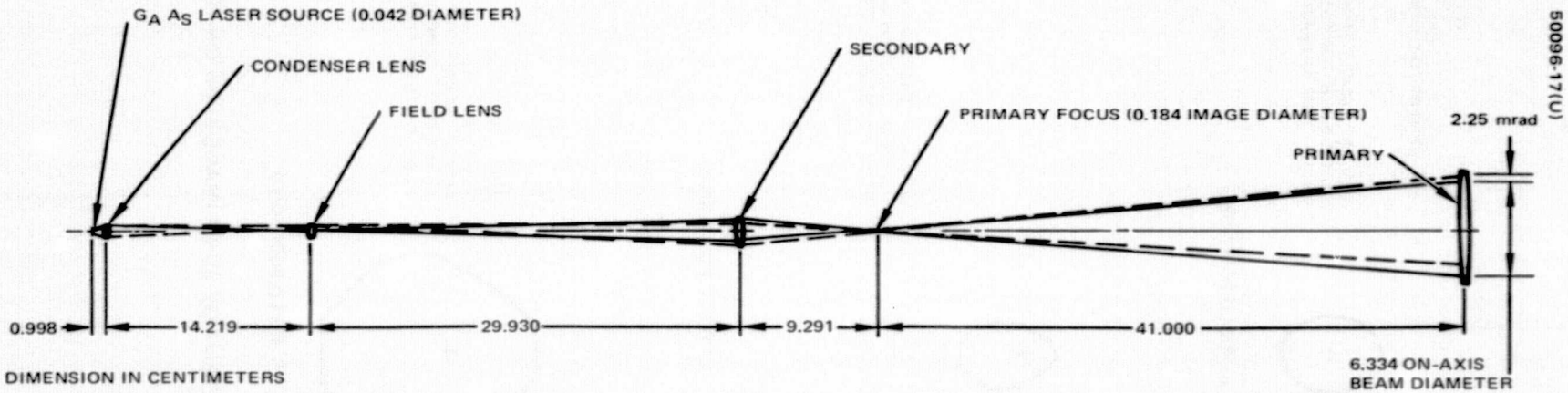

FIGURE 2-12. FIRST ORDER LAYOUT OF BEACON SYSTEM

The results presented in Figure 2-11 are not intended for the purpose of providing data for the smallest image blur size, nor the greatest solar energy concentration on the pointing mirror; instead, the graphic and relative energy data in the figure show the range of variation of solar energy distribution over the pointing mirror as the sun traverses across the field of view of the receiver. A small image blur with high solar energy concentration (as in the case of field position 4, Figures 2-10, 2-11c, and 2-11d) can lead to localized thermal distortion of the mirror surface; on the other hand, a larger blur patch with similar solar energy content (see, for example, field position 3, Figures 2-10, 2-11c, and 2-11d) can possibly have greater effect on the overall performance of the system, since a larger portion of the pointing mirror surface would be thermally deformed. Further details related to the thermal analysis are presented in Section 4 of this report.

2.5 BEACON DEVICE

As shown in 2.2, the heterodyne receiver has been so designed that a beacon device may be conveniently incorporated into the system. Based on the concept outlined in 2.2.4, a first order investigation of the beacon system has been completed, and a schematic layout of the system is shown in Figure 2-12. Referring to this figure, the GaAs laser source is imaged at the field lens position by the condenser system. Within the thin lens approximations, the appropriate focal lengths for the condenser and the field lens are 0.933 and 7.375 cm, respectively. The field lens images the condenser lens onto the aperture stop of the receiver (see Figure 2-5). In Figure 2-12, the primary and secondary mirrors of the receiver system are represented by thin lenses of focal lengths 7.09 and 41 cm, respectively.

The size of the GaAs source is taken to be 0.042 cm; the image size of this source at field lens is 0.598 cm. The secondary mirror reimages this to the focal plane of the primary mirror, and the effective size of the source image then becomes 0.184 cm. The corresponding output field angle of the beacon at the primary mirror is, therefore, ±2.25 mr.

The results of first order investigation so far indicate that a beacon system may be incorporated into the receiver optics with the addition of 1) the GaAs laser source, 2) a suitable condenser system, 3) a field lens, and 4) a Ge beacon beamsplitter plate (see Figure 2-5); the results do not, however, take into account the effects due to aberrations and central obscuration of the optical train. It should be pointed out here that, since the GaAs laser is considered to be an extended source, it may be reasonable to assume that the far field energy distribution of the beacon output is relatively unimpaired by the central obscuration of the receiver optics.

In order to complete the beacon design, the actual energy pattern of the GaAs laser source needs to be more precisely defined. It is recommended that a follow-up detailed design study of the beacon system be carried out, with the final performance evaluated in terms of far field energy distribution of the beacon output.

2.6 SUMMARY

The Gregorian optical system described meets the specifications and requirements of the 10.6 μm laser heterodyne receiver terminal. Various optical components associated with the system have been described, and the optical layout shown in Figure 2-5.

The performance of the receiver system has been evaluated in terms of the relative peak intensity of the input beam at the detector; it was found that the theoretical performance of the receiver was essentially perfect for the 10.6 μm wavelength considered. Optical tolerance study has also been performed, and the results indicate that the confocal configuration of the Gregorian system could withstand relatively large misalignments without noticeable deterioration in the RPI; therefore, this configuration is particularly suitable for space applications.

The heterodyne system is to be designed to operate even during the passage of sun across its field of view. Over the period of time in which the pointing mirror is directly exposed to sunlight, the solar image blur traced out on the mirror can lead to local thermal distortion of the mirror surface. Both the solar image blur pattern and the relative energy content have been evaluated. The results took into account the effects due to vignetting of the input solar energy by elements of the receiver optics. These data serve as input in the overall thermal analysis of the receiver.

Finally, a first order study of a beacon system which shared the same basic components of the receiver optical train has been completed.

3. OPTO-MECHANICAL PACKAGE DESIGN

Essential design techniques for space hardware, especially space optics, were combined with those techniques developed for laser heterodyne systems to produce a workable package design for the receiver opto-mechanical (OM) subsystem. Since the engineering model is intended for laboratory test purposes, the package is designed so that the components can be removed, aligned, and replaced as required during the testing and evaluation of the engineering model. Accessibility to these components is provided by the removable front cover of the OM subsystem; the design is such that it can be upgraded to a flight prototype configuration without basic changes.

3.1 GENERAL DESIGN AND LAYOUT

3.1.1 Guidelines

The configuration chosen to best meet the requirements of this program is a shell structure where the optical elements are supported on the walls and bulkheads of the shell. All elements are hard mounted with a minimum of cantilever or post supports. The materials chosen offer the best stability considering the thermal and mechanical design factors.

An important guideline acquired by experience in the design of opto-mechanical hardware for laser heterodyne systems is to provide a monolythic structure with a minimum of thermal and mechanical interstices and junctures. Under this guideline, a casting provides an ideal structure for the fabrication of the structural frame; however, a less costly method is the bracket and plate arrangement which is described in detail in 3.1.3.

3.1.2 General Specifications

The OM subsystem is shown in Figure 3-1. Details of the bracketed plate construction, the double-wall construction for the end plates, the baseplate with 160 10 to 32 tapped holes in a 1 inch grid pattern, and the baffel can be seen in the figure. The physical specifications are listed as follows:

Length	21-1/2 inches
Depth	10-1/2 inches
Height	9-5/8 + 3-1/8 inches for radiation cooler mount

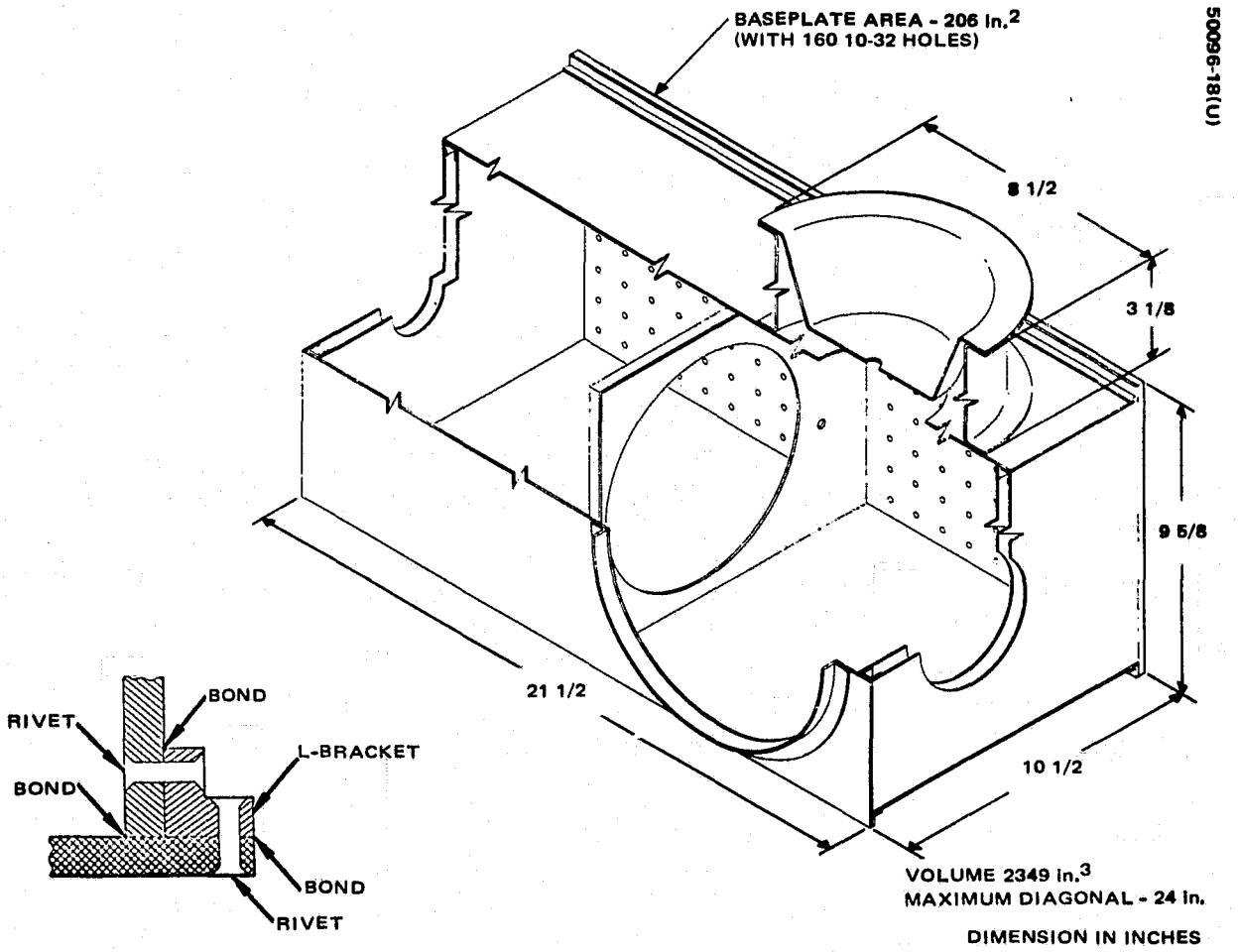

FIGURE 3-1. OPTO-MECHANICAL SUBSYSTEM STRUCTURAL FRAME

Baseplate area	206 in^2	
Volume	2349 in^3	
Maximum diagonal	24 in.	
Weight, pounds	Original Estimate	Actual
Box (empty)	9.55	10.0
Pointing mirror	2.30	2.35
Primary mirror	1.68	2.04
Secondary mirror	0.28	0.30
Gimbal	4.43	4.25
Miscellaneous	0.78	5.84*
Total weight, pounds	19.02	24.78

*Includes cables, connectors, position sensor, and IMCs not in original weight estimate.

The OM subsystem package is mounted on three point kinematic suspension on the baseplate. The mounting points are at the flanged edges of the structure where each 1/4-20 tapped mounting hole is backed with a reinforcing block. The depth of the tapped holes will be the thickness of the flange plus that of the reinforcing block, or about 1/2 inch.

3.1.3 Structural Frame: Materials and Techniques

The overriding consideration in the selection of materials for both the optics and the structural frame was that the system would be exposed to direct solar radiation. Thermal stability, that is, the resistance of the structural to mechanical deformation in the presence of thermal gradients, was the most important. Mechanical stability, the resistance of the structure to mechanical deformation in the presence of mechanical stress, was the next most important factor. The thermal stability goes directly as the thermal conductivity and inversely as the linear coefficient of expansion of the material. The mechanical stability goes proportional to the modulus (stiffness) and strength and inversely as the density of the material. Table 3-1 lists the material properties for three candidate materials: beryllium, aluminum, and magnesium. For the purpose of comparison of these materials, each factor was normalized to unity for beryllium. The overall merit was defined to be the product of the modulus, strength, and thermal conductivity, divided by the coefficient of expansion and the density. It can be seen that beryllium has an overall merit of some 15 times greater than either aluminum or magnesium.

Since beryllium was determined to be the most suitable material for both the optics and the structure, the concept of isothermal design could be used; cost of fabrication of the structure, however, must be taken into consideration. In this regard, advantage was taken of current spacecraft development techniques using beryllium sheet and L-brackets in a bond and rivet process. This process is identified at Hughes as Hughes-approved processes HP16-25 and HP20-1805. Assembly of the structure is thus simplified, and machining from large billets of material is not necessary. These techniques were thus selected for the design of the OM subsystem structure.

TABLE 3-1. COMPARISON OF CANDIDATE MATERIALS

Property	Beryllium	Aluminum	Magnesium
Modulus (stiffness)	1	0.245	0.155
Strength	1	0.71	1.14
Thermal conductivity	1	1.17	0.65
Expansion^{-1}	1	0.48	0.51
Density^{-1}	1	0.68	1.06
Overall merit	1	0.067	0.067

All structural elements are tied directly to the thermal interface (the baseplate) and to each other by continuous material couplings of large surface area. The optical elements are mounted to the opto-mechanical frame by ball joint clamp rings of a proven design. These mounts, again, provide a large mounting surface area and when filled through the injection holes with the proper adhesive bonding agent, provide a mirror mount having excellent rigidity, stability, and continuous thermal conductance.

Established and Approved Process Techniques

The methods used to fabricate and assemble the OM subsystem are part of the established Hughes process specifications. The following Hughes processes (HP) are established for use on this program:

HP 1-26	Machining and stress relief of beryllium
HP 10-25	Handling of beryllium parts
HP 4-171	Process for passivation of beryllium
HP 16-25	Bonding with epoxy type adhesives
HP 9-30	Preparation of surfaces for bonding

In addition, certain Hughes material specifications were utilized and include the following:

HMS 16-1720	Adhesive system, epoxy, for dissimilar metals
HMS 20-1805	Metal to metal structural bonding

3.2 OPTO-MECHANICAL CONSIDERATIONS

OM considerations related to the ease of construction and alignment were included early in this design study. As a result of optical housing design factors, choice of material and optical elements, and alignment considerations, a number of tradeoffs were made and some definite conclusions reached. These have been included in the basic package design layout and are further defined in the following paragraphs. These considerations are critical to the proper alignment and test of the OM subsystem.

3.2.1 Outer Housing

Figure 3-2 is a sketch of the outer housing. Surface A will be considered the basic surface since it represents the spacecraft interface. Two additional surfaces, B and C, are defined such that the inside surfaces, D and E, are perpendicular to B and C. These surfaces will establish an optical axis, 0, which is referenced to surface A. In addition, the gimbal for the pointing mirror is mounted to surface B. This means that the gimbal axis may be easily positioned to the optical axis.

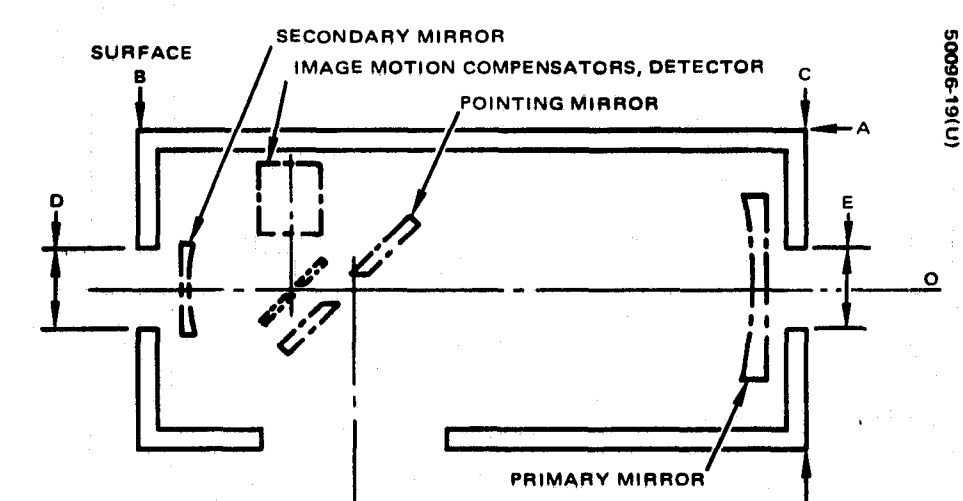

FIGURE 3-2. OUTER HOUSING SCHEMATIC

3.2.2 Optical Components

The primary, secondary, pointing, and flat folding mirrors are beryllium with an electroless nickel plating. The fabrication of optical surfaces using these materials is a routine procedure. In addition, it offers the low weight and high stability desirable in a flight unit.

The cost of optical elements is greatly affected by the tolerance specified. In most instances, close tolerances on mechanical dimensions and focal lengths are not necessary to achieve good optical performance. This is especially true if adequate consideration is given to the design of the mirror mounting mechanism. Sufficient adjustments can usually be designed into these mountings to compensate for variations from nominal focal lengths and skewed optical axes. Table 3-2 summarizes the tolerances for various mirror parameters which Hughes feels are reasonable; these tolerances are also used as guidelines for designing the mirror holding fixtures.

TABLE 3-2. TYPICAL MIRROR TOLERANCES

Parameter	Primary	Secondary
Radius of curvature, in.	±0.050	±0.050
Axial displacement, in.	0.010	0.010
Concentricity of axis, ft	5	5

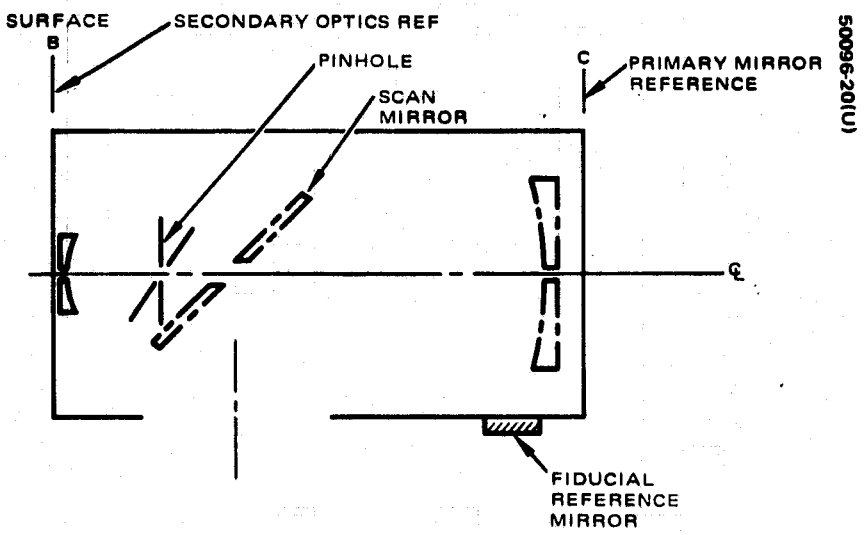

FIGURE 3-3. SCAN MIRROR ALIGNMENT

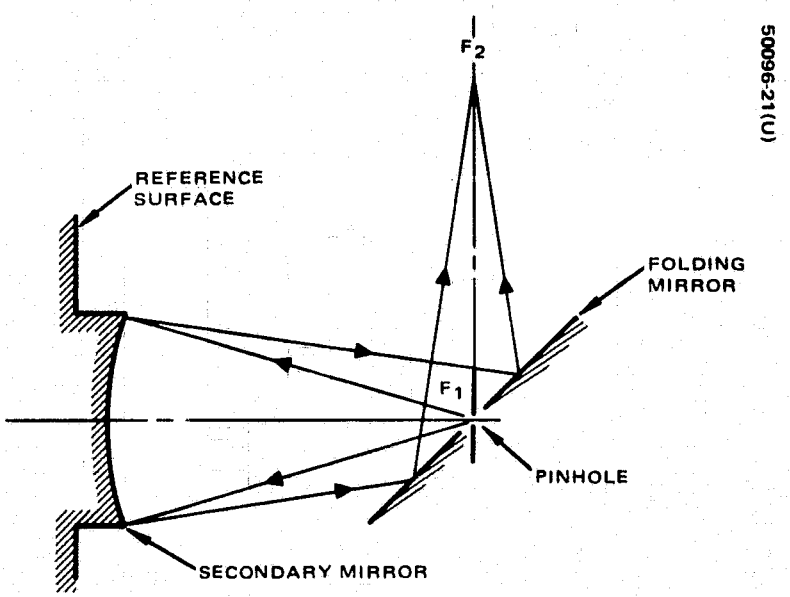

FIGURE 3-4. SECONDARY OPTICS ALIGNMENT

3.2.3 Optical Alignment Procedure

The alignment of the optical system is accomplished in several major steps. The following is a preliminary alignment procedure.

1) Outer housing, pointing mirror, reference mirror alignment, reference Figure 3-3.

   The accurately machined reference surfaces, B and C, are used to establish the optical mechanical axis through the housing. The scan mirror is adjusted into position of 45° with respect to the optical axis, and a repeatable locking mechanism is set to allow alignment verification at any time. The fiducial mirror may be set into position, adjusted, and locked.

2) Align the secondary optics assembly, reference Figure 3-4.

   The secondary optics assembly may be aligned independently of the outer housing. This may be done because the secondary optics are in a housing which is mounted on surface B. The procedure is as follows:

   a) Set pinhole in position at focal point of the ellipse.

   b) Set focus position to F_2.

   c) Adjust flat folding mirror to deviate beam 90° from optical axis.

   d) Recheck focus and repeat if necessary.

   e) Place secondary optics assembly into outer housing.

3) Primary mirror alignment, reference Figure 3-3.

   a) Insert primary mirror.

   b) Adjust position of primary mirror in X, Y, Z (focus), α, β, to achieve focus and proper position relative to pinhole in secondary optics assembly.

   c) Lock into position and recheck for focus or displacement of image.

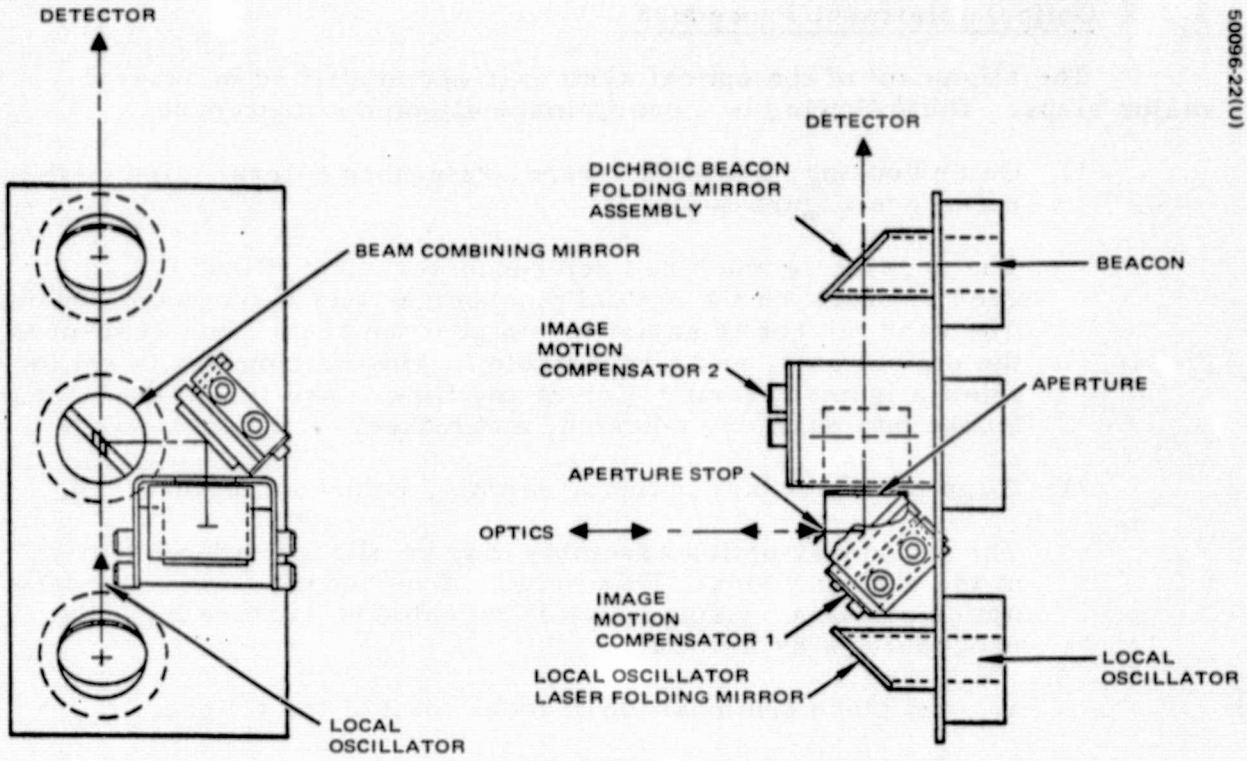

FIGURE 3-5. OPTICAL BENCH ASSEMBLY: IMCs, COMBINING MIRROR, DICHROIC BEACON BEAMSPLITTER

4) Insert IMC assembly, beam combining mirror, and beacon beamsplitter assembly, reference Figure 3-5.

   a) Check the vignetting at the aperture stop.

   b) Reposition aperture stop to minimize the vignetting.

   c) Lock into position.

5) Adjust detector to be at proper focal position.

The IMCs may be individually adjusted to align the image positionally. The vignetting at the aperture stop should be rechecked if the IMCs are moved.

3.2.4 Optical Element Mounts and Adjusting Tools

All lenses, mirrors, and beam splitters are mounted in adjustable clamp rings using ball socket hard friction mountings.

The basic optical element mount is illustrated in Figure 3-6. This figure is the mount for the primary mirror. The requirements for the alignment procedure require that this mirror have 4° of adjustment, namely

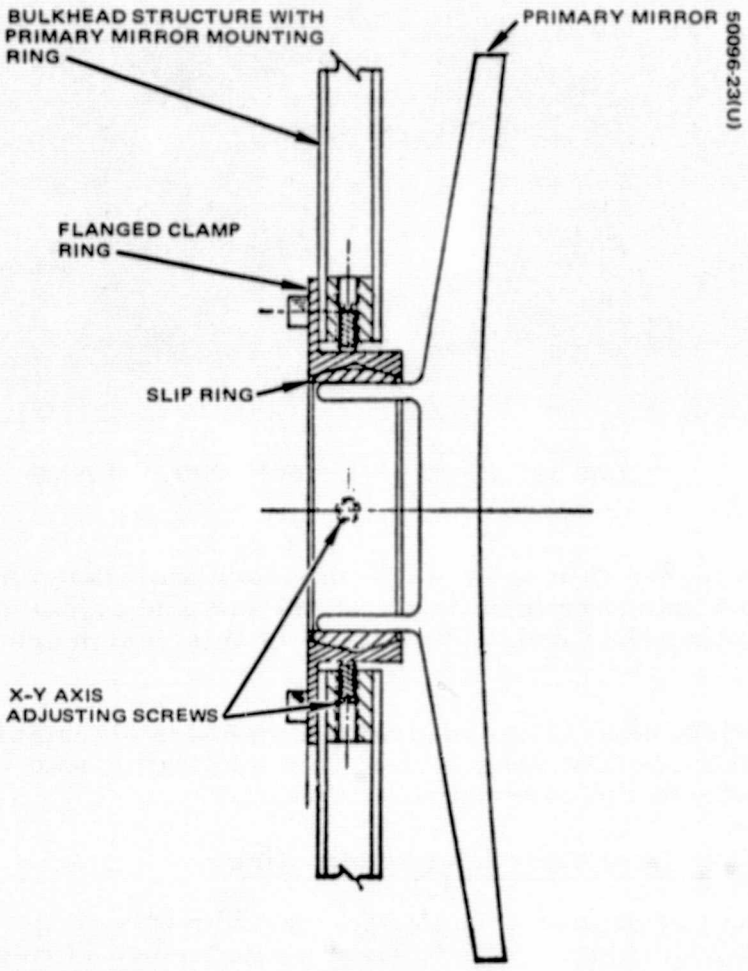

FIGURE 3-6. PRIMARY MIRROR AND BASIC OPTICAL ELEMENT MOUNT

azimuth angle (α), elevation angle (β), linear position (z), transverse position (x), and transverse position (y). The illustration shows how this is accomplished and the position secured by one locking clamp ring.

Micrometer control of angle position is obtained with special tools temporarily attached to the mirror and to the mounting bulkhead. These tools have large lever arms that provide fine adjustment control during the alignment. After both the primary and the secondary mirror are properly positioned, the clamp ring is set on each mirror. The tooling is then removed. Figure 3-7 shows the adjustment tooling in place for the primary and secondary mirrors.

3.2.5 Beacon Mount

The Sperry Rand 250 watt gallium arsenide laser illuminator is packaged in two sections; the optical head is a cylinder of 1-1/4 inches in diam-

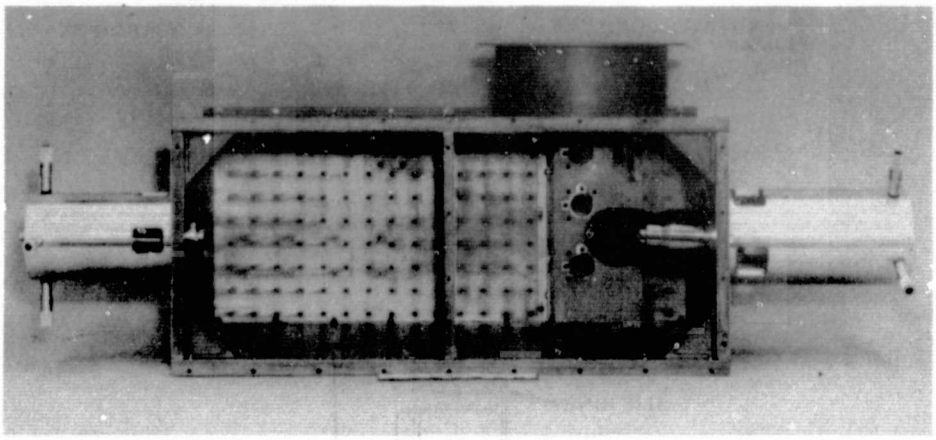

FIGURE 3-7. STRUCTURAL FRAME (PHOTO 4R35180)

eter and 1.875 inches in length, while the modulator assembly is a 1 x 1 x 1/4 inch block with power input leads at one end and signal wires to the optical head at the other end. The details of this design are given in Appendix B.

The optical head is mounted with a standard adjustable mount of the baffle partition on the OM subsystem. The modulator head is mounted by clamping directly to the base plate.

3.2.6 Local Oscillator Location and Mounting

The local oscillator assumed for use with this receiver subsystem (see Figure 2-5) is a tunable waveguide laser as described in Hughes Proposal No. 72M-3008/C7280-1. Design and testing of this subassembly is covered in Section 8.

3.2.7 Fiduciary Mirror

The fiduciary mirror is an adjustable fixture that can be mounted on the baseplate or any exterior surface of the OM structure. The mirror is calibrated with the optical train at the time of alignment of the system.

3.2.8 IMC Adjustment

The IMCs used in the subsystem will be the GTE PBM-8G beam steering element. Adjustments of the IMC position are made electrically by the application of a voltage to the PZT transducer element. Readout of the position is made through the strain gauge sensor elements on the IMC. Integral use of the PBM-8G in the closed loop servo system can be accomplished with no modification of the subsystem hardware. The details of the GTE PBM-8G beam steering element are given in Appendix A. Operation of the IMC as an integral part of the servo system is covered in Section 9.

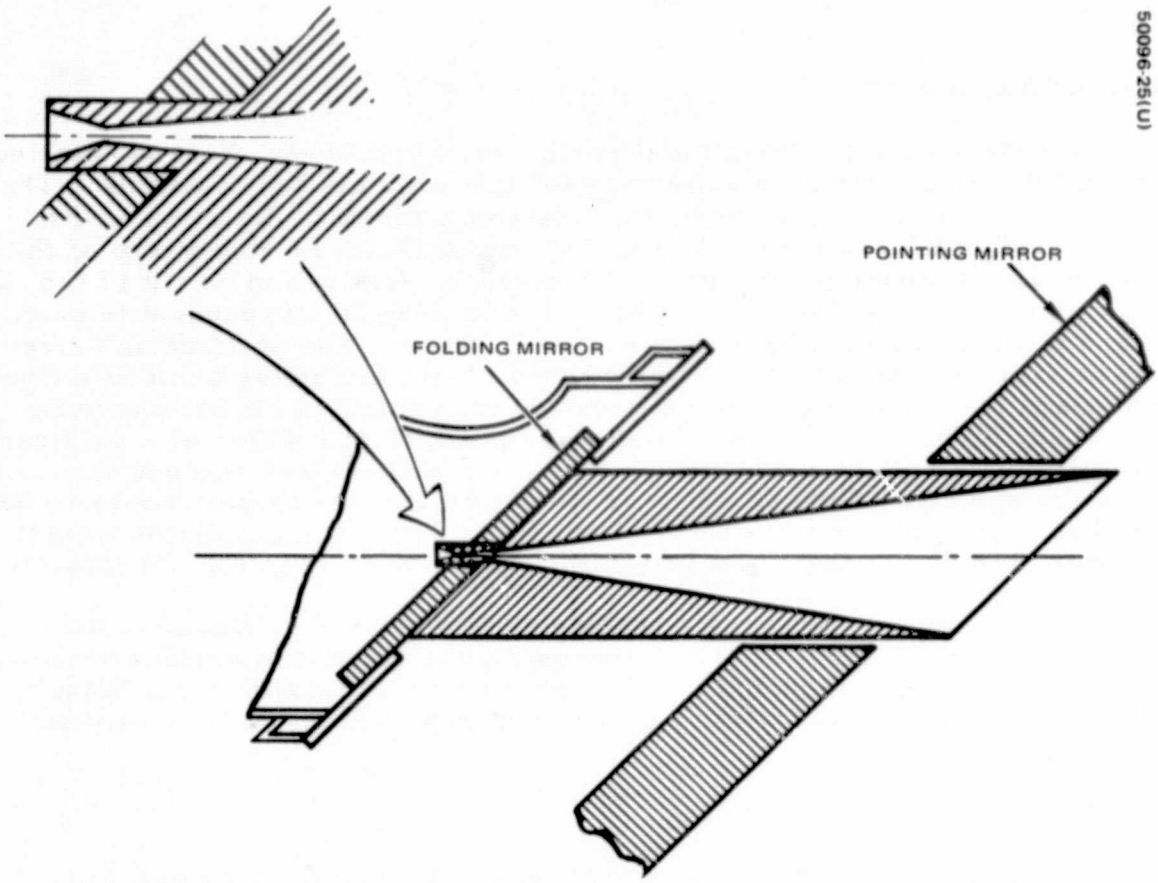

FIGURE 3-8. FIELD STOP FIXTURE INSERTED THROUGH POINTING MIRROR AND INTO FOLDING MIRROR

3.2.9 Optical Mixer Mount

The dummy optical mixer housing required under contract has been fabricated from the print specifications for the A. D. Little radiation cooler provided by NASA, A. D. Little SK-11972-1, Revision B.

3.2.10 Field Stop in Folding Mirror

Alignment procedures require a pinhole field stop at the focus of the primary mirror; however, the dynamic operation of the optical system requires a field coverage of ±0.13° for acquisition and tracking, which in turn requires that the hole in the folding mirror is at least 0.185 cm or 0.073 inch. An insertable field stop will therefore be used to reduce the field of view. A reasonably sized pinhole for this purpose is 0.004 inch, providing a field of 0.236 mr or about 1.5 times the Airy disk size. The 0.004 inch iris also satisfies with that required in the original OM Receiver Subsystem Specification 524-P1, paragraph 3.3.2.

The iris fixture is insertable through the hole in the pointing mirror and is held into place by friction of the tapered pin on the end of the fixture. A model of this device was constructed and tested to verify its suitability. Figure 3-8 shows a detail of how the fixture fits into the optical assembly.

3.3 GIMBAL DESIGN

Requirements for the gimbal design are as follows: Coarse pointing of the flat pointing mirror is achieved by a two-axis gimbal assembly. The flat mirror is mounted in a yoke on a rotatable pedestal. Rotation of the entire pedestal/mirror assembly provides the azimuth or roll sweep of the mirror while elevation positioning is obtained by declination or tilt of the mirror about its pivot axis in the yoke. Positioning is independent in each axis and is accomplished by a stepper motor drive. The positioning drive for each axis consists of spur gear reduction from the motor shaft to a final output stage that is a single thread worm gear engaging a short, matching worm wheel. The use of such a final stage permits utilization of a unidirectional spring load at the axis pivot to remove gear backlash without backdriving the system. The overall gear reduction for the tilt axis needs to be twice that of the roll axis to achieve the same effective beam displacement per motor step due to the optical doubling effect inherent in the tilt axis.

Fine angular positioning is achieved by means of an image motion compensator for each axis. These compensators consist of small mirrors within the optical path mounted on the output coil of a piezoelectric driver. The image motion compensators provide raster search as well as conical scan capability.

3.3.1 Manual Positioning Control

The coarse pointing gimbal mechanism is capable of manual (electrical) control in either axis within its prescribed range. Each axis is equipped with a stepper motor to provide appropriate open loop pointing.

The pointing mirror gimbal assembly meets or exceeds the specifications required under the contract. Table 3-3 lists the most salient of these performance characteristics.

3.3.2 Closed Loop Control (Servo System)

Operation of the gimbal in a closed loop servo system requires careful attention to the step size, overshoot, damping, and step rate. When a step occurs, an error signal must be generated which commands the IMCs to track accordingly. If the step size is too great or the IMC scan rate too slow, tracking is lost and reacquisition must be undertaken. In the design achieved, a compromise step size of 0.002°, or about 35 mr, was selected. This step size is less than one-half of the 3 dB beamwidth (82 mr).

The servo design task for the closed loop servo system is reported in Section 9. The important facts determined in the servo design are that the 0.002° step is sufficiently small to permit tracking but may cause undesirable fluctuations in the carrier during the stepping action. Should this be the case in actual experimental measurements, it will be necessary to consider even smaller steps in actual flight designs. A factor of two reduction in step size is both feasible and practical.

TABLE 3-3. PERFORMANCE CHARACTERISTICS OF POINTING MIRROR/GIMBAL ASSEMBLY

Parameter	Performance Characteristics
Rotation range	±5° tilt (elevation) ±10° roll (azimuth)
Gear ratio	15,000:1 tilt 7,500:1 roll
Step size	0.001° tilt 0.002° roll
Slew rate (maximum)	0.05 deg/sec tilt 0.10 deg/sec roll
Backlash	0 output 0.01° tilt input 0.02° roll input
Manual positioning	Within 0.13°

3.3.3 Dynamic Response of Gimbal

Dynamic response of the gimbal is crucial to the proper response of the closed loop servo system. Factors such as hysteresis, overshoot, crosstalk, and ringing must be evaluated carefully. A great deal of effort has been applied to obtaining a near ideal dynamic response of the gimbal system. The roll axis performance characteristics are shown in Figure 3-9a for 1 step/sec and in Figure 3-9b for 50 step/sec.

The tilt axis performance characteristics are shown in Figure 3-10a for 10 step/sec and Figure 3-10b for 50 step/sec. The amount of overshoot, ringing, and crosstalk are critical functions of the shape of the driving pulse to the stepper motors. Figure 3-11 shows the typical roll response and tilt crosstalk before and after pulse shaping. The pulse shape waveforms are shown in Figure 3-12. The typical overshoot and ringing are about one-half step magnitude and the crosstalk is about one-fourth step magnitude. These characteristics have been factored into the servo system simulation and are acceptable for closed loop tracking requirements.

3.3.4 Hardware Design

The OM subsystem gimbal design consists of three basic structural parts: 1) the base mount containing the roll axis drive; 2) the yoke, driven by the roll axis output, containing the tilt axis drive; and 3) the saddle, driven by the tilt axis output and containing the pointing mirror mounting provisions.

The base and the yoke are each of one-piece designs with integral motor and gear shaft supports. This method of fabrication allows line drilling of details to enable close tolerance control as well as better overall dimension control. Added expense of machining these pieces in this fashion is more than offset by savings in the assembly process and in achieving a more rugged assembly.

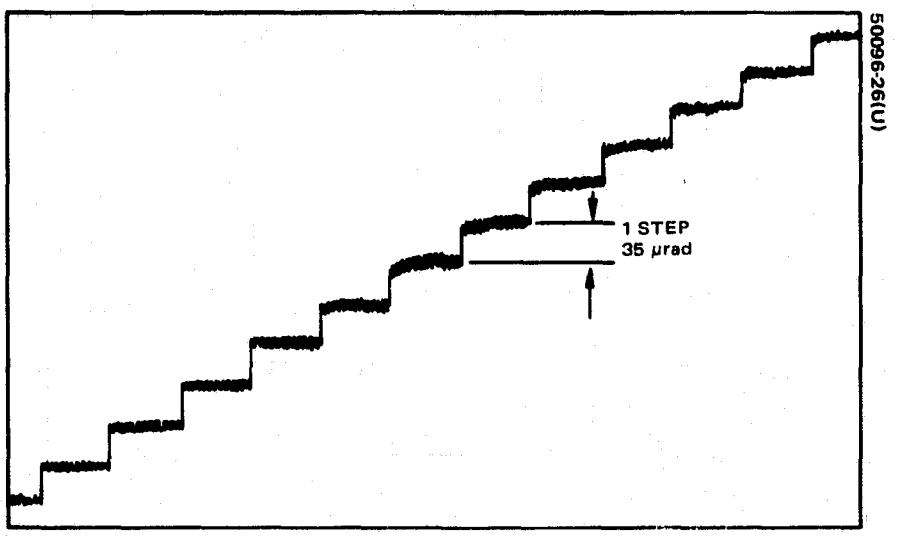

a) 1 STEP/SECOND

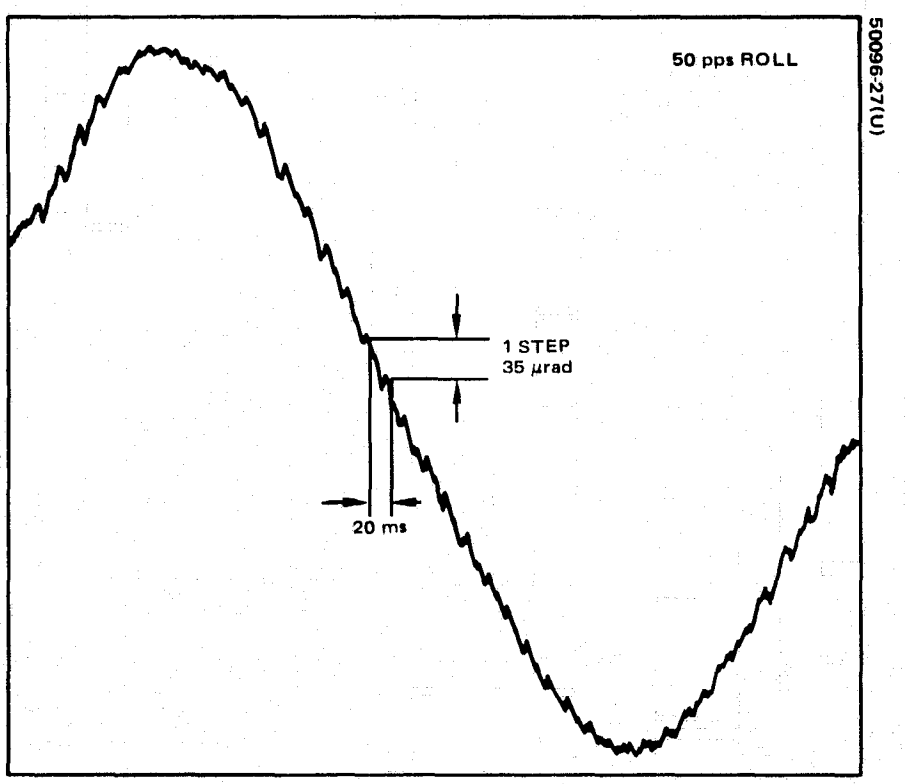

b) 50 STEP/SECOND

FIGURE 3-9. GIMBAL ROLL RESPONSE

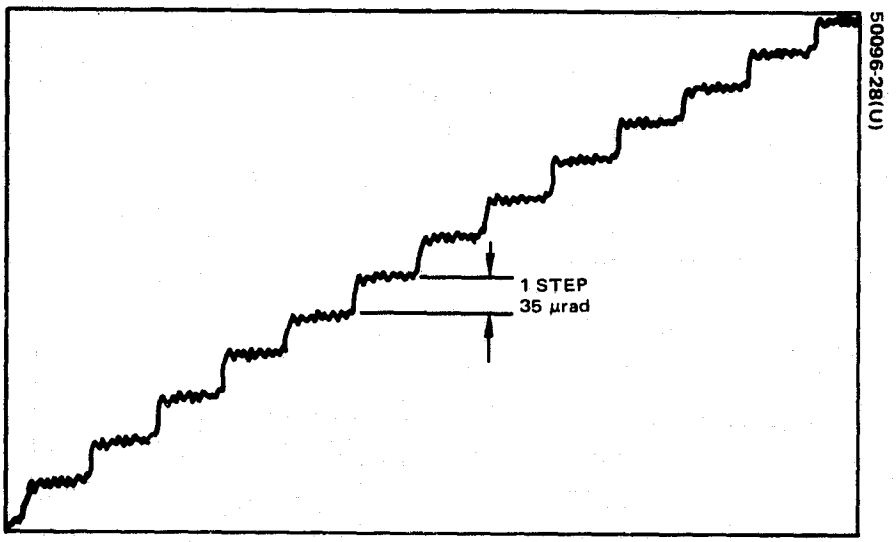

a) 10 STEP/SECOND

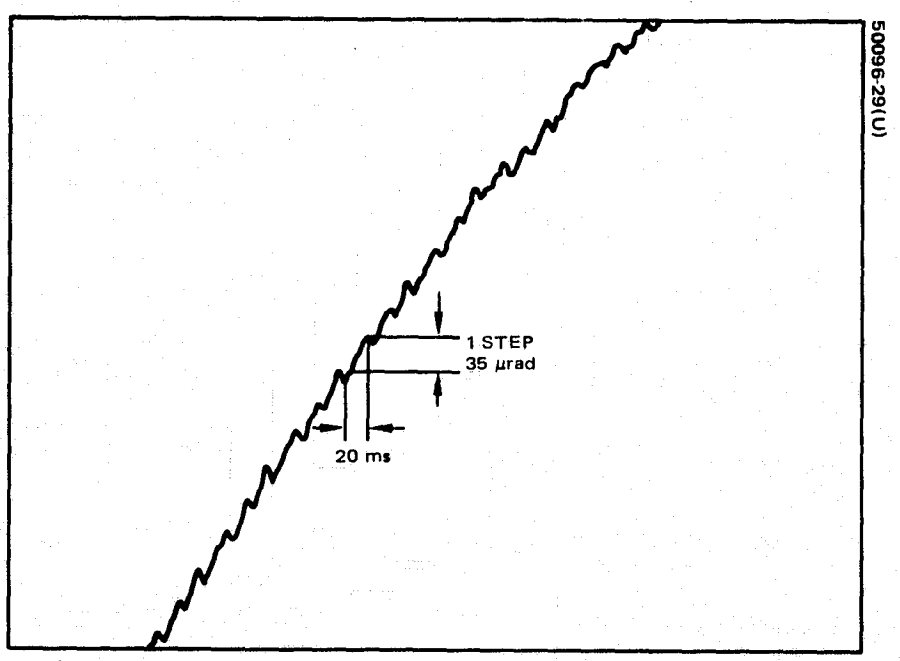

b) 50 STEP/SECOND

FIGURE 3-10. GIMBAL TILT RESPONSE

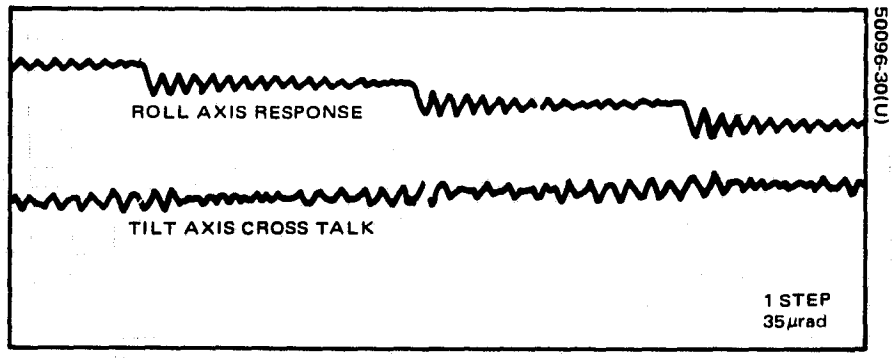

a) BEFORE PULSE SHAPING

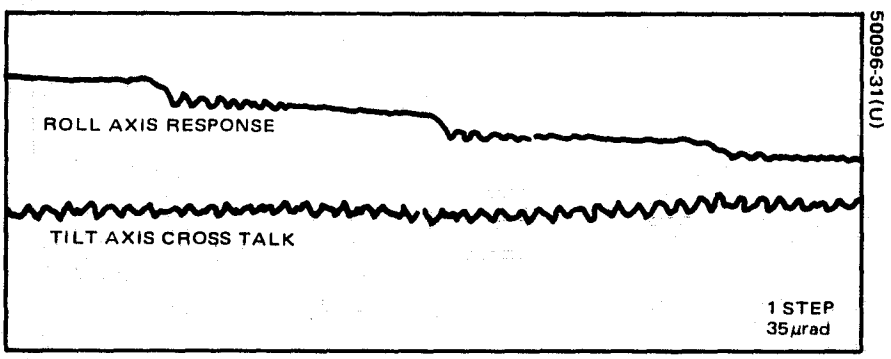

b) AFTER PULSE SHAPING

FIGURE 3-11. ROLL AXIS STOP RESPONSE AND TILT AXIS CROSSTALK

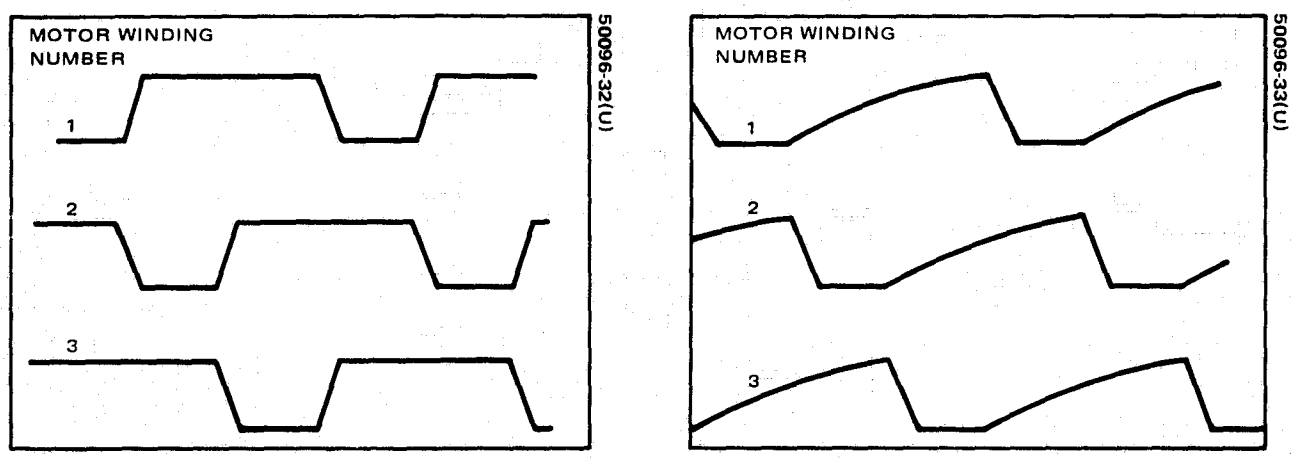

a) BEFORE SHAPING

b) AFTER SHAPING

FIGURE 3-12. MOTOR DRIVE VOLTAGE WAVEFORMS

The yoke is mounted in the base through two spring loaded angular contact ball bearings 3.0 inches ID and 3.5 inches OD. The bearing spacing together with the contact angle gives an effective bearing wheel base more than sufficient to maintain axis stability in all expected operating conditions.

The saddle is suspended in the yoke with two R166 radial deep groove bearings. These bearings are captured within the saddle and are preloaded against the uprights of the yoke structure. By this means of suspension, the tips of the opposite uprights are effectively tied together through the saddle, thereby providing a more stable framework. Stiffening members have been bonded to the yoke uprights to alleviate yoke twist caused by the off-axis forces of tilt drive operation.

The mirror/saddle interface is designed to prevent mirror warpage due to the differences in coefficients of thermal expansion between the beryllium mirror and aluminum saddle. This is achieved by equipping the saddle with three radially sliding bosses acting as mirror supports. Spherical washers between the mirror and the bosses and the bosses and the holding nuts compensate for misalignments in mounting that would otherwise cause mirror warpage.

In design of the inner gimbal yoke, particular attention was given to assure that the optical path has not been obscured and that sufficient clearance has been provided for the IMCs and other optical devices.

Piece parts, gears, bearings, etc., are selected for their commercial availability or their existence from other Hughes space programs. Moving parts lubrication is achieved by a dry film technique to avoid any film migration to optical surfaces.

Manual gimbal locks for establishing a position reference have not been incorporated as originally planned. Instead, an electro optical reference system has been incorporated in each axis to provide an indication at one specific alignment of the drive train. This approach has the advantage over a manual lock system in that 1) physical contact between parts is avoided; 2) the system may be used with the fully assembled package where manual access would be restricted; and 3) when incorporated into the servo system, more precise command control capability is allowed.

The model contains a potentiometer in each axis to assist in telemetry and position command control in the anticipated servo loop control configuration. While this item is space proven, a reliability improvement for future space hardware could be made by substituting a noncontacting differential transformer for this potentiometer. This pickoff is not required in the servo loop during normal track.

Figure 3-13 is a photograph of the completed gimbal assembly. The stepper motor for the tilt axis and its electro optical reference system are visible in the photo. The gear train for the roll axis is also visible. Figure 3-14 shows the completed gimbal with the pointing mirror installed.

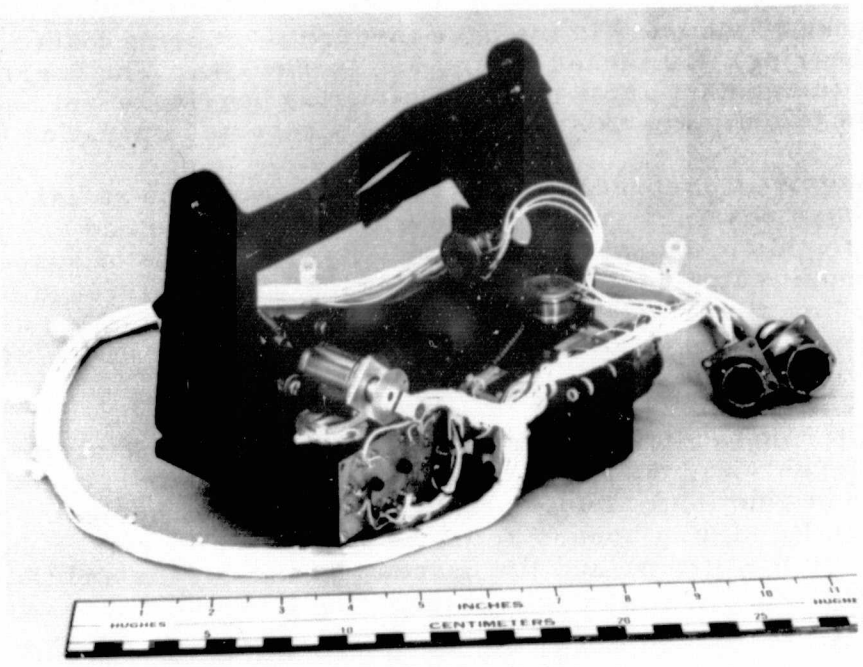

FIGURE 3-13. COMPLETED GIMBAL ASSEMBLY (PHOTO 4R37653)

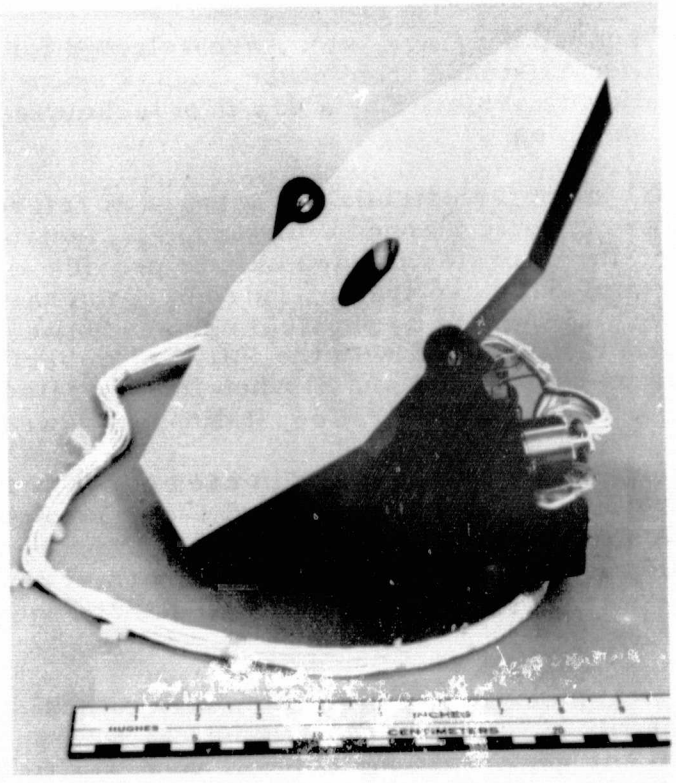

FIGURE 3-14. COMPLETED GIMBAL WITH POINTING MIRROR MOUNTED (PHOTO 4R37644)

3.4 OPTO-MECHANICAL SUBSYSTEM ASSEMBLY

This section illustrates the assembly of the structure, gimbal, and optics into the final configuration.

3.4.1 Subsystem Assembly

The structural frame consisting of the baseplate, sidewalls, and end bulkheads joined together by the riveting and bonding techniques, described in 3.1, serves as the basic optical mounting frame for all the optics. Figure 3-15 illustrates the opto-mechanical subsystem assembly with the gimbal assembly (R1801), primary mirror assembly (R1802), secondary mirror, folding mirror assembly (R1803), the IMC and combining optics assembly (R1804), the LO laser assembly (R1805), the beacon assembly (R1806), and the optical mixer assembly (R1807).

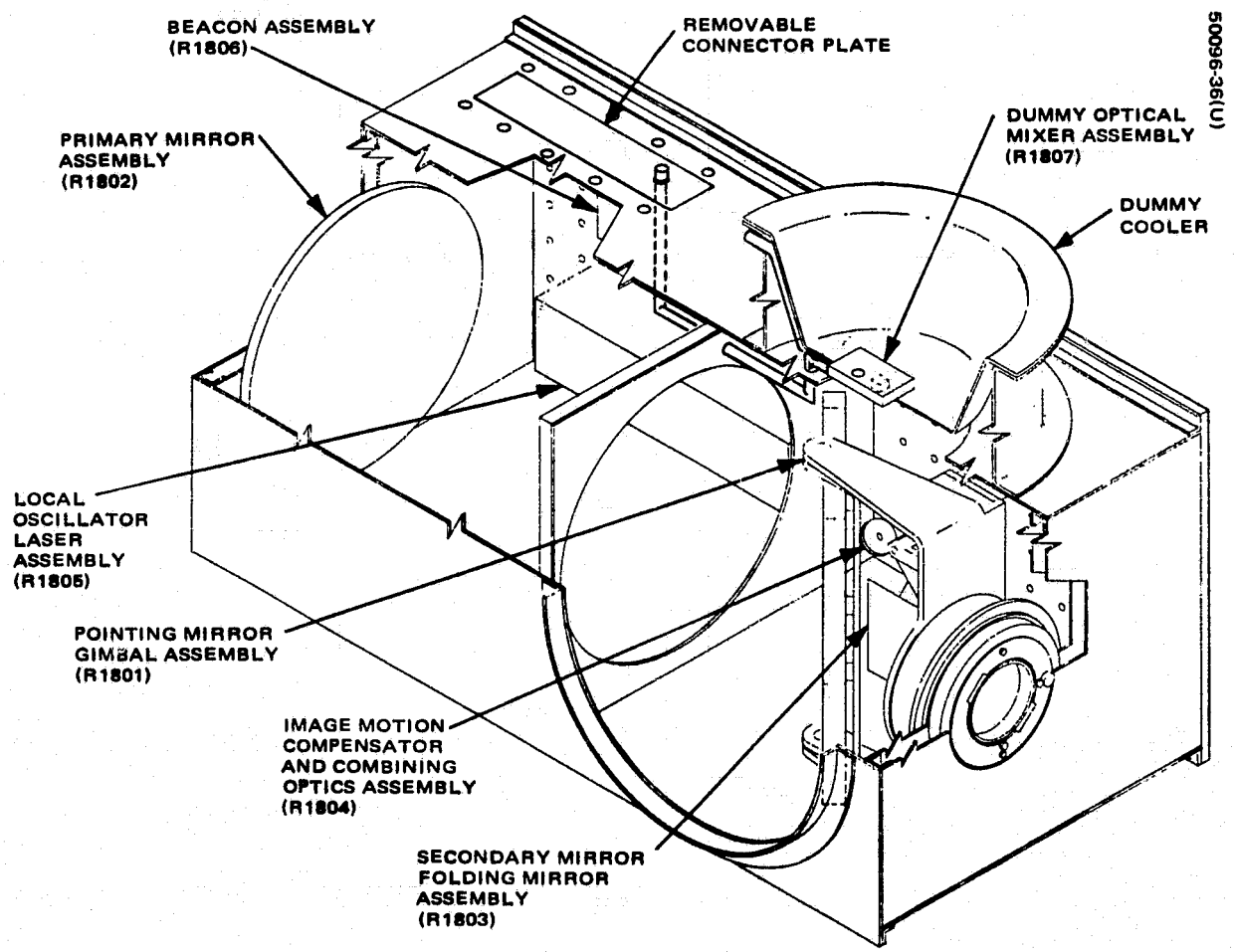

FIGURE 3-15. OPTO-MECHANICAL SUBSYSTEM ASSEMBLY

3.4.2 Subsystem Assembly Photos

Figures 3-16 through 3-23 are a series of photos showing the step-by-step assembly of the opto-mechanical package.

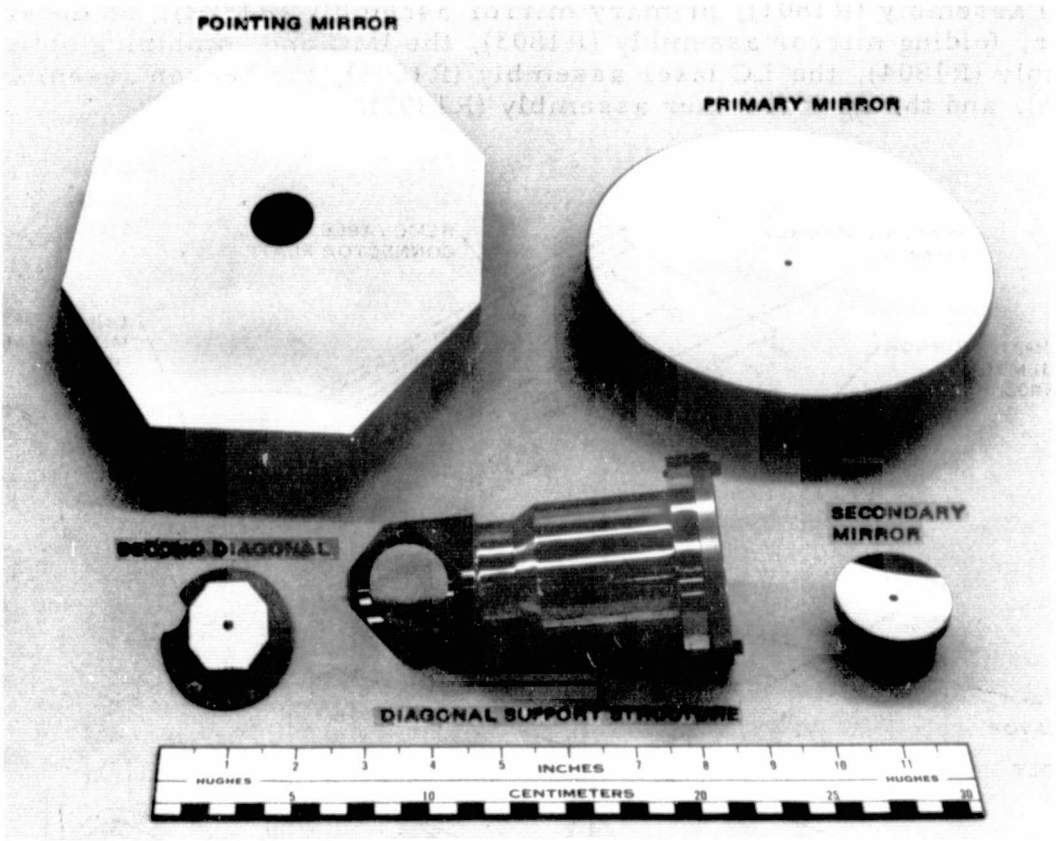

50096-37(U)

FIGURE 3-16. BERYLLIUM OPTICS

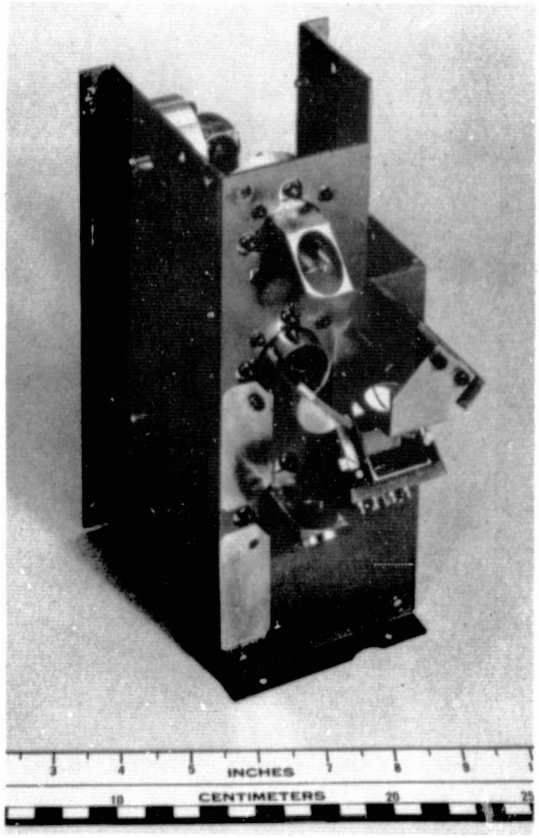

FIGURE 3-17. OPTICAL BENCH ASSEMBLY WITH IMCs, COMBINING MIRROR, AND FOLDING MIRRORS (PHOTO 4R37651)

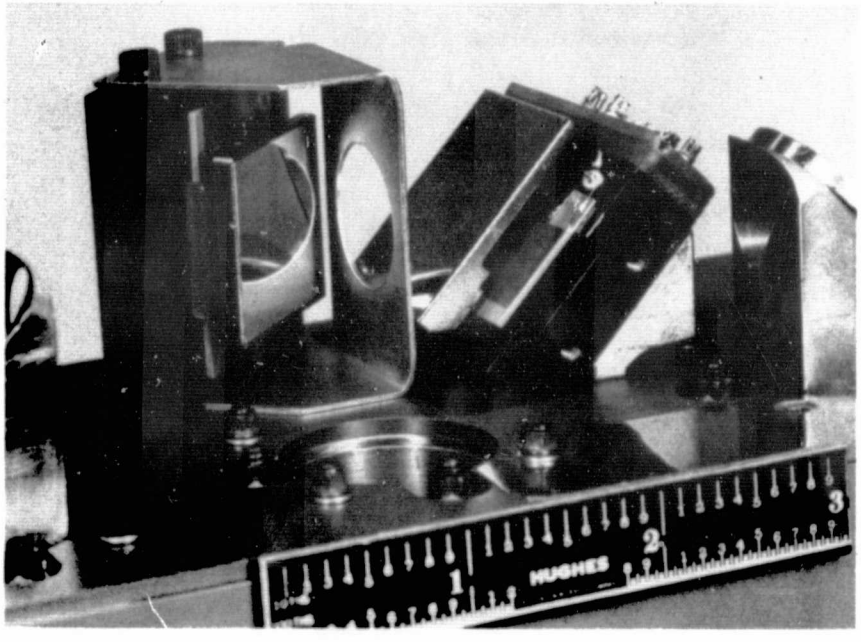

FIGURE 3-18. CLOSE-UP OF IMCs (PHOTO 4R37649)

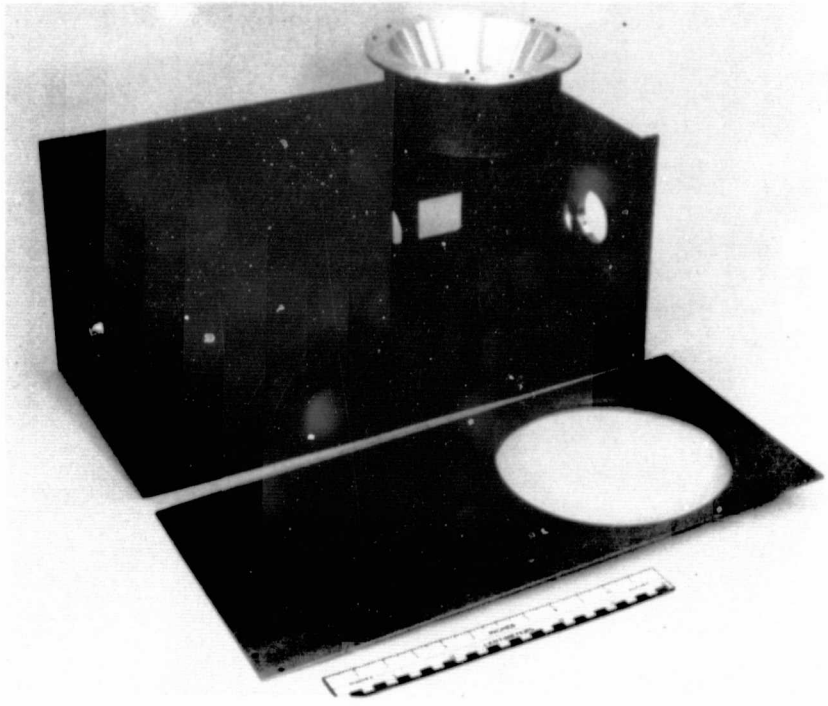

FIGURE 3-19. EMPTY STRUCTURAL FRAME (PHOTO 4R37645)

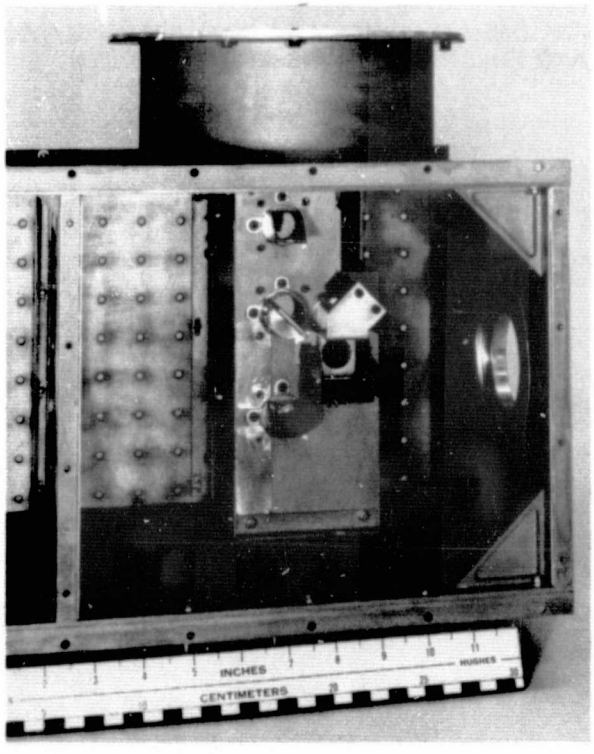

FIGURE 3-20. STRUCTURAL FRAME WITH OPTICAL BENCH INSTALLED (PHOTO 4R37647)

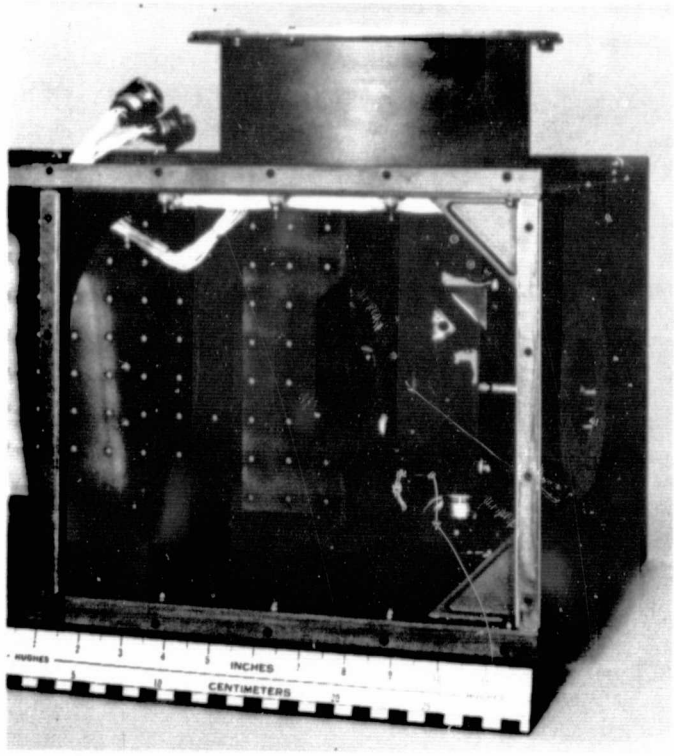

FIGURE 3-21. STRUCTURAL FRAME WITH GIMBAL INSTALLED (PHOTO 4R37648)

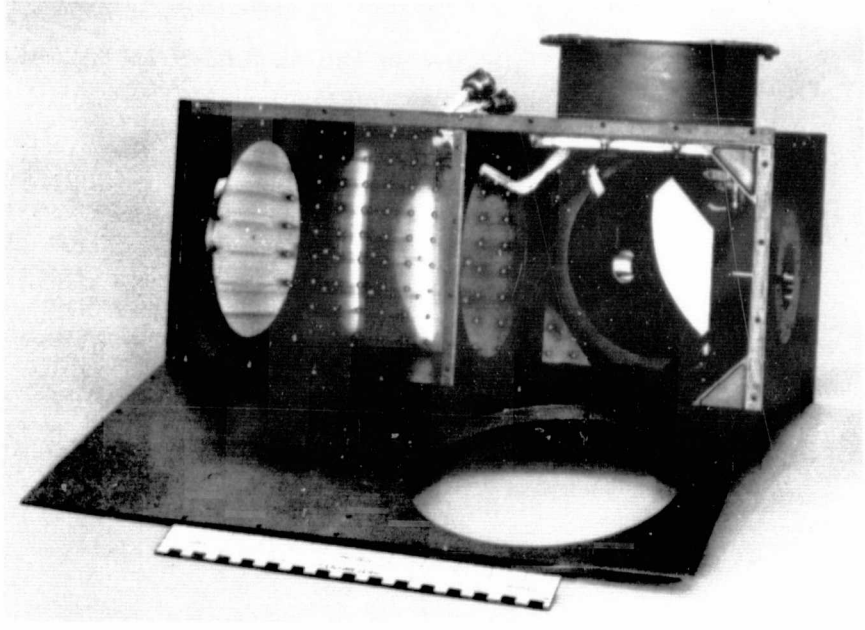

FIGURE 3-22. STRUCTURAL FRAME WITH OPTICS INSTALLED (PHOTO 4R37650)

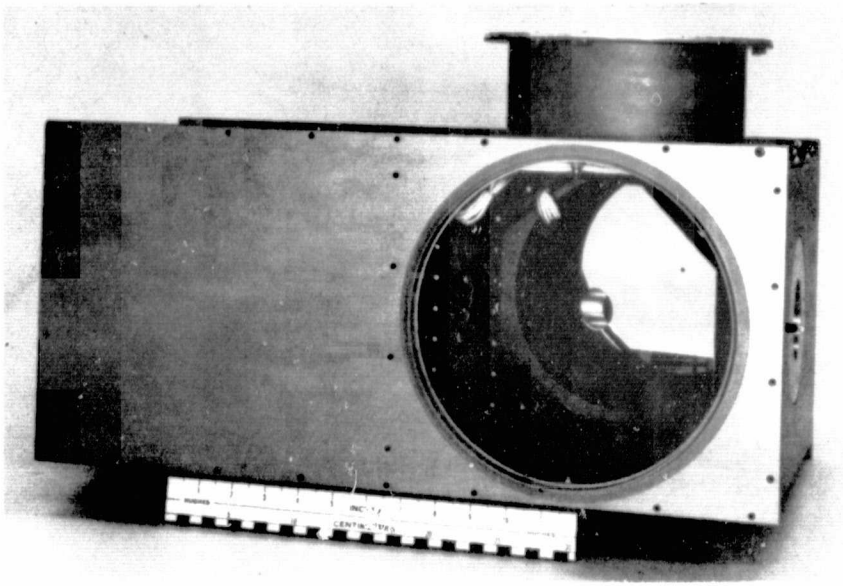

FIGURE 3-23. COMPLETE OPTO-MECHANICAL SUBSYSTEM PACKAGE (PHOTO 4R37646)

4. THERMAL MODEL

4.1 THERMAL ANALYSIS

This section describes the chronology of thermal analysis performed for the OM study. The study proceeded in two phases: 1) preliminary analysis in which thermal loads were defined and temperatures were found in an aluminum structure and 2) final analysis in which a beryllium structure was postulated and temperatures were found in mirrors and the gimbal mechanism as well.

The structural temperature distribution reported here was used to develop the mechanical distortion discussed in Section 5.

4.2 PRELIMINARY THERMAL ANALYSIS

The OM subsystem was analyzed as a simple rectangular parallelpiped to determine the distribution of the solar heat load penetrating the entrance aperture. Two situations were examined: 1) worst case identification without reference to orbit feasibility and 2) solar energy distribution in the OM housing for a geosynchronous orbit during an equinox. A worst case solar energy distribution corresponding to 12M at a winter solstice was used to estimate equilibrium temperatures in an aluminum OM structure; a simple nodal model was used to show a structural temperature distribution covering the range 50° to 85°F. The temperature analysis is conservative and intended as preliminary only; the analysis of solar fluxes is limited to a single geometry, but is final and suitable for use in making more realistic temperature calculations.

The preliminary thermal analysis addressed the following aspects of the thermal design:

1) Definition of potential worst cases due to solar heat loads

2) Solar heat load distribution for a geosynchronous orbit at equinox

3) Preliminary temperature distribution for a worst case at solstice

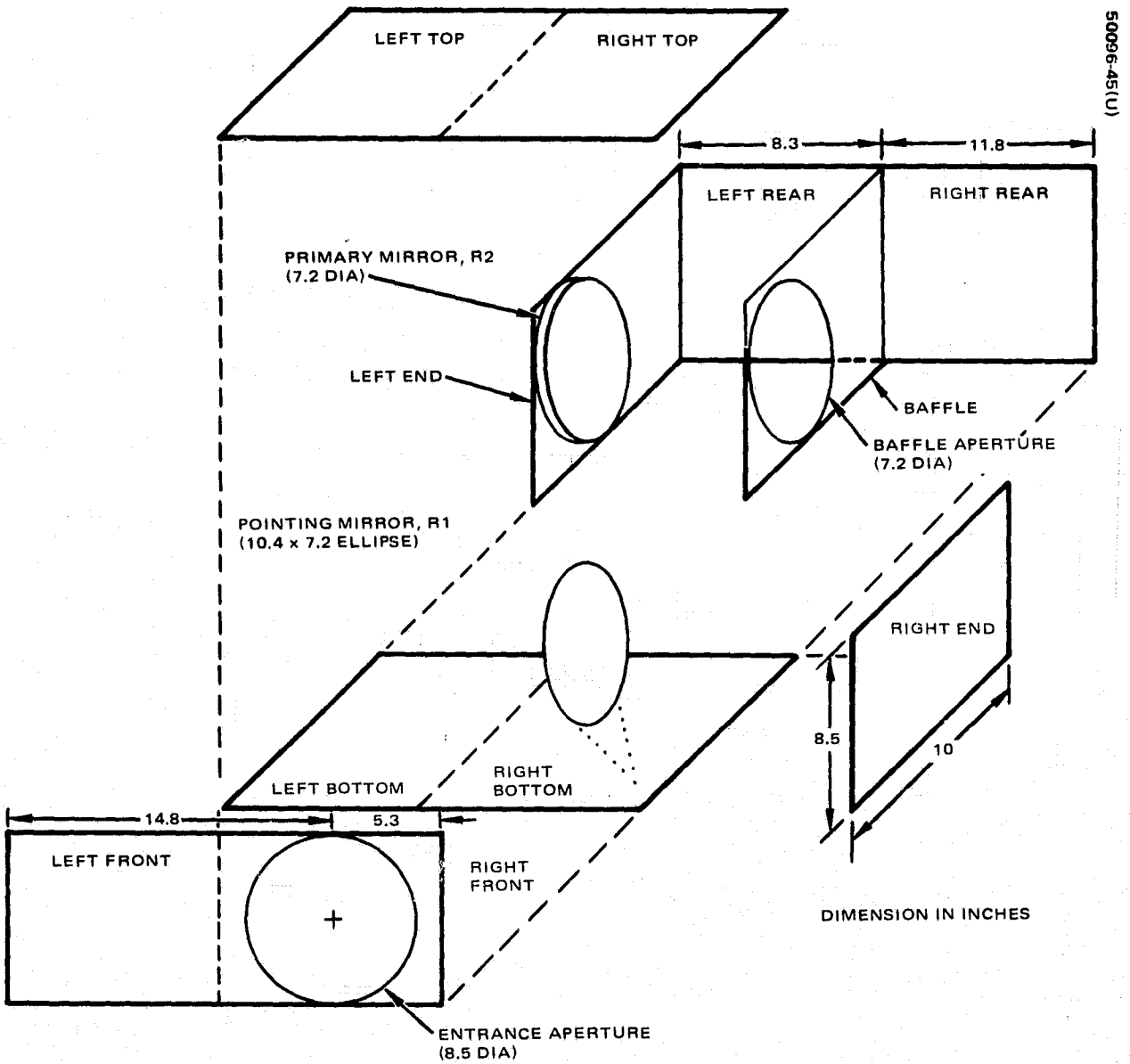

FIGURE 4-1. OPTO-MECHANICAL SUBSYSTEM: INFORMATION USED TO OBTAIN INTERNAL SOLAR HEAT LOADS

The model geometry, designations, and dimensions used to develop the internal solar heat loads were scaled from a preliminary layout drawing of the OM subsystem. An exploded view of this model is shown in Figure 4-1.

4.2.1 Problem Description

Optical misalignment of the OM subsystem may occur due to nonuniform temperatures induced in the structure by nonuniform solar heat loads and heat dissipated by electro-mechanical components housed in the structure. For the purpose of this analysis, it is assumed that all external surfaces will be isolated from direct solar heating by blankets of multi-foil insulation. In the absence of external loads, it follows that potential worst case temperature gradients will exist when collimated solar energy penetrates the entrance aperture and then, by direct and specularly reflected irradiation, is focused on only one of the interior housing surfaces at the exclusion of all other surfaces. Solar energy concentration on one surface will raise the temperature of that surface while adjoining regions not directly irradiated will be at a lower temperature.

Another situation that may create several thermal gradients occurs during the equinox seasons when a spacecraft in a geosynchronous orbit undergoes a 70 minute (approximate) eclipse. Insofar as the OM line of sight (entrance aperture) is earth pointing, the eclipse is preceded and followed by periods of maximum solar influx through the entrance aperture. In consideration of these abrupt changes in interior solar heat loads, a 24 hour solar load history for an equinox condition is required to examine a potential worst case.

4.2.2 Interior Solar Heat Loads

All interior heat loads were obtained using graphic ray tracing to define the periphery of each illumination pattern on any given panel. Full account was taken of the depth of the shallow cylindrical collar (8.5 inch diameter by 0.5 inch) surrounding the entrance aperture as a field stop limiting the solar flux entering the housing; no account was taken of the thickness of the folding mirror or the gimbal and electro-optical elements housed behind and to the right of the folding mirror. A planimeter was used to measure each illuminated area, and the local angle of incidence was measured with a protractor. The solar constant was taken as 430 Btu/hr-ft^2 (1355 W/m^2)* for areas of direct incidence, and a reflectance of 96.2 percent was used to decrease the solar flux density reflected from the pointing mirror (R1) to 415 Btu/hr-ft^2.

*The best estimate of the solar constant is 1353 ±21 W/m^2 as given by Thekaekara, M.P. in NASA TR R-351, October 1970.

Instantaneous Worst Case Analysis

Three constants were imposed to identify potential worst case solar heating conditions:

1) The top surface is always facing north while the entrance aperture is facing earth.

2) Maximize the solar power (Btu/hr) penetrating the entrance aperture.

3) Focus the solar energy on a single surface (top, rear, etc.) with minimal spillover to other surfaces.

Four cases were identified and examined quantitatively for an OM housing without the internal baffle. These cases are summarized in Table 4-1 to provide insight to the solar load distributions, but the patterns and data should not be used to determine temperature distributions for a housing with an internal baffle.

Two of these sans baffle cases deserve comment:

Case 1 – Direct plus reflected irradiation of rear surface: Approximately 43 watts (146 Btu/hr) are directly incident on the rear surface which mounts to the spacecraft heat sink. This case dramatizes the fact that the heat sink must be capable of absorbing almost all of the solar energy entering the housing while maintaining a sink temperature in the range of 20° ±10°C (68° ±18°F). If the maximum solar heat loads are unacceptable to the spacecraft thermal control system, introducing a filter at the entrance aperture or lengthening the collar outside the aperture until it becomes a radiation shield will be necessary. Thermal distortion does not appear to be serious for this case because the coupling between the rear surface and the spacecraft will provide a high thermal conductance.

Case 2 – Direct plus reflected irradiation of top surface: Approximately 42 watts (143 Btu/hr) are incident on the interior of the top (north) surface. The irradiation is strongly nonuniform and contains a small region of focused solar flux. The focused flux will create a local hot spot. Thermal distortion may be critical for this case.

Case 2 was reexamined with the internal baffle introduced as shown in Figure 4-1. This sun to aperture orientation corresponds to the condition of the spacecraft in a geosynchronous orbit at midnight during a winter solstice. A scale illustration showing the approximate irradiation pattern appears in Figure 4-2. This solar load distribution was used to generate the preliminary temperature distribution described in 4.2.3.

Equinox Orbit Heat Loads

Solar heat load histories for an equinox orbit are shown in Figure 4-3. The orbit angle $\phi_E = 0°$ corresponds to midnight, the moment of deepest eclipse. Solar energy first enters the OM housing at $\phi_E = +8.75$ (12:35 a.m.)

TABLE 4-1. CANDIDATE WORST CASES FOR SOLAR HEAT LOADS (NO INTERNAL BAFFLE)

No.	Geometry	Description	Incident Solar Loads, W
1	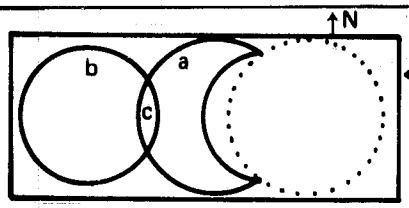	Back surface (mounted to spacecraft irradiated directly (A_a) and by specular reflection (A_b) from pointing mirror. Hot spot at A_c.	A_a: 27.2 A_b: 12.9 A_c: 3.1 Entrance: 43.6
2	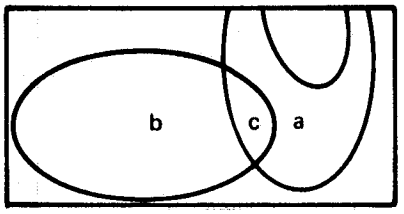	Top surface** (interior of north surface irradiated directly (A_a) and by specular reflection (A_b) from pointing mirror. Hot spot at A_c.	A_a: 13.8 A_b: 23.3 A_c: 5.0 Entrance: 45.4
3	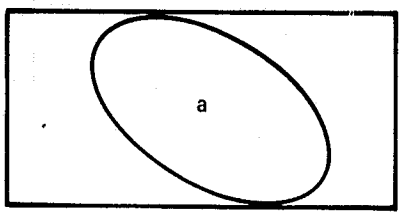	Top surface** (interior of north surface) directly irradiated.	A_a: 30.9 Entrance: 30.9
4	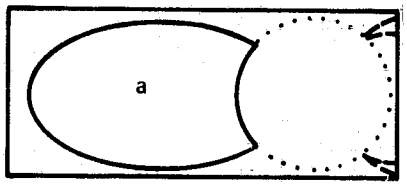	Front surface (aperture surface) (A_a) irradiated by specular reflection. (Back surface and left side irradiated directly.)	A_a: 22 Entrance: 46

*Reflectance of pointing mirror: 96.2 %.
**Same case for bottom surface (interior of south face).

as the spacecraft emerges from the eclipse and continues until $\phi_E = 83.3°$ (5:30 a.m.) when the shallow collar prevents direction irradiation of the interior. The collar is irradiated until $\phi_E = 90°$ (6:00 a.m.). Between 6:00 a.m. and 6:00 p.m. the earth facing aperture is shielded from all direct solar heating. At $\phi_E = -90°$ (6:00 p.m.) direct solar heating resumes and continues until $\phi_E = 8.75°$ (11:25 p.m.) when the spacecraft is eclipsed once more.

4.2.3 First Order Temperature Distributions

The temperature distributions reported here are preliminary insofar as they were obtained from relatively crude thermal models based on an aluminum structure; final results are presented in 4.3. The only case examined was solar heating at 12M, winter solstice. The first analytical model was assigned a single node (temperature) to each of the six enclosure

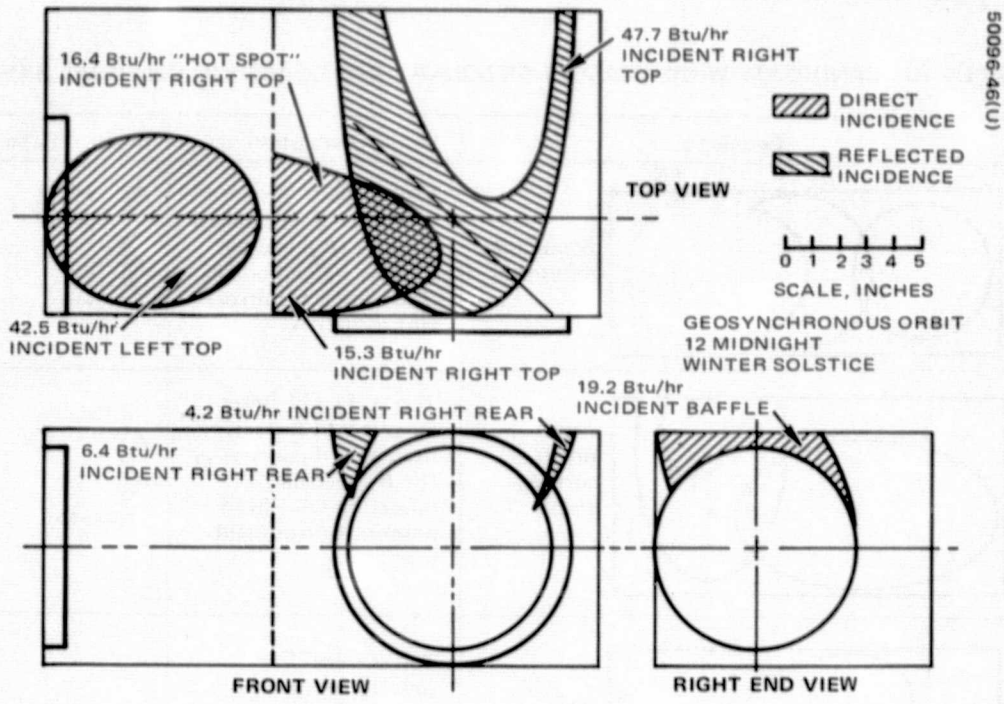

FIGURE 4-2. DISPOSITION OF SOLAR ENERGY IN OPTO-MECHANICAL HOUSING

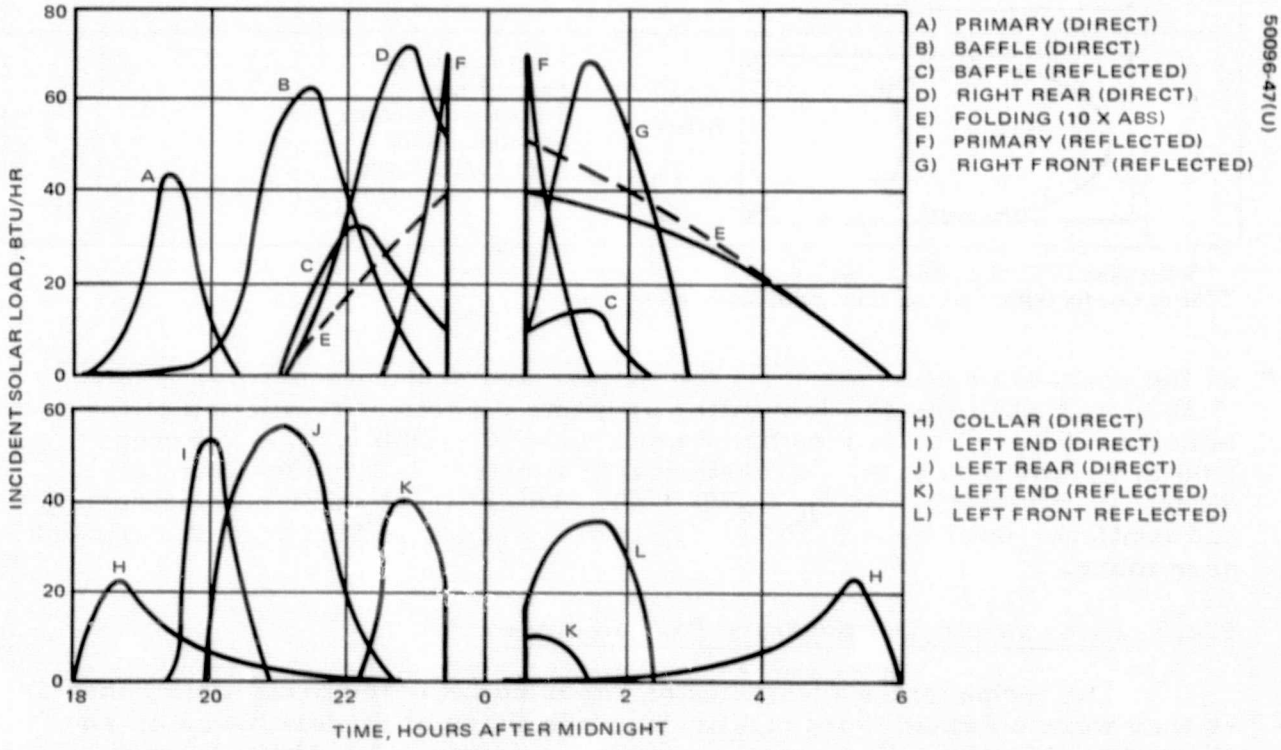

FIGURE 4-3. SOLAR HEATING HISTORY FOR OPTO-MECHANICAL INTERIOR, EQUINOX ORBIT, SOLAR CONSTANT – 430 BTU/HR-FT^2

surfaces (top, bottom, front, back, and ends), and one mode to each of the following: baffle, folding mirror, primary mirror, oscillator, and gimbal. The second analytical model was assigned 10 nodes to the top surface, one each to the baffle and five sides, and omitted mirrors, oscillator, and electromechanical elements. These primary models served to provide insight to the magnitude of structural temperature gradients and suggested the manner in which a more detailed analytical model could be developed for improved predictability.

Description of Nodal Models and Assumptions

The preliminary temperature distributions, reported next, were computed on the GE 265 Time Shared computer using small capacity programs (18 nodes, maximum) developed by the Hughes Thermophysics department. The initial model contained 11 active nodes, and the 12th node was the spacecraft heat sink treated as a boundary node maintained at a temperature of 50°F. Nodal heat inputs based on the 12M winter solstice and assumed electrical loads follow: back, 30 watts; top, 122 Btu/hr (solar); R1, 3.3 Btu/hr (solar); baffle, 19 Btu/hr (solar); oscillator, 4 watts; gimbal motors, 5 watts. Solid construction was neglected and internode structural contact conductance was assumed to be h = 150 Btu/hr-ft^2-°F based on Hughes experience with riveted/epoxy bonded joints; conductances for mirror mounts and gimbal attachments were assumed, arbitrarily, to be hA = 0.1 Btu/hr.-°F. Solar and thermal reflection and radiation within the housing was neglected; solar energy incident on the several structural panels was assumed to be completely absorbed. The complete temperature distributions are given in 6.2; the range of panel temperatures was 68° (top) to 51°F (rear).

The bulk temperatures found from the first model were not adequate for use in computing structural distortions. The results, however, suggested several modifications for a second iteration (i.e., neglect electrical heat sources and mirrors, assume the rear panel is the heat sink), and demonstrated that internal radiation transport was of secondary importance for the structure because of the low temperature levels (50° to 70°F). The second model subdivided the top panel into 10 nodes to take account of solid conduction between nonuniformly heated regions, and the results showed a temperature variation from 60° to 85°F over the top; the structure was assumed to have the properties of aluminum (6061-T6). Other panels were treated as single nodes, and bulk temperature did not change appreciably from the first model results. Mirrors, oscillator, and gimbal were omitted from this model because of limited program capacity. Both models assumed multifoil insulation of external surfaces to eliminate additional coupling to solar loads and space.

Temperature Distributions

The single bulk model temperature distribution for the steady state solstice of Figure 4-3 follows: back, 51.4°F, top, 68.0°F; bottom, 60.1°F; front, 63.3°F; right end, 60.9°F; left end, 62.1°F; baffle, 53.5°F; folding mirror (R1), 189.9°F; primary mirror (R2), 70.7°F; oscillator subassembly, 63.5°F; gimbal subassembly, 156.9°F; spacecraft heat sink (boundary condition), 50°F. A transient analysis of this model showed a time constant of

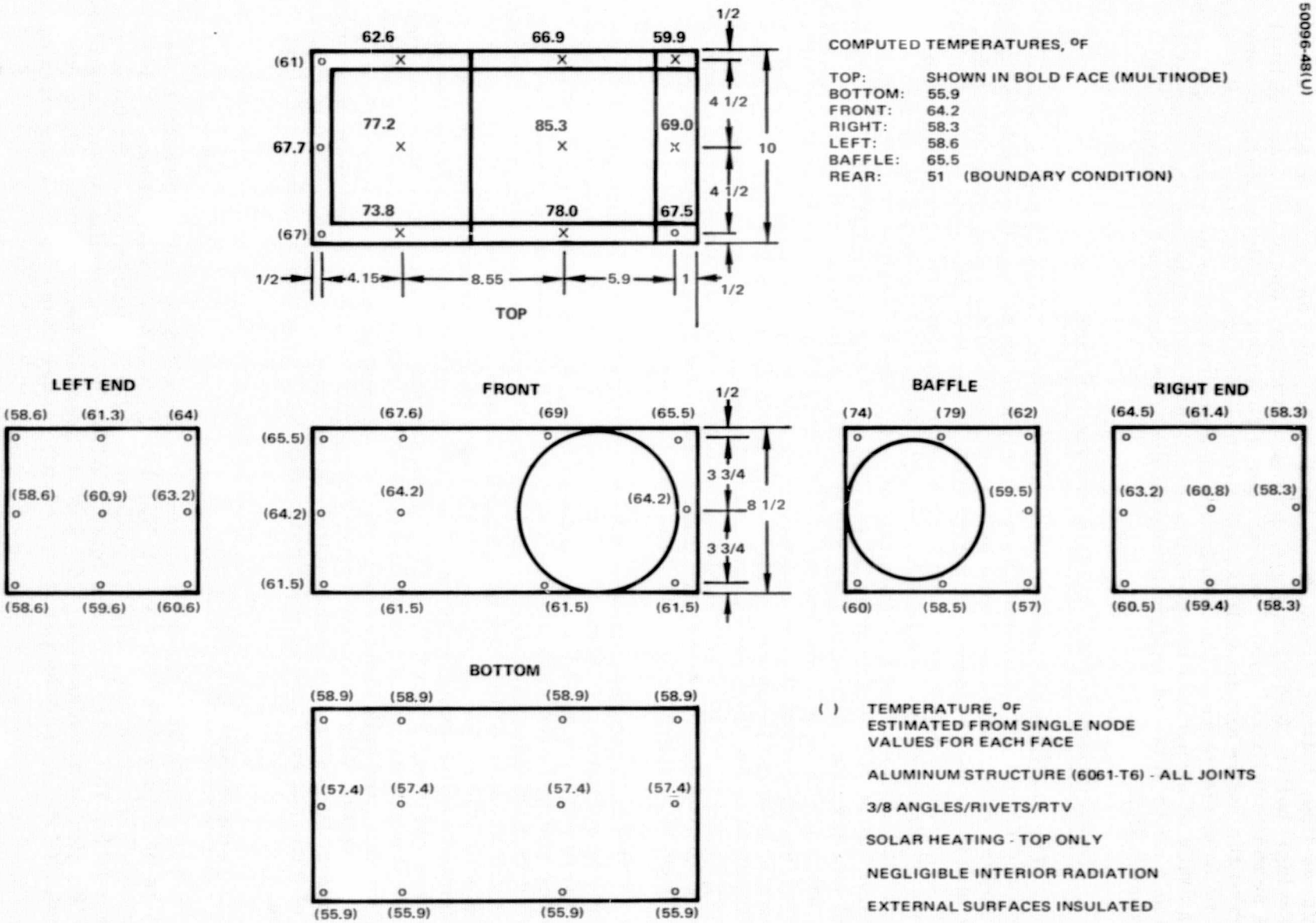

FIGURE 4-4. STEADY STATE TEMPERATURES FOR OPTO-MECHANICAL STRUCTURE

about 5 minutes for the top surface in response to a step input of the solstice and internal heat loads.

The distribution for the second model is shown in Figure 4-4. Local temperatures were computed at 10 points of the top surface and account was taken of internal conduction coupling, joint conductances, and irregular solar heating patterns. Bulk temperatures for other panels are tabulated in Figure 4-4; the local temperatures for front, sides, etc. (shown in parentheses) were interpolated from computed bulk temperatures and computed local values for the top. The maximum temperature was found at the top center (85.3°F) and the minimum temperature was on the bottom (55.9°F) with a maximum temperature difference of 29.4°F.

4.2.4 Discussion of Solar Loads and Temperature Distribution

The solar heat loads given in Figures 4-1 and 4-2 are adequate for the purpose of predicting structural temperatures. The distribution of solar loads is very sensitive to the geometry of the OM structure. Changes in the length of the collar around the entrance aperture or the addition of more internal baffles would have a pronounced influence on the shape and magnitude of the solar loads. It is important to note the following simplifications and omissions in the analysis of solar loads:

1) The solar energy specularly reflected from the primary mirror (R2) is not taken into account. The location of the defocused solar image reflected from F2 may create a local hot spot on the baffle or interior for a variety of orbit conditions.

2) The thickness of the folding mirror (R1) was neglected; the outboard edge of R1 can absorb energy and also modify the shape and magnitude of the solar loads on the rear surface, etc.

3) Solar flux streaming through the field of view aperture in R1 was neglected.

4) The solar load distributions do not account for diffuse interreflections within the OM housing.

5) Angular perturbations of the folding mirror (R1) were neglected in the worst case analysis.

The temperature distributions reported here are preliminary. The analytic models used to compute the temperatures were relatively crude, and the temperature distributions were intended to provide insight to problem areas rather than to predict structural distortions. The properties of 6061-T6 aluminum were used to obtain the local temperatures shown in Figure 4-4; the proposed OM structure will use beryllium (k_{Al} = 99 Btu/hr-ft-°F). The preliminary temperature gradients are conservative insofar as solar and thermal radiation phenomena within the housing were neglected; radiation coupling among surfaces will decrease temperature variations and tend to make the structure more nearly isothermal. It should be noted that the sun shield-radiator assembly required for detector cooling was not included.

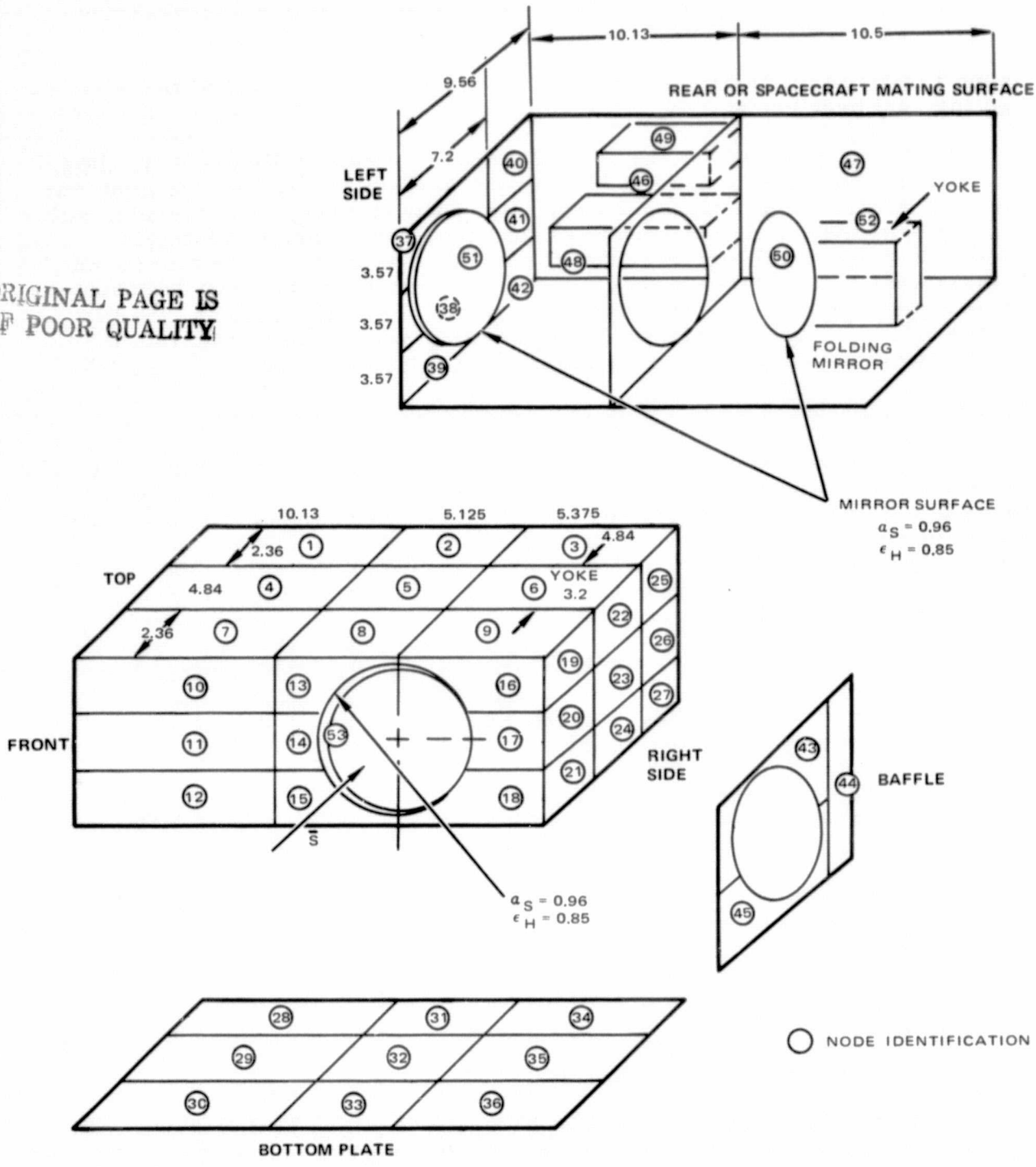

50096-49(U)

- BERYLLIUM STRUCTURAL
- ALL INTERNAL SURFACES EXCEPT MIRRORS: α_S = 0.96, ϵ_H = 0.85
- CONDUCTION STRAP (ℓ = 1.0 in., t = 0.0182, w = 0.25 in.) (38) → (51)
- INSULATION BLANKET (ϵ_{EH} = 0.025) ENCLOSES EXTERNAL WALLS OF O&M, EXCEPT AT RADIATING COOLER AND ENTRY PORT
- BEACON (49) 3^N DISSIPATION
- LOCAL OSCILLATOR (48) 30^W DISSIPATION

FIGURE 4-5. OPTO-MECHANICAL DETAILED THERMAL MODEL

4.3 THERMAL PERFORMANCE OF BERYLLIUM OM SUBSYSTEM

This subsection presents the final results of a thermal study performed to determine the transient temperature response of the opto-mechanical laser communication unit in synchronous orbit. Temperature data generated in this study are those used to perform a thermal deformation study of the OM unit.

The OM unit analyzed is a beryllium structure, hardmounted at the spacecraft interface, and insulated from the deep space environment by superinsulation blankets (ϵ_{eff} = 0.025). To minimize temperature differences between the primary mirror (R2) and its adjacent mounting surface, a conduction strap was sized to yield an effective conductance of 1.0 Btu/hr-°F.

All internal surfaces, except mirrors, are assumed to exhibit a black paint thermal finish. The thermal design is summarized in Figure 4-5.

A 53 node thermal model (Figure 4-5) was generated to determine the transient temperature response of the OM in synchronous orbit. Temperatures were determined using environmental heat loads presented in Figure 4-6b. The transient temperature responses of selective nodes are presented in Figure 4-6.

These curves illustrate when some peak temperatures and, possibly, peak temperature differences occur.

Temperature maps for the OM are shown in Figure 4-7 for selective times in orbit to illustrate temperature distribution when 1) there are no environmental loads (Figure 4-7a) and 2) when some surfaces experience their peak temperatures (Figures 4-7b and 4-7c).

No attempt was made in this study to optimize the design. The only design change made was to size a conduction strap so that temperature differences between the primary mirror and its adjacent mounting structure are small.

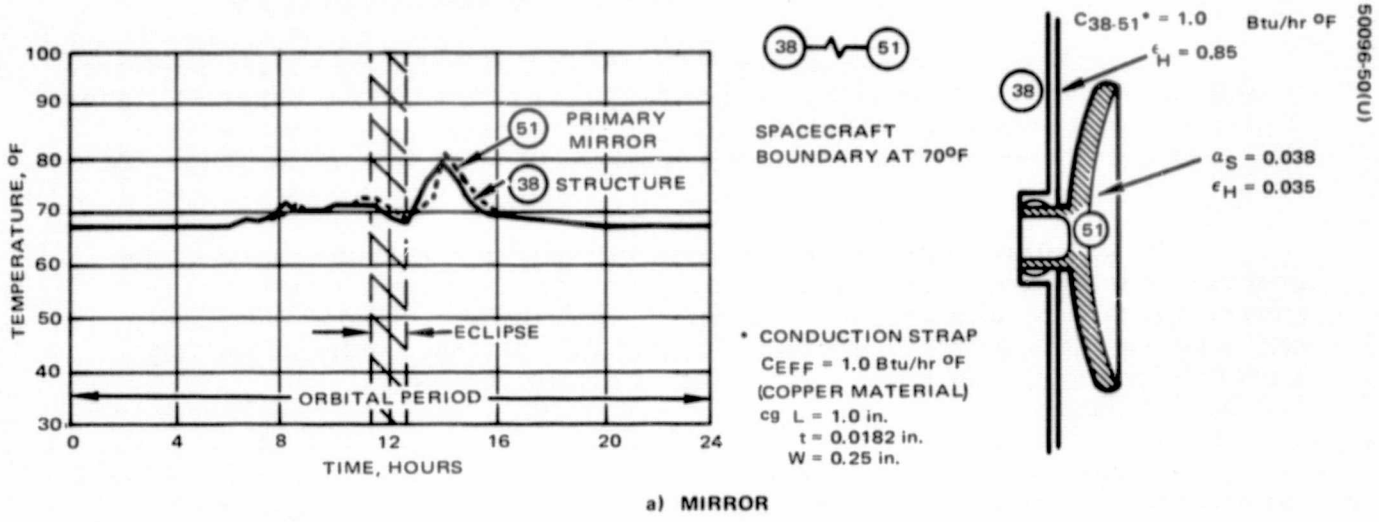

a) MIRROR

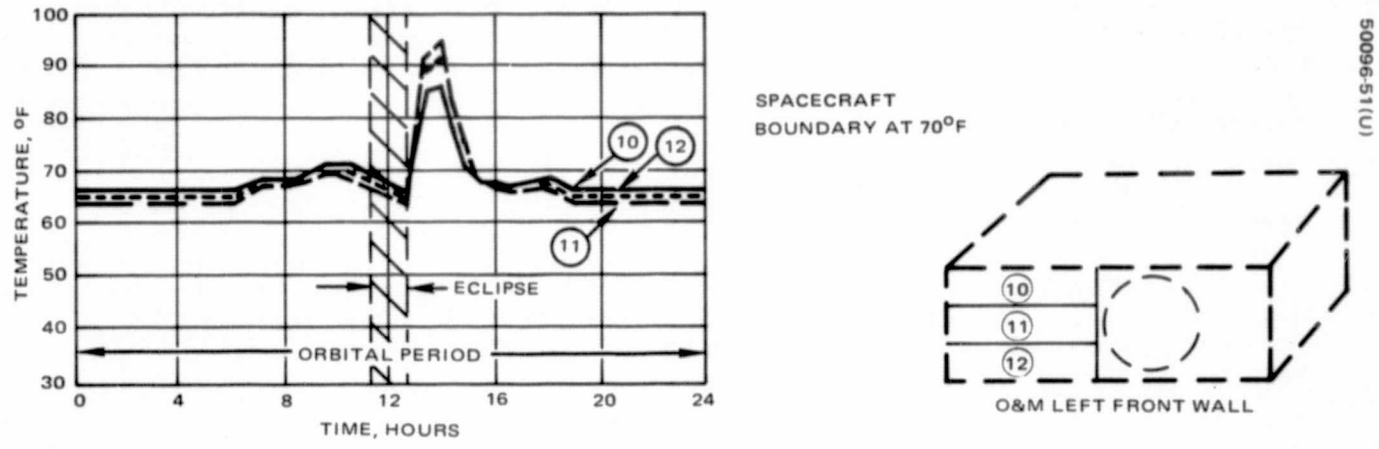

b) LEFT FRONT WALL

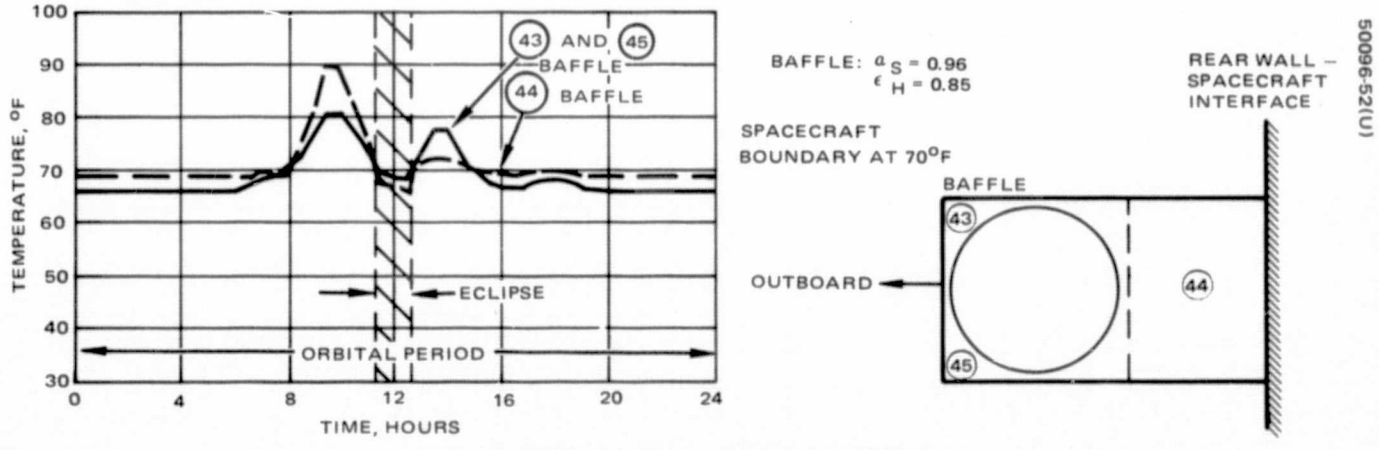

c) REAR WALL AND SPACECRAFT INTERFACE

FIGURE 4-6. OPTO-MECHANICAL TRANSIENT RESPONSE IN SYNCHRONOUS ORBIT–EQUINOX

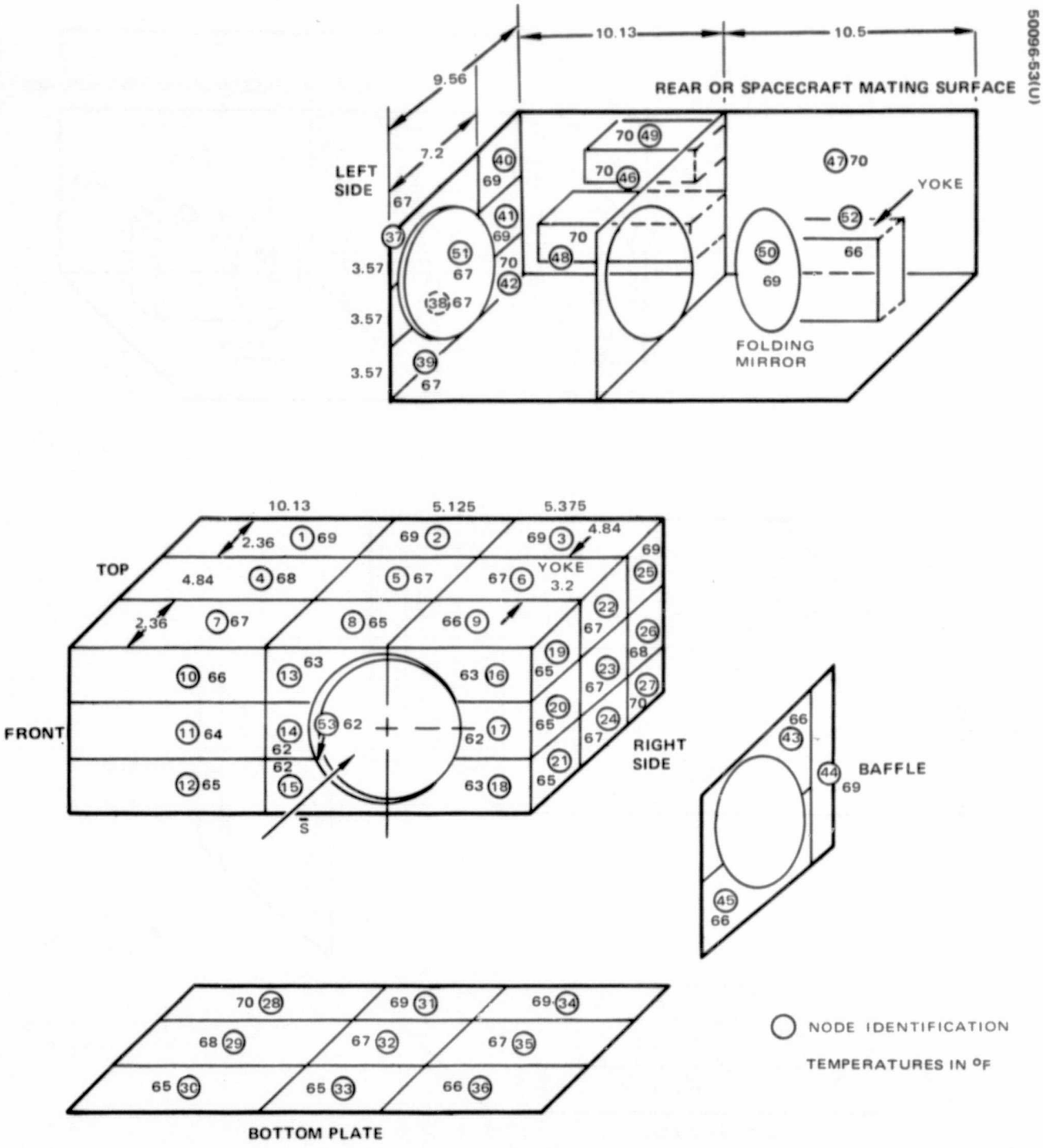

a) τ = 6.0 HOURS

FIGURE 4-7. OPTO-MECHANICAL DETAILED THERMAL MAP

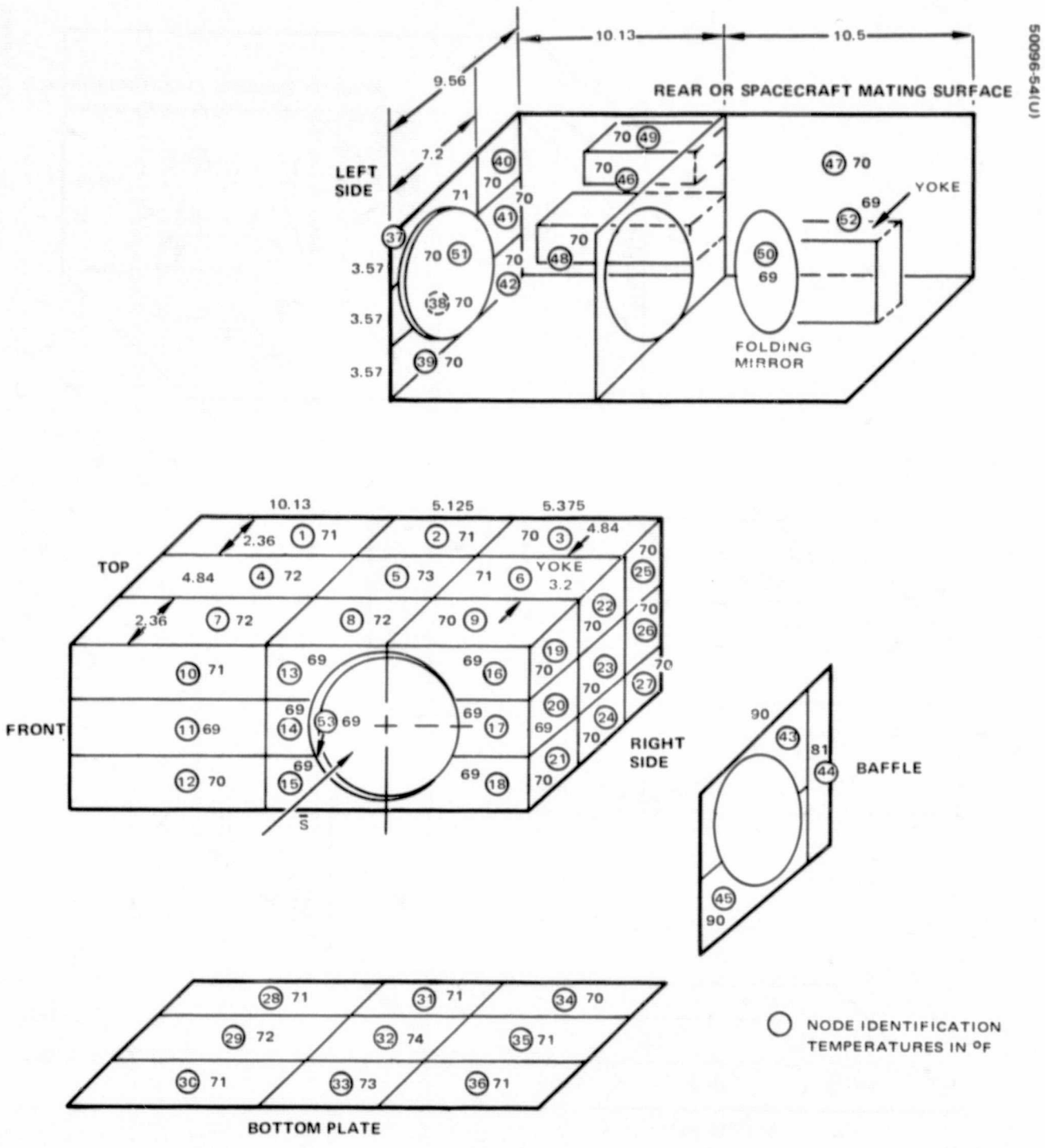

50096-54(U)

b) τ = 9.5 HOURS

FIGURE 4-7(CONTINUED). OPTO-MECHANICAL DETAILED THERMAL MAP

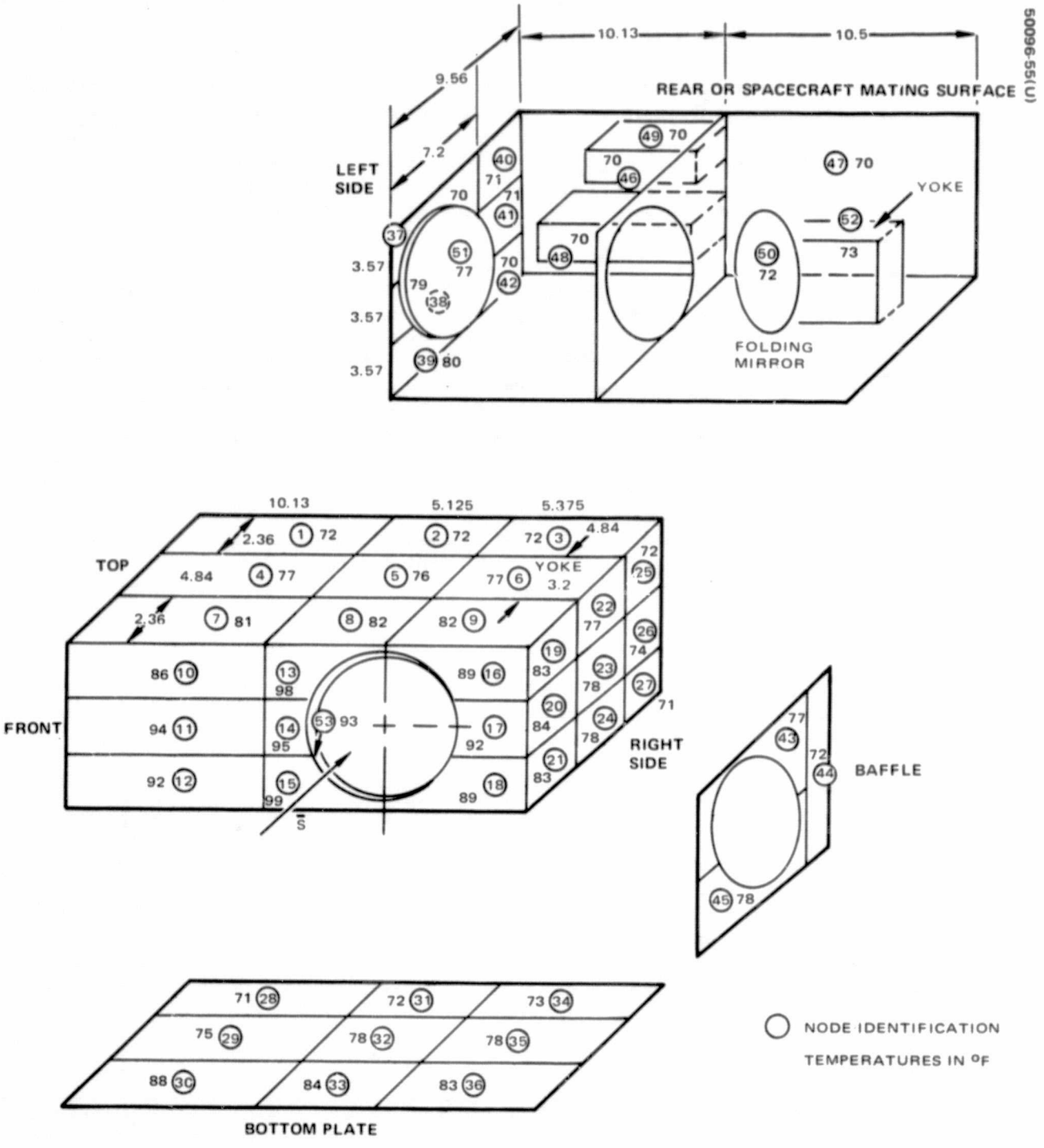

c) τ = 14.0 HOURS

FIGURE 4-7(CONTINUED). OPTO-MECHANICAL DETAILED THERMAL MAP

4.4 NONUNIFORM SOLAR HEATING OF OM PRIMARY MIRROR

Nonuniform solar heating of the primary mirror (R2) creates negligible temperature nonuniformities in the beryllium mass. The primary mirror was analyzed as a 14 node thick disk subjected to a vignetted solar heat flux moving across the reflective surface. The results may be extrapolated to the case of temperature gradients occurring in the pointing mirror as well. The case of temperature distributions due to a focused hot spot are not examined here.

The analyses reported in 4.2 and 4.3 were intended to provide detailed temperature distributions of the OM structure and mean value (bulk) temperatures for selected optical, mechanical, and electronic components. The results reported here provide additional insight to the temperature distribution in the primary mirror due to nonuniform and time dependent solar heating. The temperature response was examined for an orbital segment between 18:27 and 20:47 hours corresponding to the direct solar heat load shown in 4.2, Figure 4-3 for the orbital angles $-83.3 < \phi_e \leq 53°$. During this interval, solar flux penetrates the entrance aperture and the baffle and creates a moving vignette of these circular openings on the primary mirror. This vignetted heat load appeared to have a potential for creating a diametral temperature differential with subsequent distortion of the optical figure of the primary mirror.

4.4.1 Analytical Model

The analytical model consisted of the primary mirror, the bulkhead to which it is mounted, and a cylindrical connecting element. The arrangement of nodes is shown schematically in Figure 4-8.

The mirror contained 13 beryllium nodes (approximately 1.44 x 1.44 x 0.63 in^3), the cylinder connector was a single node, and the bulkhead was a secondary node held at a constant temperature of 70°F. Solid conduction coupling was assumed between adjacent sets of the 14 active nodes and a contact conductance, h = 100 Btu/hr-ft^2-°F, was used to couple the cylinder to the bulkhead. The moving solar heat load was transformed to a time dependent heat source at each of the 13 mirror nodes. Coupling by thermal radiation to the surroundings was neglected. The initial temperature of all nodes was taken as 70°F. This model was programmed for the GE265 Time Share digital computer.

4.4.2 Results

The maximum temperature differential between outermost diametral nodes (nodes 1 and 5) was less than 0.20°F during the entire heating interval. The maximum temperature rise of any node (above the initial value) was less than 0.50°F. These deviations from a stationary condition are due to the

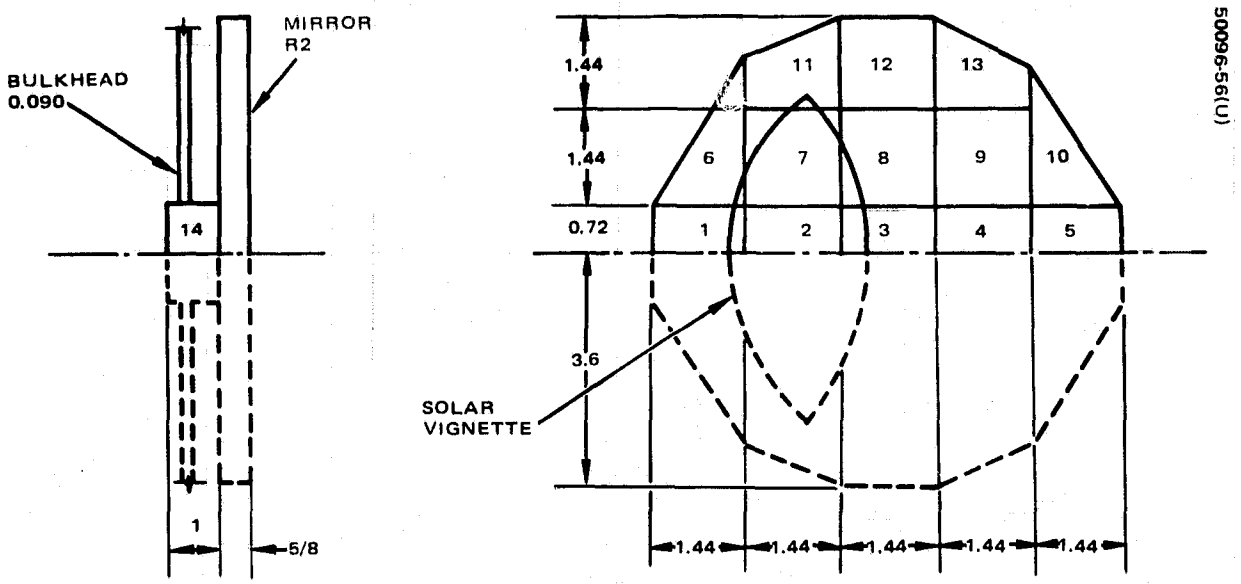

DIMENSION IN INCHES

FIGURE 4-8. MODAL MODEL OF PRIMARY MIRROR AND INSTANTANEOUS PATTERN OF SOLAR IRRADIATION

small magnitude of solar absorptance of the mirror surface (α = 0.0362) and the high thermal conductivity and specific heat of beryllium. The nodal temperatures tabulated below occur at 1.6 hours after initiation of direct solar heating; the temperature of node 5 is the highest value observed in the time span examined:

Node	Temperature, °F	Node	Temperature, °F
1	70.28	8	70.31
2	70.29	9	70.35
3	70.30	10	70.40
4	70.35	11	70.30
5	70.41	12	70.31
6	70.28	13	70.33
7	70.29	14	70.30

(An extreme, unrealistic case was also examined: a "black mirror," α = 1. For this condition, a maximum temperature differential rise of any node was 10.3°F above the initial condition. This case was run to verify the continuity of the analytical model rather than to evaluate worst case conditions.)

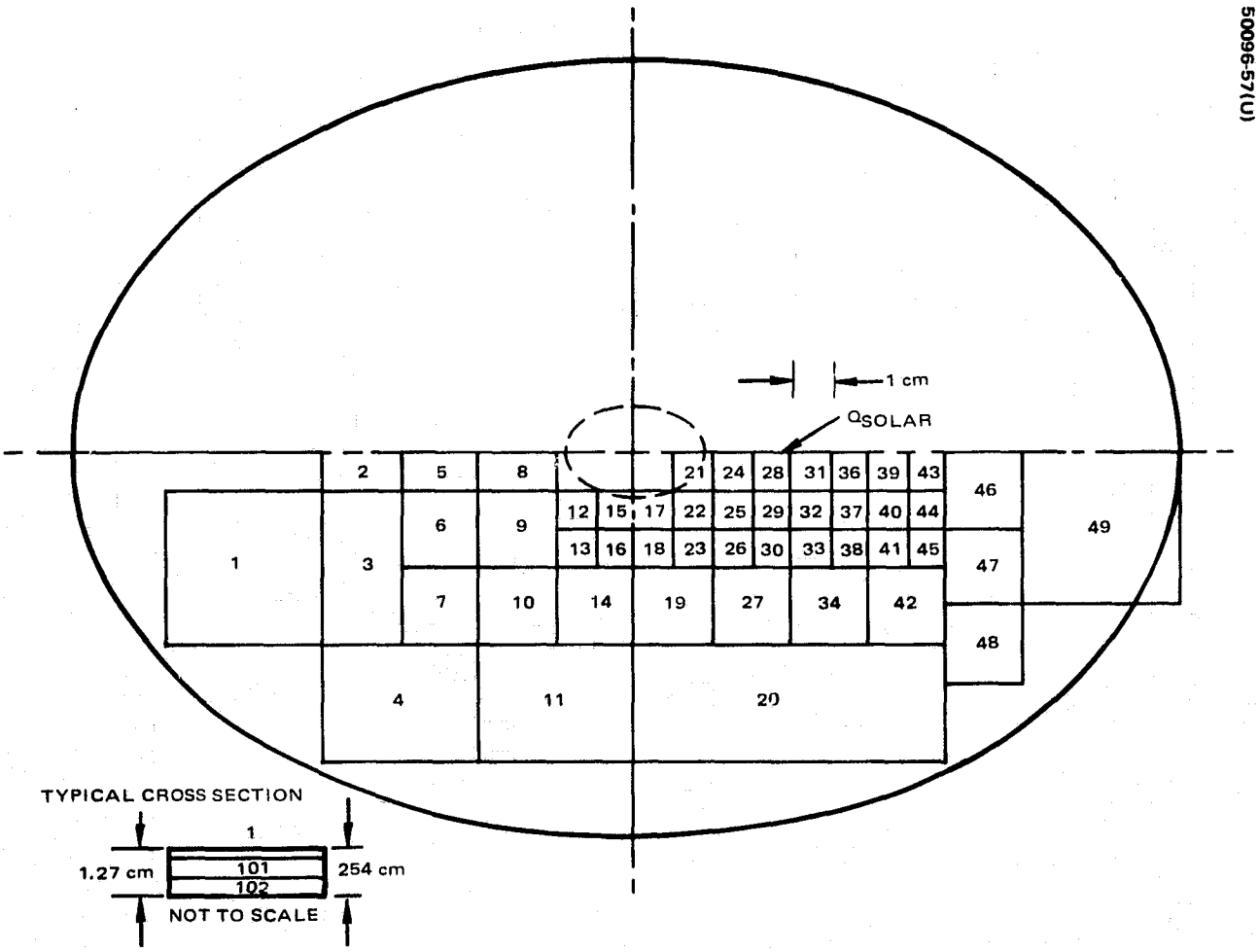

FIGURE 4-9. THERMAL MODEL OPTO-MECHANICAL POINTING MIRROR

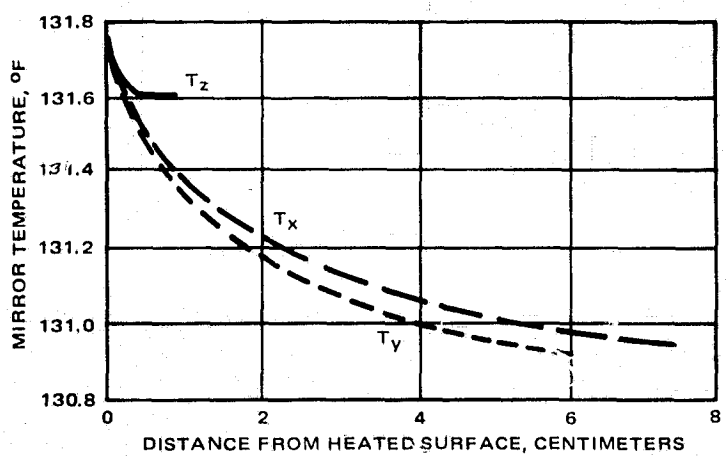

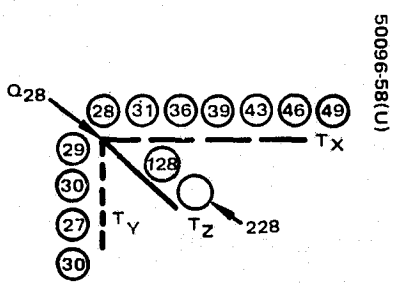

FIGURE 4-10. OPTO-MECHANICAL POINTED MIRROR TEMPERATURE DISTRIBUTION WITH CONCENTRATED SOLAR HEATING

These results suggest that the large mirrors in the OM subsystem are very nearly isothermal in responding to the low level solar heat inputs. (The case of temperature distribution due to a focused solar hot spot on the pointing mirror is discussed in the following section.) The detailed temperature distributions found in this analysis correspond to the results shown in Figure 4-6a, for the time period 6 to 8 hours in which mirror R2 was treated as a single node whose temperature followed the temperature of the bulkhead.

4.5 THERMAL EFFECTS OF SUN'S FOCUSED IMAGE ON POINTING MIRROR

Previous thermal analyses of the OM subsystem examined bulk temperature difference between mirrors and bulkheads (4.3) and temperature gradients in the primary mirror caused by nonuniform direct solar heating (4.4). The problem examined here deals with the detailed temperature distribution in the pointing mirror caused by a hot spot of solar energy focused on a 1/2 cm^2 area (position 4 as described in 2.4).

The pointing mirror was subdivided into 147 beryllium modes (49 surface nodes, 3 layers deep) using the major axis as a line conductive symmetry (Figure 4-9). The surface nodes were coupled by radiation to space and the interior of the OM structure. The data of 2.4 indicate the peak solar flux density on the mirror is experienced when the sun is at -3658° off-axis with 88.7 percent of the on-axis heat load focused on a 1/2 cm^2 area on the front surface. Numerical results were obtained using OM structure boundary temperatures and mirror radiative properties ($\alpha = \epsilon = 0.035$) reported in (4.2). Computations were made on a GE 635 digital computer using the TAP-3 Steady State program (6500 iterations, 0.00001° convergence criterion).

Selected temperatures of nodes in the immediate vicinity of the hot spot are shown in Figure 4-10. The maximum temperature occurs under the hot spot, $T_{28} = 131.75°F$, and the minimum temperature is at node 1, $T_1 = 130.57°F$. The maximum temperature drop through the 1/2 inch mirror is $T_{28} - T_{228} = 0.15°F$. The surface temperature decreases monotonically to approximately 131°F at a distance of 5 cm from the center of the hot spot.

It is not possible to assess the accuracy of the numerical results without performing additional calculations with a larger nodal mode. The present temperatures and gradients appear to be conservatively high because the back surface of the mirror is assumed to be a polished surface. It should be noted that no attempt was made to account for conduction from mirror nodes to the gimbal supports. If the temperatures reported here lead to marginal or unacceptable mirror distortion, it would be necessary to extend this analysis.

4.6 ON-ORBIT TEMPERATURE DISTRIBUTION IN GIMBAL MECHANISM

This subsection presents the results of a thermal study performed to determine the temperature distribution within the OM gimbal mechanism of the 10 μm receiver subsystem. A schematic diagram of the thermal model and an on-orbit steady temperature distribution are presented in Figure 4-11.

The gimbal mechanism is a high emittance (ϵ_H = 0.85) aluminum structure attached by bearings to a beryllium pointing mirror and a beryllium structural wall. Mirror positioning is provided by the use of tilt-and-roll motors with appropriate gearing.

The yoke is a highly conductive aluminum alloy; however, conduction across the bearings to the beryllium mirror and the structural wall is negligible. Temperature control is provided by radiative coupling of the gimbal unit to the OM structural walls.

The gimbal mechanism temperature distributions were determined assuming a 1.4 watt power dissipation in each drive motor and the boundary conditions given in 4.2. The solar load on the mirror is 3.72 Btu/hr.

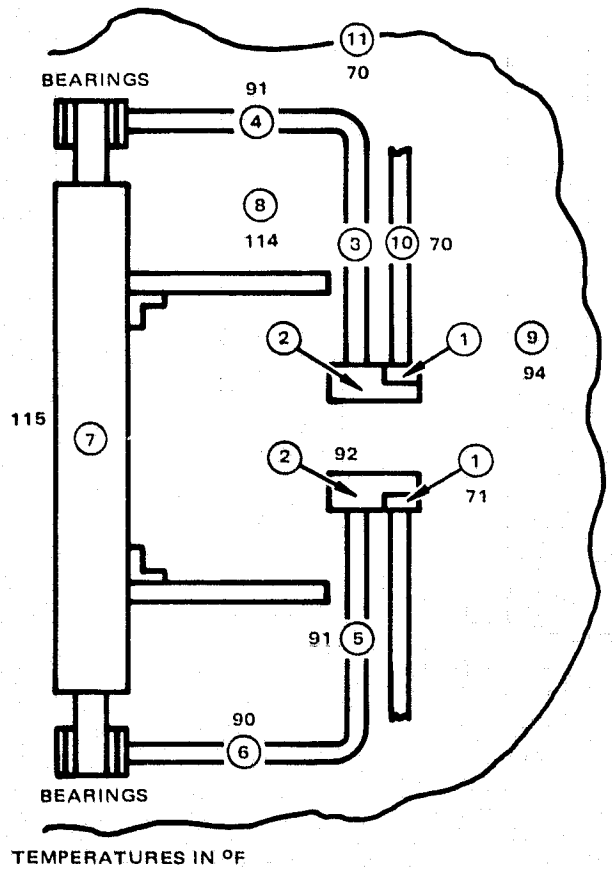

5009-59(U)

NODE	DESCRIPTION
1	BEARING/WALL INTERFACE
2	BEARING/YOKE INTERFACE
3	YOKE
4	YOKE
5	YOKE
6	YOKE
7	POINTING MIRROR
8	TILT MOTOR
9	ROLL MOTOR
10, 11	BOUNDARIES

FIGURE 4-11. OPTO-MECHANICAL GIMBAL MECHANISM

4.7 DISCUSSION OF THERMAL STUDIES

The temperature levels and distributions reported in 4.2 through 4.6 suggest there are no serious thermal problems inherent in the OM subsystem. The thermal studies had greater depth than required to demonstrate the feasibility of the design, but did not have the breadth required to optimize flight qualified hardware. It appears possible to reduce structural temperature gradients below those reported above by considering the following design options:

1) Lengthen the collar around the entrance aperture to create a "shadow tube" which limits the amount of solar energy entering the housing.

2) Use a diffuse, highly reflective, surface finish on interior surfaces, (e.g., white paint) to redistribute solar loads by interreflections.

3) Introduce heat pipes (and/or doublers) into the structure to enhance thermal coupling between hot and cold regions.

4) Design a thermal control system for the OM housing to supplement the spacecraft heat sink (e.g. louvres on the earth facing surface, heaters on various structural panels).

It is unlikely that an optimum thermal design can be achieved without specifying a definite spacecraft, mission, and weight/power requirements for the OM payload. The options just listed are intended to demonstrate several degrees of freedom which have not been exercised in the design analysis to date.

5. MECHANICAL DISTORTION MODEL

5.1 THERMAL LOADING

The structural model (Figure 5-1) has been arranged to match the thermal model as closely as possible. Temperature data obtained from the thermal model are then used to compute mechanical distortion of the opto-mechanical subsystem structure. These distortion data are used to obtain optical performance data in Section 6 of this report.

The model consists of 68 rectangular plates, 20 triangular plates, and 40 axial force members along the box edges (see Figure 5-2). Two cases of restraints are considered. First, a single node is constrained on the end of the box on which the gimbal is mounted (see Tables 5-1 and 5-2) and second, three points along the baseplate are restrained. The second case is similar to the actual three-point mounting of the box (refer to Tables 5-3 and 5-4).

Six temperature load cases are evaluated representing different times during the orbit corresponding to the transition of the sun angle through the worst case equinox condition. An earth eclipse occurs at from 11.5 to about 12.5 hours presenting a sharp transient to the OM subsystem at near direct solar incidence.

The computer program used to compute the distortion is Stardyne. Computations are presented in two forms: 1) tabular data on box elongation and tilt (see Tables 5-1 through 5-4) and 2) pictographs of the box with exaggerated distortion amplitudes (see Figure 5-3). The tabular data are used to compute the optical performance. The graphic data are for the qualitative evaluation of the box distortion.

5.2 STATIC AND DYNAMIC MECHANICAL LOADING

Analytical results have been obtained for both static 1 g loading and dynamic sinusoidal sweep loading of the opto-mechanical structure. The static loading shows extremely small deformation of the structure giving rise to negligible loss of signal. The dynamic loading shows that the lowest mechanical resonance seen is on the order of 617 Hz, far above that usually considered structurally dangerous. Further, computation of worst case internal loads shows the maximum stress is about one tenth of the material stress limit.

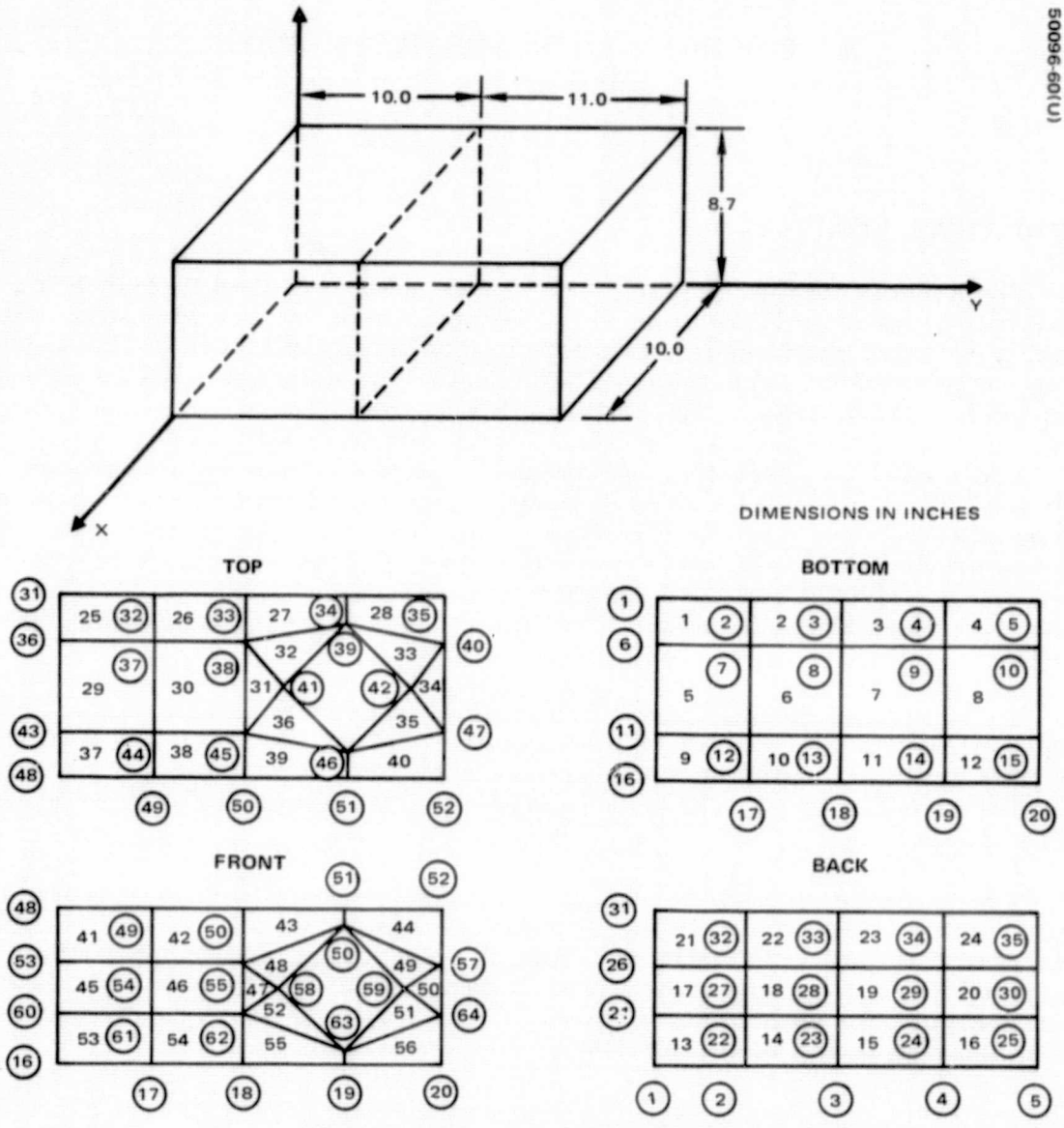

FIGURE 5-1. STRUCTURAL MODEL OF OPTO-MECHANICAL SUBSYSTEM

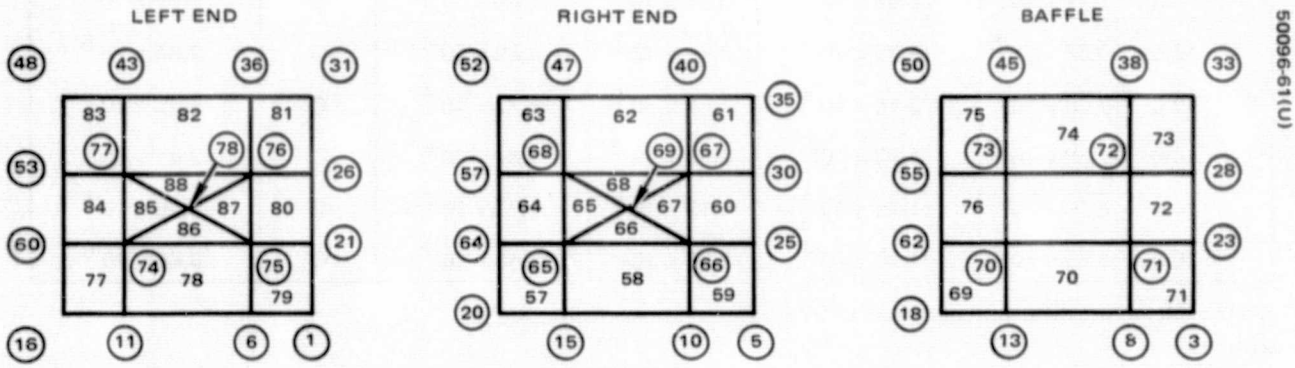

MODEL CONSIST OF

68 RECTANGULAR PLATES

20 TRIANGULAR PLATES

40 AXIAL FORCE MEMBERS (ALONG BOX EDGES)

RESTRAINTS

CASE 1 - NODE 69 RESTRAINED IN ALL DIRECTIONS

CASE 2 - NODES 5, 26, AND 35 RESTRAINED AGAINST TRANSLATION

LOAD CASES - 6 TEMPERATURE LOAD CASES AT DIFFERENT TIMES DURING ORBIT

COMPUTER PROGRAM - STAROYNE

FIGURE 5-2. COMPUTER PROGRAM – STARDYNE

TABLE 5-1. THERMAL DISTORTION AT PRIMARY MIRROR

Location Relative to Secondary Mirror Location for Beryllium Box and Reference Temperature of 70°F: One Point Suspension

Time, hr	ΔX, in.	ΔY, in.	ΔZ, in.	θ_X, rad	θ_Y, rad	θ_Z, rad
6.0	7.77×10^{-4}	2.66×10^{-4}	-3.01×10^{-5}	1.69×10^{-6}	0*	3.95×10^{-5}
10.5	9.56×10^{-5}	-5.36×10^{-5}	8.15×10^{-5}	-3.69×10^{-6}	0	7.84×10^{-6}
12.5	7.08×10^{-4}	3.18×10^{-4}	-1.58×10^{-5}	-7.77×10^{-8}	0	6.45×10^{-5}
14.0	-2.38×10^{-3}	-1.13×10^{-3}	9.65×10^{-6}	-3.67×10^{-6}	0	2.41×10^{-4}
16.5	3.09×10^{-4}	1.75×10^{-4}	-5.19×10^{-5}	1.77×10^{-6}	0	3.28×10^{-5}
18.0	3.75×10^{-4}	1.78×10^{-4}	-2.38×10^{-5}	2.65×10^{-7}	0	3.66×10^{-6}

NOTE: Maximum distortion occurs at 14.0 hr
with

$$\Delta Y = -1.13 \times 10^{-3} \text{ in.}$$

$$\theta_X = -3.67 \times 10^{-6} \text{ rad.}$$

$$\theta_Z = 2.41 \times 10^{-4} \text{ rad}$$

*$\theta_Y \equiv 0.0$ because of finite elements stiffness characteristics.

TABLE 5-2. THERMAL DISTORTION OF DETECTOR

Relative to its Rest Position for Beryllium Box and Reference Temperature of 70°F: One Point Suspension

Time, hr	ΔZ Node 39	ΔZ Node 41	ΔZ Node 42	ΔZ Node 46	ΔZ Average for Detector
6.0	2.99×10^{-6}	-8.28×10^{-5}	-7.58×10^{-5}	-1.95×10^{-4}	-8.77×10^{-5}
10.5	3.64×10^{-5}	2.87×10^{-4}	1.43×10^{-5}	-3.99×10^{-6}	8.34×10^{-5}
12.5	-1.89×10^{-6}	-7.57×10^{-5}	-6.98×10^{-5}	-1.83×10^{-4}	-8.26×10^{-5}
14.0	-5.89×10^{-5}	8.96×10^{-5}	1.87×10^{-4}	5.64×10^{-4}	1.95×10^{-4}
16.5	-1.33×10^{-5}	-7.08×10^{-5}	-3.61×10^{-5}	-9.15×10^{-5}	-5.29×10^{-5}
18.0	-6.47×10^{-6}	-5.50×10^{-5}	-2.73×10^{-5}	-9.33×10^{-5}	-4.55×10^{-5}

TABLE 5-3. THERMAL DISTORTION AT PRIMARY MIRROR

Location Relative to Secondary Mirror Location for Beryllium Box and Reference Temperature of 70°F: Three Point Suspension

Time, hr	ΔX, in.	ΔY, in.	ΔZ, in.	θ_X, rad	θ_Y, rad	θ_Z, rad
6.0	3.6×10^{-5}	2.57×10^{-4}	8.70×10^{-6}	2.56×10^{-6}	0*	4.22×10^{-5}
10.5	6.67×10^{-5}	-4.51×10^{-5}	-6.90×10^{-6}	-4.75×10^{-6}	0	4.72×10^{-6}
12.5	6.38×10^{-5}	3.09×10^{-4}	-4.28×10^{-6}	1.06×10^{-6}	0	6.76×10^{-5}
14.0	-6.42×10^{-5}	-1.12×10^{-3}	2.05×10^{-6}	-5.18×10^{-6}	0	-2.46×10^{-4}
16.5	3.4×10^{-6}	1.70×10^{-4}	-2.30×10^{-6}	2.36×10^{-6}	0	3.44×10^{-5}
18.0	2.6×10^{-6}	1.74×10^{-4}	-2.35×10^{-6}	7.31×10^{-7}	0	3.79×10^{-5}

NOTE: Maximum distortion occurs at 14.0 hr with

$$\Delta Y = -1.13 \times 10^{-3} \text{ in.}$$

$$\theta_X = -3.67 \times 10^{-6} \text{ rad.}$$

$$\theta_Z = 2.41 \times 10^{-4} \text{ rad.}$$

*$\theta_Y \equiv 0.0$ because of finite elements stiffness characteristics.

TABLE 5-4. THERMAL DISTORTION OF DETECTOR

Relative to its Rest Position for Beryllium Box and Reference Temperature of 70°F: Three Point Suspension

Time, hr	ΔZ Node 39	ΔZ Node 41	ΔZ Node 42	ΔZ Node 46	ΔZ Average for Detector
6.0	-1.72×10^{-5}	-7.33×10^{-5}	-7.68×10^{-5}	-1.66×10^{-4}	-8.33×10^{-5}
10.5	1.14×10^{-5}	2.50×10^{-4}	6.48×10^{-6}	-2.39×10^{-5}	6.10×10^{-5}
12.5	-2.18×10^{-5}	-7.14×10^{-5}	-7.20×10^{-5}	-1.61×10^{-4}	-8.16×10^{-5}
14.0	1.99×10^{-5}	8.97×10^{-5}	1.94×10^{-4}	4.93×10^{-4}	1.99×10^{-4}
16.5	-9.83×10^{-6}	-5.06×10^{-5}	-3.34×10^{-5}	-7.21×10^{-5}	-4.15×10^{-5}
18.0	-8.39×10^{-6}	-4.68×10^{-5}	-2.70×10^{-5}	-8.29×10^{-5}	-4.13×10^{-5}

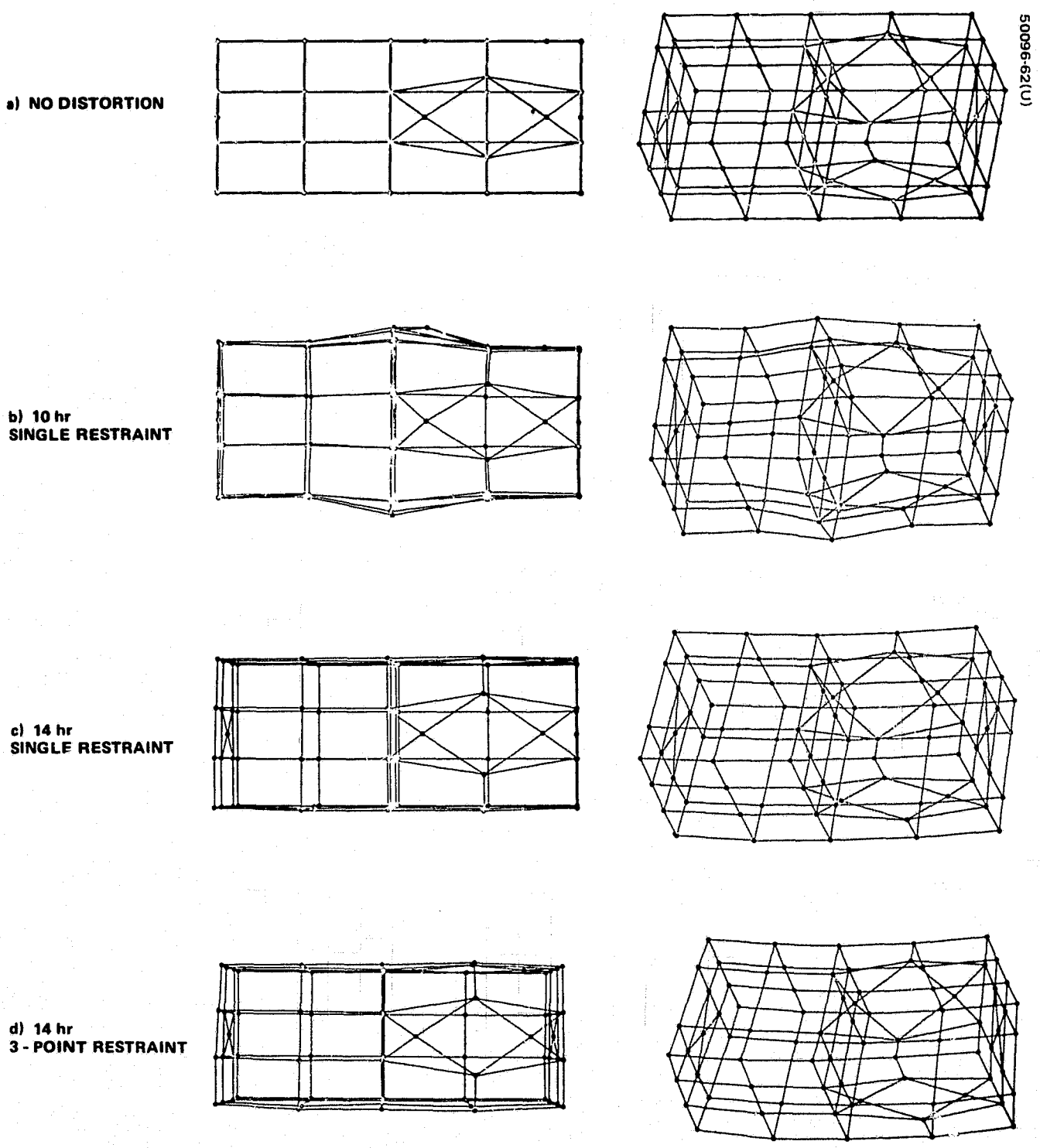

FIGURE 5-3. EXAGGERATED BOX DISTORTION – COMPUTER PICTOGRAPHS

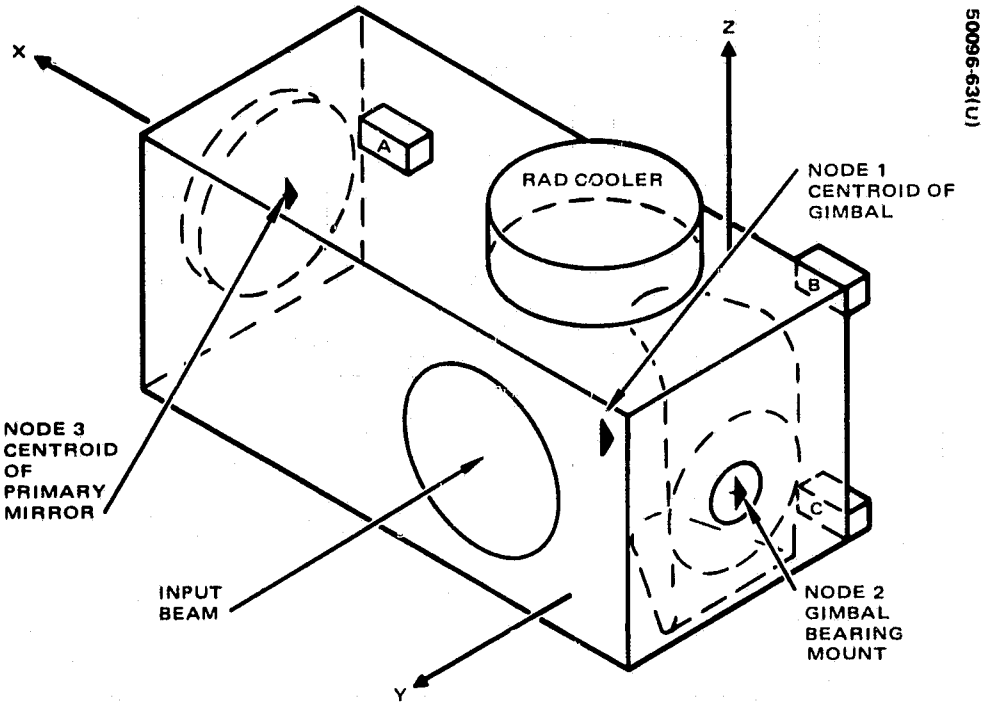

5009G-631(U)

FIGURE 5-4. IDENTIFICATION OF LOADING AXES AND POINTS USED IN STATIC AND DYNAMIC ANALYSES OF OPTO-MECHANICAL SUBSYSTEM

The mechanical structural model consists of 68 rectangular plates, 20 triangular plates, and 40 axial force members along the box edges. The computer program used to compute the mechanical distortion and g-loading is Stardyne, the same as that used for the thermal-structural computations. The analysis assumes that the box is supported by three mounting pads on the baseplate labeled A, B, and C in Figure 5-4.

5.2.1 Analysis of Static Loading

Specifications require that the signal intensity shall not change more than 1 dB as a result of arbitrary orientation in the earth's gravitational field of the rigid support structure on which the OM package is mounted. Analysis of this loading amounts to the application of a 1 g force applied along each axis individually and a determination of the change of focal position. The actual signal loss is then obtained from Figures 2-7 through 2-9 of the Design Report. The X-axis is taken to be along the length of the box, the Y-axis perpendicular to the entrance aperture, and the Z-axis perpendicular to the radiation cooler aperture.

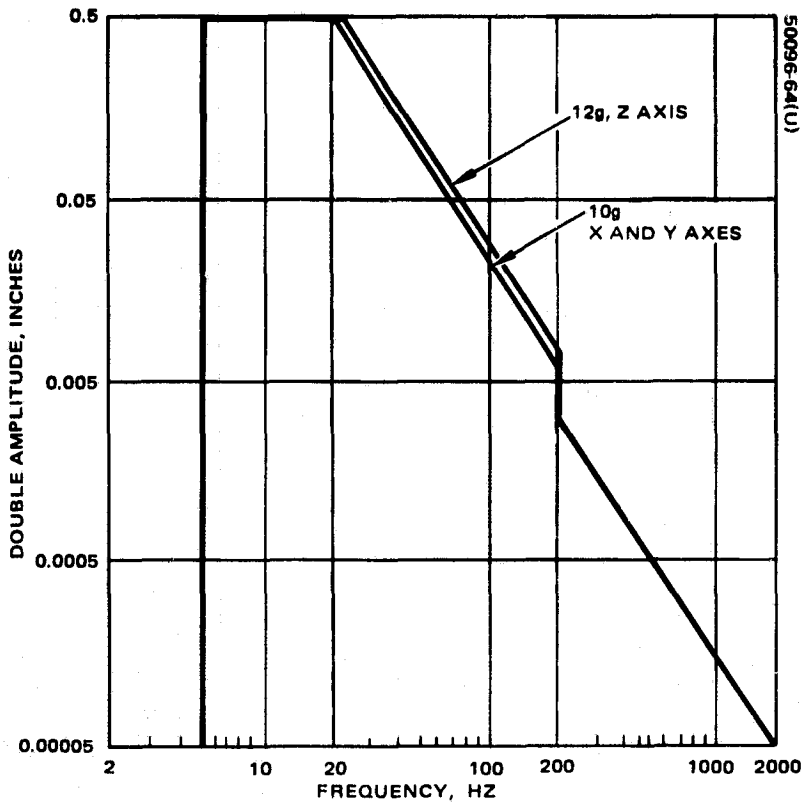

a) AS FUNCTION OF DOUBLE AMPLITUDE FREQUENCY, HZ

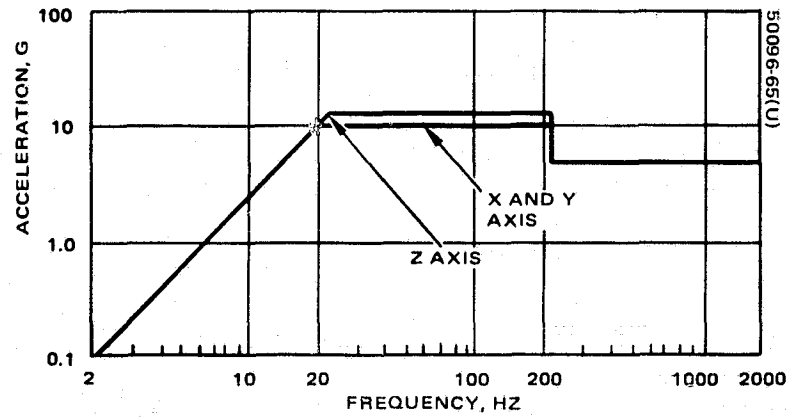

b) AS FUNCTION OF ACCELERATION

FIGURE 5-5. ATS VIBRATION PROFILE

Load Direction	Decentration, in.	Focal Position, in.	Signal Loss, %
X	0.4×10^{-6}	18×10^{-6}	0.0
Y	0.055×10^{-6}	2×10^{-6}	0.0
Z	4.3×10^{-6}	0.43×10^{-6}	0.0

5.2.2 Analysis of Dynamic Loading

In the dynamic analysis, the g-loading response of three critical points is considered: 1) the centroid of the gimbaled assembly, 2) the center of the plate on which the gimbal is mounted, and 3) the centroid of the primary mirror. For each shake axis, linear accelerations have been determined for the X-, Y-, and Z-axes, as well as the rotational accelerations about each of these axes. This results in six acceleration plots for each critical point for each shake direction, or 54 acceleration runs in all. Although this data is available and is being retained, much of it is not significant. This report will summarize the data and present only the important portions.

5.2.3 Vibration Profile

The vibration profile assumed for this analysis was obtained from GSFC Specification S-320-ATS-2, Environmental Test Specification for Components and Experiments for the ATS-F and G Satellites. This profile is given in Table 5-5 and is presented as a function of double amplitude in Figure 5-5a and as a function of acceleration in Figure 5-5b.

TABLE 5-5. SINUSOIDAL SWEPT FREQUENCY VIBRATION TEST DESIGN QUALIFICATION

Frequency, Hz	Axis	Sweep Rate	Input Level (Stated)
5 to 22	Thrust (Z-Z)	2 octaves/min	0.5 in. double amplitude constant displacement
22 to 200			12.0g (0-to-peak)
200 to 2000			5.0g (0-to-peak)
5 to 20	Lateral (X-X and Y-Y)	2 octaves/min	0.5 in. double amplitude constant displacement
20 to 200			10.0g (0-to-peak)
200 to 2000			5.0g (0-to-peak)
Total test time: 13.0 min			

5.2.4 Worst Case Acceleration History

The lowest mechanical resonance frequency observed is 617 Hz where accelerations in all directions seem to peak with higher resonances occurring at 1100, 1536, and 1777 Hz. The highest accelerations obtained are for the X-shake in the X-direction. The 617 Hz resonance appears to be that of the gimbal assembly, and the 1100 Hz resonance appears to be that of the primary mirror assembly.

The maximum acceleration in the gimbal assembly at 617 Hz is 264 g, which corresponds to a peak displacement of 0.007 inch. The maximum acceleration in the primary mirror assembly at 1100 Hz is 308 g, which corresponds to a peak displacement of 0.003 inch. The worst case is for the gimbal assembly centroid. The displacement of 0.007 inch creates a stress in the wall member of about 3,200 lb/in^2 compared to the material strength of 25,000 lb/in^2. Since this loading is far below the damage point for the material, no further computations of internal loads were made.

The worst case acceleration history for the gimbal assembly and primary mirror, X-shake, X-direction, is shown in Figure 5-6. These values are added to the driving accelerations to give the total acceleration as shown in Figure 5-7.

5.2.5 Table of Peak Accelerations

The additive accelerations obtained for all other cases are much lower values than shown in Figure 5-6. Thus, only the peak values and their corresponding resonant frequencies are given in Table 5-6. It is seen that point 3, the primary mirror, reaches 194 g at 1100 Hz during the Z-shake. This represents the single largest acceleration for either the Y- or the Z-shake. All other acceleration peaks are below 40 g and are regarded as negligible.

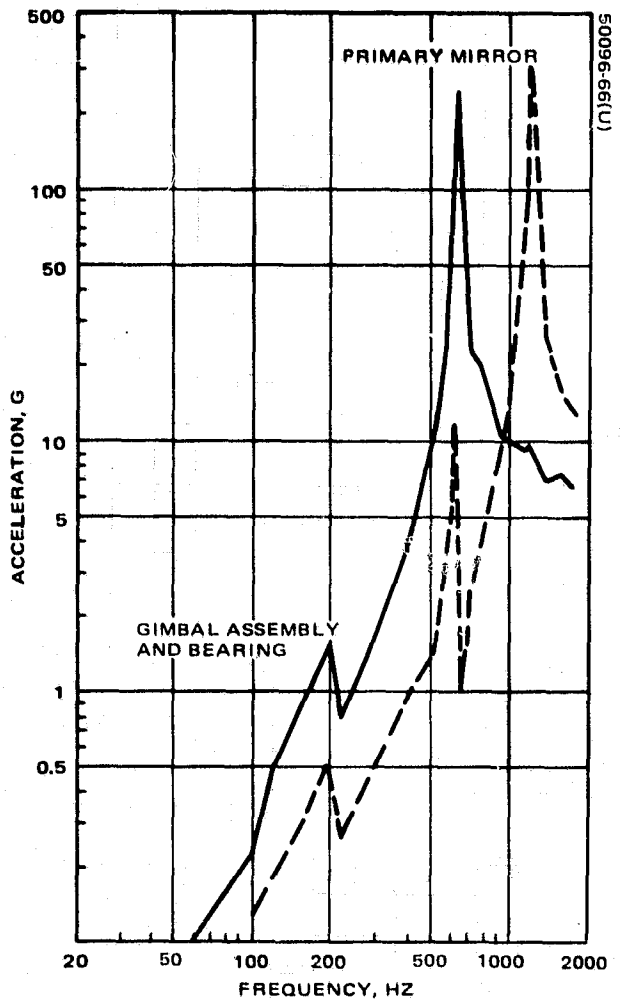

FIGURE 5-6. ADDITIVE ACCELERATIONS, WORST CASE X-SHAKE, X-DIRECTION

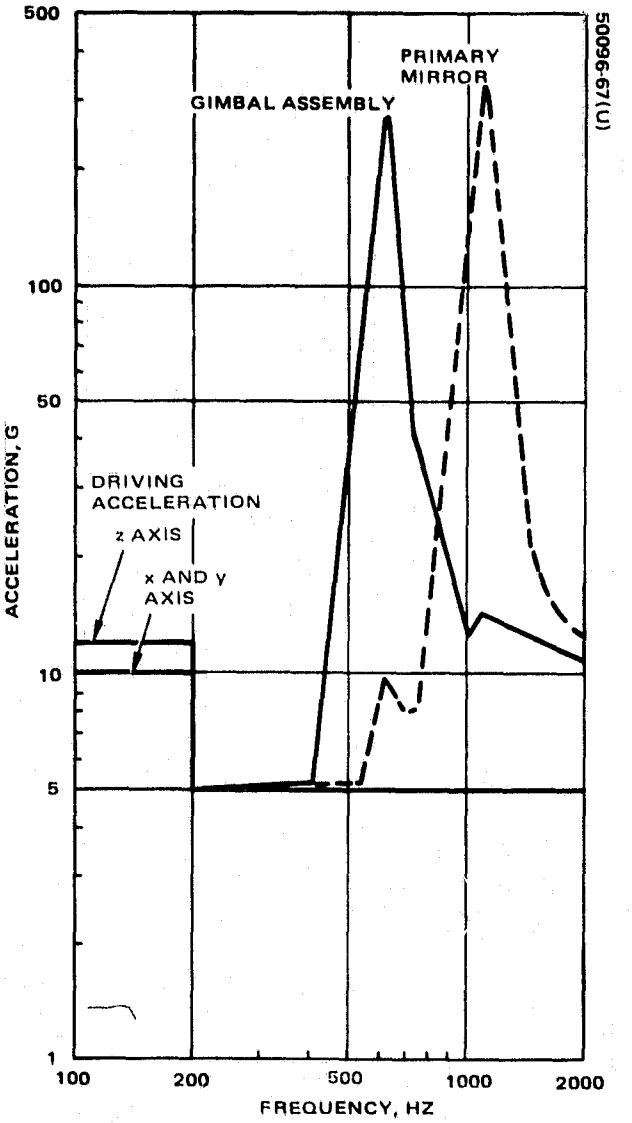

FIGURE 5-7. TOTAL ACCELERATIONS OF GIMBAL ASSEMBLY AND PRIMARY MIRROR

TABLE 5-6. PEAK ACCELERATIONS AND RESONANT FREQUENCIES

Linear Accelerations	X-Shake		Y-Shake		Z-Shake	
	Frequency, Hz	Acceleration, g	Frequency, Hz	Acceleration, g	Frequency, Hz	Acceleration, g
X direction						
Point 1	617	264	617	19	617	11.44
2	617	264	617	19	617	11.44
3	617	11.6	617	0.86	617	0.47
1	1141	9.7	1777	1.1	1536	17.9
2	1141	9.7	1777	1.1	1536	17.9
3	1173	308	1173	25	1141	40.5
Y direction						
Point 1	617	37	617	2.3	617	1.6
2	617	0.3	617	0.0	617	0.0
3	617	1.8	617	0.16	617	0.0
1	1172	7.8	1777	11.7	1172	2.0
2	1172	0.71	1777	0.23	1172	0.27
3	1172	2.5	1777	1.6	1109	1.8
Z direction						
Point 1	617	13.2	617	0.9	617	0.88
2	617	0.75	617	0.18	617	0.26
3	624	0.6	617	0	617	1.1
1	1109	5.5	1777	1.3, 5.6	1536	78
2	1109	4.4	1777		1109	30.6
3	1109	27.6	1777	6.3	1109	194
Rotational Accelerations						
θ_x direction						
Point 1		0		0		0
2		0		0		0
3		0		0		0
1		0		0		0
2		0		0		0
3		0		0		0
θ_y direction						
Point 1	617	4.1	617	0.3	617	0.21
2	617	4.1	617	0.3	617	0.21
3	617	0.35	617	0	617	0.18
1	1536	3.9	1777	0.65	1536	23
2	1536	3.9	1777	0.65	1536	23
3	1109	0.6	1777	0.79	1536	2.4
θ_z direction						
Point 1	617	11.0	617	0.8	617	0.49
2	617	11.0	617	0.8	617	0.49
3	617	0.56	617	0	617	C
1	1172	2.5	1777	3.39	1777	1.6
2	1172	2.5	1777	3.39	1777	1.6
3	1172	18.0	1172	1.5	1109	1.8

Point 1 = centroid of gimbal assembly; point 2 = gimbal bearing; point 3 = centroid of primary mirror assembly.

6. OPTICAL PERFORMANCE EVALUATION

6.1 MIXING EFFICIENCY OF OPTICAL HETERODYNE DETECTION

Coherent detection requires careful alignment between the signal beam and the local oscillator (LO) beam so that the wave fronts of these beams are phase matched at the detector surface. The optical design of the receiver takes into account the physical and geometric factors to assure that the phases are matched.

The IF carrier-to-noise ratio can be shown to be

$$\left(\frac{C}{N}\right)_{IF} = \eta \frac{P_s}{h\nu B} \frac{\left[L(\alpha)\right]^2 \left[\int \left|U_s\right| \left|U_{LO}\right| dA\right]}{\int \left|U_s\right|^2 dA \int \left|U_{LO}\right|^2 dA}$$

where

$\left|U_s\right|$ is the signal distribution function

$\left|U_{LO}\right|$ is the local oscillator distribution function, and

$L(\alpha)$ is the loss term due to tilt of the wave fronts

The geometric terms and the terms containing the integrals are equal to unity if the conditions of phase matching and beam tilt are met. Then the carrier-to-noise ratio in the IF becomes

$$\left(\frac{C}{N}\right)_{IF} = \eta \frac{P_s}{h\nu B_{IF}} \tag{16}$$

6.1.1 Case I, Signal and Local Oscillator Fields Matched

With the signal and LO fields matched, all of the energy falling on the detector is detected in the heterodyne mode, and the heterodyne efficiency increases with the size of the detector (see Figure 6-1),

$$\xi_I = 1 - J_0^2(x) - J_1^2(x)$$

$$x = \frac{\pi r}{F\lambda}$$

where J_0 and J_1 are Bessel functions of the first kind, and r is the radius of the detector, F is the f number of the collection optics, and λ is the wavelength of the light. This efficiency factor ξ_I is monotonically increasing function of the detector size and is equal to 0.84 for a detector whose size is the same as that of the Airy disk.

6.1.2 Case II, Signal Airy Function and Uniform Local Oscillator Field

This case is of particular interest because it simplifies the alignment of the signal and LO beams in an actual system (see Figure 6-1). The signal is a focussed Airy function and the LO is uniform over the surface of the detector

$$U_s(x) = \frac{2 J_1(x)}{(x)}$$

$$U_{LO}(x) = 1$$

where the variables are the same as for case I. The heterodyne efficiency can be evaluated and is found to be

$$\xi_{II} = 4 \left[\frac{1 - J_0(x)}{x}\right]^2$$

This function has a peak of 0.68 corresponding to a detector radius 72 percent of the radius of the Airy disk. If the detector is increased in size to match the Airy disk, the efficiency drops to 0.51, these computations including a central obscuration ratio of 0.15.

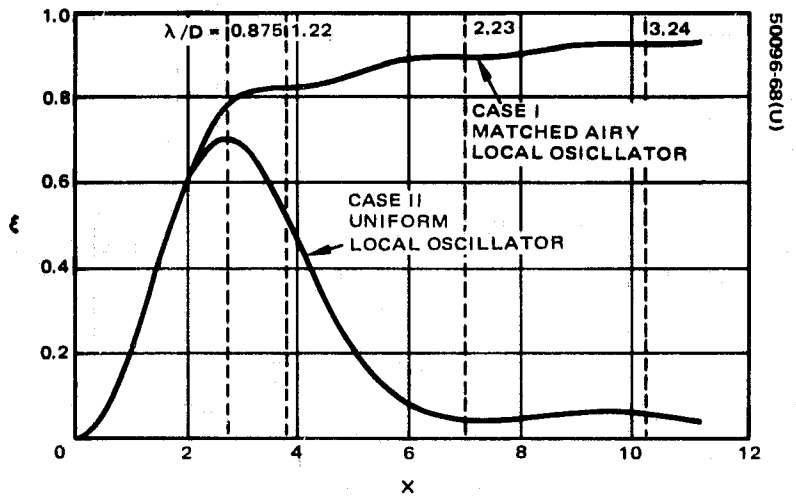

FIGURE 6-1. HETERODYNE EFFICIENCY ξ FOR AIRY FUNCTION SIGNAL DISTRIBUTIONS ON CIRCULAR DETECTOR

6.1.3 Coherent Antenna Pattern

The antenna pattern of the receiver subsystem has been analyzed using the computer program LACOMA. The configuration analyzed includes the primary, primary obscuration, secondary, and beacon beam splitter in the received signal path. The LO is assumed to be perfect with an f/40 gaussian illumination function. The IMCs are held stationary at their nominal or centered position.

The results are tabulated in Table 6-1 and plotted on Figure 6-2a. Figure 6-2b shows the relative field strength in the detector plane for the on-axis case for comparison. The horizontal axis has been converted to the input field angle and plotted on the same scale as Figure 6-2a to allow direct comparison.

The results show that the half-power field of view of the receiver is 82 μrad, or 1.28 λ/d. The first sidelobe is 19 dB below the on-axis response and is centered at about 135 μrad off-axis. There does not appear to be any significant structure beyond this first lobe.

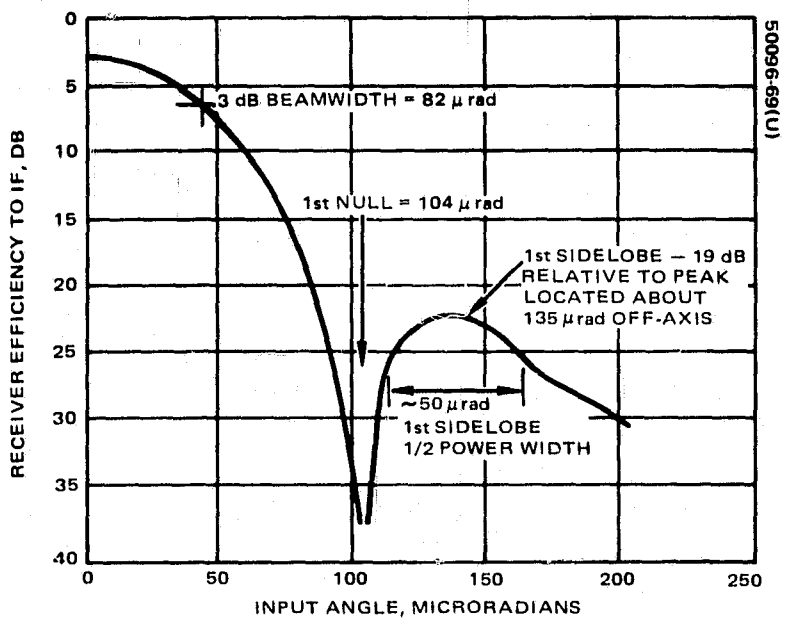

a) IF INTENSITY

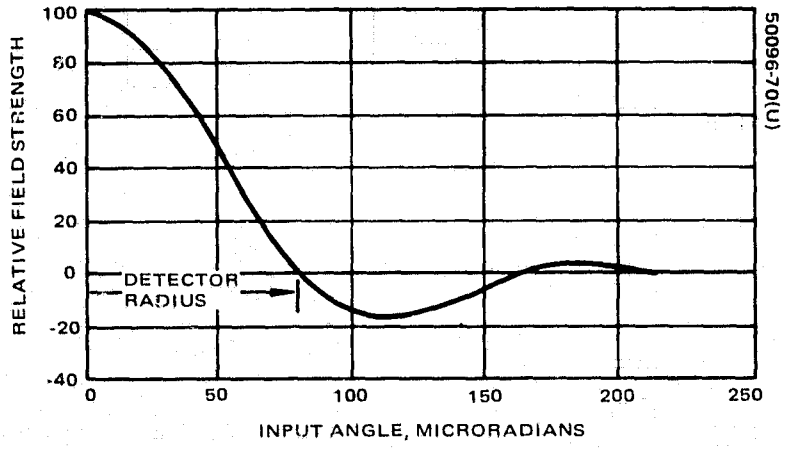

b) OPTICAL SIGNAL AMPLITUDE

FIGURE 6-2. RESULTS OF COHERENT ANTENNA PATTERN

TABLE 6-1. TABULAR RESULTS OF COHERENT ANTENNA PATTERN

Off-Axis Angle, μrad	Receiver Efficiency, dB	Relative Phase Shift, deg	Phase Match Efficiency, dB	Direct Detection Efficiency, dB
0	-3.0	0	0.0	-1.3
19	-3.5	1	-0.2	-1.3
38	-5.5	1	-0.9	-1.6
57	-9.2	2	-2.0	-2.6
76	-15.5	5	-3.9	-4.6
89	-23.2	12	-6.7	-6.7
97	-30.3	26	-9.6	-7.9
107	-37.1	115	-12.4	-9.3
114	-25.5	169	-5.5	-12.2
123	-23.6	173	-4.0	-13.6
136	-22.3	176	-2.4	-15.5
153	-23.4	179	-2.1	-16.7
164	-25.3	182	-2.5	-17.7
178	-27.6	184	-3.0	-19.2
188	-28.7	185	-3.3	-20.2
203	-30.5	188	-3.5	-22.6

6.2 DEGRADATION DUE TO OPTO-MECHANICAL DISTORTION

The optical performance of the receiver subsystem is affected by thermo-mechanical distortion of the structure because of a number of causes listed as follows:

- Primary/secondary mirror separation error
- Primary/secondary mirror tilts
- Primary/secondary mirror decentration
- Movement of detector in image plane (defocus)

The loss of signal due to these causes has been analyzed in Section 2, and the quantitative distortion data have been tabulated in Sections 4 and 5. This section combines these data to present the amount of signal loss as a function of time. Zero hour is defined when the sun is 180° from the optical aperture; the twelfth hour is defined when the sun is directly in line with the optical aperture.

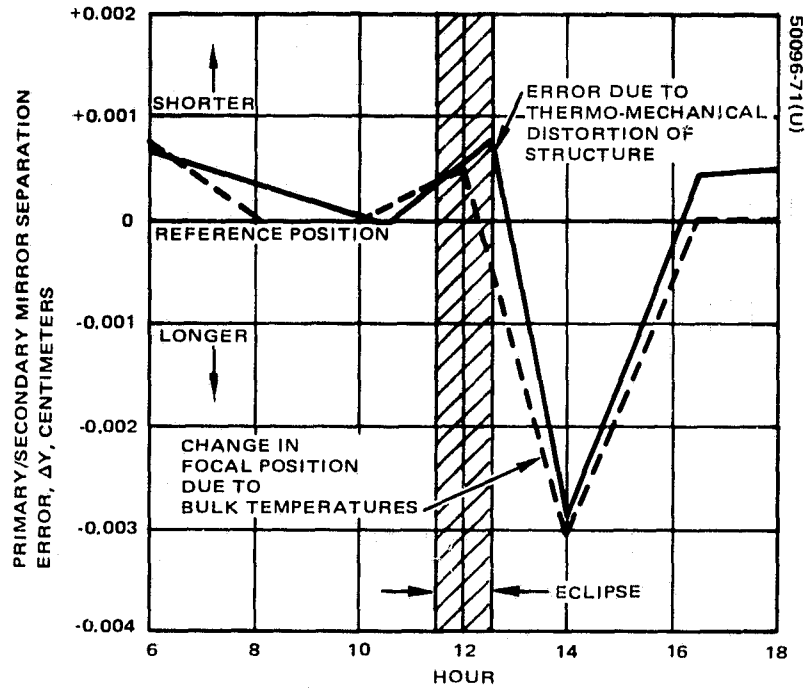

FIGURE 6-3. PRIMARY/SECONDARY MIRROR SEPARATION ERROR

Of the four distortions just listed, the primary/secondary mirror separation error is the most significant; the other causes have a negligible effect on the optical performance. Figure 6-3 illustrates the amount of primary/secondary mirror separation error as a function of time of day. Notice that the worst case occurs at about 14 where the mirror separation has changed about -0.003 cm from the focus position.

However, because the temperatures of the primary and secondary mirrors are increasing or decreasing with the box temperature, their respective focal lengths change proportionally. Also shown in Figure 6-3 is the simultaneous change in focal lengths of the mirrors. Notice that the isothermal technique provides almost complete compensation of the optical system reducing loss to negligible values. Table 6-2 lists the change in focal lengths, change in box length, net change, and the resulting loss incurred.

TABLE 6-2. NET DEFOCUSSING OF PRIMARY/SECONDARY MIRRORS DUE TO THERMO-MECHANICAL DISTORTION AND RESULTANT LOSS OF SIGNAL

Hour	Primary/Secondary Focal Length Change, cm	Box Length Change, cm	Net Change	Signal Loss, %
6	-0.000696	-0.000650	0.00005	0.2
8	0.0	-0.0003	0.0003	0.3
10	0.0	-0.0001	0.0001	0.2
12	-0.000516	-0.00055	0.00004	0.2
14	+0.003035	+0.00280	0.00024	0.3
16	0.0	-0.0003	0.0003	0.2

6.3 DEGRADATION DUE TO SURFACE FIGURE TOLERANCES

6.3.1 Specifications

Reasonably tight tolerances have been recommended for the surface figures of the optical elements in this design because the difference in cost between a marginally acceptable surface figure and an excellent surface figure is nominal. As a result, the worst surface figure tolerance specified is 3 fringes of 6328 Å light across the pointing and the primary mirrors. This surface figure corresponds to 0.09 λ or 0.56 radians at 10.6 μm. All of the other optical elements have specifications of 1 fringe of 6328 Å light or better, making the dominant phase errors caused by the pointing mirror.

The 0.56 radian of peak phase error corresponds to an rms phase error of less than 0.2 radian. The relative peak intensity due to a random phase error of this magnitude is 0.962, representing about 3.8 percent loss of signal energy.

6.3.2 Surface Figure Measurements

Surface figure data of all optical elements were recorded immediately after fabrication of the elements, after temperature cycling to liquid nitrogen temperatures, and again after optical coating where temperatures of more than 200°C were experienced. Data from the pointing mirror are shown in Figure 6-4, that from the primary mirror in Figure 6-5, and that from the secondary mirror in Figure 6-6. Each fringe represents one-half wavelength of 6000 Å light. All other optical elements show patterns better than 1 fringe at 6328 Å and are not shown.

The surface figures of the primary and secondary show overall surface quality of 2 fringes. The loss of peak energy is therefore about 1.8 percent for each surface, or a net loss of 0.13 dB.

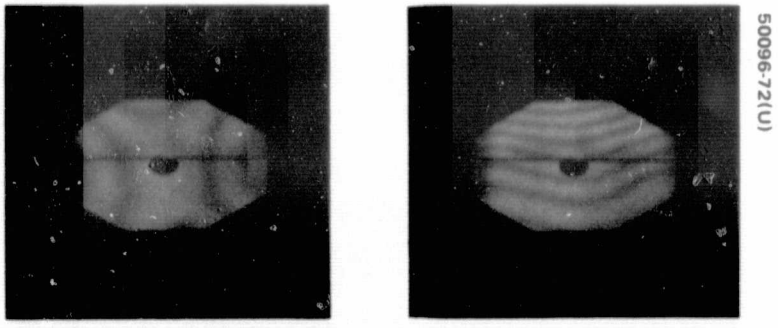

OVERALL DEVIATION - 2 FRINGES, λ = 6000 Å

FIGURE 6-4. POINTING MIRROR AFTER LN_2 TEMPERATURE AND COATING CYCLES

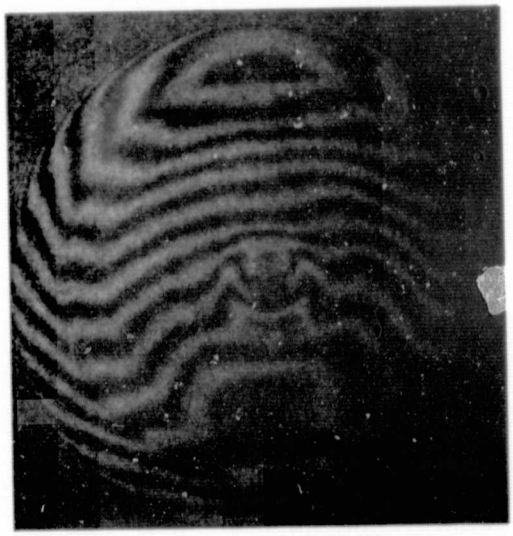

50096-73(U)

BEFORE LN_2 TEMPERATURE CYCLE

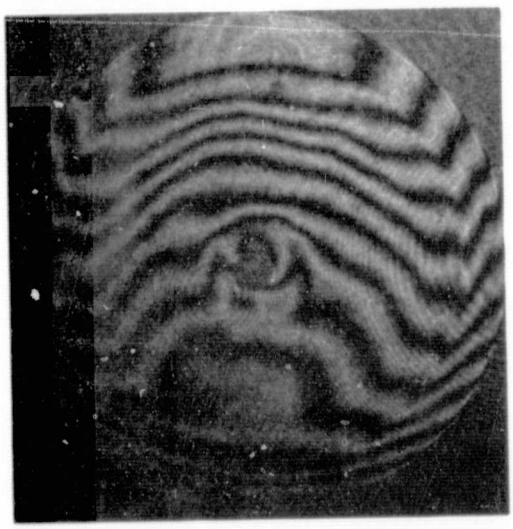

AFTER LN_2 TEMPERATURE CYCLE

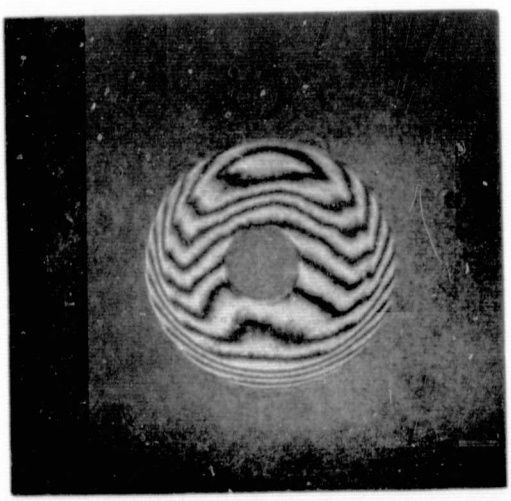

AFTER COATING CYCLE

OVERALL DEVIATION - 2 FRINGES, λ = 6328 Å

FIGURE 6-5. PRIMARY PARABOLOIDAL MIRROR

50096-74(U)

BEFORE LN_2 TEMPERATURE CYCLE

AFTER LN_2 TEMPERATURE CYCLE

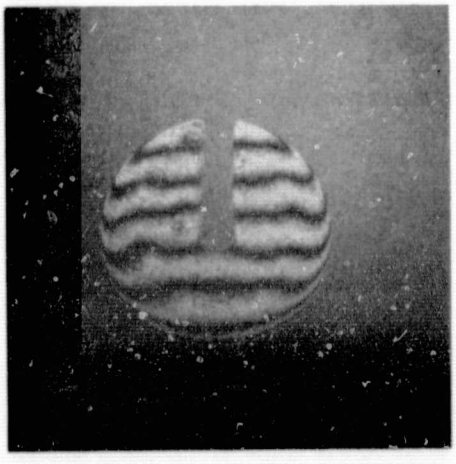

AFTER COATING CYCLE

OVERALL DEVIATION – 1/2 FRINGE, λ = 6328 Å

FIGURE 6-6. SECONDARY ELLIPSOID MIRROR

6.4 DEGRADATION DUE TO ABSORPTIVE LOSSES OF MIRROR SURFACES

The high reflectivity coating specified for these surfaces can be specified to have 1 percent absorptive loss at 10.6 μm. Since there are 7 reflective surfaces in the optical train, this accounts for a net loss of 6.3 percent since these losses are added logarithmically. The total absorptive loss amounts to 0.28 dB.

6.5 OFF-AXIS LOSSES

As shown in 2.2, the off-axis performance of the folded Gregorian optical system is equal to that of on-axis. The analysis, however, determined only the amount of energy in the Airy disk at the detector. Another loss which must be considered is that due to the tilt of the signal beam on the detector (see Figure 6-7). For a circular aperture, this is given by

$$P_{mixed} = P_o \left[\frac{2 J_1 (2\pi F\alpha)}{(2\pi F\alpha)}\right]^2$$

which can be expanded and that, to a first approximation, is equal to

$$\text{Loss} = \frac{(2\pi F\alpha)^2}{4}$$

The beam tilt α at the maximum field of view angle is 1.76×10^{-3} radians. This value corresponds to 0.264 percent loss or about 0.011 dB.

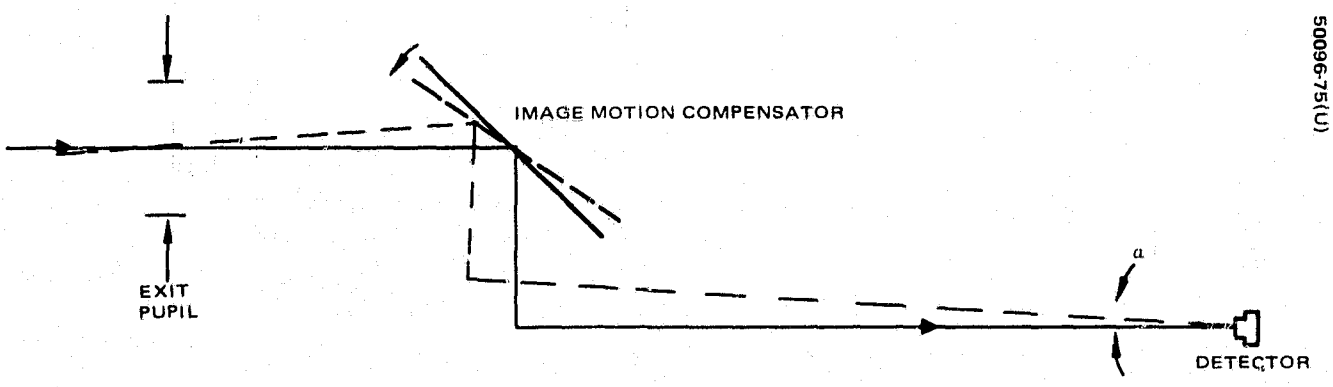

FIGURE 6-7. SIGNAL LOSS DUE TO BEAM TILT AT MIRROR

6.6 TRACKING AND SCANNING LOSSES

It has been determined that for adequate tracking of the receiver subsystem, a conical scan of sufficient amplitude must be used to generate an adequate tracking signal. The amount of loss taken in the signal channel as a result depends upon a number of factors and may vary between 0.5 to 3 dB. Since many of these factors are not known at present, these losses will not be included in those listed next.

6.7 NET ANTENNA GAIN

The net antenna gain for the OM receiver subsystem is computed as follows:

Antenna gain (16.5 cm clear aperture unobscured)	93.78 dB
Antenna losses:	
Absorption loss (1 percent per surface)	-0.28 dB
Surface figure loss (2 fringes at 6328 Å at 2 surfaces)	-0.16 dB
Distortion loss (thermal-mechanical)	
Without focal compensation	-0.06 dB
With focal compensation	-0.00 dB
Mixing efficiency (power in Airy disk divided by power in aperture, assuming 0.15 central obscuration)	-1.67 dB
Off-axis loss (beam tilt)	-0.01 dB
Total antenna losses	-2.18 dB
Net antenna gain	91.60 dB

The above value represents the worst case (uncompensated focal lengths) for thermo-mechanical distortion. Figure 6-8 shows the net antenna gain as a

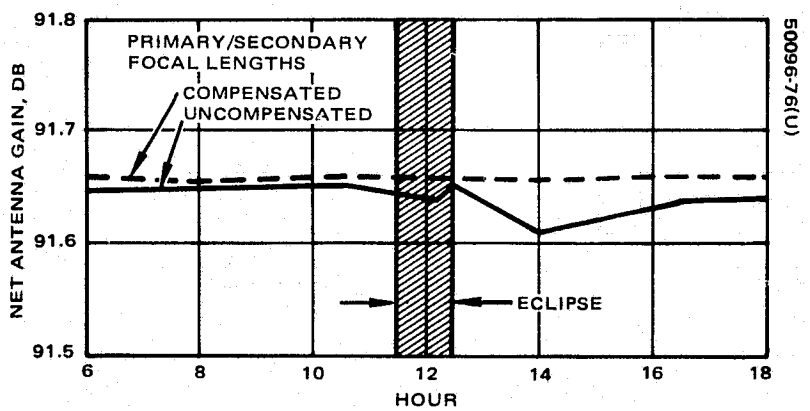

FIGURE 6-8. NET ANTENNA GAIN IN EQUINOX ORBIT, CENTER OF FIELD OF VIEW

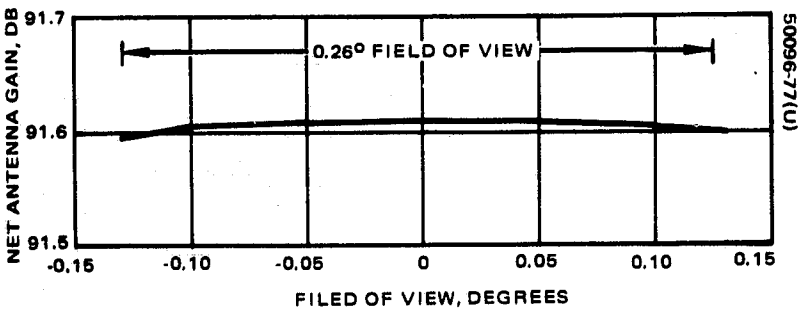

FIGURE 6-9. NET ANTENNA GAIN OVER RECEIVER OPTICAL SYSTEM FIELD OF VIEW (BEAM TILT AT MIXER 1.76×10^{-3} AT MAXIMUM ANGLE)

function of the hour of the orbit, the worst condition occurring at 14 hours. The solid line gives the value of gain for uncompensated focal lengths; the dashed line gives the value for compensated focal lengths.

Figure 6-9 gives the net antenna gain as a function of the field of view of the optical system. At the maximum angle of 0.13° either side of the central optical axis, the IMCs are at their maximum excursion generating a beam tilt at the detector. The tilt gives rise to the very small degradation in signal shown in the figure.

7. TESTS AGAINST CONTRACT SPECIFICATION

This section reports the testing of the opto-mechanical subsystem against the contract specification GSFC 524-P-1 to show that the performance specifications have been met. The tests fall into three categories: mechanical, electro optical, and computed. Table 7-1 lists the tests performed and the reference paragraph of the specification document.

7.1 MECHANICAL MEASUREMENTS

Mechanical measurements have been made to verify that the configuration meets the dimensional limits in the specification. Table 7-2 lists the mechanical measurement to be made as compared to the specification.

7.2 COMPUTED DATA

Several specifications are more conveniently verified by computing data indirectly than by measuring directly. These are antenna gain, beam tilt at the mixer, and box distortion in a 1 g environment (see Table 7-3).

7.2.1 Antenna Gain

Antenna gain, or directivity, is defined from the IEEE Standard Definition of Terms for Antennas as being equal to $4 \pi A/\lambda^2$. The clear aperture of the primary mirror is 16.5 cm, giving a gross antenna gain of 93.78 dB. The central obscuration of 0.15, however, reduces the net gain to 93.66 dB. Note that the effects of mixing efficiency have not been included in these computations. The specified minimum gain is 93.0 dB.

7.2.2 Beam Tilt at Mixer

Beam tilt at the mixer causes degradation of mixing efficiency. The amount of tilt is determined by the location of the IMCs with respect to the iris in the optical train. In the present design, the IMCs are located sufficiently close to allow only a 1.76 mr tilt at the maximum field angle (see 6.5). This value compares with the specified maximum value of 2.5 mr.

TABLE 7-1. OPTO-MECHANICAL SUBSYSTEM TEST LIST

Test Group	Test Category	Test or Measurement to Be Made	Specification	Specification Reference Paragraph
Structural frame and baseplate	Mechanical	Mounting tapped holes	1/4-20, 3 places	3.3.1
		Baseplate tapped holes	10-32 on 1 in. centers	3.3.1
		Baseplate area	120 in^2 minimum	3.3.1
		Structure volume	2500 in^3 maximum	3.3.1
		Diagonal dimension	27 in. maximum	3.3.1
Antenna	Mechanical	Diameter	16 cm minimum	3.3.2
	Computed*	Gain	93 db with obscuration	3.3.2
	Electro optical	Gain versus FOV	-1 dB maximum $\pm 0.13^o$	3.3.2, 3.4.2
	Electro optical	Coarse pointing FOV	$\pm 10^o$ minimum	3.3.2
	Electro optical	Coarse point, accuracy	$\pm 0.02^o$ repeatability	3.3.2
	Electro optical	Coarse point, hysteresis	$\pm 0.02^o$	
IMC	Electro optical	Fine point accuracy		
		Fine point hysteresis	$\pm 0.0083^o$ over 1^o range	3.3.3
	Computed**	Beam tilt at mixer	±2.5 mr maximum	3.3.3
Miscellaneous	Electro optical	Fiducial mirror boresight	$\pm 0.066^o$ maximum error referenced to beam axis	3.3.7
	Mechanical	Package weight	25 lb maximum	3.3.7
200 μm iris test	Electro optical	Loss through system	Less than 3 dB on-axis	3.4.2
			Less than 3 dB $\pm 0.1^o$ off-axis	3.4.2
	Computed***	Change in 1 g static environment	Less than 1 dB any axis	3.4.2

*Computed from $4\pi A/\lambda^2$ less central obscuration loss, reference 2.2.3.
**Computed to be 1.76 mr maximum, reference 2.2.1.
***Computed to be negligible, reference 5.2.1.

TABLE 7-2. MECHANICAL MEASUREMENTS

Measurement to Be Made	Specification	Measured Data
Mounting holes	1/4-20, 3 places	1/4-20, 3 places
Baseplate tapped holes	10-32 on 1 in. centers	10-32 on 1 in. centers
Baseplate area	120 in^2 minimum	188.71 in^2
Structure volume	2500 in^3 maximum	2349 in^3
Diagonal dimension	27 in. maximum	25.70 in.
Antenna diameter	16 cm minimum	18.5 cm OD
		16.5 cm clear aperture
Package weight	25 lb maximum	24.78 lb

TABLE 7-3. COMPUTED DATA

Computation to Be Made	Specification	Computed Data
Antenna gain	93 dB minimum	93.66 dB with obscuration
Beam tilt at mixer	2.5 mr maximum	1.76 mr
Loss in 1 g static environment	1 dB maximum	Negligible

7.2.3 Loss of Antenna Gain in a 1 g Static Environment

Cantilevered opto-mechanical designs distort easily when moved or rotated in a gravity field. The purpose of this specification is to limit the amount of loss encountered with such a design. The beryllium shell structure used in the present opto-mechanical design has superior rigidity and results in a negligible distortion and loss. These computations are reported in 5.2.1.

7.3 ELECTRO OPTICAL TESTS

The electro optical tests verify that the optical performance is in accordance with the design and that the gimbal control accuracy is sufficient to accommodate the intended servo system (see Table 7-4).

7.3.1 Electro Optical Test Configuration

The test equipment necessary to perform the electro optical tests includes a visible laser source, a 10 μm laser source, a collimator, a precision rotary table, and a power monitor. The test configuration is illustrated in Figure 7-1.

7.3.2 Fiducial Mirror Boresight

The purpose of the fiducial mirror is to provide an optical reference axis for the receiver subsystem. This test consists of initial boresight alignment of the fiducial mirror with the opto-mechanical subsystem in the centered or gimbal-lock position, scanning the gimbal through ±10° in each axis, and returning the gimbal to the center position. A comparison is then made between the fiducial mirror and the opto-mechanical subsystem axis. Tests show that the boresighting axis is maintained to less than 0.01°.

7.3.3 Gain Versus Field of View

This test uses a 10.6 μm laser signal monitored with a power meter at the 200 μm detector iris. The precision mount is rotated by 0.10°, and the correction is made with the IMCs to bring the signal back through the 200 μm iris. The power is again monitored and compared with the previous reading. Test data are given in Figure 7-2 and Table 7-4. These measurements are limited to ±0.10° by the built-in mechanical limit of the IMCs.

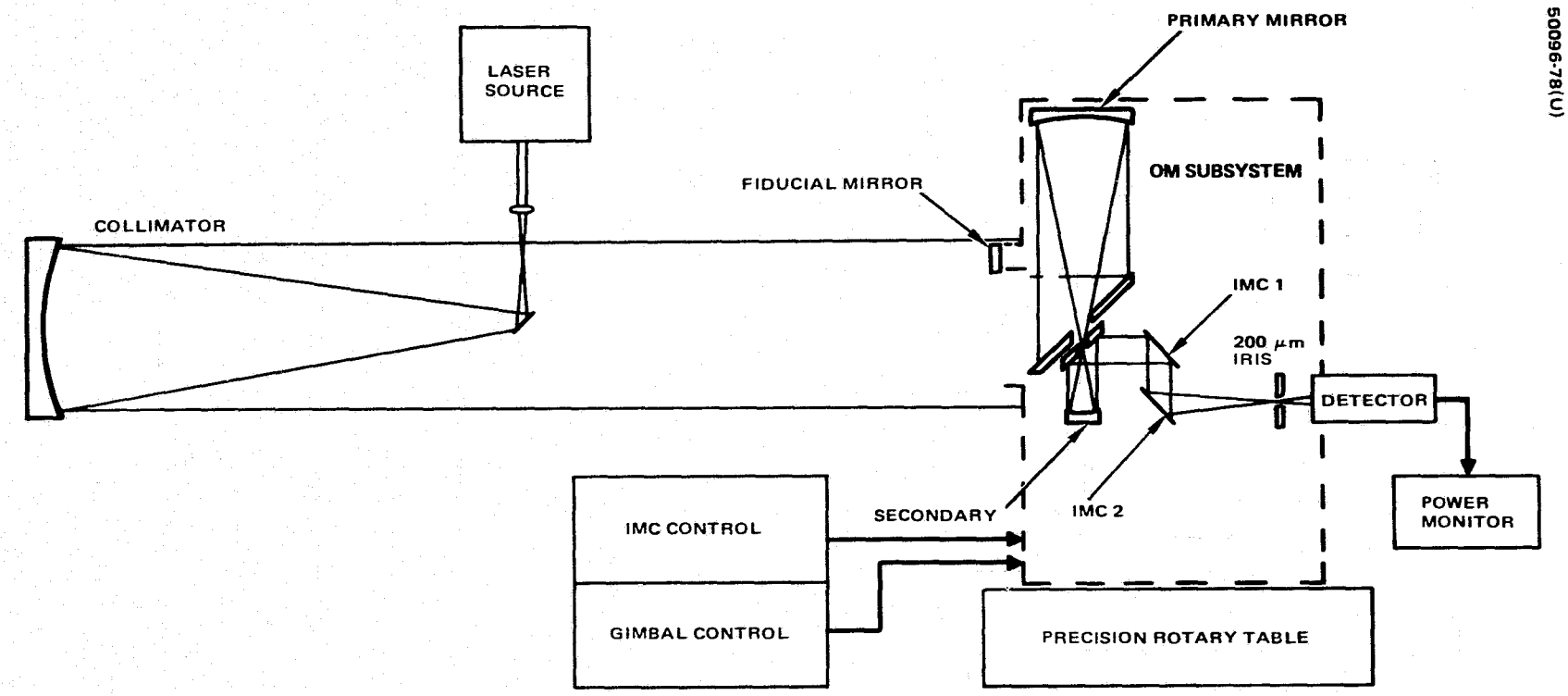

50096-78(U)

FIGURE 7-1. ELECTRO OPTICAL TEST CONFIGURATION

TABLE 7-4. ELECTRO OPTICAL TEST RESULTS

Measurement Made	Specification	Measured Data
Fiducial mirror boresight	$\pm 0.066^{o}$	$<0.01^{o}$
Gain versus FOV	-1 dB maximum at $\pm 0.13^{o}$	-0.12 dB
Coarse point FOV	$\pm 10^{o}$ minimum	$\pm 10^{o}$
Coarse point accuracy	$\pm 0.02^{o}$	$\pm 0.002^{o}$
Coarse point hysteresis	$\pm 0.02^{o}$	$\pm 0.002^{o}$
Fine point accuracy	$\pm 0.0083^{o}$ over 1^{o}	$\pm 0.005^{o}$ over 0.5^{o}*
Fine point hysteresis	$\pm 0.0083^{o}$ over 1^{o}	$\pm 0.005^{o}$ over 0.5^{o}*
Loss through system	3 dB maximum	$0.5\ dB \leq \alpha \leq 1.1\ dB$

*Optical system magnification of 10.0 permits full far field coverage of 0.10^{o} with an IMC movement of 0.5^{o}.

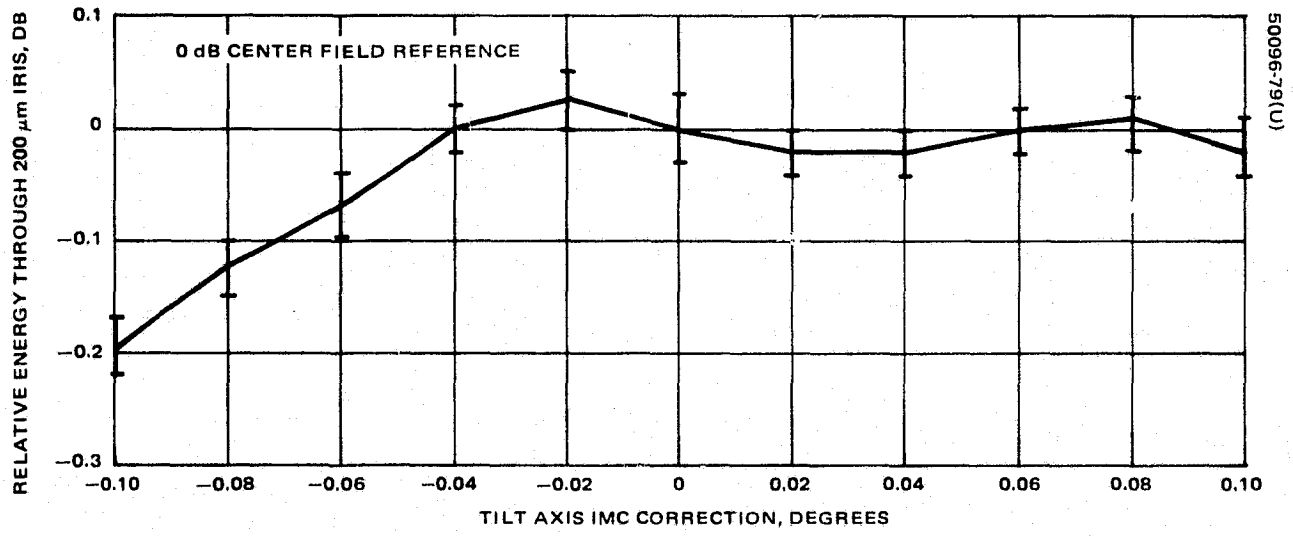

FIGURE 7-2. GAIN VERSUS FIELD OF VIEW

7.3.4 Coarse Pointing Field of View and Precision

For this test, the stepper motors are used to drive the gimbal through ±10° in each axis and checked for repeatability with the collimated source.

7.3.5 Fine Pointing Field of View and Precision

The IMCs are driven over a field of ±0.50°, which corresponds to a field of ±0.10° in the far field, and are checked for repeatability and accuracy.

7.3.6 Loss Through System

The 10.6 μm loss through the optical system is measured by two independent methods: first by measuring the flux density of the collimated beam and computing the power entering the aperture and comparing this power with that measured at the 200 μm iris, and second by sending a 1 cm diameter collimated laser beam through the system and measuring the total power at the detector plane. The second method measures the optical surface loss of all the optical surfaces while the first method also takes into account the diffraction loss. The loss per surface is measured to be less than 2 percent, and the loss through the entire system is measured to be more than 0.5 dB and less than 1.1 dB. The uncertainty in the system loss arises from the difficulty in making these measurements.

8. WAVEGUIDE CO_2 LASER LOCAL OSCILLATOR

8.1 INTRODUCTION AND SUMMARY

The purpose of this task is to develop a 10.6 μm tunable waveguide CO_2 laser for use as the heterodyne local oscillator in the doppler tracking 10μm receiver. In addition to a number of mechanical and thermal requirements, the laser must be tunable ±200 MHz from line center, be compatible with the dimensional requirements of the receiver, operate with a plasma voltage of less than 3000 volts, oscillate on a single line with greater than 100 mW on line center, and consume less than 20 watts of power.

Although a ±200 MHz tuning range was specified for the local oscillator, a design goal of ±860 MHz was included. Unfortunately, the techniques required to build lasers with tuning ranges of ±500 MHz and above include the use of square cross-sectioned waveguides. This is the only way to reduce the waveguide cross section, increase the pressure and tunability, and still maintain dimensional tolerances and surface finish. Use of square cross sections implies epoxy seals, which is inconsistent with the long life requirement on the laser (> 2000 hours). For this reason, an all metal-ceramic circular bore laser was designed with the ±200 MHz goal in mind, while an effort was made to develop alternate ceramic sealing techniques for eventual application to square cross-sectioned waveguide lasers with greater tunability. The most promising technique involved chrome-copper metalization of the ceramic with soft solder bonding. Although unsuccessful for ceramic bonds of the type needed here, the technique was partially successful for electrode seals, as discussed in Section 2.

The original program plan did not include provision for frequency control or frequency stabilization of the waveguide laser over its tuning range. One reason for this is that no satisfactory technique really existed at the time this effort was started. Recent work at the Hughes Research Laboratories (Reference 1) has resulted in a new frequency stabilization scheme, where the laser is locked to a Stark tunable resonance absorption line in NH_2D, providing a simple and accurate means of waveguide laser frequency control over the complete tuning range. Reference 1 contains a detailed description of the Stark cell stabilization and is reproduced in Appendix E for convenience. Because of the obvious utility of such a device to this program, a metal-ceramic Stark cell has been designed, fabricated, and integrated with the local oscillator package.

A photograph of the complete unit, ready for installation into the opto-mechanical receiver subsystem, is shown in Figure 8-1. Clearly visible are the laser, Stark cell, detector, gas ballast volume, and beam splitter for the laser output which provides energy for the Stark cell. Cooling is accomplished by conduction to the thermal baseplate, to which the entire assembly is bolted. Figure 8-2 shows an outline drawing of the completed unit. The dashed line shows the maximum allowable dimensions according to the specifications. Clearly, the size of the local oscillator, with the Stark cell stabilizer, is well within the allowable range.

The laser exceeds the operational specifications required for the heterodyne receiver. Power output at line center is 600 mW with less than 20 watts of power dissipated in the tube. The tuning range is ±200 MHz at the 1 dB tuning points, with ±300 MHz at the 3 dB points. The entire unit is constructed using all metal-ceramic techniques with the exception of the output window, which has an epoxy seal.

In Section 2 of this report, the laser design, construction, and performance are discussed, while the Stark cell is similarly described in Section 3. Integration of the local oscillator package with the receiver subsystem will be accomplished in the near future under another program.

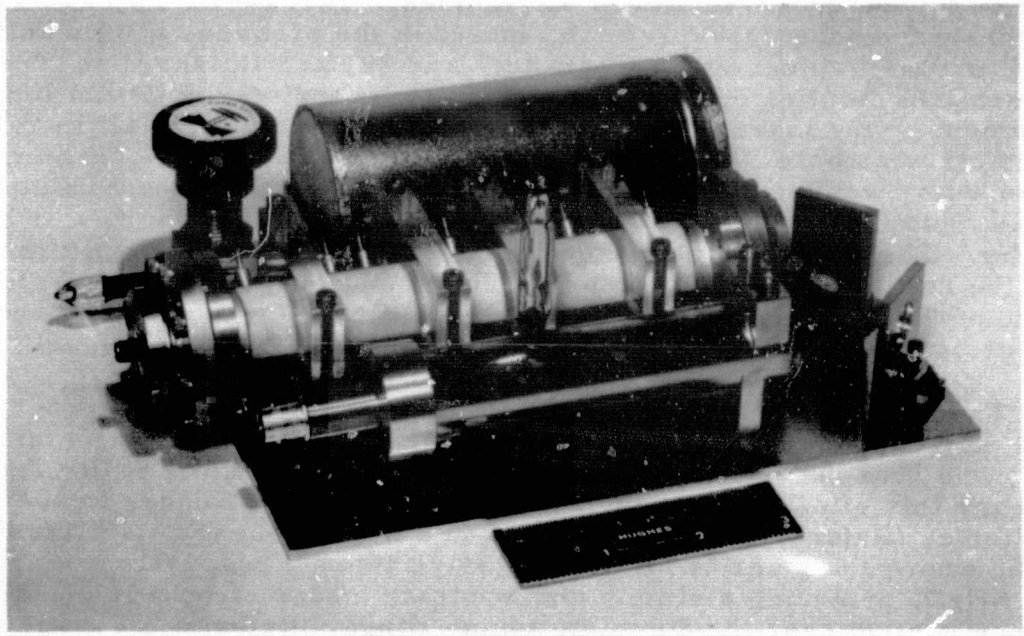

FIGURE 8-1. LOCAL OSCILLATOR UNIT (PHOTO 50096-80)

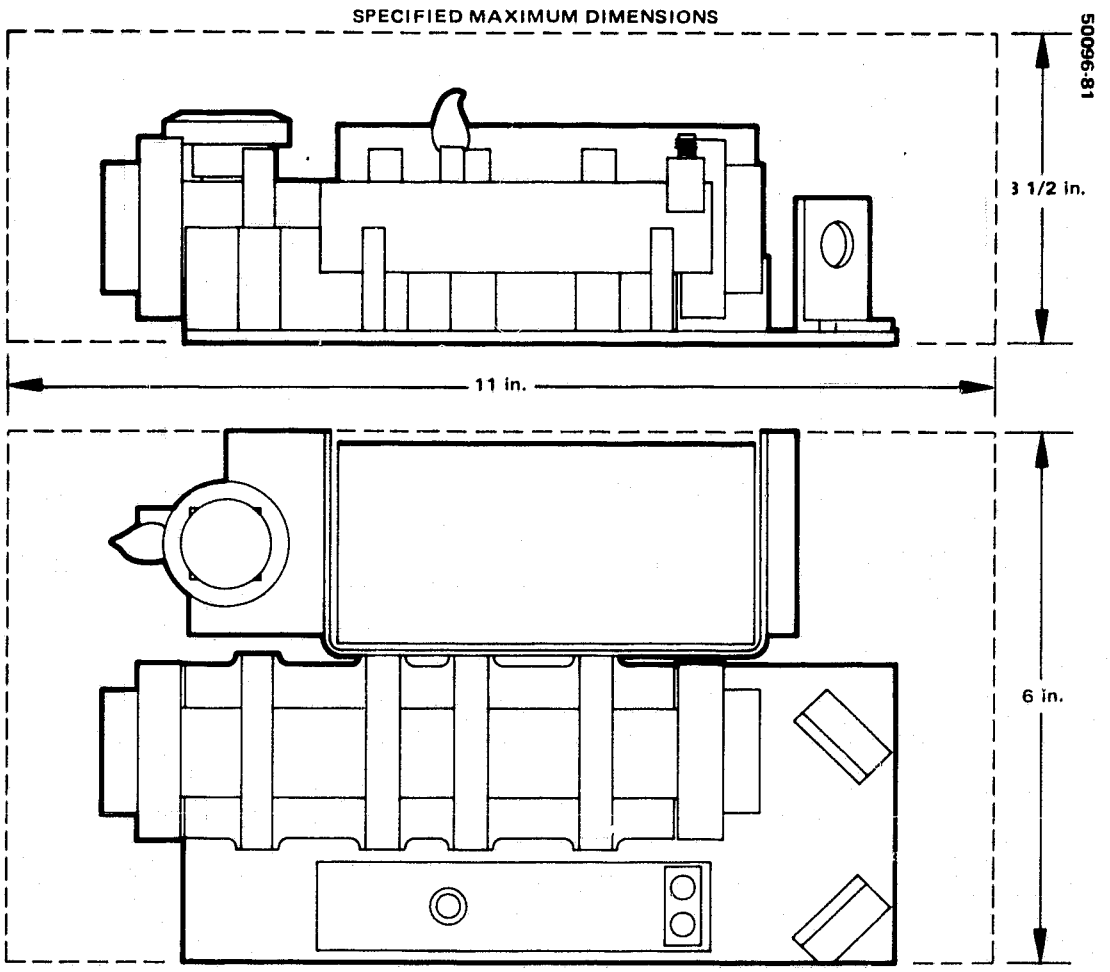

FIGURE 8-2. LOCAL OSCILLATOR UNIT

8.2 LASER TUBE

8.2.1 Design Parameters

This section describes the design parameters chosen for the laser discharge tube. The primary constraints were discharge power and voltage limitations, which placed definite limits on the allowable length of individual discharge segments and the total length of the laser. Less constraining were dimensional limitations of the package.

The discharge tube design relies on measured parameters (Reference 2) for waveguide CO_2 lasers, including discharge voltage, current, and optimum operating pressure. For a tuning range in excess of ±200 MHz, the laser gas pressure must be in the neighborhood of 100 to 150 Torr. A discharge diameter of 1.5 mm was chosen, since optimum operation of statically filled tubes at 150 Torr is possible and high quality Be0 ceramic tubes can

be obtained with this inner diameter. BeO is the chosen material not only because of its desirable thermal and mechanical properties but, more importantly, for its excellent characteristics as a 10.6 μm hollow waveguide (Reference 2).

Typical CO_2 laser mixtures, at 150 Torr pressure, require an electric field of ~0.95 kV/cm, and operate efficiently at a current of 2.0 mA. The power dissipation will be ~1.9 W/cm, so a maximum discharge length of 10 cm was chosen. To keep the voltage below 3.0 kV, four discharge sections, each 2.5 cm long, are required, with a discharge voltage of ~2.4 kV. The design parameters are summarized as follows:

Total discharge length	10.0 cm
Individual discharge section length (four each)	2.5 cm
Tube voltage	2.4 kV
Tube current (total)	8.0 mA
Power required	19 watts

It will be possible to operate the laser at slightly lower levels of current and power, if this proves desirable.

In order to operate four separate discharges in a single tube, the electrode geometry illustrated in Figure 8-3 was chosen. The advantage of this geometry is that the electrodes at the ends of the tube are at ground

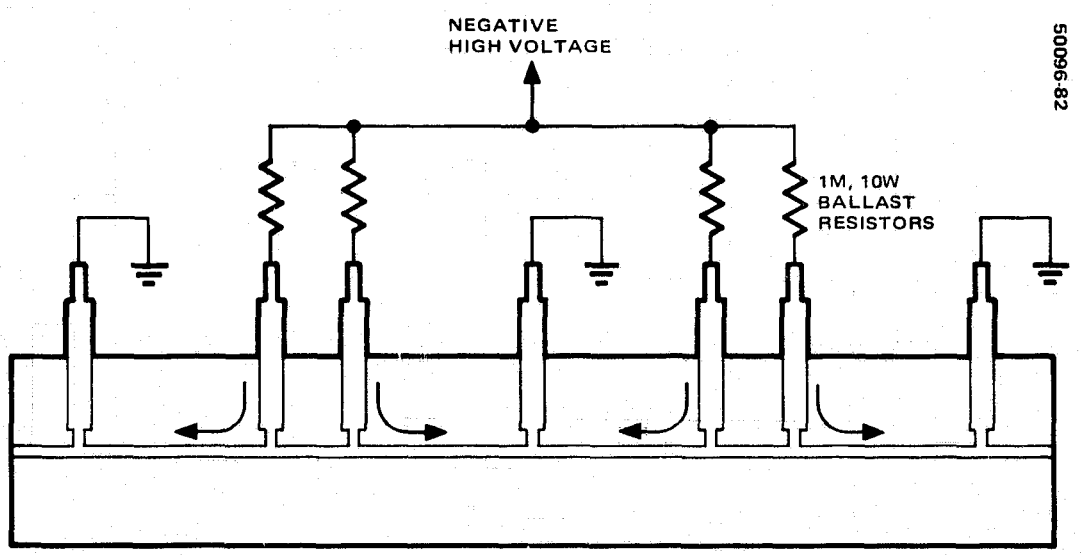

FIGURE 8-3. ELECTRODE ARRANGEMENT FOR EXCITING FOUR SEPARATE DISCHARGE PATHS

potential and also act as anodes, reducing the amount of sputtering which might accumulate on the optics. The disadvantage is that some difficulty is encountered in starting the tube. Discharge current from two adjacent cathodes must split into separate discharge paths. Once they are both lit, a stable situation is established, but if one of the discharges lights first, the second is likely to follow the same path. For this reason, a pulsed starting circuit was designed to start all discharges simultaneously. This circuit is described in the following sections.

8.2.2 Laser Fabrication

Laser Bore

The bore material used in the laser bore unit is beryllium oxide. It was chosen because of its excellent properties as a waveguide material as well as for its thermal and mechanical properties. The Be0 bore has an inside diameter of 1.5 mm, a length of 14 cm, a total discharge length of 10 cm, and an outside diameter of 2.54 cm.

Standard metal-ceramic techniques were used in the assembly of the laser bore unit. The Be0 was metallized around each electrode hole and around the diameter on each end. Nickel electrodes and their kovar eyelets were brazed in place along with kovar sleeves on each end. The mirror mount flanges were welded to the kovar sleeves on each end. The bore, electrodes, and end flanges are shown in Figure 8-4.

Although standard metal-ceramic techniques were used in the bore assembly, some time was spent investigating another type of metal-ceramic seal for Be0 laser assembly. The reason for the investigation was to achieve more flexibility in fabrication techniques, with possible application to waveguide lasers of square cross section as well as electrode seals. The technique was to metalize the ceramic with chrome-copper, in the metalized

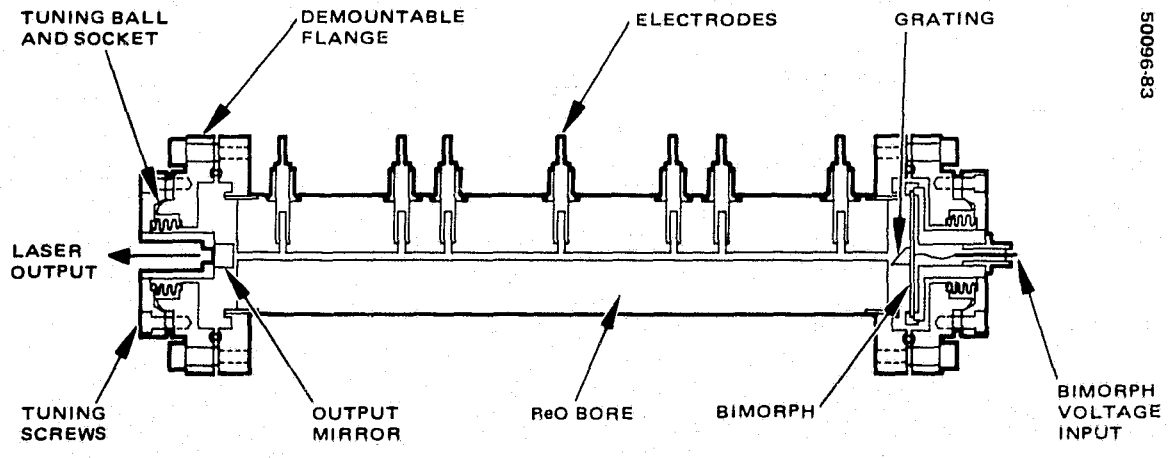

FIGURE 8-4. WAVEGUIDE LASER DETAIL

areas as well as the electrodes with 96 percent Sn, 4 percent Ag eutectic solder, and, finally, sweat the parts together. Although successful vacuum tight joints were obtained, these results were repeatable only about 50 percent of the time. Since the results of the soldering technique were less than expected, an order was placed with the BeO vendor to attach the electrodes by the standard metal-ceramic method.

Mirror Mounts

The mirror mounts (see Figure 8-4) are of the demountable type which allows for cleaning or changing of the optics should that become necessary. The seal between the mounts and tube flanges is accomplished with a copper O-ring. Adjustment of the ball-socket tuning mechanism is accomplished by loosening and tightening opposing adjustment screws. After the desired adjustment is completed, these same screws serve to lock the tuning mechanism in place. The flexible vacuum seal is a stainless steel bellows which is brazed between the ball and socket parts of the tuning mechanism.

The mirror mount on the high reflectivity end of the laser houses an internal bender bimorph. The bimorph is a 1 inch circular disk, 0.020 inch thick, and is composed of two oppositely poled piezoelectric disks, bonded together. Application of a voltage across the bimorph causes the disk to buckle slightly, resulting in a linear motion at the center of the disk, normal to its plane. The bimorph is held solidly at its periphery by two knife-edged metal rings which also serve as the electrical contacts. The bimorph voltage is fed through the vacuum wall by a hermetically sealed OSM connector. Both the grating, which is on the bimorph, and the output mirror are attached to their respective mounts with epoxy. The mirror mounts, bimorph, and optics can be seen in Figure 8-4.

Optics

The optics for the laser consist of an internal partially transmitting output mirror and a high reflectivity grating. The output mirror is zinc-selenide coated for 97 percent reflection and has 1.8 percent transmission. The grating is a replica diffraction grating made on a copper substrate, with 150 grooves/mm and a blaze angle of 36°52'. The Littrow reflectivity for this grating at 10.6 μm is 97 percent for the polarization normal to the grating grooves and 20.5 percent for the polarization parallel to the grooves. Thus, when used as a reflector, the grating acts as a polarization selector as well as a line selector. The energy reflected specularly for the 97 percent Littrow orientation is 0.6 percent, so more than 2 percent of the energy is dissipated or scattered.

The grating, mounted on the bimorph, has a right triangular cross section of 6.35 mm by 5.08 mm by 3.81 mm high and a width of 6.35 mm. The grating was cut to the above dimensions from a larger grating. This was accomplished by first covering the entire grating face with a commercial strippable coating to protect the face during the machining process. The grating was then waxed into place on a precision machined fixture and divided into smaller gratings by carefully cutting the substrate with a slowly rotating cutting wheel. The strippable coating was then removed.

Package

The laser package consists of the laser, its heat sink, and the reservoir assembly. The aluminum heat sink serves as a means of transferring heat from the laser to the system cold plate as well as the mechanical mount to hold the laser tube. The reservoir or gas ballast increases the total laser volume to approximately 250 cc for extended tube life. The reservoir has a valve attached to it to facilitate refilling the tube when its useful lifetime has been reached because of gas cleanup. Although the valve is closed, the valve connection is sealed with a glass tipoff. A photo of the laser package without the Stark cell assembly is shown in Figure 8-5.

Starting Circuit

The purpose of the starting circuitry is to provide a high voltage starting pulse which will initiate the discharge simultaneously in all four tube sections. The major components of the start unit are the power supply, EG&G KN-4 Krytron, pulse forming capacitor, and pulse transformer. The power supply furnishes voltage to charge the pulse forming capacitor and to operate the Krytron tube. The Krytron serves as a switch to allow the pulse forming capacitor to discharge through the primary of the pulse transformer. As the capacitor discharges through the transformer primary, the secondary

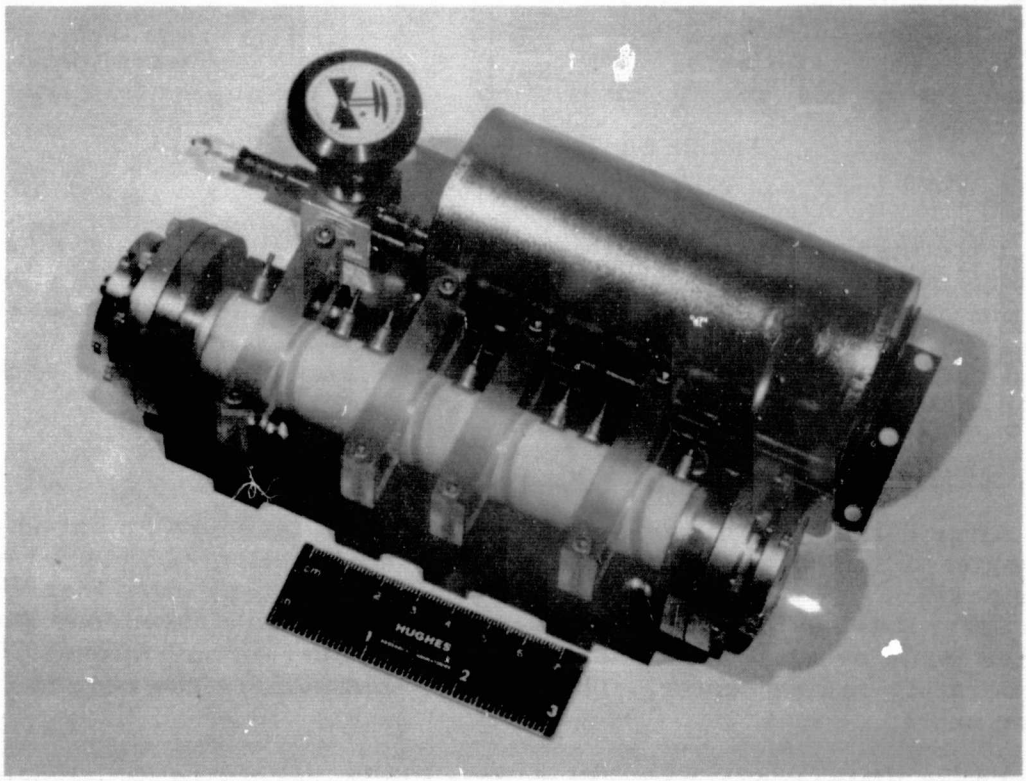

FIGURE 8-5. WAVEGUIDE LASER AND GAS BALLAST (PHOTO 50096-84)

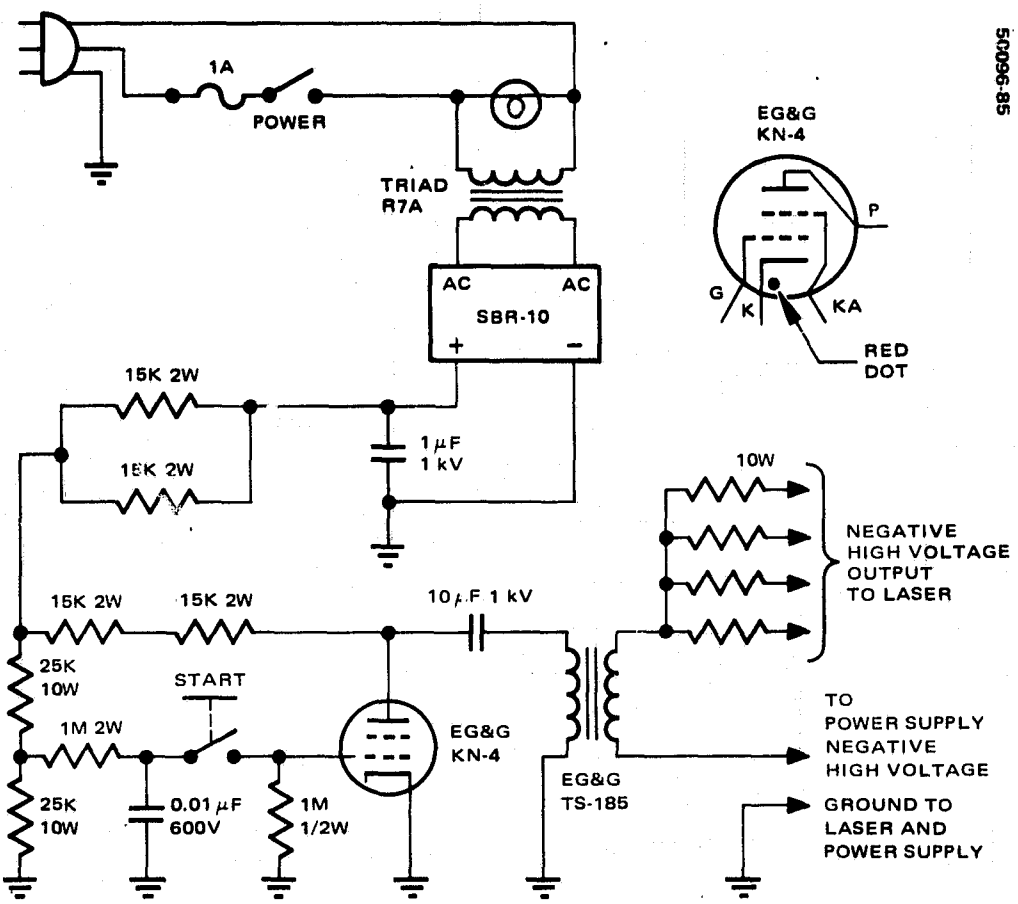

FIGURE 8-6. LASER STARTING CIRCUIT

produces the high voltage pulse which rides on top of the laser power supply voltage. Since the laser dc voltage is set just below breakdown, the pulse raises the voltage applied to the tube enough to initiate the four separate discharges. The ballast resistors for the four discharge sections are also included in the starting unit. The schematic of the starting unit is shown in Figure 8-6, and a photograph of the unit is shown in Figure 8-7.

8.2.3 Laser Performance

After completion of the laser assembly, the laser was pumped out, and a series of tuning curves were recorded as a function of gas pressure and composition. The final gas composition and pressure were then chosen, and the laser was sealed off. Measurements of the laser frequency stability were then made by heterodyne measurements against a conventional CO_2 laser operating on line center. This section summarizes the results of these measurements.

Laser tuning measurements were made by recording the signature of the laser, i.e., the laser power output as a function of bimorph voltage.

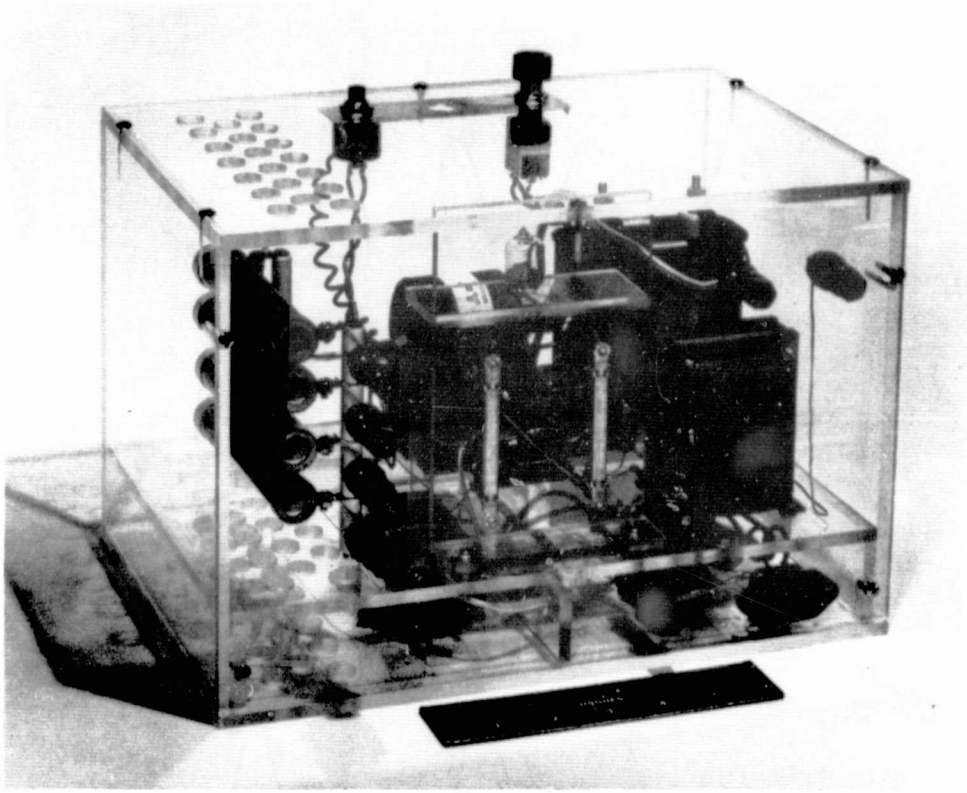

FIGURE 8-7. LASER STARTING CIRCUIT (PHOTO 50096-86)

Application of ±150 volts to the bimorph causes the cavity length to change over a number of wavelengths. One-half wavelength represents a tuning of the laser resonator over one free spectral range (C/2L). For a cavity length of 14.2 cm, this gives a free spectral range of 1.06 GHz. The fraction of one free spectral range that the laser oscillates on a single line, multiplied by the free spectral range (1.06 GHz), gives the tuning range for that transition.

The grating was tuned for oscillation on the P(20) transition, and the laser signature was recorded, either on an X-Y recorder or by an oscilloscope photograph. A series of X-Y recordings for a He:CO_2:N_2:Xe mixture of 6:1:0.5:0.25 is shown in Figure 8-8. The laser tuning range increases with gas pressure until the diminishing laser gain begins to be important (at pressures above 200 Torr). It was decided that the best compromise among laser power output, tuning, and efficiency was at a pressure of 150 Torr in the 6:1:0.5:0.25 mixture. For these measurements, the laser current was maintained at 10 mA. Measurements were also made in 8:1:.5:.25 and 4:1:.5:.25 mixtures, but are not shown here. The laser was filled and sealed off on 10 October 1974. At that time, the characteristics were:

Power output (line center)	540 mW
Discharge voltage	2.15 kV

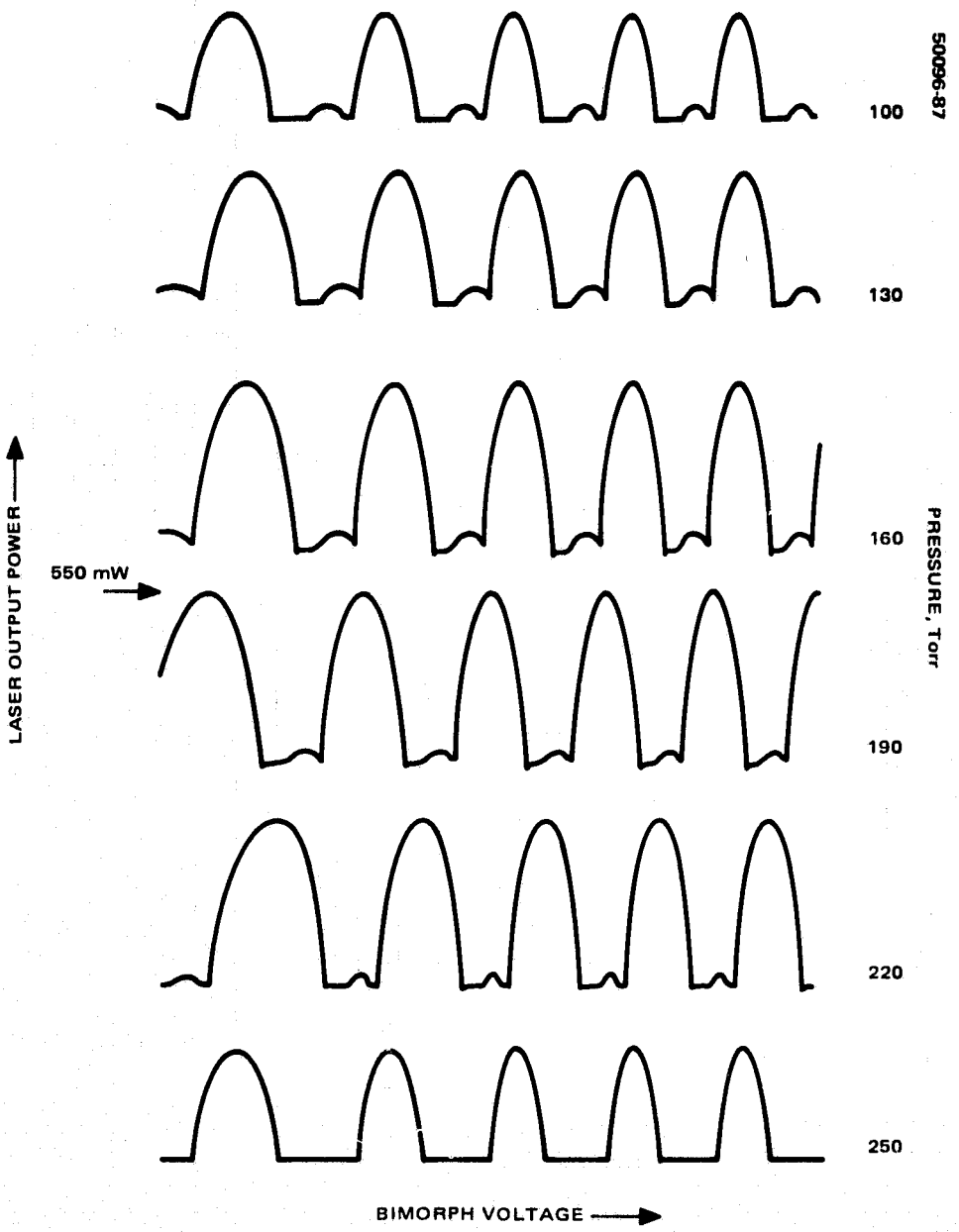

FIGURE 8-8. POWER OUTPUT VERSUS BIMORPH VOLTAGE

Discharge current	9.0 mA
Discharge power	19.4 watts
3 dB tuning range	600 MHz

Slight differences in measured output power and tuning range discussed in various parts of this report are a result of attempts to realign the grating and output mirror for improved performance. An oscilloscope photograph, showing the power tuning curve as well as the bimorph voltage for the sealed off laser, is shown in Figure 8-9. Approximately 4.5 orders (free spectral ranges) are obtained for 158 volts change in the bimorph voltage, which gives ~35 volt/order. This is only approximate as the bimorph is a non-linear device, as can be seen in the tuning curves.

A laser heterodyne measurement was made for accurate frequency tuning as well as frequency stability measurements. A small portion of the waveguide laser output was mixed with a conventional stable CO_2 laser in a HgCdTe fast photodiode (SAT detector – 50 MHz bandwidth), and the IF beat was displayed on a spectrum analyzer. The waveguide laser output power was simultaneously measured with a Scientech power meter. In this manner, the output power versus frequency characteristic of the laser could be accurately measured. The result is shown in Figure 8-10. From this curve, a 1 dB tuning range is ±300 MHz. The sharp transition at 310 MHz represents the onset of a transverse mode.

The spectral beat, as displayed on the spectrum analyzer, is shown in Figure 8-11 for two values of dispersion. The frequency instabilities are all due to the rather high acoustic background in the laboratory. It is not clear which laser is causing the fluctuations. In a quiet environment, there is no question but that the waveguide laser will be adequate as a communcation local oscillator.

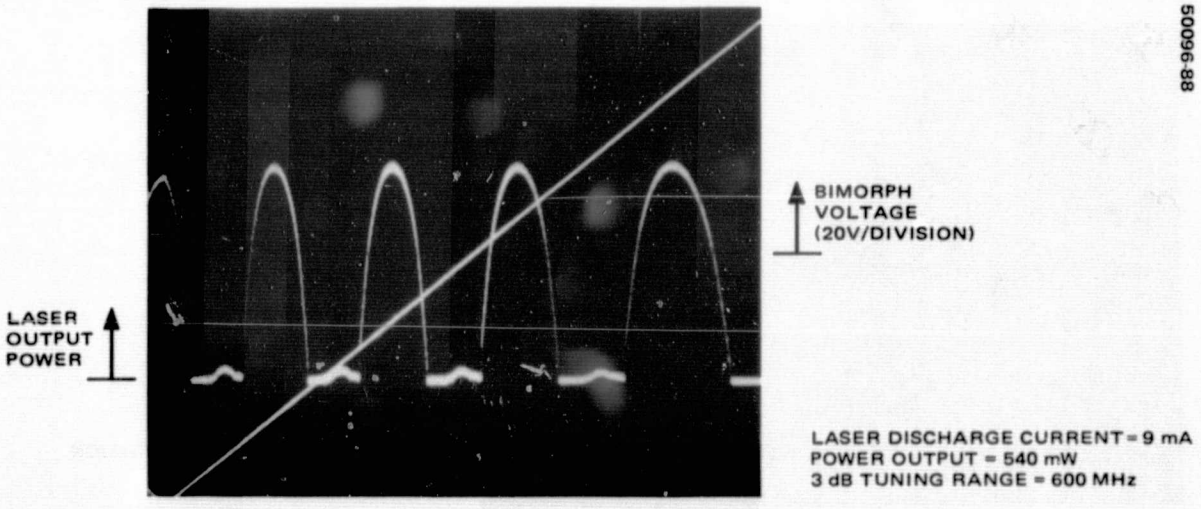

FIGURE 8-9. LASER OUTPUT POWER AND BIMORPH VOLTAGE FOR SEALED-OFF LASER (PRESSURE = 150 TORR)

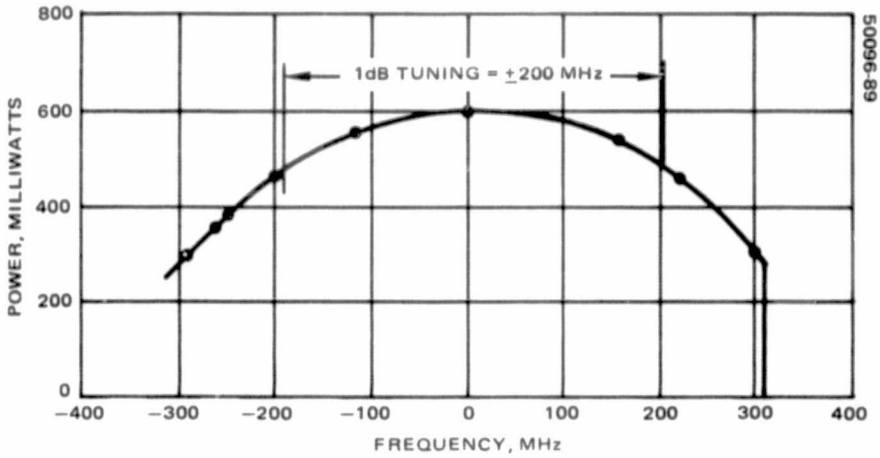

FIGURE 8-10. OUTPUT POWER VERSUS MEASURED FREQUENCY RELATIVE TO LINE CENTER

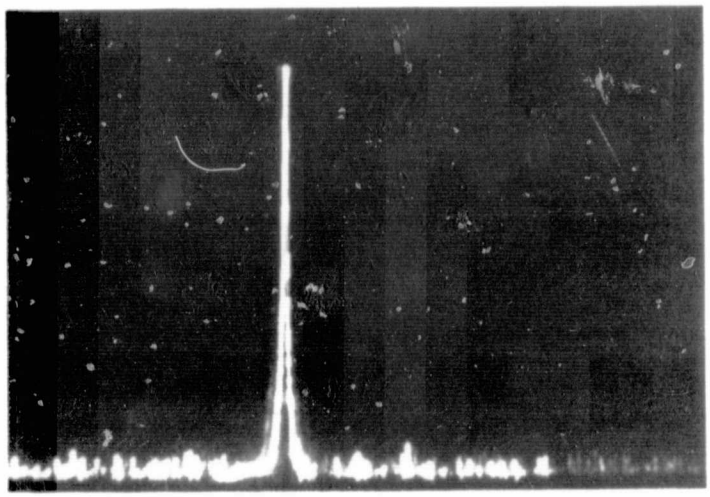

IF BANDWIDTH = 3 kHz
SWEEP RATE = 10 ms/cm
VERTICAL SENSITIVITY = 10 dB/DIVISION

50096-90

a) DISPERSION = 300 kHz/DIVISION

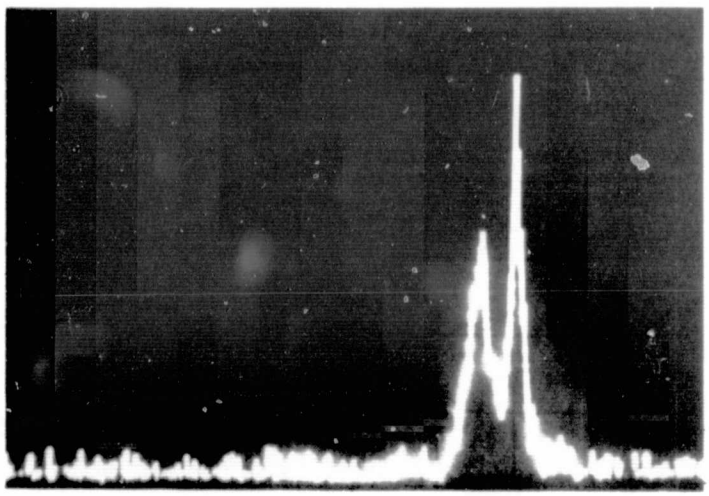

b) DISPERSION = 100 kHz/DIVISION

FIGURE 8-11. SPECTRUM ANALYZER DISPLAY OF IF BEAT BETWEEN WAVEGUIDE AND CONVENTIONAL LASERS (PHOTO 50096-90)

8.3 STARK CELL

8.3.1 Requirements

The Stark cell to be used in this system contains a mixture of ND_3-NH_3 which combine to form NH_2D as well as other mixed isotopic forms of ammonia. At a total pressure of 1 Torr, the absorption coefficient is ~0.01 cm^{-1} when the Stark cell is tuned to the P(20) line center (at an electric field of 3570 V/cm). At higher pressures, the 80 MHz wide doppler broadened absorption line becomes pressure broadened and the dc breakdown voltage of the cell is reduced. If an arc develops, dissociation of the gas occurs, reducing the signal level. A convenient set of parameters, which work satisfactorily for this application, are:

Laser transition	P(20), 10.59 μm
Cell length	10 cm
Field gap	1.28 mm
Pressure	1 Torr
ND_3:NH_3 ratio	1:1
Resonant voltage (calculated)	456 volts
Absorption coefficient (calculated)	10 percent

A 10 percent absorption coefficient is more than adequate to provide an excellent signal-to-noise ratio for locking of the laser to the Stark cell, while the 10 cm cell length is a reasonable size for the laser package. The resonant voltage of 456 volts is a convenient value, in a range where a number of precision power supplies are available.

One feature which is convenient for Stark cell applications is the ability to apply the dc potential to one of the plates, and the ac dither frequency to the opposite plate. This feature, which is incorporated in the Stark cell design, is discussed in the next section.

8.3.2 Mechanical Design

The Stark cell consists of five main components: the bore structure, end washers, end cap window assemblies, housing, and electrical feed throughs. These components can be seen in Figures 8-12, 8-13, and 8-14. A photo of the completed Stark cell is shown in Figure 8-15.

The bore structure consists of two ceramic (99.5 alumina) slabs with an evaporated gold electrode on each slab. When these slabs, whose cross section is L-shaped, are placed one on the other, they form a rectangular bore which is 1.28 mm by 6.89 mm by 101.7 mm. The cell voltage is applied across the 1.28 mm gap.

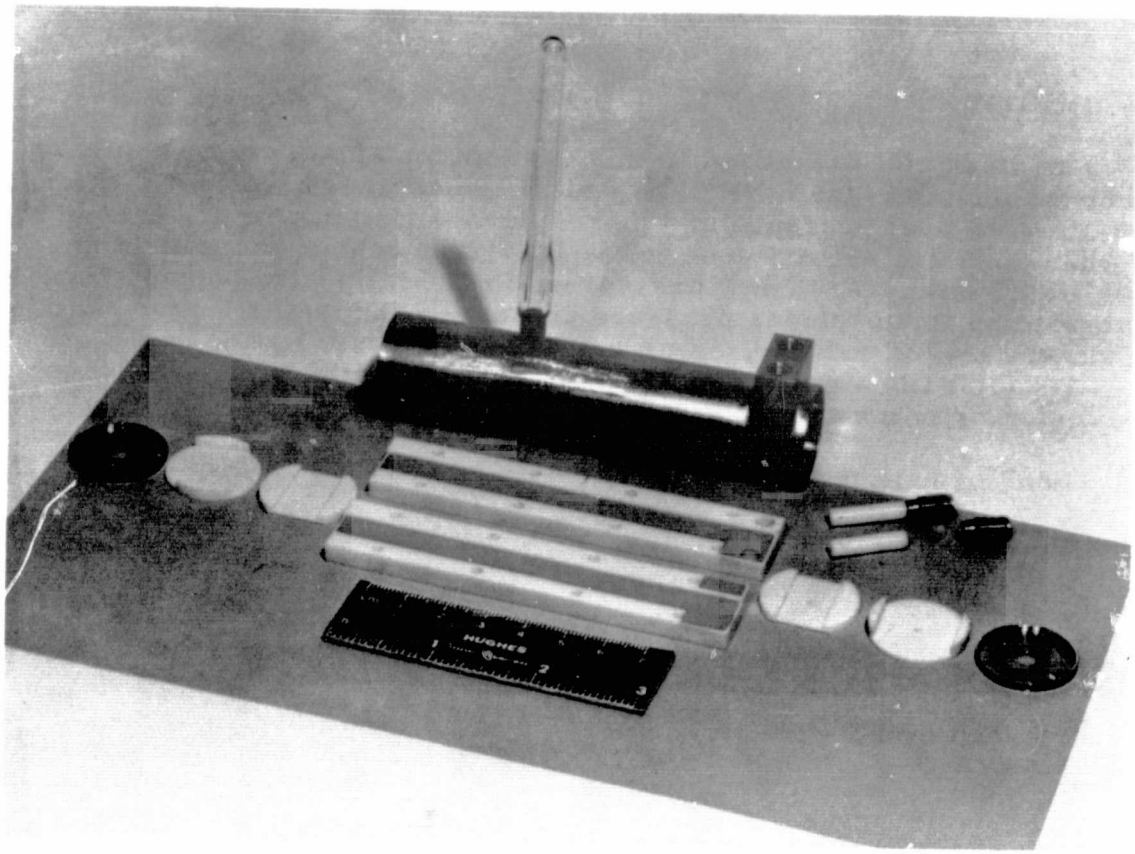

FIGURE 8-12. STARK CELL PARTS (PHOTO 50096-91)

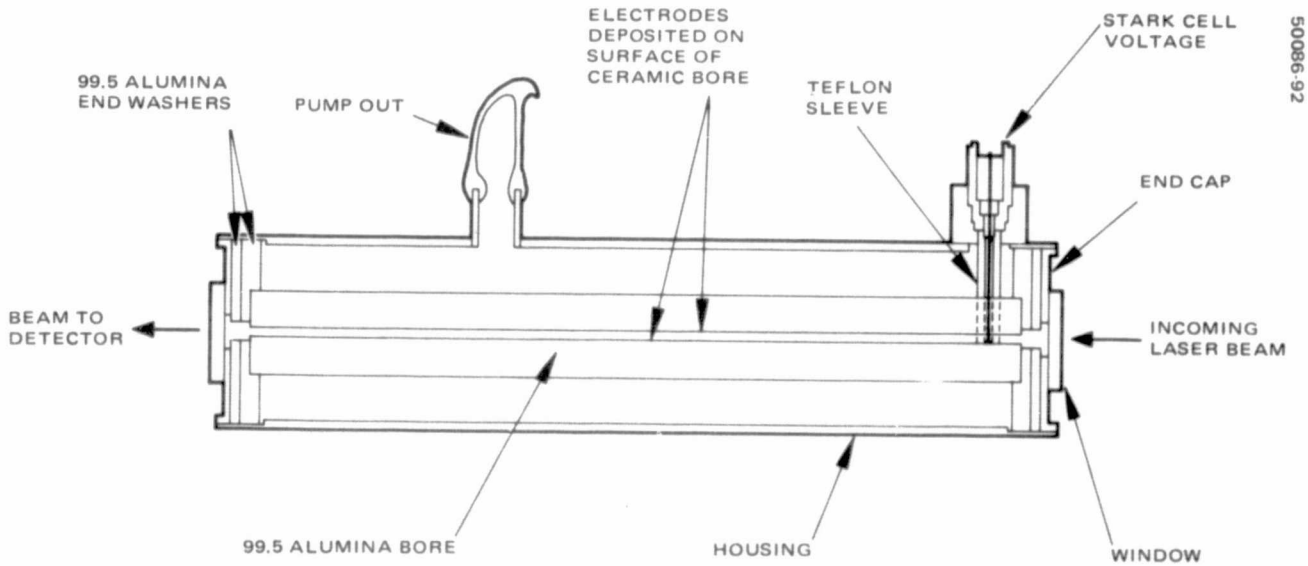

FIGURE 8-13. STARK CELL

ORIGINAL PAGE IS
OF POOR QUALITY

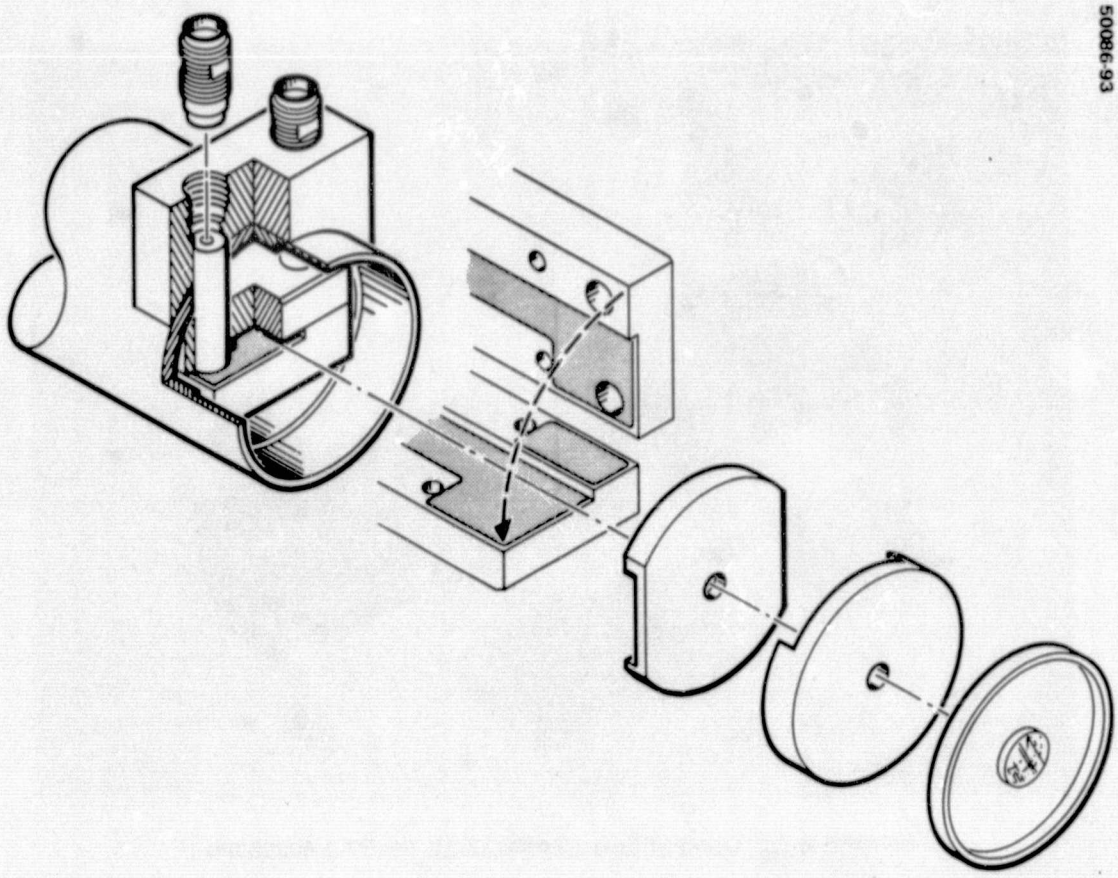

FIGURE 8-14. ASSEMBLY DETAIL AND EXPLODED VIEW OF STARK CELL

Each end washer is composed of two contoured ceramic disks which are also made of 99.5 alumina. When the two disks are fitted together, they form a circular washer with a rectangular recess which fits over the end of the bore structure. The washers mechanically position the bore in the center of the housing and also electrically isolate the bore electrodes from the metal end caps.

The housing and end caps, which are made of stainless steel, form the vacuum jacket for the Stark cell. The housing contains a tubulation for pumpout and processing and a flange for the electrical connectors. After the end caps are welded to the housing, the AR-coated Irtran II windows are attached with epoxy.

Two electrical connections are provided, one for the electrode on each of the ceramic slabs. This allows the dc potential to be applied to one electrode and the ac dither frequency to be applied to the opposite electrode, and keeps both electrodes isolated from ground. The voltages are applied to the electrodes through OSM hermetically sealed connectors by means of a flat platinum ribbon. The ribbon is surrounded by a dual-function teflon sleeve. The sleeve serves as an electrical insulator and provides a compression contact between the electrode and the ribbon, which is bent over the end face of the sleeve.

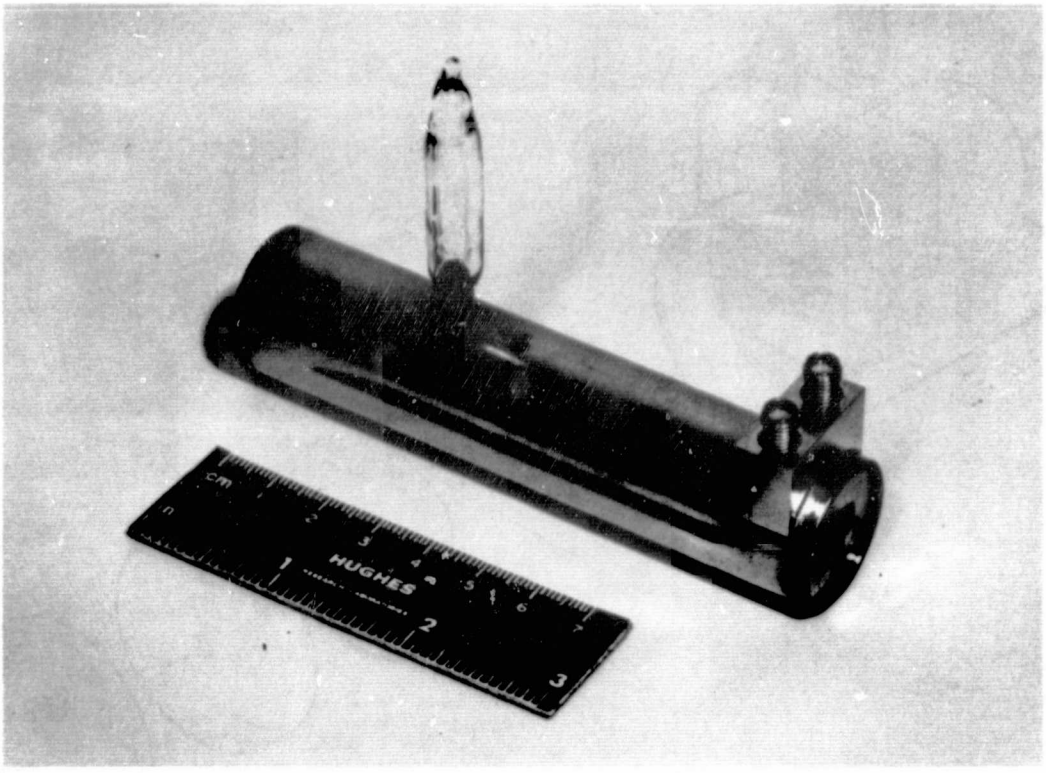

FIGURE 8-15. COMPLETED STARK CELL (PHOTO 50096-94)

Another method of attaching the windows to the end plates is being investigated. This method involves evaporation of chromeindium onto both the window and end plate. The two pieces are then attached by the use of an ultrasonic bonder. Future tubes will be of an all metal-ceramic construction without the use of epoxies.

8.3.3 Cell Performance

After hard pumping and backing to 100°C, the Stark cell was filled with a 1:1 mixture to a pressure of 15 Torr and left for 48 hours. After this time, the cell pressure dropped to 8 Torr. The cell was then pumped out to 1.0 Torr, where the pressure was stable. This filling procedure was found to be necessary to avoid rapid cleanup of the NH_2D onto the clean surfaces. Monitoring of the cell absorption has shown that the cell is stable for greater than 300 hours.

The measured characteristics for the P(20) laser transition are as follows:

Peak absorption	9.5 percent
Resonant cell voltage	451 volts

Breakdown voltage	>1000 volts
Cell tuning rate	~4.6 MHz/V

Using breadboard laboratory electronics, a CO_2 laser has been locked to the cell without any difficulty. Other resonance absorptions exist in the cell, to which the laser may be stabilized. The laser transitions which can be used include P(20), P(14), R(12), P(26), and R(18). The last two are associated with $N^{15}H_2D$ which is a part of the mixture used to fill the cell. Table 8-1 lists all of the transitions for which Stark tunable signals are observed, their measured J values, and the resonant voltages. The data were taken from oscilloscope photographs, so the voltages are only approximate.

8.3.4 Breadboard Electronics

A breadboard system for control of the local oscillator frequency was fabricated to test the Stark cell. The final version of the electronics will be built under another contract for incorporation into the 10.6 μm receiver. The final electronics will differ from the breadboard only slightly in the servo loop filter and in the detector preamplifier.

TABLE 8-1. SUMMARY OF TRANSITIONS ON WHICH STARK MODULATION IS OBSERVED

Laser Line	Molecule	J	Stark Voltage	Approximate % Absorption in 10 cm
P(20)	$N^{14}H_2D$	4	442,595,880	>10
P(14)	$N^{14}H_2D$	4	570,760,1140	>10
R(12)	$N^{14}H_2D$	4	760,895	>10
R(14)	Deuterated $N^{14}H_3$		820	*
R(26)	Deuterated $N^{14}H_3$		850	*
P(26)	$N^{15}H_2D$	4	170,235,355,730	12
R(18)	$N^{15}H_2D$	6	580,700,880	8
P(10)	Deuterated $N^{15}H_3$	11	380,420,460 520,600,710,860	*
P(28)	Deuterated $N^{15}H_3$	Second order Stark effect	260	*
R(24)	Deuterated $N^{15}H_3$		910	*

*Less than 3% absorption.

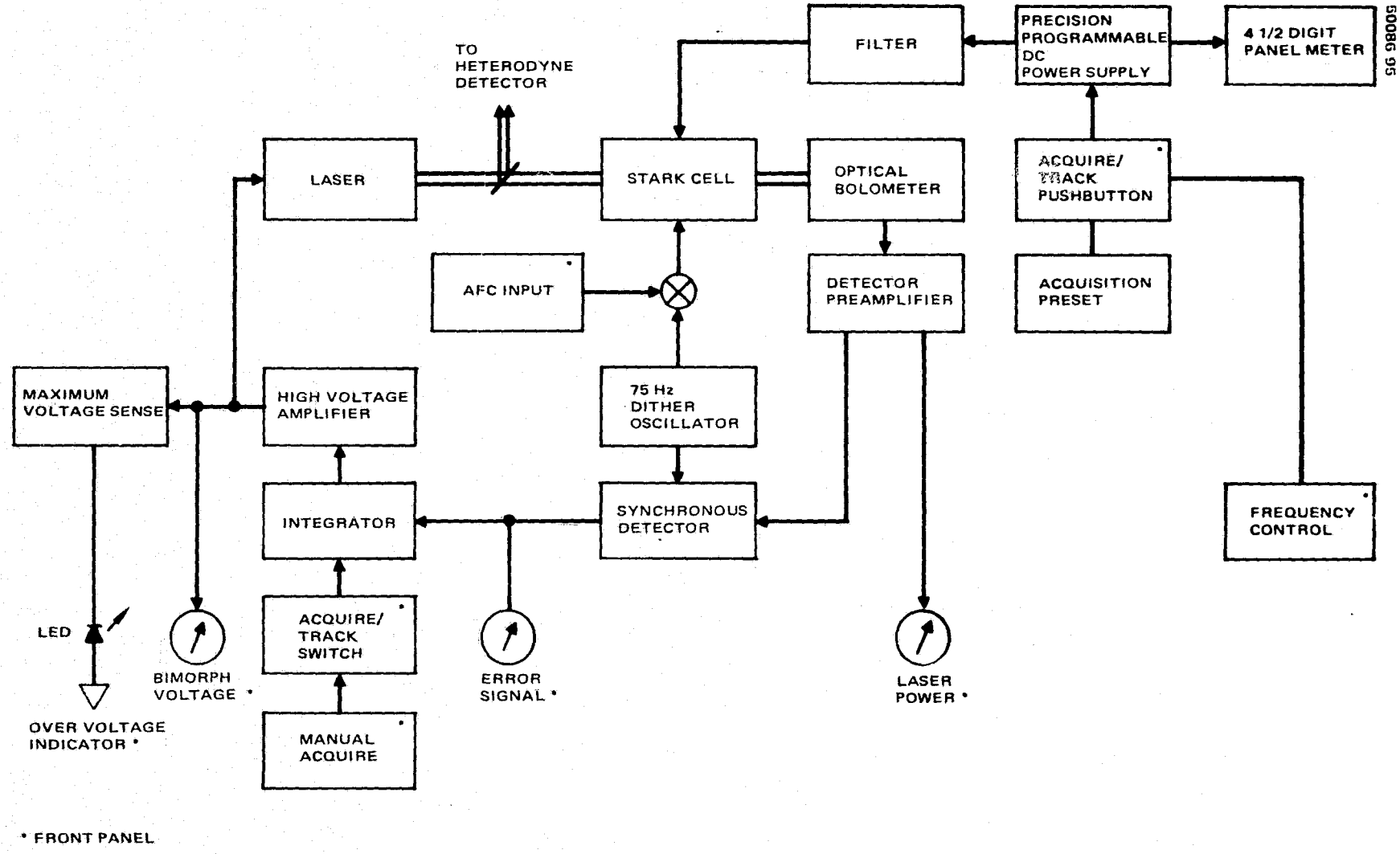

FIGURE 8-16. STARK CELL BREADBOARD ELECTRONICS

Figure 8-16 is a block diagram of the breadboard system. A perturbation or "dither" modulation is used to generate error signals of the proper sense. These errors are filtered, amplified, and fed back to the laser to maintain the laser frequency equal to the Stark cell absorption frequency.

A precision dc power supply sets the frequency of the Stark cell absorption line. The supply is adjustable to allow laser tuning; a 4-1/2 digit panel meter monitors the voltage. (The supply may be remotely programmed to simulate telemetry commands at a later date if desired.) A pushbutton is incorporated for initial acquisition; the button sets the power supply to a voltage where there is no possibility of an ambiguous lock due to two Stark resonances (see Appendix E). After acquisition, the voltage returns to the desired control voltage at a rate which the servo can track.

A 75 Hz, 20 volt peak-to-peak signal is applied to the other Stark cell electrode. Provisions are incorporated to apply a dc coupled signal to this electrode for system test or for AFC tracking without disturbing the power supply setting.

The amplitude modulation on the laser beam is detected by a dc coupled bolometer consisting of a matched pair of thin film thermistors. The dc component of this signal is used to drive a meter for an indication of laser power. The 75 Hz component is separated, amplified, and synchronously demodulated to establish an error signal. This signal is filtered and amplified, then routed to the laser bimorph for frequency correction. An integrator is incorporated in the loop filter to eliminate static tracking errors.

8.3.5 References

1. T.A. Nussmeier and R.L. Abrams, Appl. Phys. Letter 25, 615 (1974), and reproduced in the Appendix.

2. R.L. Abrams and W.B. Bridges, IEEE Journal of Quantum Electronics QE-9, 940 (1973).

9. OPTO-MECHANICAL SERVO SYSTEM

9.1 INTRODUCTION

This section covers the design and performance tests of the servo system for the opto-mechanical subsystem of the 10.6 μm coherent receiver. The receiver opto-mechanical subsystem itself, which has already been reported, consists of a gimbal assembly, structure, and Gregorian telescope and will eventually include associated instrumentation for receiving and decoding a 300 Mbps data stream impressed on a 10.6 μm laser beam. A picture of the opto-mechanical package of the receiver is shown in Figure 3-22. The gimbal assembly is also shown separately in Figure 3-14. The incoming laser beam is reflected off the gimbaled flat mirror and thereby directed onto the primary mirror. The gimbaled mirror is driven about each of two axes to provide coarse control over the pointing direction of the telescope. Fine control is provided by an image motion compensator (IMC) subsystem located at the field stop of the telescope. After passing the IMC subsystem, the received laser beam is combined with a local oscillator beam and focused onto an optical detector. Tracking error is developed in the detector circuit by synchronously detecting the conical IMC scanning voltages with the amplitude of the signal on the detector.

The function of the OMSS basically is to keep the laser target beam properly aligned with the local oscillator beam on the optical detector. This involves both beam acquisition and beam track. Servo control of the gimbals and the IMC subsystem is required for both functions. The servo system to perform these functions has been designed, built, and tested. This section covers both the system design and the test results.

9.2 REQUIREMENTS AND CONSTRAINTS

The performance requirements of the OMSS and the constraints under which these requirements must be met are determined largely by the design of the opto-mechanical package and the mission operational constraints. The detailed opto-mechanical design is covered in previous sections of this report.

Table 9-1 lists the requirements and constraints on the servo subsystem. The basic requirement is to acquire a target anywhere within the ±10° range of the gimbals and, following this, to maintain track to within a certain accuracy. The tracking accuracy as used here refers to the angular misalignment between

TABLE 9-1. SERVO SUBSYSTEM REQUIREMENTS AND CONSTRAINTS

Parameter	Value	Remarks
Peak tracking error	51 μrad	Based on a 5 dB S/N degradation
Beam diameter (3 dB)	80 μrad	Referred to target space
Carrier S/N	15 dB	Based on 50 kHz bandwidth
Telescope FOV	±0.1	
Maximum target rate for acquisition	0.03 deg/sec	Sum of real target motion and opto-mechanical base motion
Gimbal range	±10°	Refers to beam deflection in target space
Atmosphere produced beam steering	±25 μrad	Assumed frequency of 5 Hz; applicable only to ground tests

detector and target as referred to target space and is not the same for this system as the servo error. The physical size of the detector is optimally matched to the size of the target image in the plane of the detector to yield the maximum detector power. The maximum allowed tracking error is determined by the loss of power as the target moves off the detector, as compared to the maximum power loss that is tolerable. For this system, the 3 dB error is 40 μrad (3 dB beam diameter of 80 μrad), and the maximum tolerable loss is 5 dB, which allows a maximum error of 51 μrad.

This error specification is based on a maximum signal-to-noise ratio (S/N) of 15 dB in a 50 kHz bandwidth. An S/N this large in a 50 kHz bandwidth will produce a very high S/N in the servo bandwidth, since generally the noise voltage is proportional to the square root of bandwidth. Therefore, the detector will contribute negligible noise to the servo loop.

The telescope field of view (FOV) establishes the required range of the IMC, but also specifies the pointing accuracy of the synchronous spacecraft to which the receiver is attached. The selected value of ±0.1° is approaching the limit for spacecraft using horizon sensors for attitude reference, but would be well within the capability of satellites using RF beacons, such as the ATS-F, or those using star trackers, such as the OAO. In any case, the ±0.1° FOV is given as a constraint to the OMSS design, as mentioned earlier, and it is not the intention here to rigorously justify these constraints.

The maximum target rate during acquisition is the sum of the linear motion of the target and the angular motion of the opto-mechanical base. The assumed mission (a synchronous satellite receiver tracking a low earth orbit satellite transmitter) produces a maximum linear motion contribution of 0.007 deg/sec. The instability of the opto-mechanical base is strongly dependent on the design of the synchronous satellite attitude control system and operational constraints placed on that system. Firing a reaction jet during acquisition, for example, might produce a rate of 0.1 deg/sec, but if this is prohibited during acquisition, the maximum rate would probably be less than 0.01 deg/sec. The value of 0.03 deg/sec total rate listed in the table was chosen somewhat arbitrarily as a tradeoff among maximum possible value, the most likely value, and the largest value convenient to implement. Thus, selecting the design target rate of 0.03 deg/sec means that some targets moving at 0.1 deg/sec may slip

by undetected. On the other hand, if it turns out in design of the operational system that target rates up to 0.1 deg/sec must be accommodated, this can be done without the major changes in the present design. The ±10° gimbal range (beam deflection in target space) is chosen to cover the synchronous orbit to low earth orbit case. This range will handle low earth orbit satellite altitudes up to approximately 500 n. mi.

The last specification in Table 9-1, atmospheric beam bending, is included only to cover the case of ground tests of the system over a path that includes a significant atmosphere. The value of 25 μrad at 5 Hz is believed to be conservative at 10.6 μm wavelength.

9.3 DESIGN APPROACH

The basic conceptual design of the system is illustrated in Figure 9-1. An incoming laser beam is received by an optical system consisting of the gimbaled mirror, the all reflecting Gregorian telescope, the image motion compensation (IMC) mirror, and an optical detector. The gimbal mirror rotates about two orthogonal axes so as to receive the laser beam throughout a ±10° cone relative to the telescope. This mirror, which is driven by a stepper motor, compensates for slow angular movements of the incoming laser beam, as caused by either base motions (e.g., satellite angular motion) or by transmitter linear motion. Fast angular jitter of the incoming beam is compensated by the IMC mirror which is driven by a piezoelectric actuator.

The communication data on the incoming beam are recovered as follows: First, the optical beam is mixed with a local oscillator beam to produce a difference signal, still carrying the data, whose frequency lies in the RF portion of the spectrum. Second, the RF signal is processed as in a conventional microwave receiver to recover the data. Following the RF detection circuitry are automatic gain control (AGC) circuits and beam presence logic. The RF signal also contains an amplitude modulation which is impressed by the conical scan of the IMC device, which circularly sweeps the beam on the detector. This amplitude modulation contains the servo error information, which is recovered in a synchronous demodulator. After suitable shaping, the error signal is applied to the IMC drive loop in such a phase and magnitude to reduce the detected error.

The IMC drive loop consists of a piezoelectric actuator, a high voltage driver amplifier, a strain gage pickoff and associated instrumentation amplifier, and the necessary shaping network to give the desired servo response. The stepper motor driving the gimbal is actuated by a threshold circuit operating on the strain gage signal, which energizes the stepper when the IMC exceeds a preset higher threshold and turns the stepper off when the IMC position is forced back below a low threshold. The stepper motor can also be energized manually to drive the gimbals to any desired position within their range. The actual position of the gimbal is measured by two means: a digital counter which displays the accumulated stepper motor pulses and an analog meter which displays the voltage of a gimbal driven potentiometer. The digital counter is initialized by a discrete from a gimbal actuated photo-sensor which senses

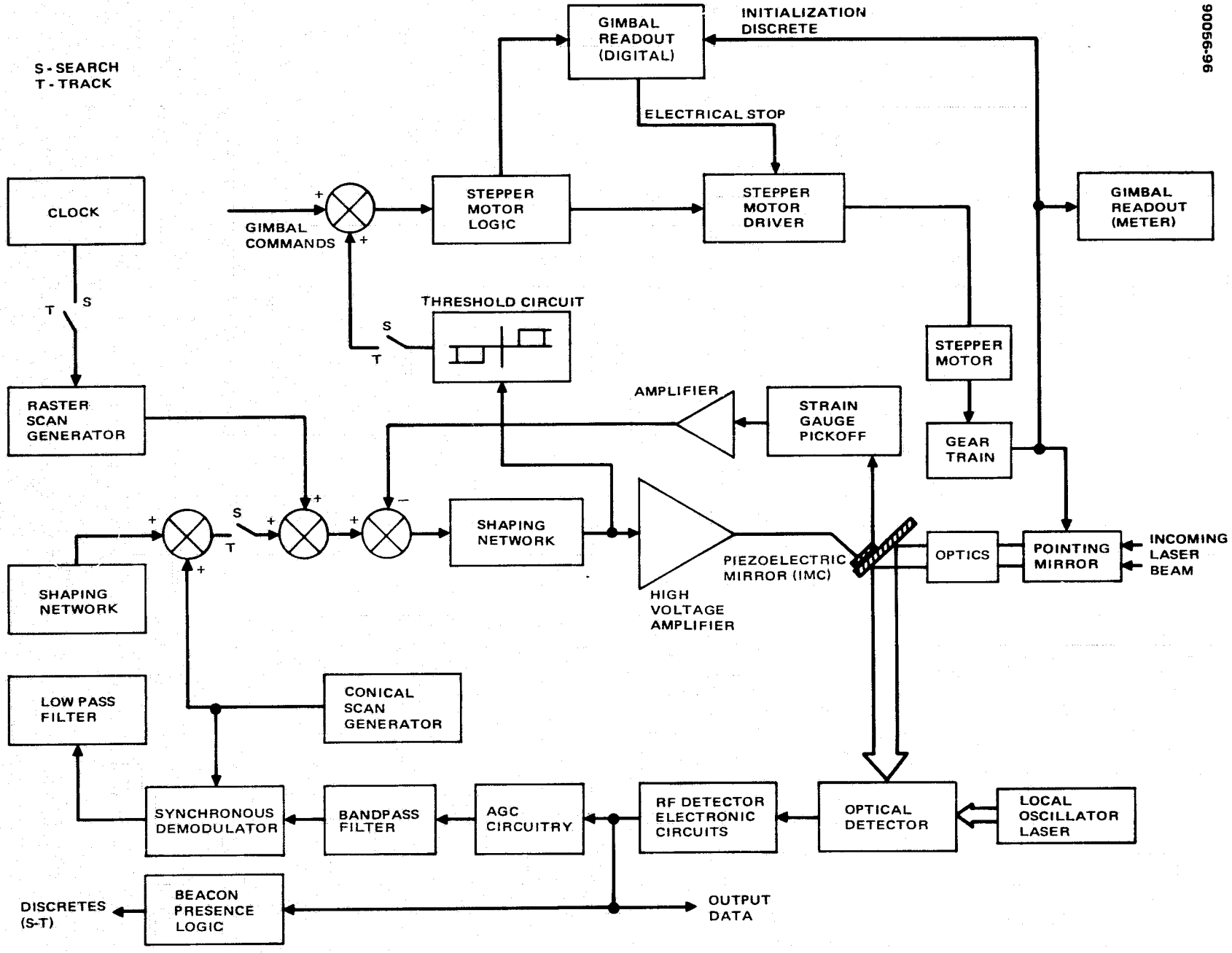

FIGURE 9-1. OPTO-MECHANICAL SUBSYSTEM SINGLE-AXIS BLOCK DIAGRAM

when the gimbal crosses through zero. The pulse counter also supplies an electrical stop to prevent the gimbal from exceeding its range.

The search/track switches choose between the search raster scan and closed loop track modes. These switches are actuated by a discrete from the beacon presence logic. In the search mode the IMC loop is driven by the raster scan generator. Upon acquisition of the beacon presence, the raster scan is stopped (but not disconnected), and the combined error (which initially is zero) and conical scan signal are added to the existing raster scan generator. This approach avoids the necessity of storing the acquisition beam position for use in initializing the track loop.

9.4 DETAILED SERVO DESIGN

9.4.1 Raster Scan

The basic requirements of the IMC loop are established by the characteristics of the raster scan. The raster scan is sketched in Figure 9-2, where the target beam size is drawn approximately to scale. The maximum allowable frame time and required sweep rate are determined by the target velocity. For the design target velocity of 0.03 deg/sec, the 0.2° field width will be traversed in 6.7 seconds, which is the maximum allowable frame time. To complete the vertical frame in 6.7 seconds requires that the sweep move vertically at an average rate of 0.03 deg/sec. The relative speed of the target and sweep (assuming opposite directions) is 0.06 deg/sec on the average. However, examination of the figure will show that the time between two consecutive lines is an entire sweep period, which means the effective line velocity in terms of target capture probability is only 0.015 deg/sec. Therefore, the time required to traverse one beamwidth is 0.1 second for the worst case condition of target moving opposite the sweep. The minimum triangular sweep frequency, then, is 10 Hz.

The minimum IMC servo bandwidth for the raster scan is determined by the scan frequency. It is desirable to be able to stop the scan directly on the target upon receipt of a beam presence signal. This requires that the servo error at time of acquisition be no greater than some fraction of the beamwidth. Using a half-beamwidth criterion, assuming a velocity control law, and representing the 10 Hz triangular wave by the sum of the fundamental and third harmonic, the required bandwidth (BW) is:

$$BW = \frac{(0.667)(FOV)(\text{sweep frequency})}{\text{beamwidth}}$$

$$= \frac{(0.667)(0.2)(10)}{0.0046}$$

$$BW = 290 \text{ Hz}$$

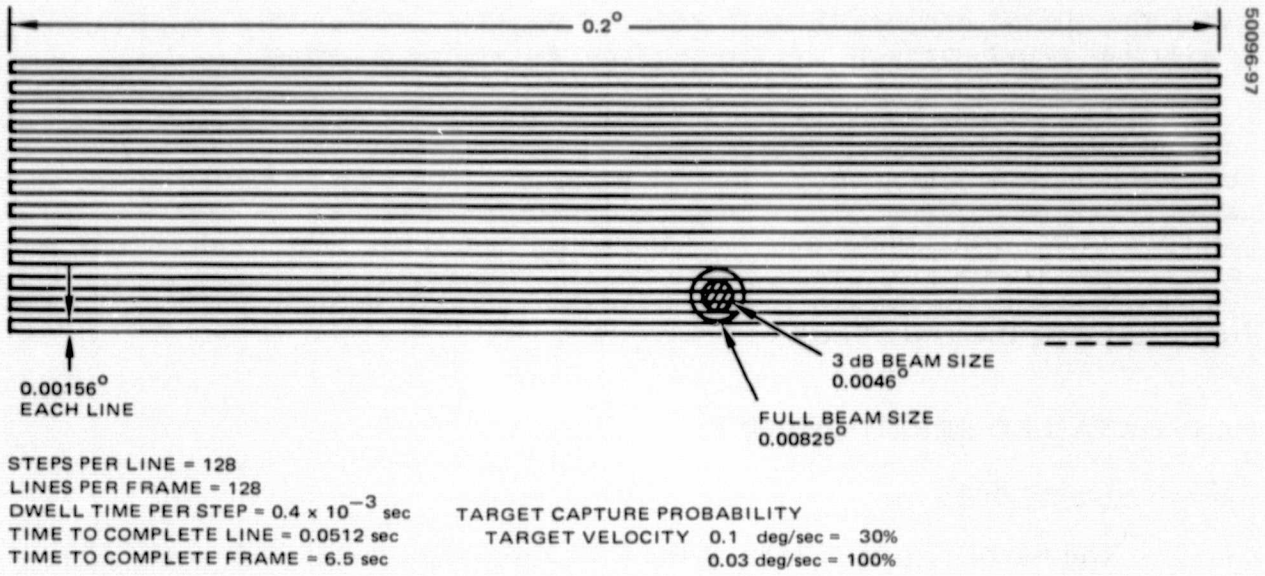

FIGURE 9-2. RASTER SCAN DATA

The factor 0.667 in the above expression accounts for the fact that the magnitude of the third harmonic is down by a factor of 9 compared to the fundamental, but the servo is only one-third as effective at the harmonic frequency. The resultant required bandwidth is not too high for an IMC loop using piezoelectric actuators, but would be high for mechanical actuators. The required bandwidth can be reduced slightly by assuming the actual beamwidth is larger than the 3 dB beamwidth. But to obtain a substantial reduction in the required bandwidth, the effective target velocity must be decreased or another approach to acquisition used. One other approach, for example, would be to store the measured IMC position at time of receiving a beam presence signal, then use this as a new reference position for the IMC loop. The required bandwidth then applies only to the readout device and not to the entire loop.

9.4.2 IMC Loop

The IMC loop serves two functions. In the acquisition mode it controls the raster scan position during target search. After acquisition the IMCs control the beam position during track. It is the raster scan that imposes the greatest requirement on the IMC loop. As discussed above, the raster scan requires an IMC amplitude of 0.1° peak at a frequency of approximately 300 Hz.

A block diagram of the IMC loop is shown in Figure 9-3. The piezoelectric actuator deflects the IMC mirror and therefore the incoming beam, in response to signals from the piezoelectric driver, which is a high voltage operational amplifier. The actual mirror movement is accurately measured with a strain gage bridge. The resulting low level signal is fed back through a low drift amplifier and combined with the input drive signal. The resulting error signal, after proper shaping, is fed back to the piezoelectric driver.

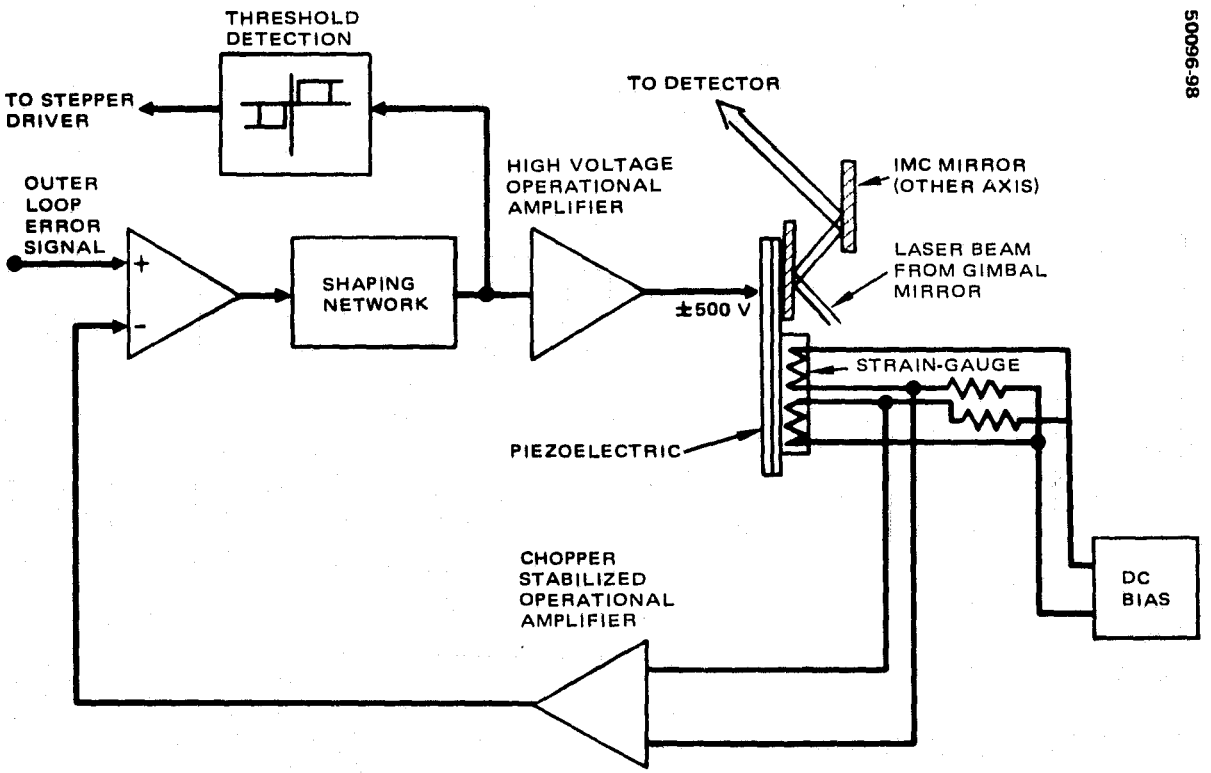

FIGURE 9-3. IMC LOOP BLOCK DIAGRAM

The measured frequency response characteristics of one of the IMC actuators are given in Figure 9-4. Also given in the figure are the vendor test data on which the preliminary design was based. The resonance of the actual hardware is down by a factor of two from the vendor data. Also, as can be seen from the figure, the dynamics of the real system above resonance are quite complex. The practical result is that the loop bandwidth must be limited to around 500 Hz.

A servo block diagram of the IMC loop, including shaping networks and numerical data, is given in Figure 9-5. The poles and zeroes of the filter network are chosen to stabilize the piezoelectric resonance. The zeroes are chosen to be close to the piezoelectric poles but slightly below, so that shifts in the dynamics of either the filter or the piezoelectric actuator will not cause a phase inversion and the associated instability. Only one dipole above resonance is included in the block diagram, which represents the system dynamics as simulated on a digital computer to obtain the time response.

The results of the simulation are given in Figure 9-6 for the case of a 0.1 deg/step magnitude. In practice, the system will not see a step that large. The loop damps out to 95 percent of the final value in less than 4 ms. The ringing on the output is more than is desirable. However, given the dynamic characteristics shown in Figure 9-4, the additional damping can only

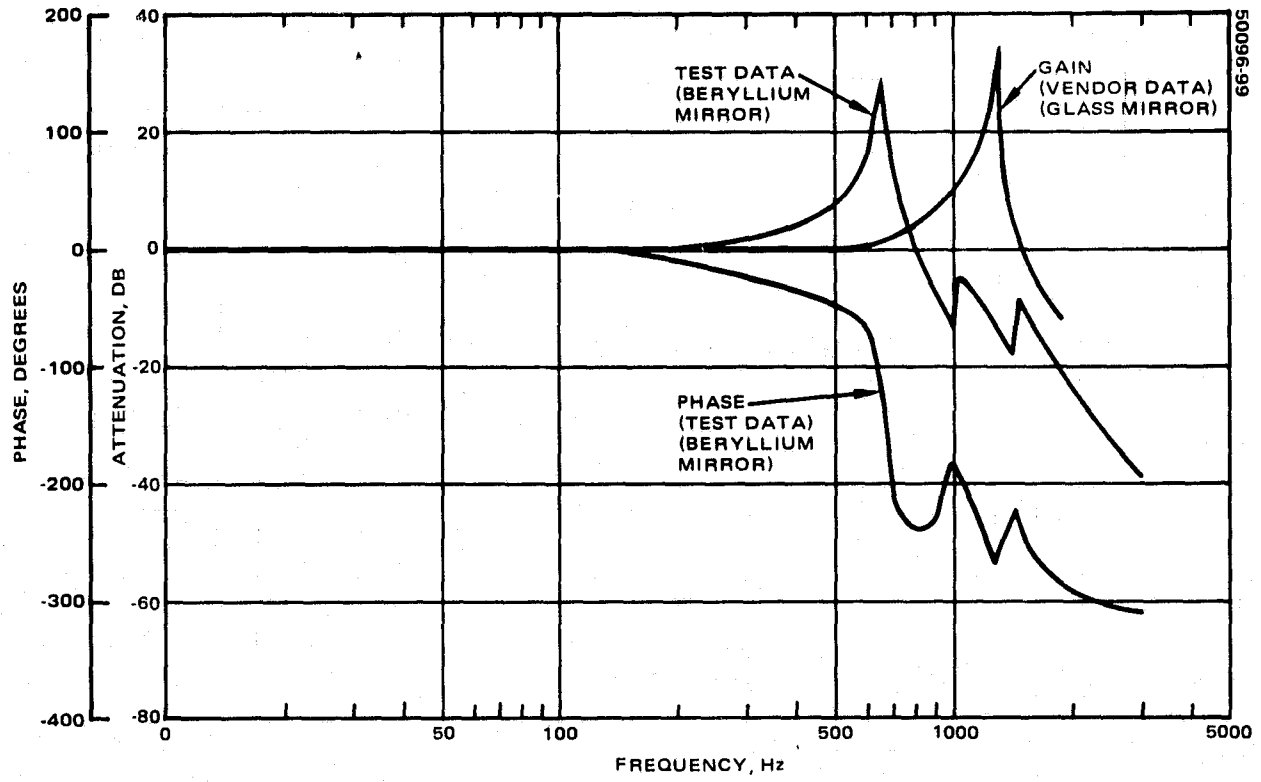

FIGURE 9-4. BODE PLOT FOR IMC DYNAMICS

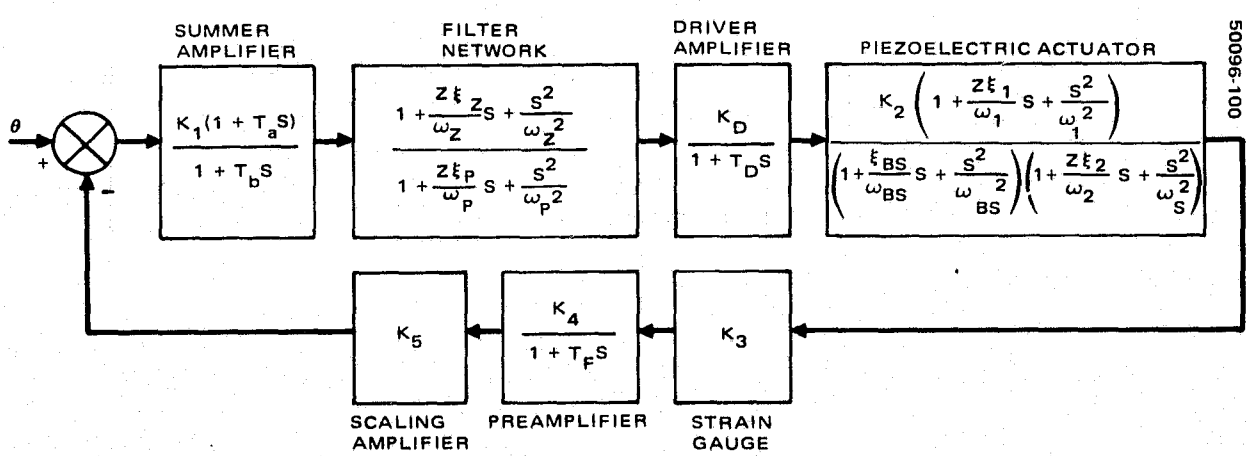

K_1 = 217 V/V	T_a = 1.9×10^{-4} sec	ξ_1 = 0.1
K_D = 100 V/V	T_b = 0.1 sec	ω_1 = 5477 rad/sec
K_2 = 2×10^{-4} deg/V	ξ_Z = 0.05 sec	ξ_2 = 0.1
K_3 = 0.04	ω_Z = 3500 rad/sec	ω_2 = 6000
K_4 = 675	ξ_P = 0.707	ξ_{BS} = 0.02
K_5 = 3.7	ω_P = 2500 rad/sec	ω_{BS} = 4086 rad/sec
	T_D = 1.9×10^{-4} sec	T_F = 9.37×10^{-5} sec

FIGURE 9-5. IMC LOOP SERVO BLOCK DIAGRAM

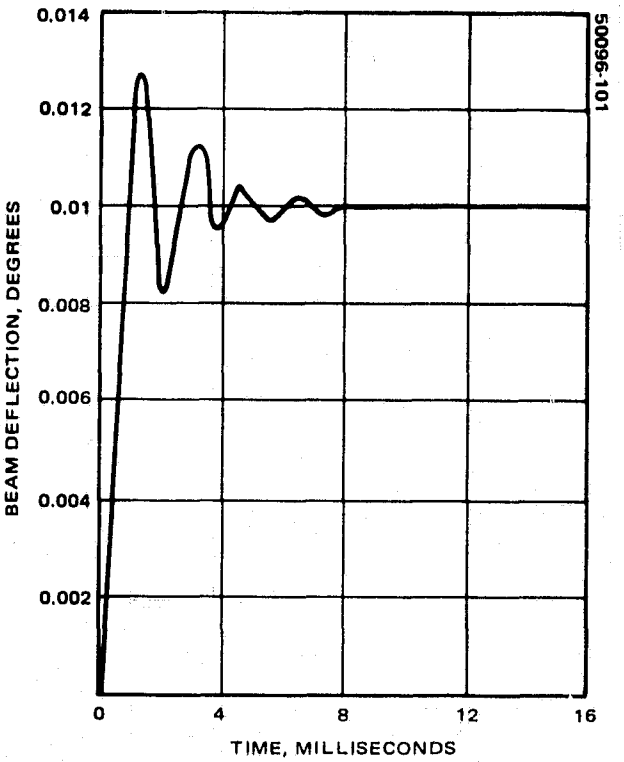

FIGURE 9-6. IMC STEP RESPONSE (FROM COMPUTER SIMULATION)

be achieved by reducing the bandwidth considerably or by going to an alternate shaping network which requires an inner loop. The required inner loop was actually designed to be ready during the test phase if needed. The concern, really, was not that the response shown in Figure 9-6 would be unsatisfactory, but that the actual loop response might be worse. Test results, which are covered in Section 9.6, show that this is not the case. The alternate design, therefore, was never implemented.

9.4.3 Error Detector

The error detection system includes the conical scan modulation, the optical detection characteristics, the synchronous demodulator, and the associated filtering. The error detector transfer function is defined in Figure 9-7 for the single-axis case. The incoming laser beam angular position is defined by a single number representing the angular displacement of all optical rays (all of which are parallel) relative to the optical axis. The relative detector output as a function of this beam angular displacement is given in the figure. This curve is taken from a computer simulation of the optics for 10.6 μm coherent reception rather than from measured data for the servo performance tests, which are covered in Section 9.6; this curve is simulated by a direct detection sensor operating at 0.63 μm.

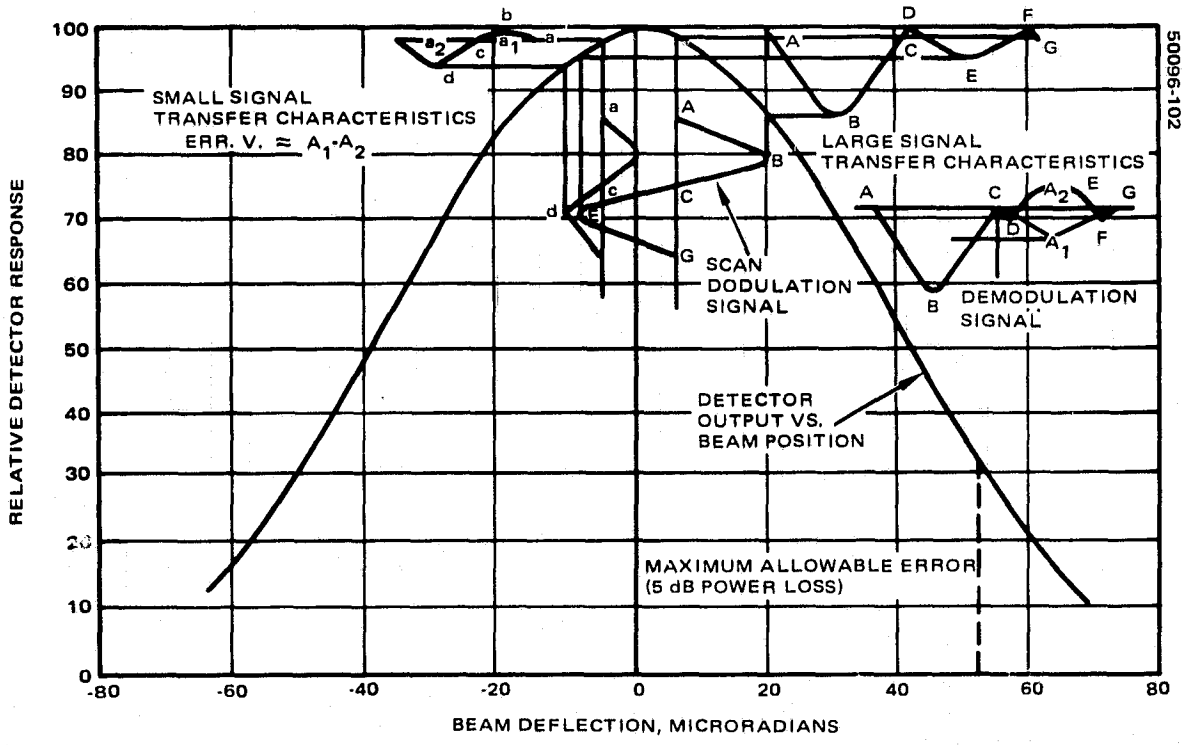

FIGURE 9-7. CONICAL SCAN ERROR SENSOR TRANSFER CHARACTERISTICS

The effect of superimposing a scan modulation onto the beam position is illustrated in the figure. Two modulation characteristics are obtained: one for small scan signal amplitudes and the other for large amplitudes. For large modulation amplitudes the detector output curve appears to be straight line. For this case, the transfer characteristics tend to saturate at an error offset equal to the scan amplitude, since, for a straight-line case., the output voltage is not a function of position once the entire modulation signal is on one side of the axis. For the small signal case, the modulation output depends on the rate of change of slope with error offset and does not saturate, therefore, until the slope tends to become constant.

Error detection transfer characteristics are shown in Figure 9-8. These curves are taken from a computer simulation of the characteristics shown in Figure 9-7. For small scan amplitudes the error sensitivity is low and highly linear. As the scan amplitude increases, the sensitivity also increases, but nonlinearities start to appear. Generally, it is desirable to have a high sensitivity to improve the S/N and a wide linear range to provide fast recovery from large disturbances. For this system the S/N should not be a problem (in the tracking loop). Therefore, any modulation amplitude above, say, 5 μrad should be adequate.

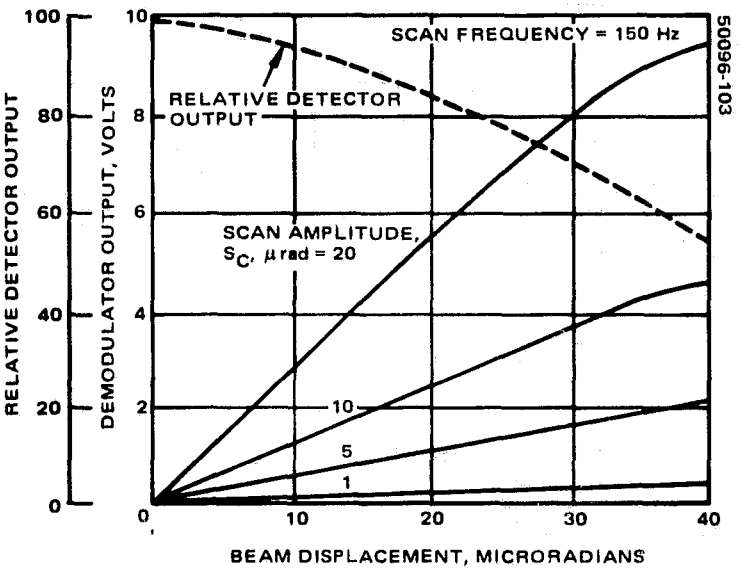

FIGURE 9-8. ERROR DETECTOR TRANSFER CHARACTERISTICS

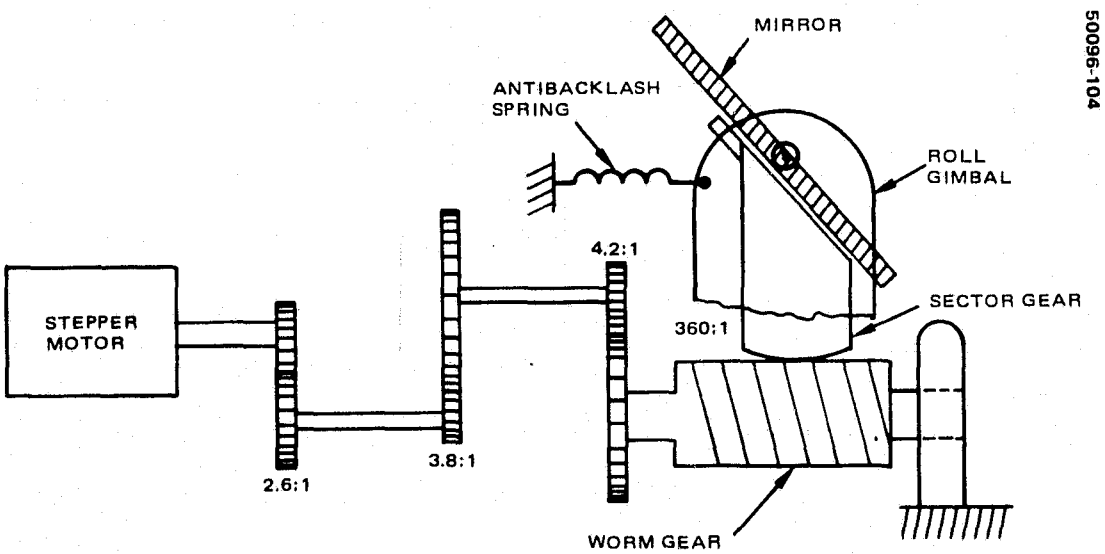

FIGURE 9-9. GEAR TRAIN FOR ELEVATION DRIVE

9.4.4 Stepper Motor Gimbal Drive

The gimbals are driven by stepper motors through large gear reductions (approximately 15,000:1 for roll and 7500:1 for elevation). A schematic of the elevation drive is shown in Figure 9-9. The first three gear stages are spur gears, and these are followed by a worm gear driving a sector wheel which actuates the gimbal mirror. To reduce backlash in the worm gear drive, an antibacklash spring is used. The construction of the worm gear is such that backdriving of the motor shaft by the spring through the gear train is prevented.

The gimbal drive system was designed as part of the opto-mechanical package shown in Figure 3-22. The system had been designed and partly built before the servo design was initiated, but had not been tested. Subsequently, tests have shown the gimbal drive system to be a problem area. The basic approach to the drive system was to choose a step size and rate such that the IMC tracking loop would be required to respond only to the average value of the gimbal rate (0.1 deg/sec). For this to be true the step size should be no larger than that required to produce a 1 dB loss in power, which for the characteristics given in Figure 9-7 is approximately one-eighth of a beam diameter, or 10 μrad (0.000573°). The actual step size of 0.002° is high, therefore, by a factor of 3.5. Decreasing the step size would require that the step rate be increased by the same factor to maintain the same average gimbal speed.

Another problem with the present drive system is that the stepper motor acts as a vibration source which tends to excite the gimbal/gear train structure. The result is that the real transient motion of the gimbals is much greater than the step increment of 0.002°. (The 0.002° step size was chosen originally because the beamwidth was expected to be much larger.)

The gimbal dynamic response is illustrated in Figure 9-10. Three separate curves are given. First, there is the theoretical response of the unloaded motor based on manufacturer's data. This response, which shows a 25 percent overshoot and a characteristic frequency of 330 Hz, dies out completely before initiation of the next step. The actual roll gimbal response to a pulse train is also given. This response exhibits a natural ringing frequency of 100 Hz which does not die out between steps. The elevation gimbal

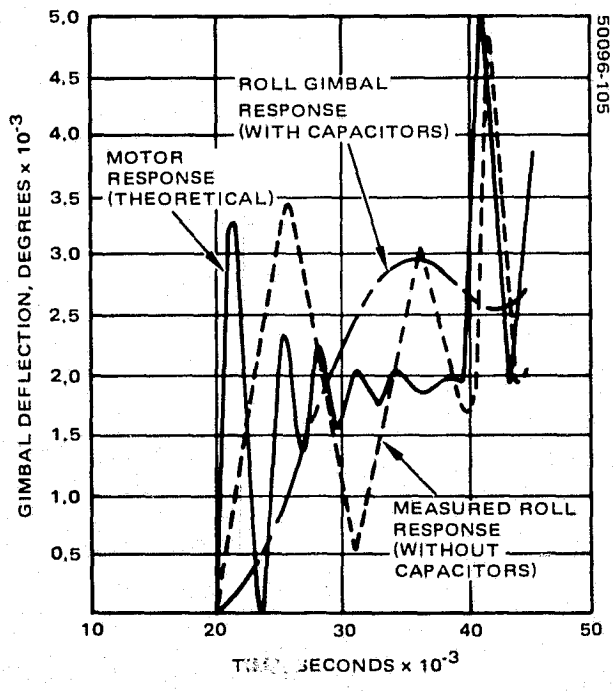

FIGURE 9-10. MEASURED AND THEORETICAL GIMBAL DYNAMICS

response, not shown, is larger. The reason for illustrating the roll gimbal characteristics rather than those of the elevation gimbal is that structural modifications to the latter were undertaken during the design phase to bring the performance of the elevation gimbal up to that of the roll gimbal. The results of the modifications are discussed in Section 9.6.

The third curve illustrated in Figure 9-10 is the response of the roll gimbals when large pulse shaping capacitors are placed across the windings. This curve represents approximately the worst case stepper disturbance, according to simulation results, that will allow the specified tracking error of 51 μrad to be met. It was hoped that, through simple means, such as pulse shaping and "beefing up" the elevation gimbal structure, the dynamic response of both gimbals could be improved to that indicated in the third curve.

9.4.5 Acquisition Logic

The acquisition procedure consists first of pointing the gimbal mirror to the direction of the target beam. Presumably the beam is already "flood lighting" the receiver, so that once the FOV of the detector is pointing in the right direction, acquisition can take place. The direction of the target must be known, in the telescope reference frame, to within the FOV of the telescope which is ±0.1°. The second step is to scan the center of the detector FOV in a raster scan throughout the ±0.1° acquisition field, as discussed in 9.4.1.

Once the detector is scanned across the target, the acquisition sequence is initiated. The logic sequence for this is illustrated in Figure 9-11. Initially, only the raster scan is enabled. All other logic variables are false. At time zero, beacon presence occurs as the raster scan brings the beam onto the detector. A few milliseconds later (relay pull-in time) the acquisition-hold relay locks up. A few milliseconds after this, in the example, the beacon presence vanishes momentarily (caused, for example, by atmospheric scintillation or any number of other reasons). The acquisition-hold relay does not fall out unless the interruption exceeds 15 ms.

The raster scan is disabled immediately (within microseconds) after beacon presence occurs. The track enable signal is delayed to allow the AGC loop to lock in, which is assumed to require 13 ms (for a 25 ms AGC time constant). The maximum scan amplitude prevails at conical scan enable and is held there for a certain period before decaying to the final scan amplitude over another period. (These two periods are somewhat arbitrary; 15 ms is adequate delay, but in the electronic implementation the total delay is 3 seconds.)

The stepper motor is inhibited for 45 ms after track-loop enable to allow most of the transient error associated with acquisition to be taken out before imposing the transient caused by the stepper. This last feature would only apply, of course, for the case of beacon acquisition outside the stepper threshold limits.

The case of beacon presence loss for greater than 15 ms is shown in the figure. All the variables under logical control are held for the full 15 ms. The AGC loop, which depends only on detector voltage and time, will open up within a few milliseconds.

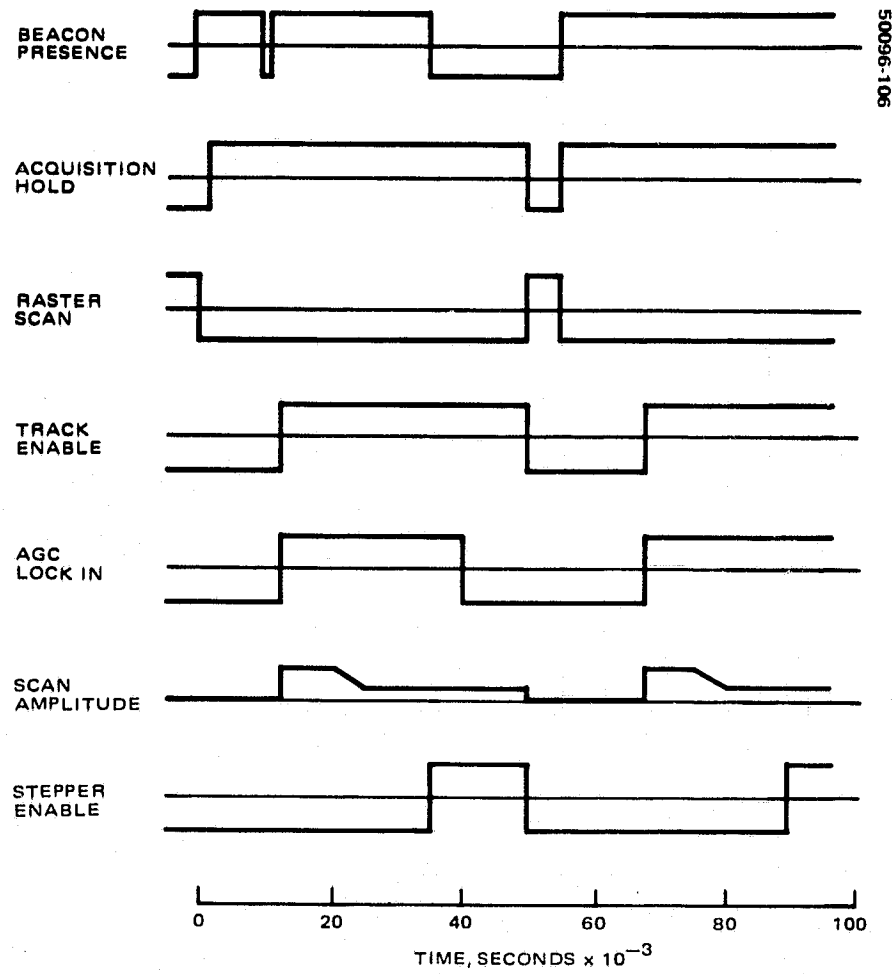

FIGURE 9-11. ACQUISITION LOGIC AND TIME SEQUENCE

9.4.6 Tracking Loop

The tracking loop consists of the error detector, bandpass filter, demodulator, shaping circuitry, IMC subsystem, and conical scan generator. A single-axis block diagram of the loop is given in Figure 9-12. A linearized servo diagram is also given in the figure. On the linearized model, the detector is represented by a scale factor, the bandpass filter by a first order lag, and the demodulator by a scale factor. The shaping network consists of a low pass filter, an integrator, and a lead term to cancel the phase shift caused by the lag terms. The IMC loop is represented by a scale factor and bandpass term. The linearized model was used for preliminary design, but the design was verified through a digital computer simulation of the entire two-axis system, including the acquisition raster scan.

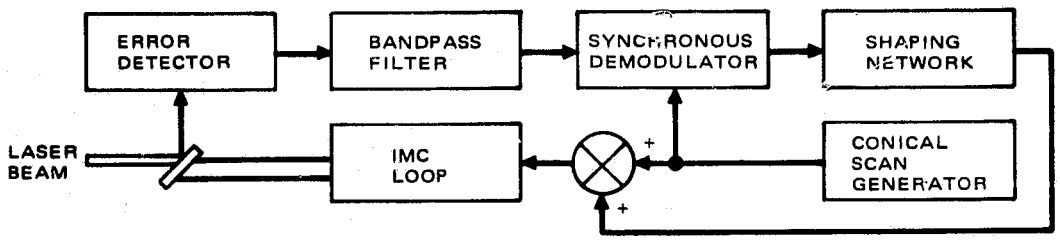

a) SINGLE AXIS BLOCK DIAGRAM

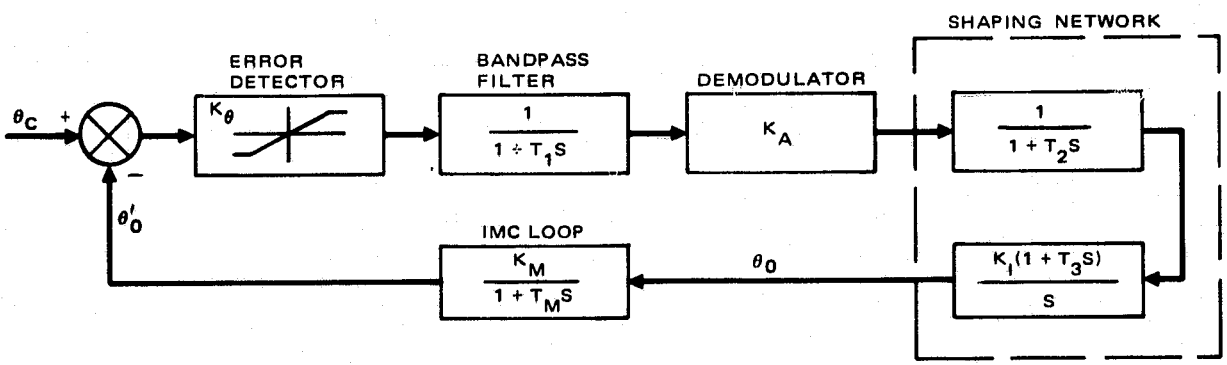

K_θ = 1500 V/deg
K_A = 0.63 Vdc/V_{ACP}
K_I = 150 V/V
K_M = 0.01 deg/V

T_1 = 2×10^{-4} sec
T_2 = 0.05 sec
T_3 = 0.01 sec
T_M = 4×10^{-4} sec

b) SERVO DIAGRAM

FIGURE 9-12. TRACKING LOOP DIAGRAMS

A log-magnitude/phase diagram (Bode plot) of the linearized model of the outer loop is given in Figure 9-13. The crossover frequency is approximately 60 Hz, which for the relative stability shown gives a closed loop bandwidth of approximately 50 Hz.

A time response for the case of acquiring a moving target is given in Figure 9-14. This response is taken from the overall computer simulation of the system as configured for the servo performance tests. The test configuration differs from the final operational system in that a direct detection rather than a 10.6 μm coherent sensor is used for these tests. For the servo system, the most significant difference which results is that the test configuration does not contain an AGC circuit. However, simulations of the coherent detection system, including the AGC feature, have shown that the system still acquires and tracks properly, providing that the AGC time constant is properly chosen.

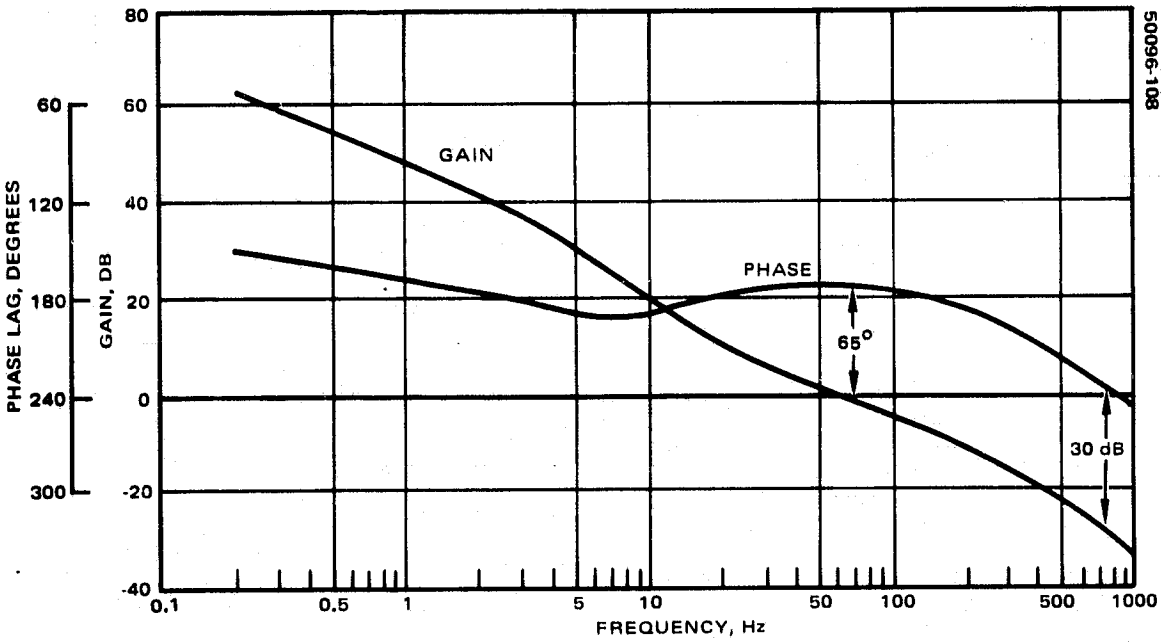

FIGURE 9-13. FINE TRACKING LOOP BODE PLOT

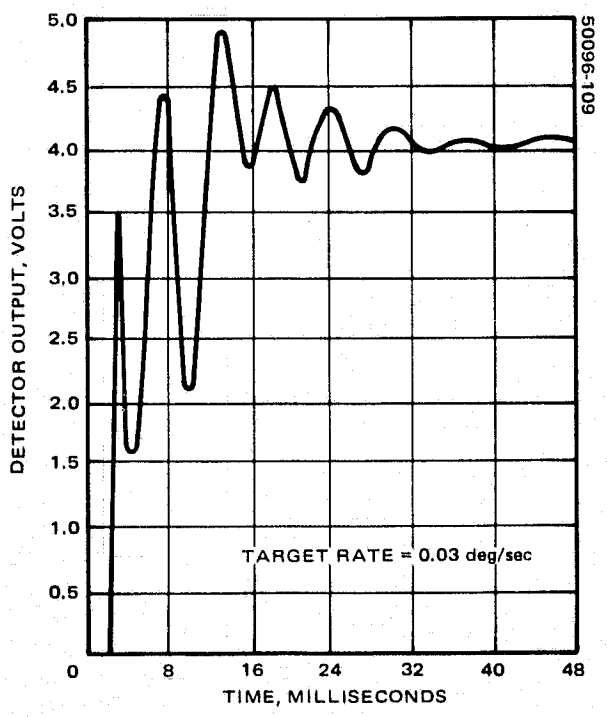

FIGURE 9-14. TIME RESPONSE FOR ACQUISITION OF MOVING TARGET

In the simulation response shown in Figure 9-14, the beam is swept across the detector at approximately 3 ms after the system is initialized. This means that the target was located on the first raster line in the upper left corner of the raster field (see Figure 9-2). (The reason for choosing this location of the target is to minimize simulation time.) The initial transient is caused by the IMC dynamics, which die out in a few milliseconds. The remainder of the transient results from the conical scan modulation of the error signal. For this particular run the outer loop gain was less than is shown for the Bode plot of Figure 9-13, which represents the design as implemented. Therefore, the simulated response shows more cycles of the conical scan than does the actual test configuration.

9.5 SERVO ELECTRONICS

9.5.1 General Description

A functional diagram of the overall electronics is given in Figure 9-15. The electronics are all housed in an electronics rack, except for the stepper motor and IMC electronics mounted in the opto-mechanical package. The rack electronics include the control panel chassis, the high voltage amplifier chassis, and the power supply chassis. A sketch of the rack layout is given in Figure 9-16.

Most of the servo electronics are located in the control panel chassis. In Figure 9-15 these are shown as individual functional blocks. These blocks are packaged as plug-in cards for mounting in the control panel chassis, except for the control panel electronics, which are mounted to the back of the panel. The layout of the plug-in cards is illustrated in Figure 9-17. Altogether there are 13 cards, 3 of which are common to both axes, with the other 10 cards comprising two essentially duplicate sets of electronics for the two separate axes. The three common cards are the error signal processor, the conical scan generator, and the raster scan generator, which are mounted in the middle section of the chassis as shown in Figure 9-17.

Referring again to Figure 9-15, the input to the error signal processor is the filtered video signal from the RF electronics, which are mounted in a separate electronics rack and are discussed in another report.* The received detector signal, which has the error information residing as phase modulation on a conical scan carrier, is passed through a bandpass filter to the demodulator. The received level is also compared against a threshold setting to determine if the laser beam is present. If the beam is present, an inhibit discrete is sent to the raster scan generator, which holds the generator output at its current state. Also, after a delay (to provide AGC lock in time in the RF electronics), the tracking loop is closed and the conical scan is turned on.

*T. Flattau, Infrared Wideband Receiver Backend, AIL Report No. A191-1, April 1974.

If the beam is temporarily lost, the dropout delay in the error signal processor prevents the raster acquisition from resetting until a fixed time has elapsed (currently set at 15 ms). This feature presents premature loss of acquisition due to electrical transients or atmospheric effects.

The conical scan generator includes an amplitude change feature so that, if required due to a low S/N, the conical scan amplitude can be greater during acquisition than during track. The amplitude is reduced by an amplitude factor, which can be set by a pot, after a fixed time which also can be set. The amplitude change occurs as an exponential delay from the higher level to the lower.

The raster hold feature in the raster scan is inhibited in the manual mode by a discrete from the manual/auto select switch on the control panel. The output of the raster scan generator is also inhibited in the manual mode.

The functions of the demodulator/summer card and shaping/threshold detection card are to implement the IMC loop, providing a summing junction for the outer fine track loop and threshold detection for closure of the stepper motor loop. The stepper motor loop is inhibited from closing until a fixed time has elapsed after acquisition of the beam. This prevents the stepper motor from disturbing the beam until after the track loop has settled.

The function of the auto/manual motor gating card is to provide for both automatic and manual control of the stepper motors. Inputs from the fine track loop threshold circuit are inhibited during manual operation, and, similarly, inputs from the manual control logic are gated out when in the auto mode. To protect the gimbals against being driven hard against a mechanical stop, electrical stops are provided during both manual and auto modes. When the gimbal angle exceeds a set maximum in either direction, as indicated by the gimbal readout potentiometer, the inputs to the driver logic are inhibited.

The function of the driver logic, of course, is to transform individual pulses from the gating circuitry into the three-phase pulses necessary to drive the stepper motor. There is one further inhibiting feature on stepper motor operation. To allow the motors themselves to be disabled while all the drive logic functions normally, an enable-disable switch is placed on the front panel. The purpose of this switch is to allow operation in the auto mode without energizing the steppers.

Also, for synchronizing the counters, a photo-sensor circuit in the opto-mechanical package produces a discrete signal when the gimbal is in the zero position. This signal is displayed as a boresight indicator on the control panel. The five-digit counter also counts the pulses to the motor and should therefore display a zero count when the boresight light is on. If, for any reason, the motor loses synchronism with the counter, the problem can be corrected by initializing the counter logic when the boresight light is on.

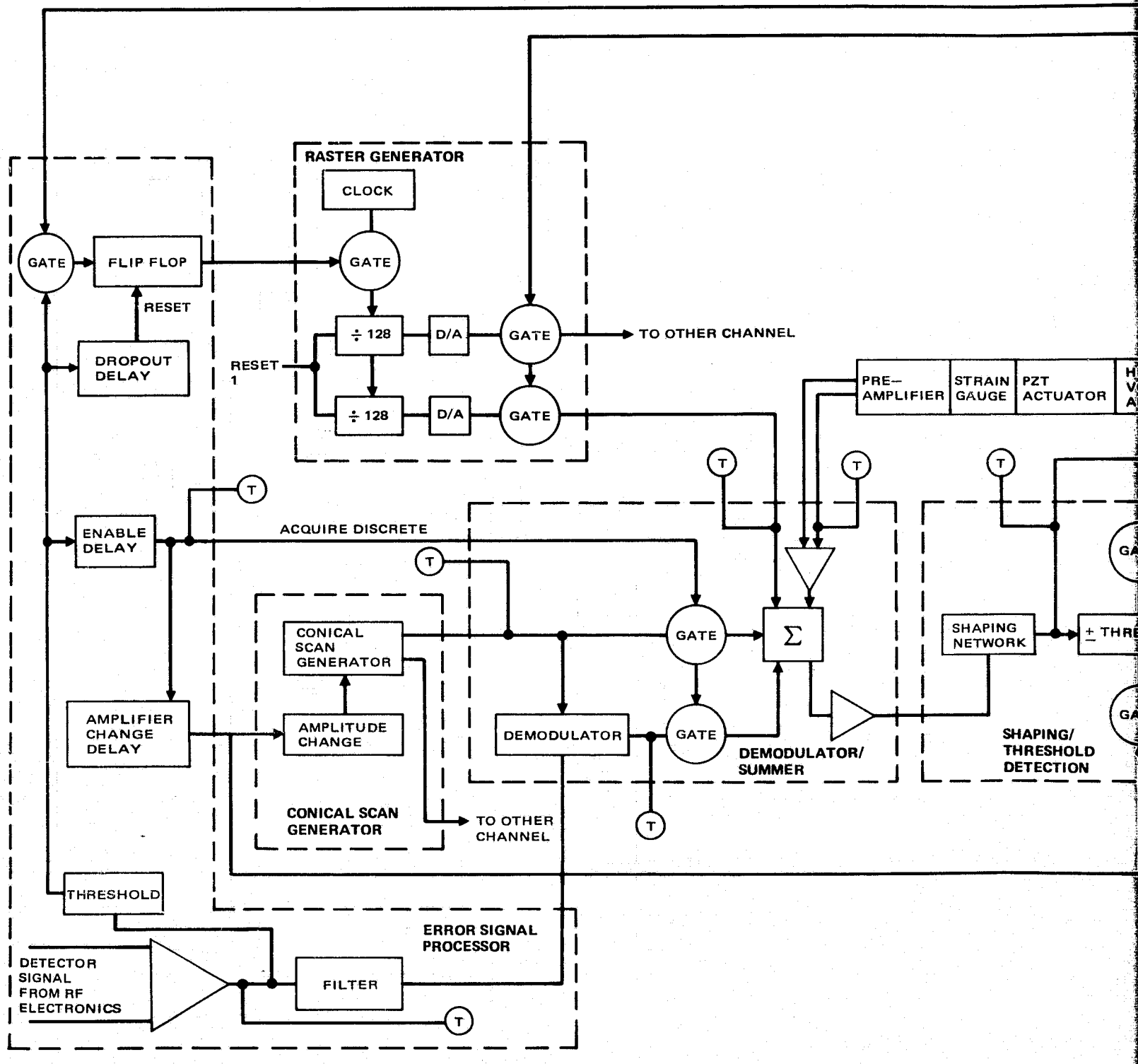

FIGURE 9-15. OVERALL SYSTEM SINGLE-AXIS BLOCK DIAGRAM

FOLDOUT FRAME

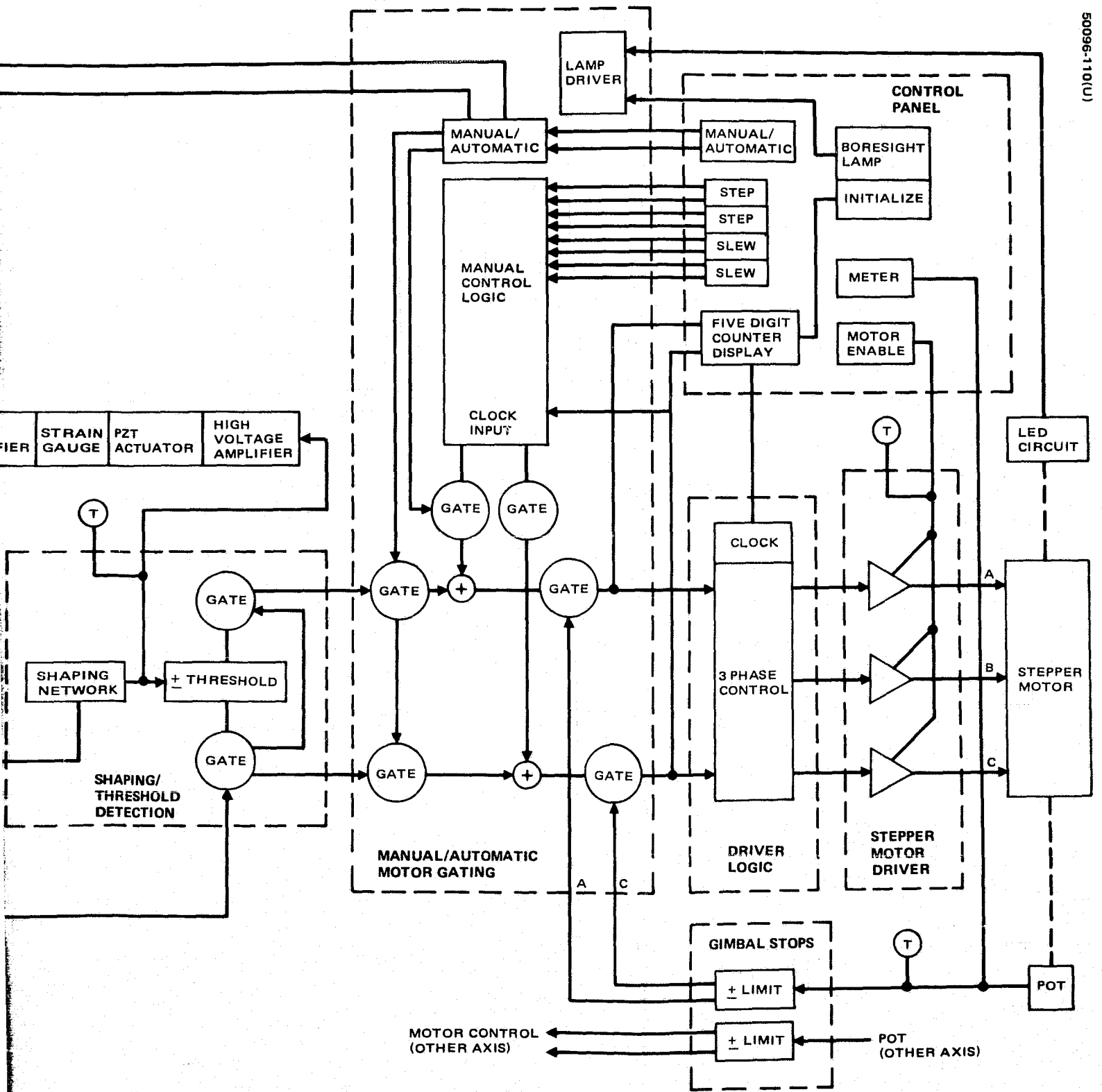

FOLDOUT FRAME

2

Two operating modes are provided for the motor: a step mode and a slew mode. The slew mode provides a constant string of pulses at a fixed rate of 50 steps/sec. The step mode provides for single-stepping the motor. The latter mode is used for fine placement of the gimbals, whereas the former is used for fast slewing from one position to another. The slew mode is used during auto operation.

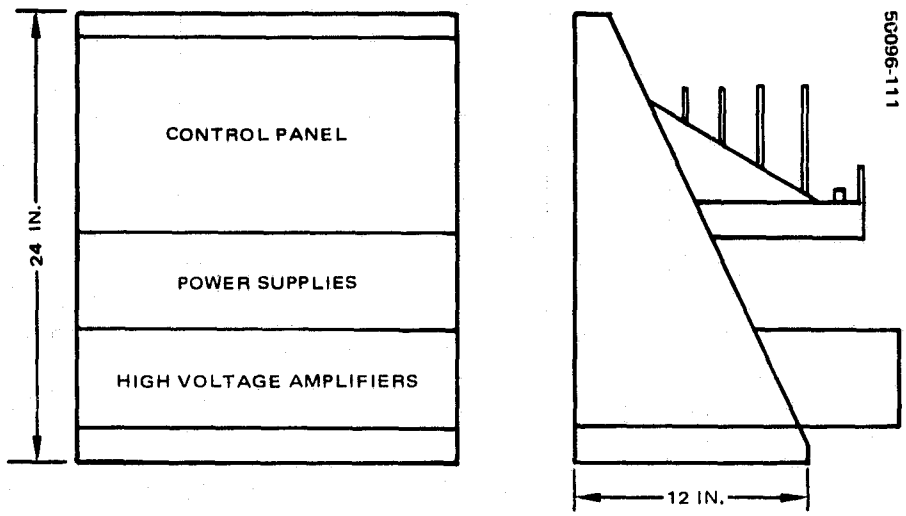

FIGURE 9-16. RACK LAYOUT OF ELECTRONIC PANELS

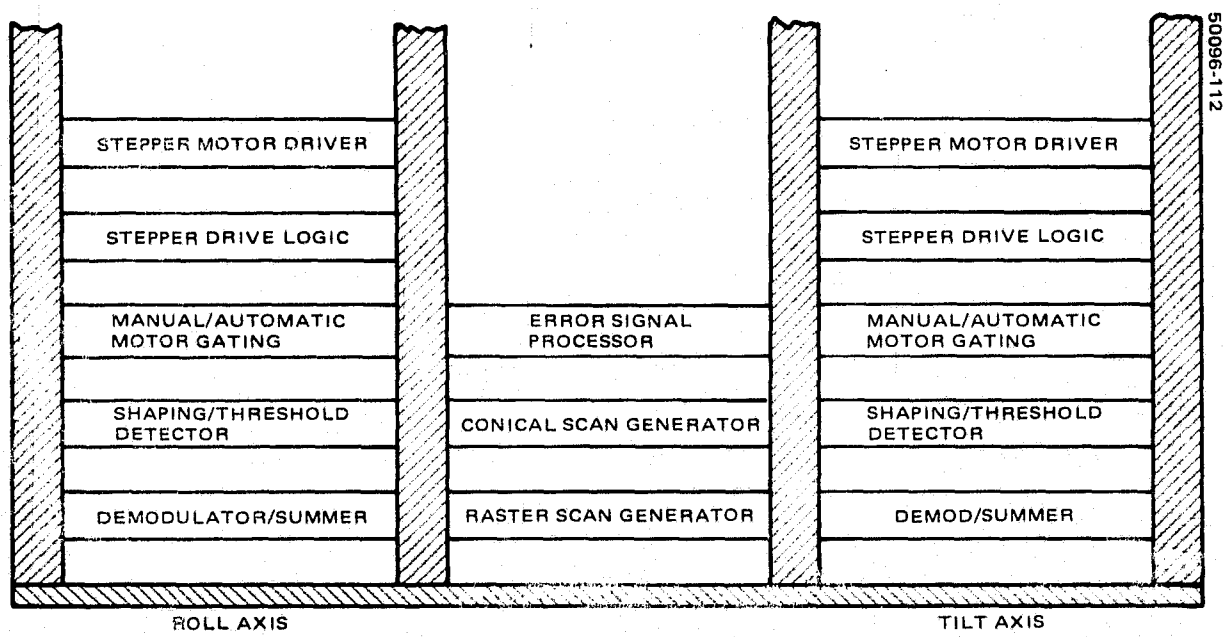

TOP VIEW, FRONT PANEL

FIGURE 9-17. CHASSIS LAYOUT OF PLUG-IN CARD MODULES

9.5.2 Controls and Displays

A picture of the control panel is shown in Figure 9-18. Except for the manual/auto and stepper disable switches, which are common to both axes, the controls and displays are located in two duplicate groups for the two axes. The analog gimbal display for the tilt axis has been placed horizontal, since in the normal orientation for laboratory tests a tilt gimbal movement produces a horizontal beam deflection. A test point access matrix is also provided on the panel.

Most of the controls have been alluded to or discussed in detail in the previous section. However, for convenience, the functions of all the controls and displays are described briefly as follows:

Manual/Auto Switch - Provides selection between manual and automatic modes. In the manual mode, the fine track and raster scan search functions are disabled. The gimbals can be manually driven to any point in their range, provided the stepper motor enable switch is on. In the automatic mode, the manual control function is disabled, and the raster search is automatically initiated at any time the beam presence discrete bit is not on.

Enable/Disable Switch - Enables or disables the stepper motors. The other controls work normally when the motors are disabled.

Boresight Switch - Lights when the gimbal is at its null position. When pushed, this switch resets the counter for that axis to a count of 5000, which corresponds to zero gimbal angle.

Digital Display - Displays a five-digit number from which the gimbal angle can be precisely determined. A count of 5000 corresponds to 0°, and an increment of one count represents a 0.002° apparent movement of the laser beam in target space. Thus, the range of 0 to 10,000 counts covers the gimbal range of ±10°. The digital display must be boresighted by pushing the boresight switch when that switch is lighted.

Analog Gimbal Angle Display - Displays the gimbal angle position as indicated by a potentiometer readout voltage.

Step Control - Single-steps the stepper motor each time the switch is pushed. If the motor is disabled, the counter will still operate giving an erroneous display of gimbal movement. This switch operates only when the manual/auto switch is set on manual.

Slew Control - Steps the motor at a constant rate of 50 steps/sec when the manual/auto switch is set on manual. Same comments as above apply to the case of slewing with motor disabled.

Test Point Matrix - Provides access to 36 selected test points within the electronics. Most of these points are identified on the diagram in Figure 9-15. A complete definition of the points is given in Table 9-2.

TABLE 9-2. ASSIGNMENT OF TEST POINTS

	1	2	3	4	5	6	7	8	9
A	Tilt motor current	+15V	Tilt potentiometer voltage	Ground	Tilt HV amplifier input	Detect error signal	Ground	Tilt conical scan output	Unused
B	Roll motor current	−15V	Roll potentiometer voltage	Ground	Roll HV amplifier input	Tilt raster	Ground	Roll conical scan output	Unused
C		+5V	Tilt IMC preamplifier output	Ground	Tilt demodulator output	Roll raster	Ground	Unused	Unused
D		Ground	Roll IMC preamplifier output	Ground	Roll demodulator output	Beam presence discrete	Ground	Unused	Unused

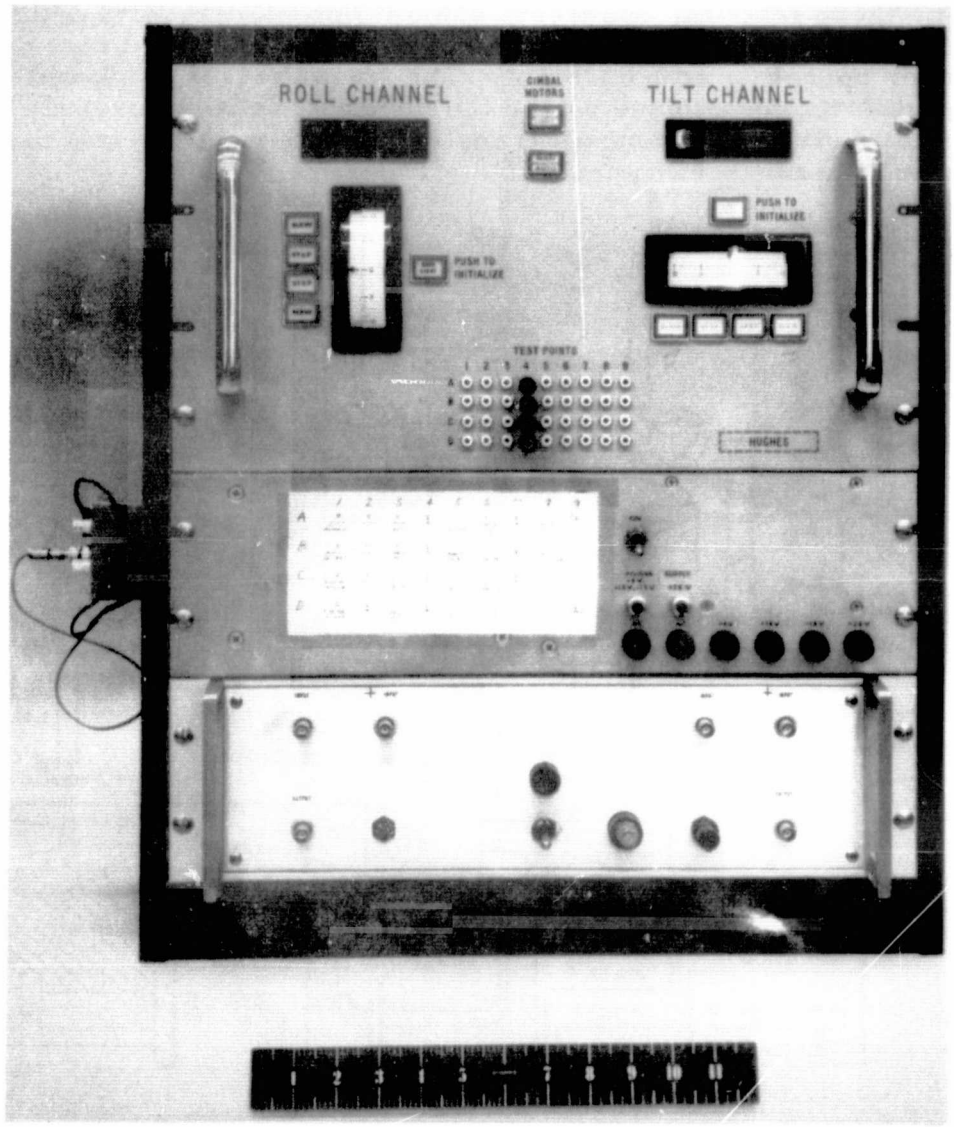

FIGURE 9-18. SERVO SYSTEM CONTROL PANEL (PHOTO 74-31679)

9.6 SYSTEM TESTS

9.6.1 Test Setup

A sketch of the test setup is shown in Figure 9-19. The opto-mechanical assembly is mounted to the top of a precision rotary table which is free to rotate within constraints about the vertical axis. The rotation angle about the vertical is continuously displayed as a seven-digit number, which gives a read-out resolution of 0.0001°. A signal proportional to the rate about the vertical axis is also available for recording. The other axis is adjustable by hand, but no readout is available. The rotary table, which has a massive base, is placed on the laboratory floor. The input reference beam is produced by a laser, and a 20 inch collimator is mounted on a granite table.

For these tests the coherent 10.6 μm optical detector, which will be used in the final integrated configuration, is replaced by a direct detection photo sensor operating at 0.6328 μm. The photo sensor is placed behind a pin hole located in the focal plane where the coherent sensor normally is placed. The pinhole is sized to produce a transfer curve similar to that produced by the coherent system (see Figure 9-7).

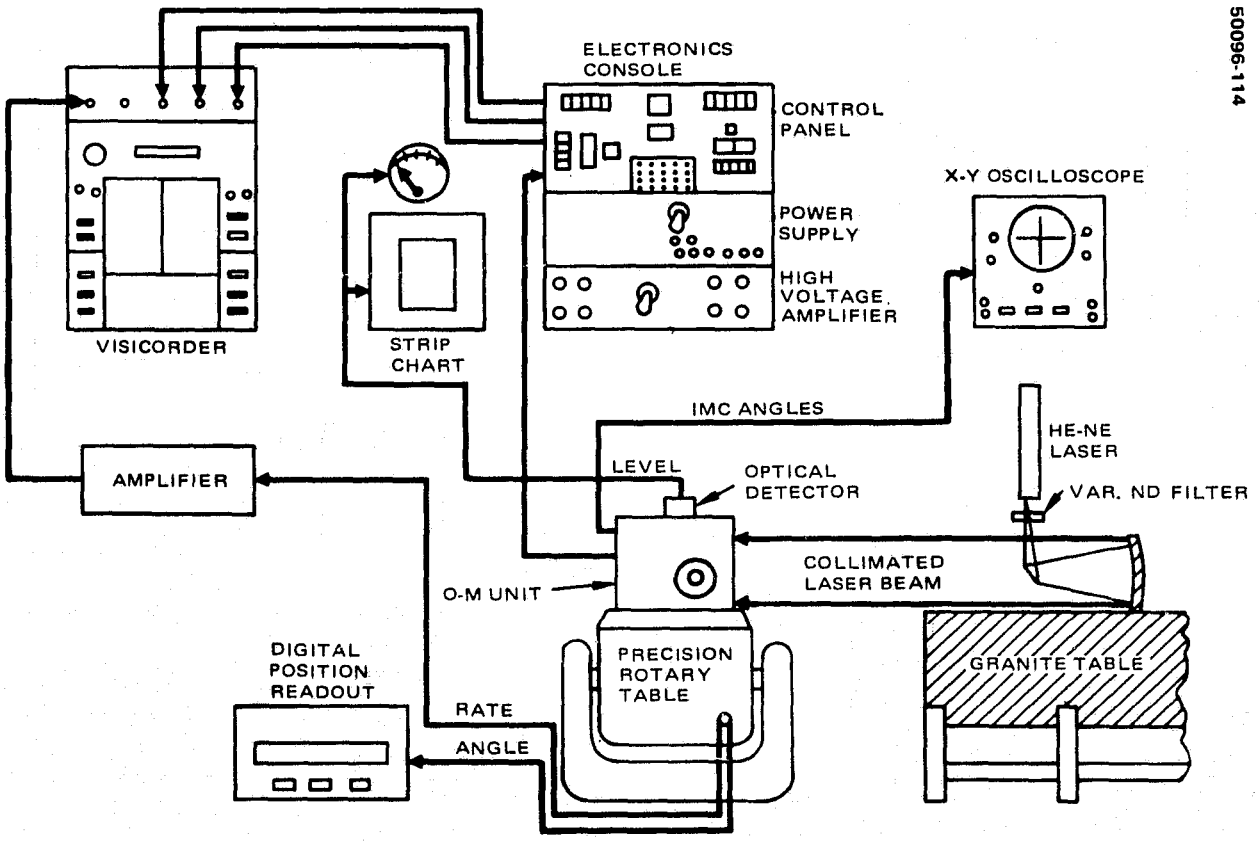

FIGURE 9-19. TEST SETUP

The output of the optical detector, in addition to being used in the electronics, is also under continuous monitor on a level meter and a strip chart recorder. The IMC angles are also continuously monitored during the tests. By applying the tilt and roll IMC angles to the respective axes of an X-Y oscilloscope display, the acquisition sequence of raster scan, large conical scan, reduced conical scan, and final track are more easily visualized as a two-axis phenomenon than would be the case of monitoring the individual signals as functions of time.

Most signals of interest for monitoring or recording during the tests are available at the test point access matrix on the front control panel. (Table 9-2 lists the available signals.) The exceptions, of course, include the rotary table signals.

9.6.2 Fine Loop Tracking Performance

The test results are summarized below for each of the major elements contributing to tracking error.

Error Transfer Characteristics

The measured transfer characteristic of the error detector is given in Figure 9-20. The beam is not symmetrically shaped for large excursions each side of zero. The half-power point is approximately 65 μrad for movement in one direction, but is only 50 μrad for movement in the other direction. This means a large circular (conical) scan will produce a sinusoidally varying detector output, whereas a symmetrical characteristic would produce a constant detector output for all conical scan amplitudes. The characteristics shown in Figure 9-20 are for movement along a single axis. The transfer characteristic for movement along the orthogonal axis is similar. The operating point for the loop (scan amplitude) is marked on the curve.

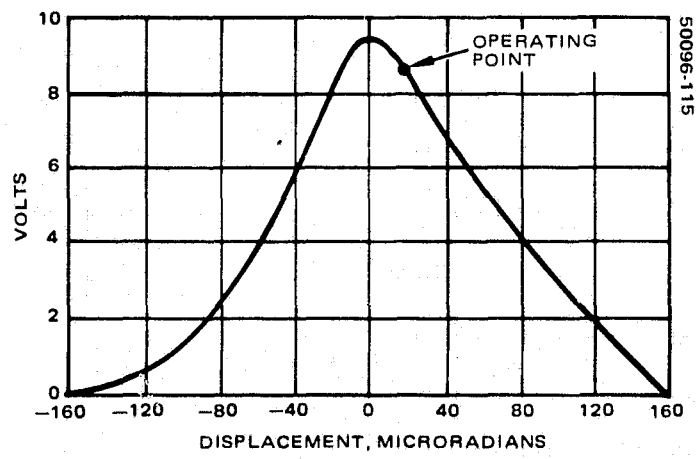

FIGURE 9-20. DIRECT DETECTOR TRANSFER CHARACTERISTICS

Tracking Error Under Static Conditions

A sketch of the detector output voltage under steady state tracking conditions is given in Figure 9-21. The fluctuations in this signal are caused by noise in the IMC drive loop, amplitude fluctuations in the laser beam, mechanical vibration of the structures, and electrical noise generated in the sensor. The sum of all these factors generates an rms error amplitude of approximately 7 μrad.

How much of this error is attributable to the tracking loop is not clear, since it is not possible to separate the various contributions at the subarcsecond level without use of elaborate metrological instrumentation. Certainly it is reasonable to assume that most of this measured noise comes from the control loop, either from the outer loop or from the IMC loop. The noise in the outer loop as measured at the output of the integrator is shown in Figure 9-22. This signal consists of a 60 Hz component equivalent to 1.3 μrad peak plus a noise component of 1.2 μrad rms, for a total rms amplitude of 2.13 μrad equivalent. The only way to measure the true contribution of the IMC loop would be to set up separate instrumentation for the purpose, which has not been done for

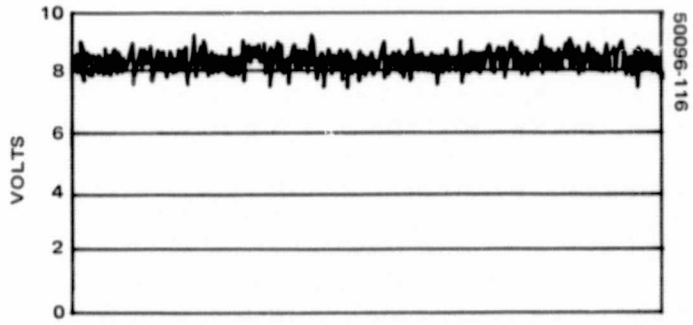

FIGURE 9-21. DETECTOR NOISE LEVEL UNDER STATIC CONDITIONS

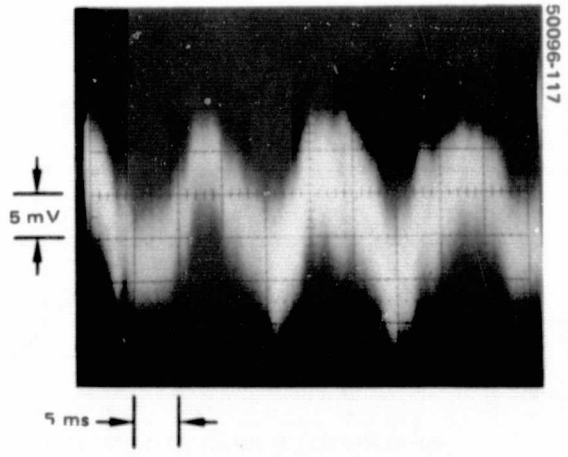

FIGURE 9-22. NOISE AT INPUT TO IMC LOOP (5 mV ≅ 1 μ rad)

these tests. Therefore, it is assumed that all observed amplitude fluctuations come from the control loop.

Tracking Error Produced by Stepper

The detector output voltage during a particular tilt stepper sequence is illustrated in Figure 9-23. The individual steps, which occur at 20 ms intervals, as well as the ringing between steps are visible in the picture. The horizontal line represents the zero level. A typical minimum voltage caused by stepper operation is 6 volts, corresponding to approximately 55 μrad on the transfer characteristic shown in Figure 9-20. The normal scan amplitude of 17 μrad added to the discrete 35 μrad step produces an excursion of 52 μrad under the best conditions. Therefore, the typical disturbance for this axis, which produces a 4 dB loss in power, is not much worse than the best case.

For the worst case, however, the power level drops considerably below the 6 volt level and can go as low as 3.5 volts. Fortunately, the worst cases are not that common. Analysis of a long run (several hundred steps) of the type of data shown in Figure 9-23 shows that only 1.3 percent of the steps causes the detector voltage to drop below 4 volts, while 2.8 and 5.3 percent of the steps cause drops below 5 and 6 volts, respectively.

In terms of decibel loss, the stepper produced disturbances are not that severe for the characteristic used in the tests and shown in Figure 9-20. A 4 volt minimum on a given step represents only a 3.76 dB total power loss, which would be acceptable. However, the problem arises from the fact that this great a power loss represents approximately a 70 μrad excursion. This large an angle transposed to the expected coherent detection curve will produce an unacceptable power loss of 20 dB for the communication channel. Therefore, either these largest stepper disturbances will have to be eliminated through modification of the design, or interruption of communications must be expected and accepted a small percentage of the time.

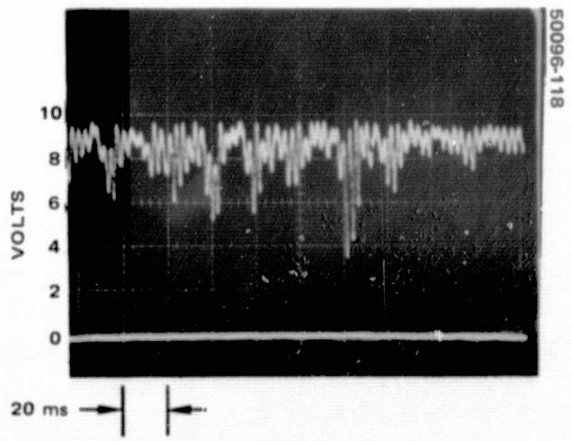

FIGURE 9-23. EFFECT OF STEPPER DISTURBANCE ON DETECTOR VOLTAGE

Tracking Error With Target Motion

Target motions up to 0.03 deg/sec produce errors no greater than 3.5 μrad. Such a small error is hardly discernible on the detector output voltage for the detector used in the tests. For the coherent detector this error will be more noticeable but still negligible compared to stepper produced disturbance.

9.6.3 Summary of Performance Data

Performance test data are summarized in Table 9-3. The design objectives are also given for comparison. The most critical elements are the tracking parameters which have already been discussed in detail. Some of the other parameters have been measured and reported on previously (see Section 3), and the data from that section are included in Table 9-3. These data include the IMC FOV and gimbal range, for example.

TABLE 9-3. PERFORMANCE DATA SUMMARY

Unit/Parameter	Design Objective	Measured Performance
TRACKING LOOP		
Static tracking error (NEA), μrad	5	7
Tracking error caused by 0.03 deg/sec target motion, μrad	3.5	3.5
Peak tracking error with stepper disturbance, μrad	50	70
Tracking loop bandwidth, Hz	50	>50
Acquisition FOV, deg	0.2 x 0.2	0.2 x 0.2
Maximum target velocity for acquisition, deg/sec	0.1	>0.1
GIMBAL LOOP		
Gimbal tilt, deg	±10	±10
Range tilt, deg	±10	±10
Gimbal X-axis, deg/sec	0.1	0.1
Step rate Y-axis, deg/sec	0.1	0.1
Gimbal readout accuracy, deg	0.02	0.002 (resolution)
Gimbal IMC alignment, deg	<1	0.017
Gimbal dynamic cross coupling, μrad	35	<35
IMC LOOP		
IMC noise level, μrad	<5	7
Pointing accuracy μrad	5	7
IMC bandwidth	>400	405

It should be noted that the values labeled "design objectives" are just that, objectives, rather than hard and fast requirements. The design objective of 0.002° for the gimbal readout accuracy, for example, was adopted simply because the required resolution through step counting was available, not because of an inherent requirement for that kind of accuracy. Similarly, the objective of target acquisition at 0.1 deg/sec is not a realistic requirement for the synchronous orbit for which the receiver is designed, but may be required for other missions using the same acquisition approach.

In summary, the test results show that the design objectives generally have been met. The notable exception is the stepper produced tracking error. This was known to be a problem area before the tests were performed, and several minor improvements had already been incorporated as discussed in Section 5. To completely fix the stepper problem requires that the gear train be redesigned to produce a smaller step, and that the step rate be increased to compensate for the smaller step. Since the steppers are operating at speeds well below their maximum, this approach should be straightforward.

APPENDIX A. GTE TYPE PBM-8G OPTICAL BEAM STEERING ELEMENT

This appendix contains design and performance information of the beam steering elements used in the OM subsystem. The outline and mounting of the element, as modified for Hughes, is shown in Figure A-1, GTE Drawing 842-700-001. The mirror shown on the unit in Figure A-1 is the standard 1 x 0.7 inch glass mirror. The optical design requires a slightly larger mirror size, approximately 1 x 1.3 inches. Beryllium mirror elements have been fabricated for the units that will go into the OM subsystem.

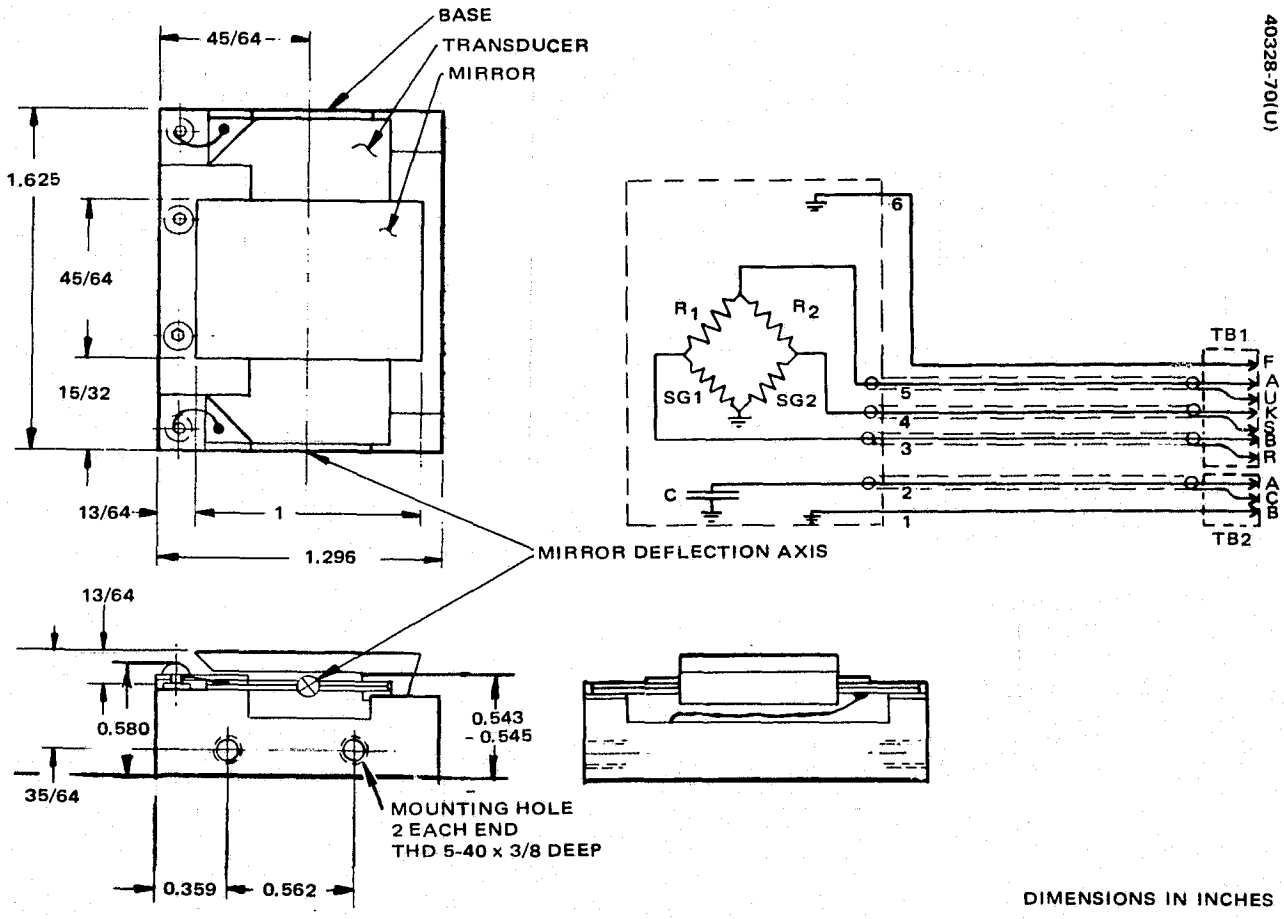

FIGURE A-1. MOUNTING DIMENSIONS PBM-8G BEAM STEERER

Measured static performance data of units 005, 006, 007, and 008 are shown in Table A-1. The linearity, amplitude, and phase characteristics are shown in Figure A-2.

Environmental Test Specifications for the beam steering element are given in Table A-2 and Figure A-3.

TABLE A-1. MEASURED PERFORMANCE VALUES, MODEL PBM-8 BEAM DEFLECTORS

S/N	Deflection Angle, arcmin	Deflection Voltage, V	Strain Gage Resistance, ohms		Resonant Frequency (with mirror)
			No. 1	No. 2	
005	23.5	500	49.68	48.84	1155
006	22.2	500	50.86	48.93	1156
007	22.6	500	48.13	48.32	1148
008	24.1	500	51.08	53.38	1136

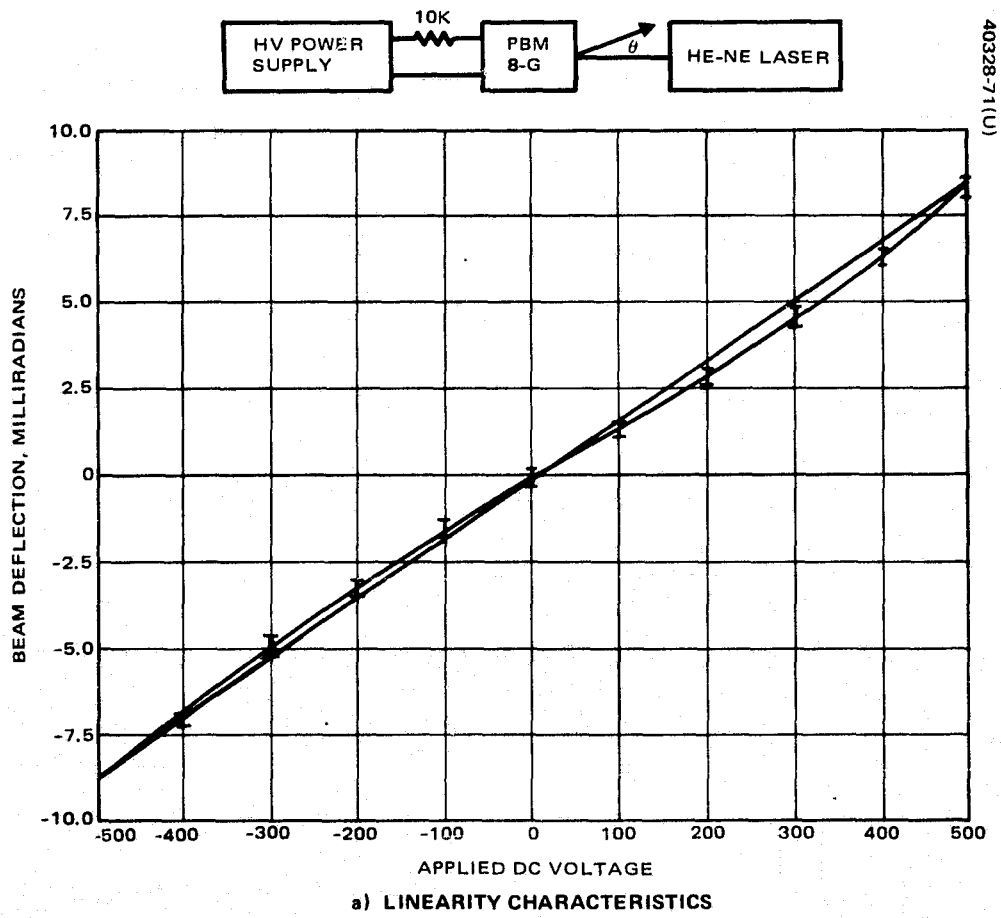

a) LINEARITY CHARACTERISTICS

FIGURE A-2. PBM-8G BEAM STEERER NO. 006

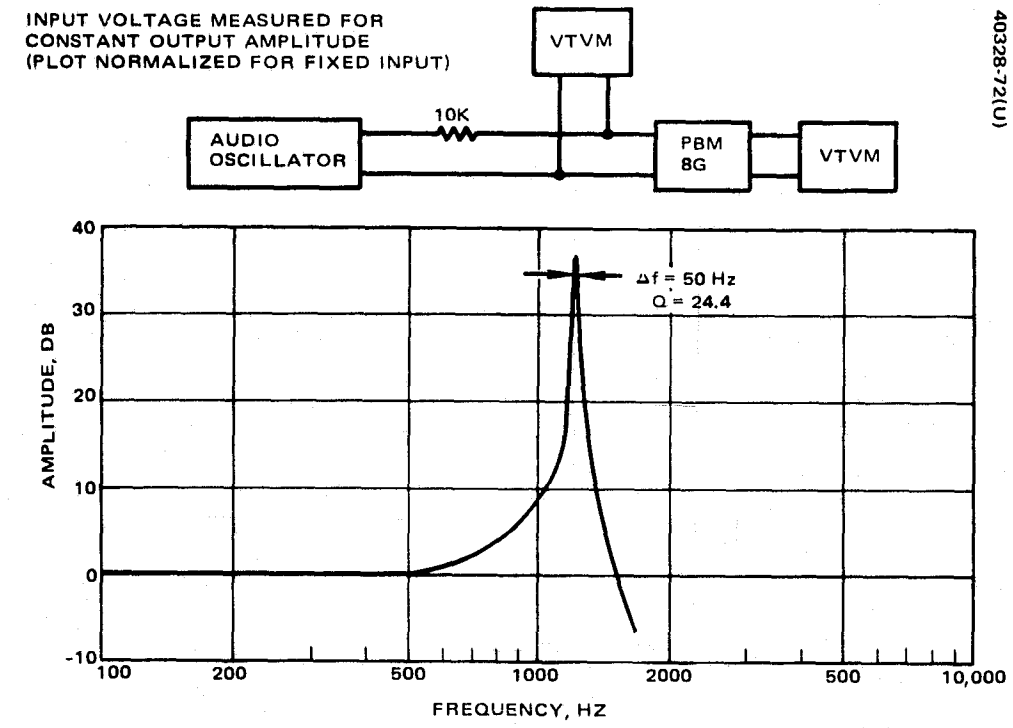

b) AMPLITUDE CHARACTERISTICS

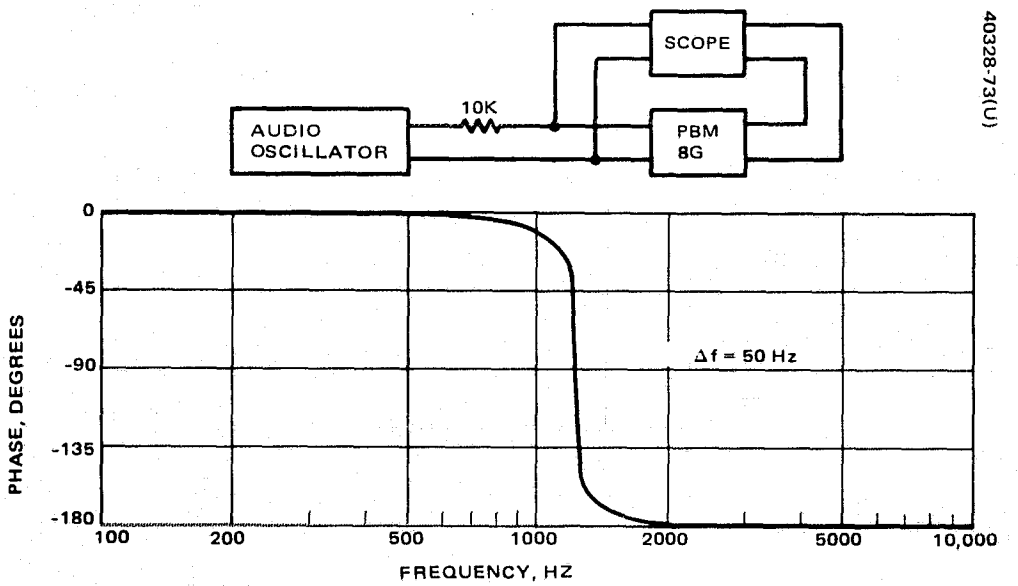

c) PHASE CHARACTERISTICS

FIGURE A-2 (CONTINUED). PBM-8G BEAM STEERER NO. 006

TABLE A-2. ENVIRONMENTAL TEST SPECIFICATIONS FOR MODEL PBM-8G OPTICAL BEAM DEFLECTOR

VIBRATION (ALL THREE AXES)

Random

Broadband random

Flat 20 to 80 Hz at 0.05 g^2/Hz
Rolloff below 125 Hz at 5.5 dB/octave
Flat 125 to 560 Hz at 0.1 g^2/Hz
Rolloff above 560 Hz at 3.5 dB/octave
Flat 1000 to 2000 Hz at 0.05 g^2/Hz
Overall: 12.7 g (rms)

Narrowband sweep – 0.25 g^2/Hz narrowband sweep between 180 and 2000 Hz with overall value of 3.53 g (rms) and an equivalent bandwidth of 50 Hz.

Sinusoidal

Frequency Range, Hz	Amplitude
5 to 18	0.5 in. (peak-to-peak)
18 to 22	5.0 g (0 to peak)
22 to 400	5.0 g (0 to peak)
400 to 2000	7.5 g (0 to peak)

ACCELERATION

8 g - all three axes

PRESSURE

Atmospheric to 10^{-9} Torr

SHOCK

All three axes – 20 g for 11 ms

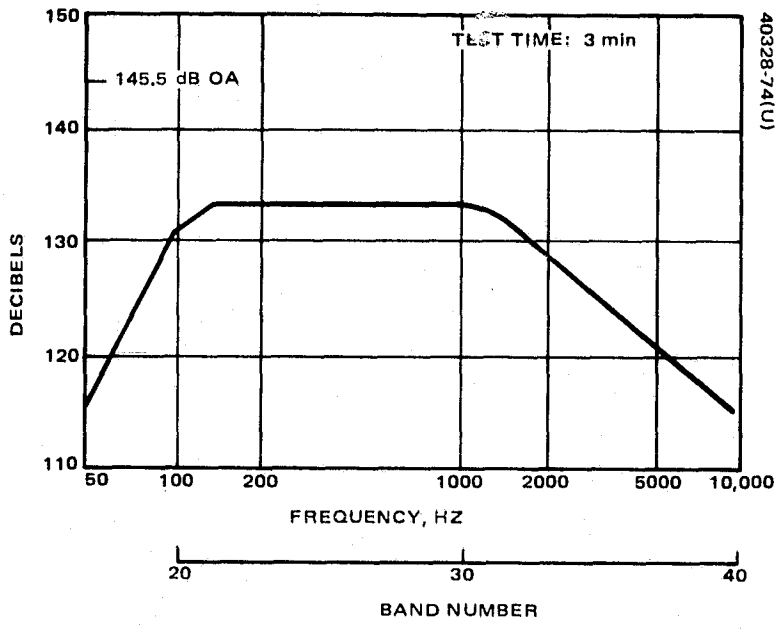

FIGURE A-3. ENVIRONMENTAL TEST SPECIFICATION FOR MODEL PBM-8G OPTICAL BEAM DETECTOR, ACOUSTICAL VIBRATION SPECTRUM

APPENDIX B. SPERRY RAND 250 WATT GALLIUM ARSENIDE ILLUMINATOR BEACON

This appendix contains design information related to the Sperry Rand gallium arsenide beacon which was used as a model in the OM subsystem design. Figure B-1 shows the outer mechanical dimensions of the optical head. This optical head is connected electrically to the modulator, a 1 x 1/2 inch electrical assembly shown in Figure B-2. The modulator substrate is mounted in contact with a suitable heat sink.

Tentative performance specifications are given in Table B-1.

The performance of the gallium arsenide 0.26° beacon in the system is dependent upon the illumination pattern of the 0.017 inch source. Since the optical system images this pattern at the far field of the optical system, it is important that the pattern characteristics be known precisely.

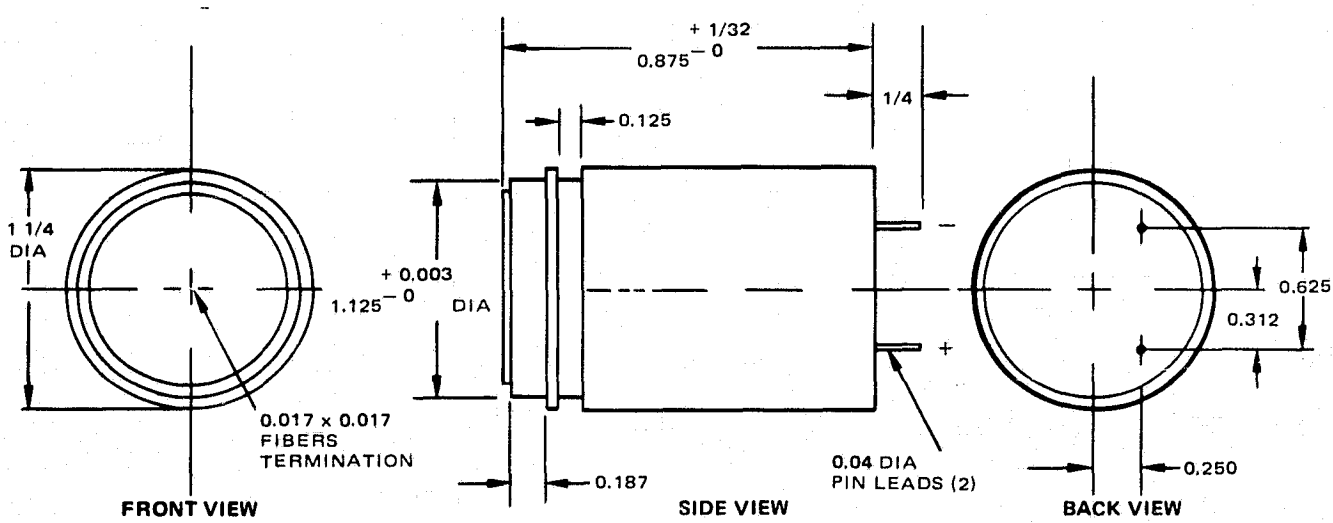

FIGURE B-1. GALLIUM ARSENIDE 250 W FIBER ARRAY ASSEMBLY

TABLE B-1. 250 WATT PEAK POWER GaAs ARRAY SPECIFICATION

ELECTRICAL
Peak power – 250 W/min
Repetition rate – 5 kHz ±5%
Input drive pulse width – 100 +0 ns, -20 ns
Peak pulse drive current – 75 A maximum
OPTICAL
Source Area – 0.017 x 0.017 in. consisting of 17 0.001 x 0.017 in. fiber ribbon optics coupled individually to 17 GaAs laser diodes, bundled to provide the source area aperture.
PHYSICAL SIZE
See drawing 4228-SKTP900

Note: All specifications apply at ambient temperature of 80 ±5°F.

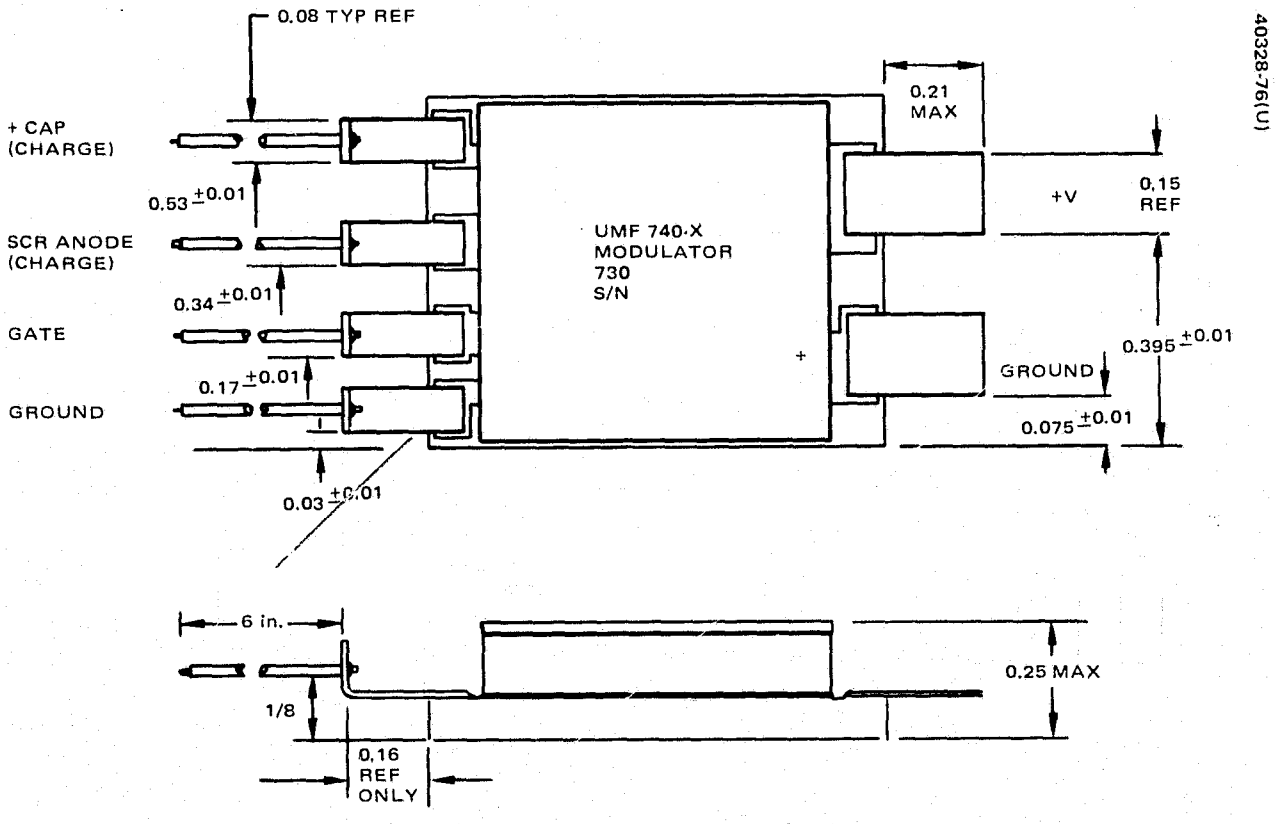

FIGURE B-2. MODULATOR ASSEMBLY

B.1 TEST SPECIFICATION FOR IR MODULATOR

All modulator part numbers 4283-00740-4 through 6 are tested using the following test equipment and procedure:

Test fixture 2448-79200
Test fixture 2448-79201 - Charger driver
Power supply high voltage - NJE Model S-325
Power supply low voltage - KEPCO Mod ABC 30-0.3 or equivalent
Pulse generator - Data Pulse Inc. Mod 101
Digital multimeter - Fluke Mod 8000A
Oscilloscope - Tektronix Inc. Type - 585 Type 82 plug in

The modulator is carefully placed in test fixture 2448-79200 paying close attention to the handling of the leads while connecting them to their proper terminals. Secure the clamp with enough pressure to just hold the modulator. See Figure B-3. Then tighten down on the two 2-56 Allen head screws connecting the 1 ohm load to the modulator.

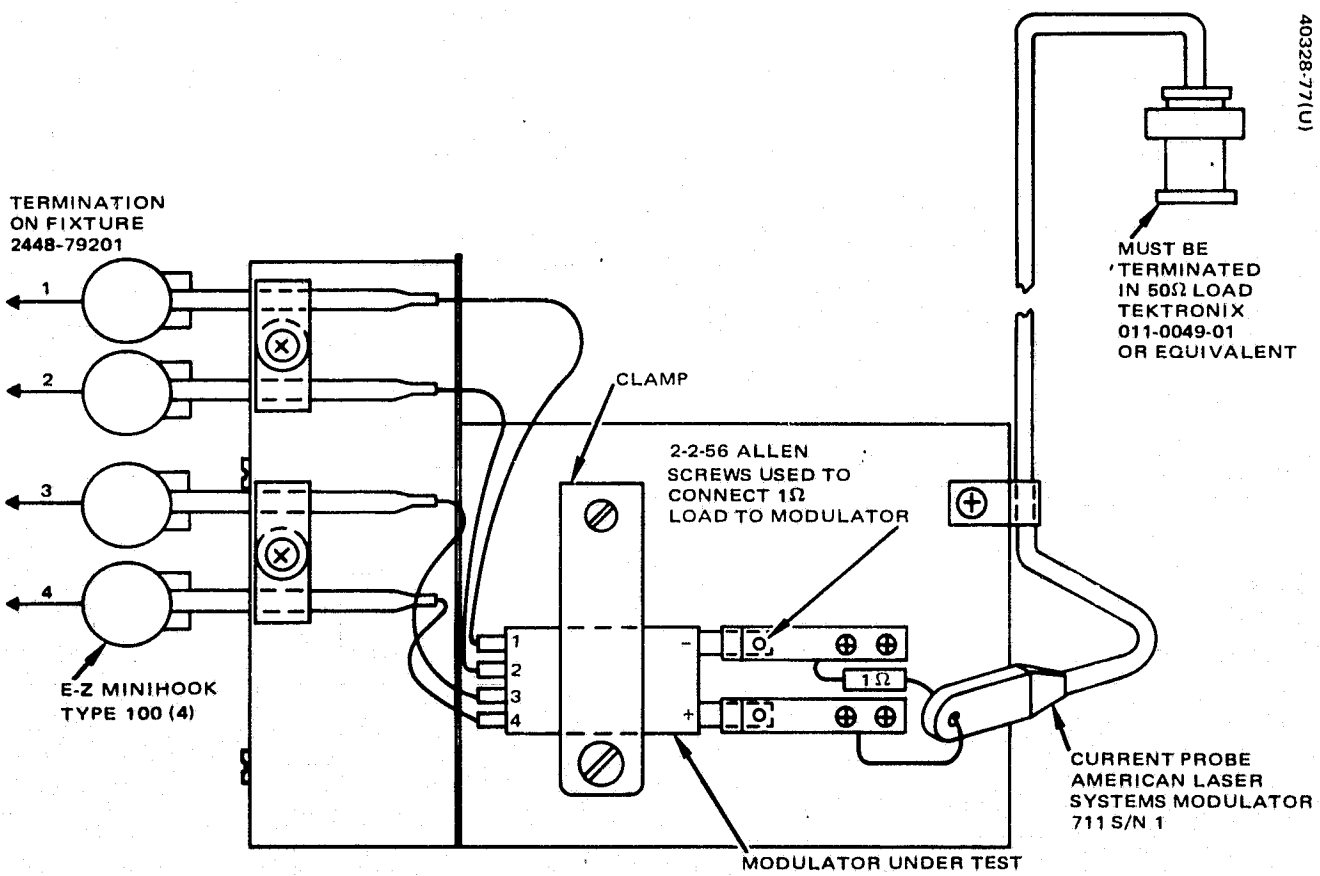

FIGURE B-3. TEST FIXTURE – HOLDING

Set the pulse generator as follows:

Repetition rate = 5 kHz ±5%
Pulse width = 300 to 500 ns
Pulse amp = +5 ±0.1 V

Connect the positive output to fixture 2448-79201 and also to the external sync terminal on oscilloscope type 585.

Check that the low voltage and the high voltage supplies are correctly connected to fixture 2448-79201 as per Figure B-4 and Figure B-5.

Connect the current probe which is part of fixture 2448-79200 and its 50 ohm termination to channel A of type 82 plug in amplifier of Tektronix oscilloscope type 585. Set the controls as follows:

Sync pulse = external ac
Sweep = 50 ns/cm
Amplitude = 20 V/cm
Polarity = positive

Input = dc
Channel selector = A only
Sync pulse polarity = positive

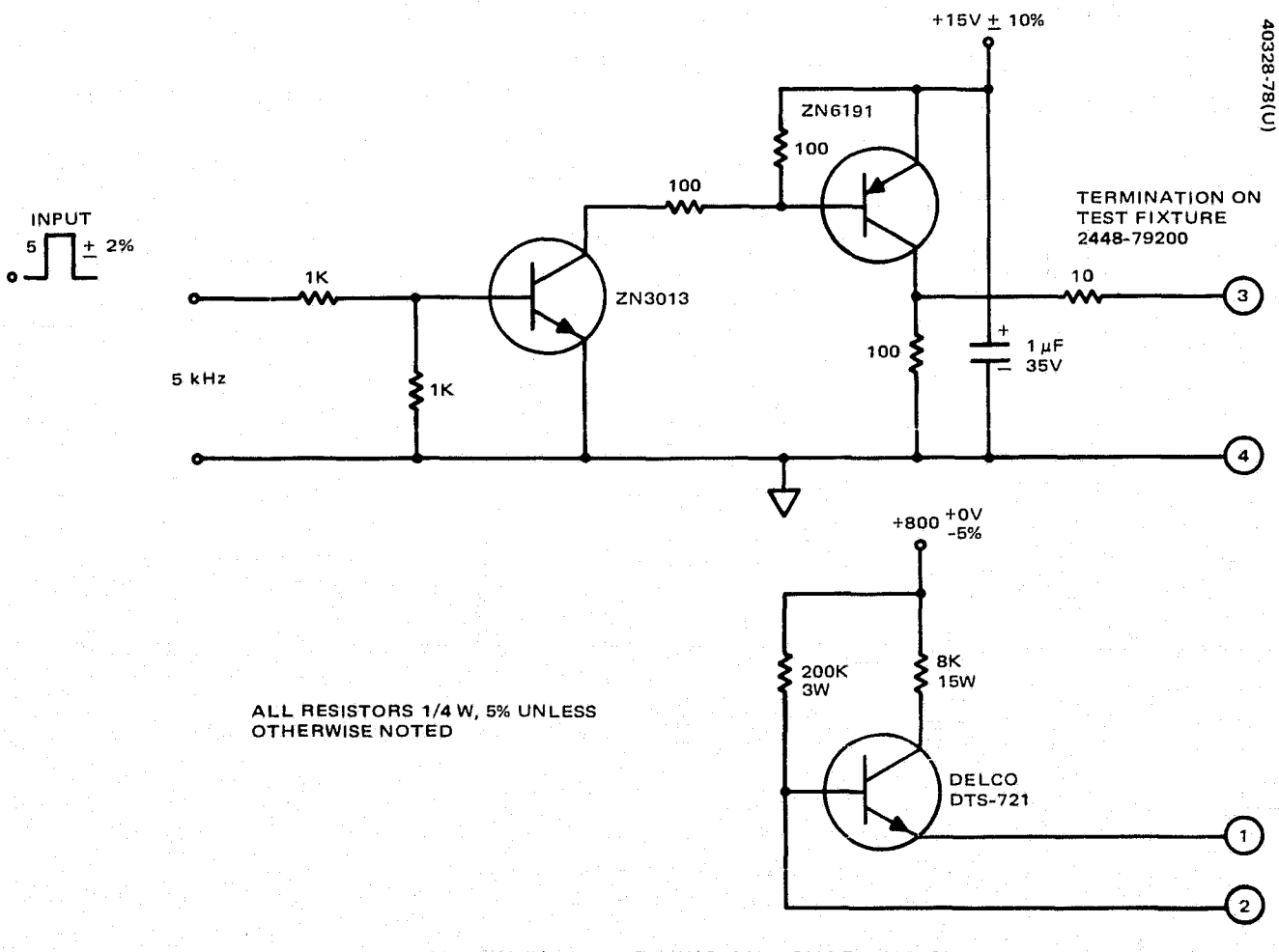

FIGURE B-4. TEST FIXTURE – DRIVING AND CHARGING CIRCUIT

Turn on H.V. power supply first and using the digital multimeter, measure the voltage. Adjust the supply to read 800 $^{+0}_{-2}$ volts percent. Leave the multimeter connected as a monitor.

Turn on the low voltage power supply which had previously been set to 15 volts ±1 Vdc.

Caution: In all testing, it is important that when applying power to the circuit, the high voltage supply must be turned on before the low voltage supply.

With all power on and the oscilloscope adjusted properly, the following data should be taken and fall within the limits specified:

Unit Type 4203-00740	-5	-4	-6
Output pulse	63 A ±10%	57 A ±10%	70 A ±10%
Output pulse width measured at one half current points	40 ns ±10%	36 ns ±10%	44 ns ±10%

Also record the following: part number and serial number.

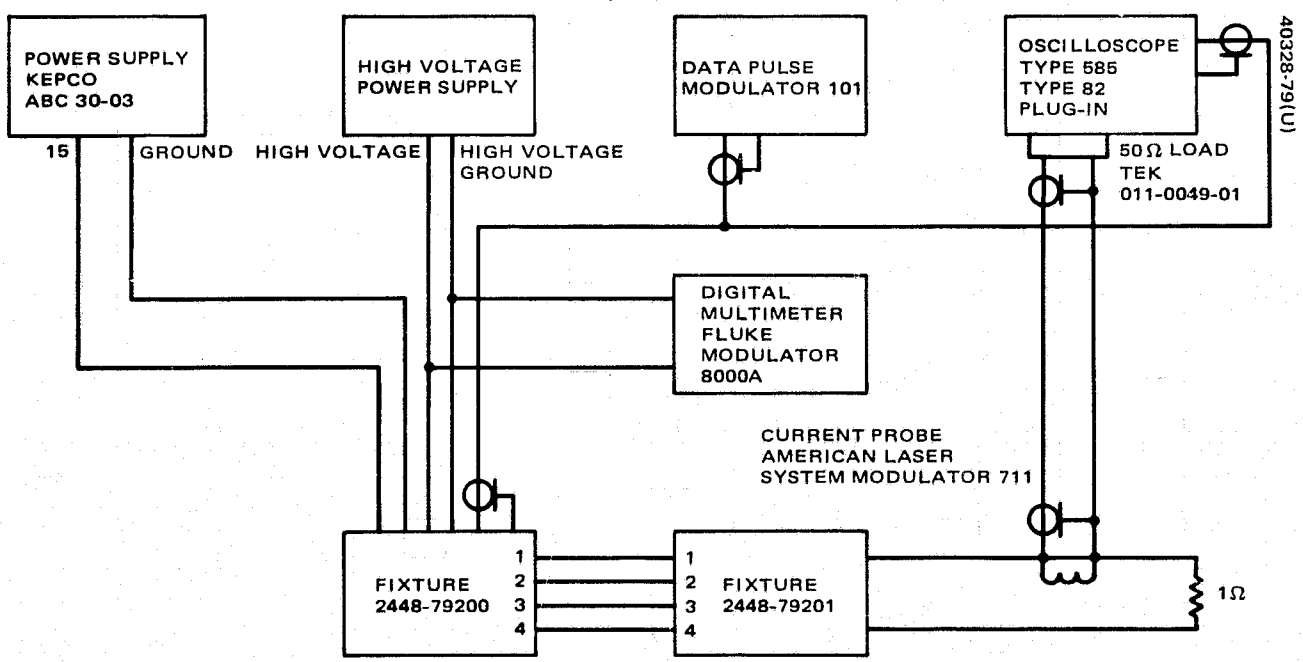

FIGURE B-5. IR MODULATOR TEST FIXTURE

APPENDIX C. OPTICAL COATING DATA

The optical coatings selected for the exposed optics are designed for high reflectance in the visible part of the optical spectrum and at 10.6 μm. The thermal analysis in this report assumed a net absorptance of solar energy of 3.8 percent. Under this assumption, mirror distortion due to solar absorption is negligible, approximately 0.01 λ at 10.6 μm. A much greater absorptive loss can be tolerated without causing undue distortion of the mirrors.

The assumption of 3.8 percent absorption was based upon the best solar rejection coating available. The actual coatings applied to the mirrors of the receiver subsystem have an effective solar absorption of 14 percent, or nearly four times greater than the coating assumed. Still, this results in less than λ/10 mirror distortion. Further, the 14 percent coating loss is clearly out of specification; new test sample coatings have been made that show typical absorption loss of about 4 percent.

The net coating absorption is obtained from integrating the product of the solar spectrum and the mirror absorption over the spectral range from 0.1 to 2 μm. The resultant net absorption coefficient for solar energy on the mirror surface over the entire solar range is obtained. Figure C-1 shows the solar spectrum intensity as a function of wavelength. Figure C-2 shows the reflectance profile of several coatings over the critical spectral region. These coatings are identified in Table C-1 and the net solar energy absorption values for each coating are given.

The fact that three coatings tested show absorption of 4 percent or less indicates that the Valpey coating is clearly out of specification; however, since the coating is satisfactory at 10.6 μm, and also since the thermally induced distortion from solar energy is not sufficient to cause loss of mirror figure, these coatings will remain as they are. If recoating them at a later date is desirable, the mirrors can be easily removed from the receiver subsystem.

New specifications have been determined for achieving the right type of solar rejection coatings in the future. Drawing modifications for the optical elements have been made.

TABLE C-1. NET SOLAR ABSORPTION OF SELECTED COATINGS

Coating No.	Type	Manufacturer	Net Solar Absorption, %
1	Ag (evap)	Theoretical	3.9
2	Enhanced Ag	Exotic materials	3.6
3	Multilayer over Ag	OCLI	3.8
4	ThF_4 over Ag	HRL	4.0
5	Multilayer over Ag	Valpey	14

Note: The deflectance of all coatings at 10 μm is greater than 99%.

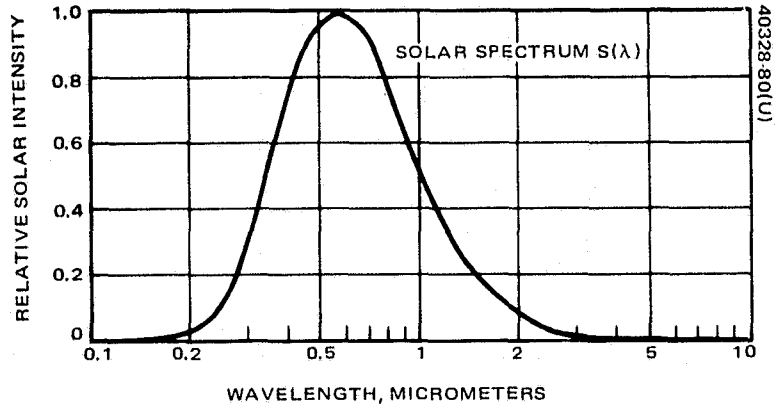

FIGURE C-1. RELATIVE SOLAR INTENSITY AS FUNCTION OF WAVELENGTH

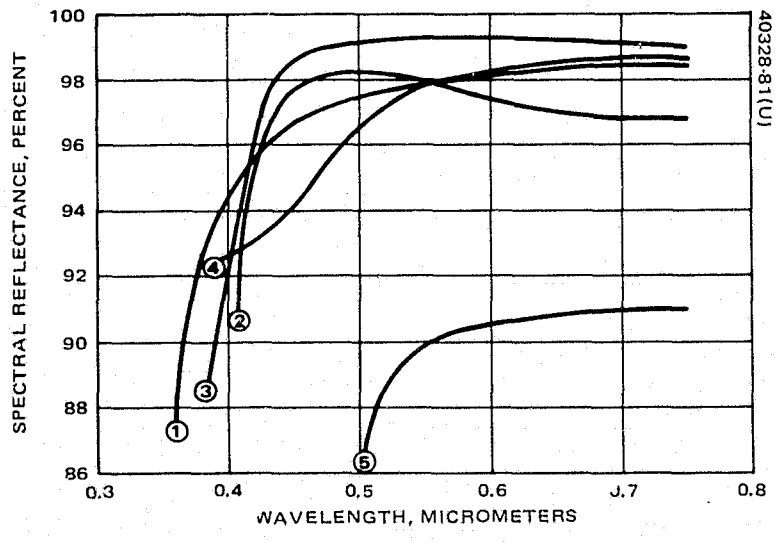

FIGURE C-2. SPECTRAL REFLECTANCE OF COATINGS

APPENDIX D. LIST OF DRAWINGS

This appendix provides a list of drawings, produced to date, related to the development of the opto-mechanical subsystem. There are 117 finished form 2 drawings and 1 precision layout.

OPTO-MECHANICAL SUBSYSTEM

Assembly	Size	Drawing Number	Nomenclature	Date	Revision	Quantity		Remarks
						Assembly	Subassembly	
Laser heterodyne Receiver assembly	E	1026550	Final assembly	8-13-73		1		4 sheets
	E	1026566	Installation control	7-6-73		1		
	D	1026569	Plate, 200 μM, iris, detector	6-28-73		1		
	E	1026581	Mirror, primary, paraboloidal	6-13-73	A	1		Revision A not dated
	D	1026585	Ring, clamp, flanged-primary mirror	6-20-73		1		
	C	1026586	Ring, inner-primary mirror	6-19-73		1		
	F	1026587	Support, optical mixer		A	1		Revision A dated 1-30-74
	E	1026592-1,-2	Witness sample, mirror	7-17-73	A	1(-1),1(-2)		Revision A not dated
	C	1026650	Plate, mounting, connector	7-7-73		1		
		1026600	Adjusting tool, primary mirror			1		Drawing number is 1026651 on final assembly drawing
		1026652	Adjusting tool, secondary mirror			1		Missing - never drawn
Housing, receiver	E	1026551	Assembly	6-22-73	A	1		(On final assembly). 2 sheets, Revision A dated 10-4-73
	E	1026552	Baseplate, mounting	6-12-73		1		
	E	1026553	Plate, radiation, cooler	6-6-73		1		
	D	1026554-1,-2	Stiffener	6-7-73		2(-1),2(-2)		
	C	1026555	Stiffener, short	7-6-73		2		
	F	1026556	Plate	6-6-73		1		
	D	1026565	Stiffener, long	7-7-73	A	1		Revision A dated 10-4-73
	C	1026567	Gusset	6-8-73		4		
	E	1026590	Support, cooler, radiation	6-25-73		1		
	C	1026667	Insert	7-30-73		2		
	C	1026594	Insert, plate, mounting	6-28-73		12		Not listed (or called out) on receiver housing assembly
Baffle	D	1026559	Subassembly	6-18-73		1		Used on 1026551 assembly
	D	1026559-99	Plate	6-18-73			1	Used on 1026559 subassembly
	D	1026561-1,-3	Stiffener	6-15-73	A		1(-1), 1(-3)	Revision A dated 10-2-73
	D	1026593-1	Stiffener, long	6-18-73	A		2	Revision A dated 10-2-73
End plate, primary mirror	F	1026560	Subassembly	6-20-73		1		Used on 1026551 assembly
	F	1026560-98	Strip	6-20-73			1	Used on 1026560 subassembly
	F	1026560-99	Plate	6-20-73			2	
	D	1026561-1,-2	Stiffener	6-15-73	A		1(-1),1(-2)	

Opto-Mechanical Subsystem (continued)

Assembly	Size	Drawing Number	Nomenclature	Date	Revision	Quantity		Remarks
						Assembly	Subassembly	
End plate, primary mirror (continued)	D	1026562	Ring	6-26-73			1	Used on 1026560 subassembly
	D	1026593-1,-2	Stiffener, long	6-18-73	A		1(-1),1(-2)	
End plate, secondary mirror	E	1026563	Subassembly	6-15-73		1		Used on 1026551 assembly
	D	1026561-1	Stiffener	6-15-73	A		2	Used on 1026563 subassembly
	E	1026563-98	Stiffener	6-15-73			1	
	E	1026563-99	Plate	6-15-73			2	
	D	1026564	Ring, mounting, gimbal	6-14-73			1	
	D	1026593-1	Stiffener	6-18-73	A		2	
Support, optical	F	1026599	Subassembly	7-6-73		1		Used on 1026551 assembly, 2 sheets
	C	1026555	Stiffener, short	7-6-73			2	Used on 1026599 subassembly
	D	1026565	Stiffener, long	7-7-73			1	
	F	1026599-93	Stiffener block	7-6-73			1	
	F	1026599-94	Stiffener block	7-6-73			1	
	F	1026599-95	Stiffener block	7-6-73			1	
	F	1026599-96	Stiffener block	7-6-73			1	
	F	1026599-97	Plate	7-6-73			1	
	F	1026599-98	Plate	7-6-73			1	
	F	1026599-99	Plate	7-6-73			1	
Mirror, pointing	E	1026579	Assembly	6-12-73	A	1		(on final assembly)
	E	1026579-99	Mirror	6-12-73			1	Used on 1026579 assembly
	B	1026589	Stud, mirror	11-14-73			3	
LO and cond.	?	1026582	Assembly	?		1		(on final assembly) Missing - never drawn
Beacon	?	1026583	Assembly	?		1		(on final assembly) Missing - never drawn
Cover	F	1026588	Assembly	6-27-73		1		(on final assembly)
	F	1026557	Plate, cover	6-8-73		1		Used on 1026588 assembly
	D	1026558	Sun shield	6-7-73		1		
Mirror, secondary and folding	D	1026598	Assembly	7-17-73		1		(on final assembly)
	D	1026578	Support, folding mirror	7-13-73		1		
	C	1026573	Ring, inner secondary mirror	6-13-73		1		
	C	1026572	Ring, clamp secondary mirror	6-13-73		1		
Mirror, secondary	C	1026574	Subassembly	6-19-73		1		Used on 1026598 assembly
	C	1026574-99	Support	6-19-73			1	Used on 1026574 subassembly
	E	1026575	Mirror, secondary ellipsoidal	6-12-73	A		1	Revision A not dated

Opto-Mechanical Subsystem (continued)

Assembly	Size	Drawing Number	Nomenclature	Date	Revision	Quantity		Remarks
						Assembly	Subassembly	
Mirror, folding	C	1026591	Subassembly	7-18-73		1		Used on 1026598 assembly
	C	1026576	Plate	7-14-73			1	Used on 1026591 subassembly
	E	1026584	Mirror, secondary folding	7-13-73	A		1	Revision A not dated
Mirror, beam combining	D	1026663	Assembly	8-9-73		1		(on final assembly)
	F	1026653	Housing	7-9-73		1		
	D	1026656	Ring, inner	7-20-73		1		
	F	1026657	Ring, clamp	7-10-73	B	1		Revision B dated 10-8-73
	E	1026662	Mirror	6-12-73	A	1		Revision A not dated
Laser and beacon folding mirror	D	1026664-1	Assembly	8-10-73		2		(On final assembly)
	F	1026654-1	Mirror housing	7-7-73		1		
	D	1026656	Ring, inner	7-20-73		1		
	F	1026657	Ring, clamp	7-10-73	B	1		Revision B dated 10-8-73
	E	1026661	Mirror, folding	6-12-73		1		
Laser and beacon folding mirror	D	1026664-2	Assembly	8-10-73		1		(On final assembly)
	F	1026654-2	Mirror, housing	7-7-73		1		
	D	1026656	Ring, inner	7-20-73		1		
	F	1026657	Ring, clamp	7-10-73	B	1		Revision B dated 10-8-73
	E	1026661	Mirror, folding	6-12-73		1		
Laser and beacon folding mirror	D	1026664-3	Assembly	8-10-73		1		(On final assembly)
	D	1026577	Beacon beam splitter	7-18-73		1		
	F	1026654-2	Mirror housing	7-7-73		1		
	D	1026656	Ring, inner	7-20-73		1		
	F	1026657	Ring, clamp	7-10-73	B	1		Revision B dated 10-8-73
Image motion compensation	D	1026665	Assembly	8-9-73		1		(2 if IMC 1 and IMC 2 are the same), (used on final assembly)
	D	1026596	Aperture stop	6-15-73		1		Needs to be redrawn — IMC 1 and IMC 2
	C	1026597	Base, mounting	6-15-73		1		Are superimposed - also IMC mirrors are not called out Dimension A and C need to be changed
	E	1026660-1	Mirror	6-12-73	A	1		Revision A not dated
	E	1026660-2	Mirror	6-12-73	A	1		

Opto-Mechanical Subsystem (continued)

Assembly	Size	Drawing Number	Nomenclature	Date	Revision	Quantity		Remarks
						Assembly	Subassembly	
OM gimbal subsystem	J	3406000-100	Assembly	8-3-73	A	1		(On final assembly) was No. 1026580 on final assembly drawing - Revision A dated 11-19-73
	A	908303-2	Motor		H	2		5 sheets - no release date
	D	255336	Resistor, variable	4-28-71	A	2		R
	C	3184869	Washer, wavy	10-14-68		1		
	B	3217701	Spacer	8-11-69		AR		
	J	3406002	Yoke - OM gimbal	5-10-73	A	1		Revision A dated 11-19-73
	E	3406003	Gimbal	5-14-73		1		
	C	3406004	Spring retainer	5-14-73		1		
	C	3406005	Potentiometer, support	5-14-73		1		
	C	3406008-1,-2	Gear sector, elevation	5-22-73		1(-1),1(-2)		
	C	3406009-1,-2	Azimuth sector gear	7-5-73		1(-1),1(-2)		
	C	3406010	Shaft	7-5-73		2		
	C	3406011	Bushing	7-5-73	A	12		Revision A dated 10-2-73
	C	3406015	Shaft, worm-elevation	7-5-73		1		
	C	3406016	Shaft, worm-azimuth	7-5-73		1		
	C	3406017	Shaft, transfer	7-5-73		2		
	C	3406049	Pin-index	8-1-73		2		
	F	3393360	Saddle	6-5-74		1		Replaces 3406006
	D	3424751	Bushing, collar	11-14-73		3		
	D	3424752	Nut, bushing	11-15-73		3		
	C	3424887	Screw, adjustment	4-15-74		2		Replaces 3406007 - screw, support
	C	3424893	Bushing, screw-gimbal	4-17-74		2		
Bearing, ball -angular contact	C	3225394	Subassembly	3-18-69				Used on 3406000-100 assembly — 3 sheets
	A	988298-1,or -2	Bearing	9-11-68			1	Used on 3225394
		3225396	Retainer	3-20-69			1	subassembly
	C	3406014	Retainer, bearing	7-5-73		2		
10.6 μm Laser heterodyne receiver	E	SK2228	Optical layout	4-20-73				

APPENDIX E. STARK CELL STABILIZATION OF CO_2 LASER

Stark cell stabilization of CO_2 laser

T. A. Nussmeier and R. L. Abrams

Hughes Research Laboratories, 3011 Malibu Canyon Road, Malibu, California 90265
(Received 8 August 1974)

A technique is demonstrated for locking of a GHz tunable waveguide CO_2 laser to a voltage programmable absorption line in NH_2D. Precision frequency control is demonstrated over the tuning range of the laser and long-term frequency stability of better than ± 100 kHz is demonstrated. The advantages of the present technique are that no frequency modulation of the laser is required to generate an error signal and the laser frequency is determined by a linear relationship to the Stark cell voltage.

A number of approaches to the problem of laser frequency stabilization have been demonstrated, including frequency lock to a fixed absorption line in an external gas cell,[1] which may be either the same or a different molecule as the lasing species, and dither stabilization to the center of a Lamb dip in the power tuning curve,[2] which results in stabilization of the laser to line center. Most of the previously demonstrated techniques are designed for very accurate fixed frequency operation of gas lasers, for use as frequency standards and for spectroscopic applications. These approaches lack the versatility of continuous frequency control and, in most cases, require some form of laser frequency modulation to generate control signals. For many applications in optical communications and radar, a need exists for frequency control of gas lasers over their complete tuning range with moderate precision (on the order of 1 MHz). In particular, the recently developed gigahertz tunable waveguide CO_2 laser[3] is likely to become very useful for heterodyne optical communications systems, but no simple technique has been devised for frequency control within this tuning range.

In this paper, we demonstrate a technique for frequency stabilization of a CO_2 laser to an external gas cell, where the resonant frequency is controlled by the linear Stark effect. Error signals are generated by dither modulation of the Stark cell voltage rather than dithering of the laser, eliminating the sometimes troublesome frequency modulation of the laser output. Stabilization of a waveguide CO_2 laser to the Stark cell is accomplished with continuously programmable frequency tracking over the laser tuning range. Long-term frequency stability and measurements of precision of frequency reproducibility are described.

Stark tuning of molecular absorption lines has been studied extensively and has been used by several investigators for laser modulation.[4,5] A resonance absorption[6,7] in deuterated ammonia (NH_2D) was used by Johnston and Melville[8] to modulate the $P(20)$ 10.6-μm CO_2 laser transition. The reasonably high absorption and fortuitous location of this transition made it an ideal choice for the present investigation. The spectroscopic characteristics of the Stark-tuned absorption have been described previously,[6,7] and are briefly reviewed below.

The $P(20)$ 10.6-μm laser transition frequency exceeds the zero field splitting of the $(0_a 4_{04}) - (1_a 5_{05})$ transition in NH_2D by 1720 ± 60 MHz. The lower level $(0_a 4_{04})$ is nearly degenerate with and lies 644 MHz below the $(0_s 4_{14})$ level. These two states are strongly coupled by an electric field, resulting in a high-field linear Stark effect. The $(1_a 5_{05})$ upper level exhibits only a negligible second-order Stark effect.

In the high-field limit, the resonant absorption frequency δ, relative to $P(20)$ 10.6-μm line center is given by[7,9,10]

$$\delta = -2042 + 0.143|M|E, \tag{1}$$

where δ is given in MHz, M is the z component of J and can assume integer values from -4 to $+4$, and E is the electric field in V/cm. Thus, for $M = \pm 4$, an electric field of $E = 3570$ V/cm brings one component of the NH_2D absorption into resonance with the $P(20)$ 10.6-μm transition. Clearly, by variation of the field, the resonance can be tuned above or below the $P(20)$ line center. It is this effect which we have used to provide a voltage tunable reference frequency for stabilization of the CO_2 laser.

A diagram of the apparatus used to investigate Stark cell stabilization of the CO_2 laser is shown in Fig. 1. The laser is a tunable CO_2 waveguide device with a tuning range of ± 600 MHz from line center.[3] One mirror is mounted on a piezoelectric transducer arranged to control the length of the resonant cavity thus allowing control of the laser frequency. The opposite reflector is a 150 lines/mm diffraction grating used in the Littrow configuration with the specular component recovered as the laser output. The Stark cell consists of a 10-cm by 2-cm-diam glass tube sealed with NaCl windows and contains two polished stainless steel electrodes. Glass spacers maintain an even spacing between electrodes of 0.130 cm. The cell is filled with a 1:1 mixture of ND_3

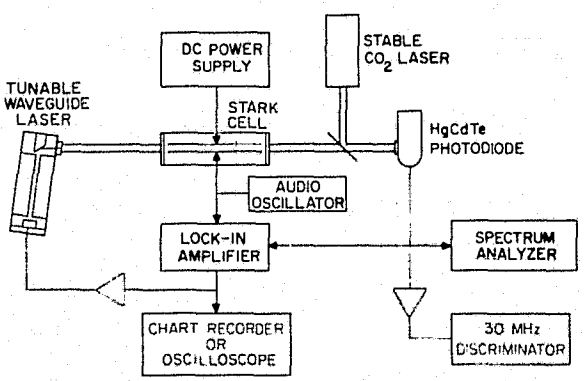

FIG. 1. Experimental arrangement for Stark cell stabilization measurements.

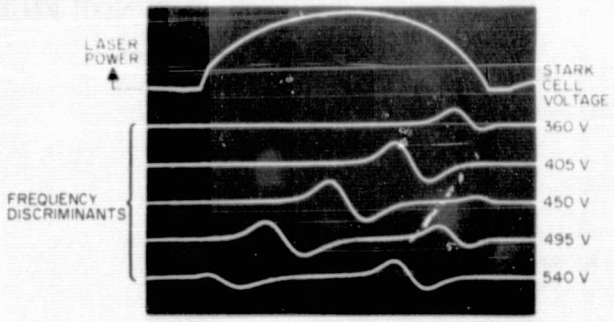

FIG. 2. Laser frequency discriminants for various Stark cell voltages. Top trace is the laser power profile, with frequency increasing to the left. The second resonance appearing at the higher voltages corresponds to $M = \pm 3$.

and NH_3, which combine to form NH_2D as well as other isotopic products (see Ref. 6). The optical detector is a high-speed HgCdTe photodiode direct coupled to provide a measure of total laser energy. The detector is also used to detect the Stark cell modulation and responds to the heterodyne difference frequency when a reference laser is used.

Laser frequency measurements were made by introducing a stable CO_2 laser onto a beam splitter located before the detector. This reference laser is dither stabilized to within ± 250 kHz of $P(20)$ line center with a peak-to-peak dither excursion of ± 4 MHz. The difference frequency between the two lasers is routed through a 0.01−500-MHz wide-band amplifier to a spectrum analyzer or to a 30-MHz electronic frequency discriminator.

One of the Stark electrodes is dc biased with a voltage from a precision high-voltage power supply, and the second electrode is driven at 10 kHz by an audio oscillator. The signal from the optical detector is phase-sensitively detected with respect to the modulating signal in a lock-in amplifier. The lock-in output, which becomes the laser frequency discriminant, drives a chart recorder, oscilloscope, or is amplified and fed back to the laser bimorph to complete the frequency control servo loop.

As the ac drive voltage to the Stark cell is increased, the peak absorption frequency deviation increases to the point where it becomes an appreciable fraction of the absorption linewidth. Further increases cause harmonic distortion and a loss of fundamental signal strength, thus an optimum ac voltage exists for a given linewidth (which is equal to the 84-MHz Doppler width for the pressures used in this experiment). To determine this voltage, the slope of the frequency discriminant at line center was measured as a function of ac voltage, and a broad maximum was found for a 20-V peak- to-peak drive. This value was used in all subsequent experiments.

The frequency discriminants for various Stark cell voltages are illustrated in Fig. 2. For these measurements, the waveguide laser frequency was swept through its tuning range and the lock-in output displayed on an oscilloscope. The top trace is a recording of the laser power profile for reference; five traces at different Stark voltages were recorded below. At the higher voltages the second resonance corresponding to $M = 3$ also appears within the laser power profile, leading to the possibility of a false lock. This is easily avoided by acquiring initially at a lower voltage where no ambiguity exists, and then tuning to the higher frequency by increasing the Stark voltage.

When the Stark cell is tuned near the edge of the laser tuning range, the discriminant becomes assymmetric due to the variation of laser power with frequency. The zero crossing, however, depends only on the Stark cell voltage and not on the slope of the laser power tuning curve. This would not be true, however, if the discriminant were generated by frequency modulation of the laser, as is required for stabilization to a fixed absorption line.

With the frequency control loop closed, the gain and time constant of the lock-in were adjusted empirically to achieve a stable system. Using the spectrum analyzer the laser frequency was measured with respect to the reference laser as the voltage on the Stark cell was varied. It was found that near line center the laser frequency would repeat to within the accuracy of measurement (± 200 kHz limited by the fm on the dither-stabilized reference laser), but that near the edges of the power-versus-frequency profile, laser frequency would only repeat within ± 2 MHz. A decrease in frequency stability at these frequencies, as well as reduced repeatability, implies that the nonlinear servo gain modulation caused by the slope of the power profile reduced the servo loop stability. Although unnecessary for many applications, sophisticated servo design techniques for nonlinear compensation are available to improve these figures.

The servo loop was opened and the laser frequency adjusted manually to set the discriminant output at the zero crossing. When the heterodyne frequency versus

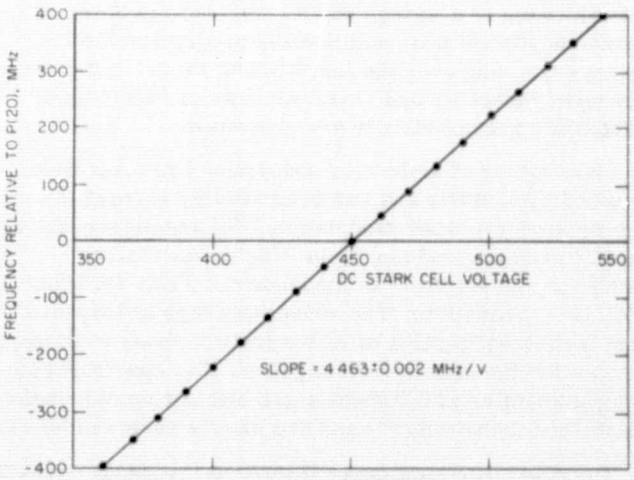

FIG. 3. Measured frequency of the NH_2D absorption versus Stark cell voltage. Solid line is a least-squares fit of the data to a straight line. The extrapolated zero voltage intercept is −2011.9 ± 0.9 MHz below line center.

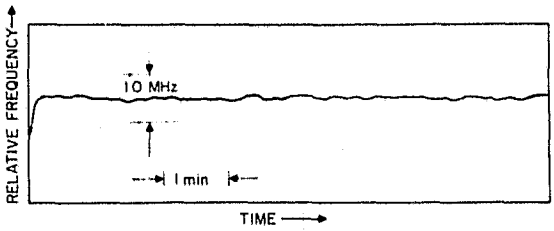

FIG. 4. Relative frequency between line-center-stabilized reference laser and Stark-stabilized waveguide laser. Run continued for 2 h without change. The initial transient occurred when servo loop was closed, locking the laser to the Stark cell.

Stark voltage is measured using this technique, repeatability is limited only by measurement accuracy at all frequencies. These data, plotted in Fig. 3, were fitted to a straight line with a resultant slope of 4.463 ± 0.002 MHz/V and an extrapolated zero voltage linear intercept of -2011.9 ± 0.9 MHz relative to line center. These numbers and the predicted values [Eq. (1)] agree within the accuracy of the Stark electrode spacing measurement ($\pm 1\%$).

In order to test the long-term stability of this technique, we made a 2-h frequency stability run. The waveguide laser was stabilized to the Stark cell 30 MHz off line center and the heterodyne signal was demodulated with an electronic discriminator. The discriminator output was filtered to remove the reference laser dither modulation and recorded on a strip chart, a portion of which is shown in Fig. 4. The two lasers maintained a constant offset within ± 100 kHz throughout the test. By contrast, the unstabilized laser drifted outside the discriminator passband (± 5 MHz) within 5 min.

A new technique for frequency control and stabilization of the CO_2 laser has been demonstrated. The technique will provide a means for frequency control of the newly developed tunable waveguide CO_2 lasers and should increase the versatility of CO_2 lasers for spectroscopy and other related laboratory applications.

The reported experiments were all conducted using the $P(20)$ 10.6-μm CO_2 laser transition. NH_2D can also be used to stabilize several other lines, including the $P(14)$ and $R(12)$ transitions of the 00^01-10^00 vibrational band. Stark effect modulation has been reported on virtually all of the important CO_2 transitions[11] and work is presently underway to apply Stark stabilization to additional laser wavelengths.

We wish to acknowledge helpful discussions with R. G. Brewer and A. R. Johnston, and to thank A. R. Johnston and M. Shumate for furnishing a sample of ND_3.

[1]C. Freed and A. Javan, Appl. Phys. Lett. **17**, 53 (1970).
[2]C. Borde and L. Henry, IEEE J. Quantum Electron. **QE-4**, 874 (1968).
[3]R. L. Abrams, Appl. Phys. Lett. **25**, 304 (1974).
[4]A. Landman and H. Marantz, IEEE J. of Quantum Electron. **QE-5**, 330 (1969).
[5]P. C. Claspy and Y. H. Pao, IEEE J. Quantum Electron. **QE-7**, 512 (1971).
[6]R. G. Brewer, M. J. Kelly, and A. Javan, Phys. Rev. Lett. **23**, 559 (1969).
[7]M. J. Kelly, R. E. Francke, and M. S. Feld, J. Chem. Phys. **53**, 2979 (1970).
[8]A. R. Johnston and R. D. S. Melville, Jr., Appl. Phys. Lett. **19**, 503 (1971).
[9]The Stark tuning factor is determined by the dipole moment between the nearly degenerate lower states. We calculated the dipole moment using the equations and tables of Ref. 8, but our value differs slightly from that given in Ref. 6.
[10]C. H. Townes and A. L. Schawlow, *Microwave Spectroscopy* (McGraw-Hill, New York, 1955), pp. 254—255.
[11]J. M. Martin, V. J. Corcoran, and W. T. Smith, IEEE J. Quantum Electron. **QE-10**, 191 (1974).

APPENDIX F. SERVO SYSTEM TEST PROCEDURES

The following subsections delineate the parameters to be measured in the servo tests and briefly describe how the measurements are made.

F.1 TRACKING LOOP

1) Noise Equivalent Error – This test is a measure of the noise equivalent angle (NEA) of the tracking loop, when the input beam is not power limited. This quantity is determined by measuring the rms voltage at the output of the detector and relating this voltage through the proper scale factor to input beam jitter. For this test, the rotary table will be fixed.

2) Tracking Error With Target Motion – This procedure is the same as above except the table is moved by hand back and forth within the 0.2° by 0.2° IMC field of view at rates up to 0.03 deg/sec.

3) Tracking Error Caused by Stepper Disturbance – This procedure is the same as above except that the table is rotated to cause the stepper to be energized. The output of the detector is recorded. For this test the peak error is of interest.

4) Tracking Loop Bandwidth – This bandwidth is determined by injecting a constant amplitude sinusoid into the outer loop at the integrator output and measuring the relative amplitude and phase of the signal after transversing the loop and returning to the integrator output. As the frequency is increased the relative amplitude will decrease. The frequency at which the relative ratio = 0.707 is the bandwidth.

5) Acquisition Field of View – Determined by moving the rotary table each side of zero with the gimbal loop disabled and determining when the HV 0 ampere driver saturates.

6) Acquisition Dynamics – For this test the gimbal loop is disabled. The beam is placed in a known position just outside the 0.2° by 0.2° IMC field of view. With the tracking loop enabled, the rotary is swept slowly through the IMC field of view. This is repeated for increasing rates up to 0.03 deg/sec.

7) IMC Bandwidth – Procedure is the same as for the tracking loop bandwidth except the generator signal is injected at the unused input to the HV amplifier, and the output is recorded at the other input.

F.2 GIMBAL LOOP

1) Gimbal Range – The maximum gimbal range for each axis is determined by rotating the table slowly in each direction and noting when the electrical stops are actuated.

2) Gimbal Step Rate – The gimbal step rate is determined by measuring the time required to traverse a selected gimbal range, which is measured by the table readout.

3) Gimbal Tracking – The table is moved by hand within the 20° by 20° field of view, while angle position, IMC drive voltage, and table rate are monitored.

4) Gimbal Angle Readout Accuracy – The point-to-point repeatability of the gimbal readout will be determined as follows: The tracking systems are disabled (manual mode). The rotary table is rotated to bring the beam within the detector field of view to give a peak detector response. The table is then rotated to a selected angle, and the gimbal is stepped manually until the response is again at a peak. The table angle and gimbal angle readouts are then recorded. This procedure is repeated for several points throughout the gimbal range.

5) Gimbal/IMC Alignment – Determined as follows: First the gimbals are "zeroed" using the optical slip reference. Next the tilt gimbal will be manually rotated to 0.05°, while the system is tracking. The gimbal angle and IMC position (Burr-Brown output) for both axes will be recorded. If the X-axis IMC has an output other than zero, the roll gimbal is adjusted in steps, and the above test is repeated until the X-axis IMC shows a minimum dc offset. The required roll axis adjustment is recorded.

6) Gimbal Axes Orthogonality – With the roll axis adjusted as in item 5, the gimbals $\pm 0.05°$ are stepped (in turn) and the IMC outputs for both axes are recorded.

7) Gimbal Axis Cross-Coupling Dynamics – With the system tracking, each gimbal is stepped in turn for short bursts and the filtered error signal for each axis is recorded.